Ph. D. thesis

Development of artificially engineered nanoparticles by surface modification and their biomedical applications

Aminul Islam

Ph.D. Registration No.: 11

Session: 2015-2016

Re-registration No: 75, Session: 2020-2021

Department of Physics

University of Dhaka, Bangladesh

DEPARTMENT OF PHYSICS, UNIVERSITY OF DHAKA

JULY 2023

Ph.D.Thesis

DEVELOPMENT OF ARTIFICIALLY ENGINEERED NANOPARTICLES BY SURFACE MODIFICATION AND THEIR BIOMEDICAL APPLICATIONS

Aminul Islam
Ph.D. Registration No.: 11
Session: 2015-2016
Department of Physics
University of Dhaka, Bangladesh

Supervisor:
Professor Dr. Ishtiaque M. Syed
Department of Physics
University of Dhaka, Bangladesh

Co-Supervisor:
Dr. Engr. Sheikh Manjura Hoque
Chief Scientific Officer
& Head, Materials Science Division
Atomic Energy Centre, Dhaka

Acknowledgements:

I would like to express my sincere gratitude to my supervisor, Professor Dr. Ishtiaque M. Syed, for providing me with invaluable guidance and unwavering support. I have greatly benefited from his exceptional mentorship, insightful feedback, and encouragement in shaping my research and achieving my academic goals.As a researcher, I have thrived due to his dedication to academic excellence and his unwavering commitment to his students.

I want to express my deepest gratitude to Dr. Engr. Sheikh Manjura Hoque for her invaluable support, guidance, and inspiration throughout my Ph.D. journey. Her vast knowledge, expertise, and dedication have been instrumental in shaping my research and helping me overcome various challenges. Her insightful feedback and constructive criticism have pushed me beyond my limits and helped me develop my research skills. I will be forever grateful for her guidance and support.

I would like to acknowledge the support provided by the Materials Science Division, Atomic Energy Centre, Dhakafor this work. All the scientists, researchers, and staff of the materials science division help me lot in carrying out my research. I want to thank the Atomic Energy Commission members for their help and encouragement.

I am also grateful to the Annual Development Project (ADP) of the Planning Commission, Government of Bangladesh (the project ID 5003, Nano Project), and the International Science Program, Uppsala University, Sweden, for their support in this research work.

Moreover, I would like to thank the Department of Physics, Semiconductor Technology Research Centre (STRC) and Centre for Advanced Research in Sciences (CARS) of the University of Dhaka, for supporting this research.They have provided guidance and resources for this research project. Their expertise and enthusiasm have been invaluable in helping bring this research to fruition.

Finally, I would like to express gratitude to my family for their constant support during the research work. Without their encouragement and guidance, this research would not have been possible.

Dedicated to my parents, sisters and family.

CANDIDATE DECLEARATION

It is hereby declared that this thesis or any part of it has not been submitted elsewhere for the award of any degree or diploma.

Aminul Islam
Ph.D. Registration No.: 11
Session: 2015-2016
Department of Physics
University of Dhaka, Bangladesh

Certificate of Approval

We certify that Aminul Islam's thesis, "Development of artificially engineered nanoparticles by surface modification and their biomedical applications" is the result of his original research conducted under our supervision. We extensively reviewed the thesis and determined that it satisfied the required standards of the Doctor of Philosophy (Ph. D) degree in Physics from the University of Dhaka. To the best of our khowledge, this thesis still has not been submitted or used for any other academic honour or degree.

Co-Supervisor: **Dr. Engr. Sheikh Manjura Hoque**
Chief Scientific Officer
& Head, Materials Science Division
Atomic Energy Centre, Dhaka

Supervisor: **Professor Dr. Ishtiaque M. Syed**
Department of Physics
University of Dhaka, Bangladesh

ABSTRACT

The effectiveness of cobalt-substituted magnesium ferrite $Mg_{1-x}Co_xFe_2O_4$ (MCFO) ($0 \leq x \leq 1$ with $\Delta x = 0.1$) and polymer nanohybrids for biomedical applications, particularly as the contrast agent for magnetic resonance imaging/angiography and thermotherapeutic applications for malignant lesion, was investigated by synthesizing these nanoparticles using the chemical co-precipitation method. Nanomaterials employed as effective media for successful applications in the disciplines mentioned above are determined by the engineering parameter, which works as the figure-of-merit: the relaxivities (r_1 and r_2) for MRI and specific loss power (SLP). Particle size, shape, distribution, and coating agent affect magnetization and anisotropy, which impacts the parameters of relaxivities and specific loss power. It is intriguing to note that the anisotropy and particle volume substantially control the relaxivities and specific loss powers, which Néel and Brownian relaxation govern. Relaxivities and specific loss of power can be either beneficial or detrimental by hysteresis loss. When the ratio of the MRI negative relaxivity values (r_2) to the positive reference value (r_1) is high, the contrast agent has a negative effect, and vice versa when the ratio is low. The values of r_1 and r_2 are highly sensitive to the nanoparticle's magnetic and structural characteristics. Again, SLP is highly dependent on magnetic anisotropy, and limited anisotropy will always increase the value of SLP, leading to better hyperthermia performance. Spin flip at radio rf magnetic fields and Neel relaxation are impeded under higher anisotropy conditions. Again, Brownian relaxation is frustrated by the large particle size. Anisotropy and structural characteristics were investigated in Co-substituted Magnesium ferrite with an atom fraction increase of x = 0.1. MRI/MRA contrast agents were studied using particles

of all compositions in their as-prepared state. Particle size dependence SLP and temperature rise for hyperthermia and/or laser ablation were studied by varying the size of the particles through controlled annealing at 200°C, 400°C, 600°C, and 800°C, and then encapsulating the particles in chitosan. This study aims to learn the structure-property relationship and their effect on magnetic nanoparticle-mediated MRI and thermotherapy using MCFO and chitosan/dextran/polyethylene glycol (PEG) nanohybrid.

Table of contents

List of Figure

Content Page

List of table

Content Page

List of Abbreviations

ACF	Autocorrelation Function
AMF	Alternating Magnetic Field
ARRIVE	Animal Research: Reporting of In Vivo Experiments
A-site	Tetrahedral Site
BF	Bright Field
B-site	Octachdral Site

CA	Contrast Agent
Caco-2	Colorectal Adenocarcinoma
CAN	A Controller Area Network
CCD	Charged-coupled Device
DI	Deionized
DLS	Dynamic Light Scattering
DMEM	Dulbecco's Modified Eagles' Medium
DVLO	Derjaguin, Verwey, Landau, and Overbeek's
EDAX XEDS	Energy-dispersive X-ray Analysis
EDS	Electron Diffraction Spectroscopy
EELS	Electron Energy-loss Spectroscopy
ELNES	Energy-loss Near-edge Structure
EPI	Echo-planar Imaging
FA	Flip Angle
FID	Free Induction Decay
FOV	Field Of View
FSE	Fast Spin Echo
FTIR	Fourier Transform Infrared
HAADF	High-angle Annular Dark-field
HEK293	Human Embryonic Kidney
HRTEM	High-resolution Transmission Electron Microscopy
LMH	Local Magnetic Hyperthermia
IR	Infrared
LRT	Linear Response Theory
MCFO	$Mg_{1-x}Co_xFe_2O_4$ $(0 \leq x \leq 1$ with $\Delta x = 0.1)$
MFH	Magnetic Fluid Hyperthermia
MH	Magnetic Hyperthermia
MIP	Maximum Intensity Projection
MNPs	Magnetic Nanoparticles
MR	Magnetic Resonance
MRA	Magnetic Resonance Angiography
MRI	Magnetic Resonance Imaging
MTT	3-[4,5-Dimethylthiazol-2-yl]-2,5 Diphenyl Tetrazolium Bromide
NMR	Nuclear Magnetic Resonance
PC	Phase-contrast
PCS	Photon Correlation Spectroscopy
PEG	Polyethlene Glycol
PPMS	Physical Property Measurement System
RF	Radio Frequency
SAED	Selected Area Diffraction
SAR	Specific Absorption Rate
SCSAM	The Swagelok Center for Surface Analysis of Materials

SKBR-3	Breast Adenocarcinoma
SLP	Specific Loss Power
SNR	Signal-to-noise Ratio
STEM	Scaning Transmission Electron Microscopy
TE	Echo Time
TEM	Transmission Electron Microscopy
THK	Thickness
TOF	Time-of-flight
TR	Repetition Time
VH	Vertical or Horizontal
VSM	Vibrating Sample Magnetometer
VV	Vertically Vertical
XRD	X-ray Diffractometer

CHAPTER 1: INTRODUCTION

1.1. Introduction

There are many biological objects smaller than the nanoparticles of superparamagnetic spinel ferrite. Several biomedical applications can thus be achieved with them. These are local magnetic hyperthermia, magnetic resonance imaging (MRI) contrast dye, targeted drug delivery, tissue repair, immunoassay, detoxification of body fluids, cell separation, etc[1–6]. In today's world, these nanoparticles are of great significance for diagnosis and treatment at the molecular level. Nanoparticles' size, shape, and homogeneity are extensively studied for colloidal suspensions. Nanoparticles' composition is essential in enhancing their magnetic and physical properties. Nanoparticles are typically in the range of <20 nm in size, allowing them to have a large surface area[7,8]. Due to the intense surface activity, surface modification enables targeted distribution and biocompatibility. Organic polymers (dextran, chitosan, polyethylene glycol, polysorbate, polyaniline, etc.), organic surfactants (dodecyl amine, sodium oleate, etc.), inorganic materials (gold, silica, carbon, etc.), and bioactive molecules (liposomes, peptides, ligands, etc.) are just a few examples of the many possible coating materials for nanoparticles.

The significant parameters necessary for biomedical applications can be effectively controlled by coating and maintaining the surface's shape, size, surface charge, pH, and hydrodynamic diameter. Smaller particles with consistent physical and chemical characteristics have a higher magnetic moment for biomagnetic applications[3,9,10]. The magnetic properties of ferrite nanoparticles are susceptible to the cation distribution of the tetrahedral (A-site) and octahedral (B-site) sites. The environment of the preparation technique can control its size and cation distribution.

Magnetic fluid hyperthermia (MFH) was paid substantial attention as a therapy for cancer employing radio frequency (RF). Malignant cells are locally heated when nanoparticles are gathered inside them. Magnetic nanoparticles mediate the magnetic field for localized heating. Localized hyperthermia based on magnetic fluid causes the tumour temperature to rise to 42–46°C when an RF magnetic field is applied for 30-60 minutes. As a result of this heat generation, the cancerous tissue is damaged or weakened. The disordered assembly of blood vessels in tumours and cancerous tissues makes them porous. The damage is therefore caused to locally confined tumours or deeply rooted tumours. Magnetic fluid hyperthermia has many advantages over other magnetic thermotherapy methods, such as thermoabalation. During thermoablation, cancerous cells are heated to 56^{o}C for a short time, which may cause widespread necrosis, coagulation, and carbonization of cancerous tissue[11–14].

MRI visualizes brains, soft tissues, nervous systems, cardiovascular function, and tumors. Nanoparticles have remarkable properties that make them ideal MRI contrast agents. These properties include their tiny size, enormous surface area, high magnetic moment, and zero or negligible coercivity. MRI contrast enhancement occurs as particles of different sizes, magnetic moments, and anisotropy constant interact with adjacent water protons. T_2 MRI contrast agents could be made from magnetic nanoparticles with high crystallinity[15–21]. Using gadolinium-based nanoparticles as contrast agents in hospital MRIs helps identify weak kidneys. For many MRI applications, particularly those involving the detection of malignant tissue, a contrast agent is necessary. Even though ferrite nanoparticles have been the subject of extensive research as MRI contrast agents, it still needs to be determined to establish a biocompatible and effective composition.

Magnetic resonance angiography (MRA) is a considerably advanced clinical tool for noninvasive vascular imaging[22–24]. Therefore, it is extensively utilized to diagnose injuries like stenosis, intracranial aneurysms, aortic coarctation, aortic dissection, the cause of a stroke, heart disease, and blockage of vessels[25–29]. Also, MRA is one of the best additions for investigating suspected venous thrombosis inside the chest, abdomen, and pelvis, which will most probably replace formal X-ray angiography by resuming technical progress[27,30].

A contrast agent is required for many MRI applications, especially those involving the detection of cancerous tissue. Even though ferrite nanoparticles have been the topic of in-depth investigation as MRI contrast agents, it is still being determined what composition will be the most effective and biocompatible[10]. Phase-contrast (PC) and time-of-flight (TOF) angiography were two methods utilized in MRA to measure the motion characteristics of blood [26,31]. PC MRA can observe and quantify blood flow by recording the flow velocity in the MR signal phase. The MR signal's phase changes due to the passage of blood along a magnetic field gradient. On a PC, pairs of images with various flow sensitivities are received. For instance, positive phase shifts are produced during one photograph of each couple using a gradient of positive polarity. A negative polarity gradient causes negative phase shifts in the other image. Blood vessels can be seen by removing the stationary tissues via image subtraction[32–34]. The foundation of TOF in MRA is that T_1 for moving water is shorter than T_1 for stagnant water. The variance is related to the spins being saturated by radiofrequency stimulation when stationary, which causes the spins to vary.

Additionally, as new spins with complete magnetization replace the static spins, the signal is increased. The perception of TOF MRA systems depends on spin saturation. In the TOF MRA investigation, a contrast agent (CA) improves the contrast between blood and tissue, reducing the T_1 relaxation time and improving the clarity of the vascular tree [35–37]. Some literature reviews are

executed in the next section to find appropriate superparamagnetic spinel ferrite nanoparticles and surface modification for biomedical applications.

1.2. Literature review

Hoque[10] investigated the Chitosan and PEG-coated superparamagnetic $Fe_xCo_{1-x}Fe_2O_4$ synthesized by chemical co-precipitation process. Saturation magnetization, transverse relaxivity, and magnetic hyperthermia properties improved with the addition of cobalt content for both Chitosan-coated and PEG-coated $Fe_xCo_{1-x}Fe_2O_4$ nanoparticls. All the Chitosan-coated and PEG-coated $Fe_xCo_{1-x}Fe_2O_4$ exhibited significant effect on cell death of tumor cells.

Gupta[5] discusses in his review article that superparamagnetic iron oxide nanoparticles having proper surface chemistry were extensively utilized experimentally for several biomedical and bioengineering applications, which require high magnetization values and smaller sizes to get uniform physical and chemical properties. These applications require a biocompatible surface coating of the nanoparticles, which permits precise particle localization and targeted delivery. How nanoparticles are coated on the surface dramatically affects their biokinetics and biodistribution in the body.

Ramnandan[38] analyzed the $MgFe_2O_4$ nanoparticles prospect to deliver the doxorubicin anticancer drug. The band shift of Fourier transform infrared spectroscopy was used to demonstrate that the $MgFe_2O_4$ nanoparticles in their investigation were produced by the glycol-thermal technique and surface functionalized with chitosan, polyvinyl alcohol, and polyethylene glycol. They investigated that chitosan-coated superparamagnetic $MgFe_2O_4$ nanoparticles encapsulate the highest 84.28% doxorubicin and polyvinyl alcohol-coated $MgFe_2O_4$

nanoparticles encapsulate the lowest 59.49% doxorubicin. In the human embryonic kidney (HEK293), colorectal adenocarcinoma (Caco-2), and breast adenocarcinoma (SKBR-3) cell lines, all of the chitosan, polyvinyl alcohol, and polyethylene glycol functionalized $MgFe_2O_4$ nanoparticles were discovered to be harmless. When those particles were loaded with doxorubicin, they significantly diminished cell viability dose-dependently. Among them, doxorubicin encapsulated chitosan-coated $MgFe_2O_4$ nanoparticles retained superior anticancer activity.

Khot[39] studied $MgFe_2O_4$ nanoparticles with sizes near 20 nm prepared by a combustion method and coated with dextran to investigate their magnetic particle hyperthermia properties. The maximum temperature rise obtained was 73.32 °C, and the maximum specific absorption rate was 85.57 Wg^{-1} for 10 mg ml^{-1} dextran-coated $MgFe_2O_4$ nanoparticles at 26.7 kAm^{-1} alternating magnetic field. The dextran-coated nanoparticles exhibited good viability on mice fibroblast L929 cells.

Mazarío[40] investigated the colloidal, magnetic, and relaxometry properties of cobalt ferrite nanoparticles synthesized in aqueous media by an electrochemical synthesis technique. Using the MTT (3-[4,5-dimethylthiazol-2-yl]-2,5-diphenyl tetrazolium bromide) assay, a durable and biocompatible targeting conjugate nanoparticle-folic acid was created, positively targeting folic acid receptors in HeLa (human cervical carcinoma) cells. The conjugate of cobalt ferrite nanoparticles and folic acid in colloidal suspension had a transverse relaxivity of 479 $mM^{-1}s^{-1}$. Cobalt ferrite nanoparticle-folic acid can be a feasible contrast agent in magnetic resonance imaging because in vitro testing on HeLa cells revealed a critical effect in negative T_2 contrast. Omelyanchik[41] examined how the annealing temperature affected how cobalt ferrite nanoparticles implanted in an amorphous silica matrix were created using the sol-gel auto-

combustion method. The findings demonstrate that heat treatments control a complicated magnetic anisotropy equilibrium between core and surface contributions. The effective magnetic anisotropy constant rises with lowering annealing temperature, and particle size rises with rising annealing temperature.

Zahraei[41] studied manganese zinc ferrite nanoparticles synthesized by the hydrothermal method. Manganese zinc ferrites were coated with chitosan by the ionic gelation method using sodium tripolyphosphate as a crosslinker to improve the colloidal stability for biomedical applications. The hydrodynamic size of chitosan-coated manganese zinc ferrite nanoparticles is 300 nm, and the polydispersity index is 0.3. The values of transverse and longitudinal relaxivities of the investigated chitosan-coated manganese zinc ferrite nanoparticles were 315.8 and 5.0 mMs^{-1}.

Kamlesh[42] synthesized cobalt ferrite nanoparticles using co-precipitation and investigated structural and magnetic properties. The average crystalline size was observed at 20 nm, and the saturation magnetic moment was 83 $emug^{-1}$. 2.0 $\times 10^{6}$ $ergcm^{-3}$ obtains the anisotropic constant of cobalt ferrite nanoparticles at 300 K.

Balavijayalakshm[43] prepared cobalt-substituted magnesium ferrite nanoparticles by co-precipitation, annealed them at 600 °C, and analyzed their characteristic properties. The average crystallite size was 7–9 nm, and the lattice parameter was 8.3939 Å. As cobalt concentrations increase, the prominent absorption bands of FTIR spectra shift to higher values. Cobalt substitution enhances magnetic properties.

A series of manganese zinc ferrites were produced into ultrafine crystallites by Hoque[45] using the wet chemical co-precipitation technique and calcination at 200 for four hours. The ferrite powders were created, and their potential as an MRI contrast dye was examined by coating them

with biocompatible chitosan. Higher relaxivity values are present in every composition of sequences, ensuring their probability as contrast agents.

Cobalt ferrite nanoparticles of a 4 nm size were created by Rana[46] using a reverse micelle method. The FTIR spectra of as-prepared $CoFe_2O_4$ nanoparticles showed the IR absorption bands at 460 and 615 cm1, which correspond to the metal-oxide bonds of the octahedral and tetrahedral sites, respectively. After annealing, the frequency of the absorption band changed towards the lower frequency range.

In a one-pot solvothermal process utilizing acetylacetonates as precursors, Ajroudi[47] looked into the electric and magnetic characteristics of $Co_xFe_{3-x}O_4$ nanopowders. Co^{2+} was shown to have a solid attraction to tetrahedral sites. These nanoparticles have a substantially larger magnetocrystalline anisotropy constant than bulk ferrites.

Localized heat induction is a state-of-the-art method that Mohapatra[48] describes as being used for cancer treatment, thermally induced drug release, and remote activation of cell processes. It uses magnetic nanoparticles in an alternating magnetic field. This paper discusses the most recent developments in improving the magnetic characteristics of spinel ferrite nanoparticles for efficient heat induction. Their inherent and extrinsic magnetic characteristics enhance the heating efficiency of the magnetic nanoparticles. The magnetic particle's size, composition, and shape are crucial to successful magnetic heating.

Xiang[15] reported that superparamagnetic iron oxide MR contrast dyes form dextran-coated nanosized iron oxide crystals or carboxy dextran. Clinically approved superparamagnetic iron oxide MR contrast agents are ferumoxides and ferucarbotran, explicitly approved for liver MRI. Ferumoxides have transverse and longitudinal relaxivities of 98.3 and 23.9 $mM^{-1}sec^{-1}$, respectively, while ferucarbotran has transverse and longitudinal relaxivities of 151.0 and 25.4

$mM^{-1}sec^{-1}$. Ferumoxtran-10 used in reticuloendothelial system imaging, contains the transverse and longitudinal relaxivities of 60 and 10 $mM^{-1}sec^{-1}$, respectively.

Inverse spinel ferrite nanoparticles that have been created interact with protons in bulk water to provide magnetic resonance imaging contrast enhancement. This interaction depends on the succimer-coated inverse spinel ferrite nanoparticles' initial susceptibility, magnetization, and anisotropy. Kim[16] studied inverse spinel ferrite nanoparticles of superparamagnetic MFe_2O_4 (M = Mn^{2+}, Fe^{2+}, and Co^{2+}) with average diameters of 6–8 nm that were produced by a diol reduction of organic metals. The surface was modified to be hydrophilic by coating with succimer. $MnFe_2O_4$, Fe_3O_4, and $CoFe_2O_4$ had transverse and longitudinal relaxivity ratios of 12.2, 23.1, and 62.3, respectively, pointing to the potential use of these magnetic nanoparticles as T_2 contrast agents for MRI.

In a review article, Amiri[13] introduces magnetic effects, synthesis techniques, and medical applications for cobalt ferrite nanoparticles, like hyperthermia, magnetic resonance imaging, drug delivery, and magnetic separation. Cobalt ferrite has a high Curie temperature, high coercivity at room temperature, high saturation magnetization at room temperature, high anisotropy constant, excellent chemical stability, mechanical hardness, and electrical insulation, for which they are optimistic candidates for medical applications, including magnetic drug delivery, radio-frequency (rf) hyperthermia, MRI and medical diagnostics.

Druc[44] synthesized cobalt-substituted magnesium ferrite using glycine as a chelating/explosive agent in the sol-gel auto-combustion method. It was found that all samples formed spinel monophase within the Fd3m space group.

Liu[45] shows that the spin-orbital angular momentum coupling in $MgFe_2O_4$ and $CoFe_2O_4$ spinel ferrite nanoparticles is correlated with their superparamagnetic properties. Because of emphasized magnetic couplings from Co^{2+} lattice sites, $CoFe_2O_4$ nanoparticles have a higher blocking temperature than $MgFe_2O_4$ nanoparticles of the same size. $CoFe_2O_4$ nanoparticles have higher magnetic anisotropy than similar-sized $MgFe_2O_4$ nanoparticles. These studies suggest chemically adjusting the magnetic anisotropy energy can regulate nanoparticles' superparamagnetic properties.

Using a chemical co-precipitation approach, Varshney[46] investigated the effects of Zn and Mg levels on synthesized cubic cobalt ferrites' structural and magnetic properties. It was found that all of the samples had a cubic structure with the Fd3m space group in a single phase. Magnetic measurements were conducted on samples of cobalt ferrite doped with Zn and Mg, and the highest saturation value was determined.

Zhao[11] studied magnetite nanoparticles prepared by coprecipitation with an aqueous NaOH solution. The Fe_3O_4–chitosan magnetic mixed nanoparticles with a core–two-step produce shell structure of diameter 30–50nm via a suspension cross-linking method. The inductive heating effects of Fe_3O_4–chitosan mixed nanoparticles in an alternating current magnetic field were investigated. Fe_3O_4–chitosan composite nanoparticles' potential was evaluated for localized hyperthermia treatment of cancers. The Fe_3O_4–chitosan composite nanoparticles would be suitable thermoseeds for localized hyperthermia cancer treatment.

Joshi[47] synthesized cobalt ferrite magnetic nanostructures by a high-temperature solution-phase approach and investigated the effect of the size and shape of cobalt ferrite nanostructures. The nanostructures' saturation magnetization and relaxivity coefficient increase with increasing

particle size. The faceted irregular cobalt ferrite nanostructures showed lower saturation magnetization and higher relaxivity coefficient than their spherical counterparts. The cobalt ferrite nanoparticles are a potential candidate for biomedical applications.

Fe_3O_4 magnetic nanoparticles limited with oleic acid or polyethylene glycol (PEG) produced by a co-precipitation technique were heated inductionally by Ghosh[53]. The average crystallite sizes of Fe_3O_4 nanoparticles, Fe_3O_4 nanoparticles with oleic acid caps, and Fe_3O_4 nanoparticles with PEG checks were 12, 6, and 8 nm, respectively. It was discovered that every particle was superparamagnetic. When the magnetic nanoparticles were coated with oleic acid and polyethylene glycol, there was a decrease in the aggregation of particles. The Fe_3O_4 magnetic nanoparticles capped with oleic acid showed the best killing rate in the human breast cancer cell (MCF7) and the best induction heating compared to other Fe_3O_4 magnetic nanoparticles investigated in this study.

Na[21] focuses on superparamagnetic iron oxide as a liver MRI contrast agent, with a large surface area and efficient contrasting effect. Magnetic iron oxide nanoparticles are broadly utilized as MRI contrast dyes in the liver, spleen, and bone marrow due to their capacity to curtail relaxation times (T_2^*). Without the contrast agent, such information-rich pictures are unobtainable. Newly, a comprehensive investigation has been piloted to design nanoparticle-based T_1 contrast mechanisms to overwhelm the disadvantages of iron oxide nanoparticle-based negative T_2 contrast agents. Additionally, consistent ferrite nanoparticles with high crystallinity have been successfully used as fresh T_2 MRI contrast agents with an improved mechanism and physical approach.

Hoque[48] notifies the thermotherapeutic applications of chitosan and PEG-coated nickel ferrite nanoparticles prepared by the co-precipitation process. A superparamagnetic to ferromagnetic

transition occurs with increasing particle size. Manipulating the solution's size, shape, magnetization, and concentration can produce enough heat for hyperthermia therapy. The chitosan and PEG-coated nickel ferrite nanoparticles are suitable for magnetic resonance imaging as a T_2 contrast agent.

When doing time-of-flight magnetic resonance angiography, Edelman[55] proposed that using magnetization transfer contrast agents would enhance flow contrast. Low-power radiofrequency radiation was used to create two- and three-dimensional flow-compensated gradient-echo pictures with and without contrast agents. Low-power radio-frequency radiation offsets the bulk "free" water resonance frequency before the radio-frequency excitation pulse to generate magnetization transfer contrast images. The standing tissue's signal intensity decreased as the power provided for the magnetization transfer contrast pulse increased. As counted in the superior sagittal sinus, a shorter decrease appeared in venous signal intensity. The central cerebral artery's estimated arterial signal intensity slightly changed, but there was no magnetization transfer contrast effect in the cerebrospinal fluid. The characterization of the highest-intensity projection images was strengthened by the small vessel with magnetization transfer contrast. According to the authors, magnetization transfer contrast can significantly improve brain time-of-flight magnetic resonance angiography.

Miraux[49] committed magnetic resonance angiography of rodents employing time-of-flight magnetic resonance imaging techniques. After injecting a gadolinium-enhanced agent, veins with low flow velocity were become apparent due to the gadolinium effect.

Alawi[50] presented in his review article that magnesium is a biocompatible cation essential for the human body. It is essential for blood pressure regulation, bone formation, cardiac contraction, glycemic control, and muscle contraction. Magnesium, a cofactor for more than 300

enzymes, has daily intake recommendations for adult males and females of 420 mg and 320 mg, respectively.

Lison[51] reported that cobalt is also an essential element for humans. Cobalamin, or vitamin B_{12}, is an essential human body component. The adult human body contains about 1 mg/ml of cobalt, of which 85% is found in vitamin B_{12}. The average person needs 5 to 50 g of cobalt each day.

Based on the above literature, chemical co-precipitation was employed to synthesize $\mathbf{Mg_{1-x}Co_xFe_2O_4}$ $\mathbf{(0 \leq x \leq 1 \text{ with } \Delta x = 0.1)}$ (MCFO) nanoparticles. In this study, Magnesium is deliberately substituted by cobalt to control the size, shape, magnetic moment, coercivity, and anisotropy constant for finding suitable material for biomedical applications. Though cobalt is more toxic than Magnesium, adding a small amount of cobalt can significantly Alter the magnetic characteristics of magnesium cobalt ferrite, which reduces the dose of the magnetic particle in biomedical applications. This study investigated both composition dependence and sintering temperature dependence structural and magnetic properties. Then the surfaces of the nanoparticles are functionalized by Chitosan, PEG, and Dextran to make them colloidal and biocompatible for biomedical applications.

1.3. Objective

This study aims to find the best combination of Chitosan, PEG, and Dextran-coated MCFO magnetic nanoparticles for

i) local magnetic hyperthermia,

ii) MRI contrast, and

iii) MRA contrast agents.

The MCFO materials were selected in this investigation because cobalt has anisotropic properties and higher magnetic moments. The tumour treated by Local magnetic hyperthermia (LMH) treatment with Fe_2O_4 regrows after a few days. However, the tumour treated by LMH with anisotropic $CoFe_2O_4$ did not regrow after a few days. Furthermore, replacing magnesium with cobalt of MCFO materials also improves their magnetic properties, which is crucial for LMH studies, MRI and MRA contrast agents.

To achieve this, we need to optimize the composition, sintering temperature, concentration, and dose while ensuring the structural and magnetic properties are suitable for the ferrite's structure. To study the magnetic properties of MCFO materials, their structure and particle properties were analyzed using techniques like Transmission electron microscope (TEM), X-ray Diffractometer (XRD), Fourier Transform Infrared (FTIR), and Raman spectroscopy. The materials need higher magnetic moments and lower hydrodynamic diameters to be suitable for local magnetic hyperthermia, MRI, and MRA contrast materials. Therefore, the magnetic properties were further analyzed using Physical Property Measurement System (PPMS) and Mössbauer spectroscopy. Then, the MCFO materials were coated with Chitosan, PEG, and Dextran. The hydrodynamic sizes of the MCFO materials were investigated using DLS measurement. Finally, the in-vitro LMH properties and in-vivo MRI and MRA contrast properties within the rat head were investigated to find suitable MCFO materials for LMH and MRI treatment. Details of the measurements are discussed in Chapter 3, and the results are discussed in Chapters 4 to 6.

CHAPTER 2: THEORETICAL BACKGROUND

2.1. Introduction

In the last two decades, extensive concentration has been maintained in preparing nanoscaled materials. Recently, materials made of a few atoms to hundreds of particles have been able to be synthesized, and their properties have been effectively determined, thanks to the development of new fabrication and characterization approaches[52,53]. Due to the increased surface-to-volume ratio and quantum confinement effects in these dimensions, nanosized materials exhibit distinctive optical, electrical, and magnetic properties corresponding to their bulk counterparts[54,55]. These new nanoparticle segments offer them the prospect of being utilized in an exhaustive range of technical, environmental, energy, and biomedical applications. In biomedical applications, metallic, magnetic, fluorescent, polymeric, and protein-based nanoparticles are employed. Much of the analysis in this field is concentrated on magnetic nanoparticles[56,56–58]. Cobalt-doped magnesium ferrites were surface-engineered in this research work using different coating materials. This chapter discusses the theoretical background of this research work.

2.2. Origin of Magnetism

The magnetism arrives from the basic properties of an electron containing a magnetic dipole moment. The dipole moment comes from the more elemental property of the electron connected to the quantum spin. The spin of electrons in atoms is the principal source of ferromagnetism, although there is a tiny contribution from the orbital angular momentum of the electron around the nucleus. Atomic electrons possess magnetic moments originating from two different sources. One source is its orbital motion, where a rotating charge creates a tiny magnetic field, similar to a current loop. During electron trajectory, this magnetic field creates a magnetic moment.

Another is associated with the spinning electron around an axis which generates the spin magnetic moment on the spin axis. Accordingly, an individual electron in an atom is a miniature magnet keeping permanent orbital and spin magnetic moments.

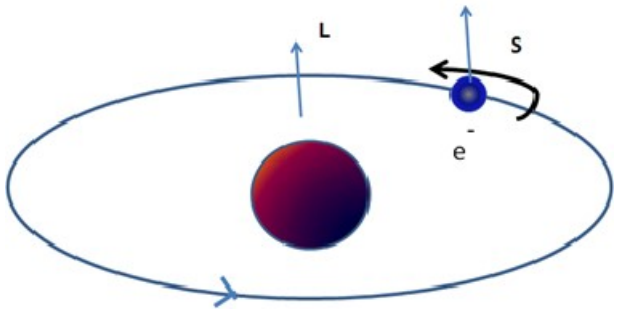

Figure 2.1: The magnetic moment linked to an electron's spinning and orbital movement

The way an electron moves around the nucleus is comparable to current circulation in a circular wire. The magnetic moment of a current-carrying conductor is provided by μ = I.A, where I is current, and A is the area[59].

2.2.1. Orbital magnetic moment

The equation used to determine the magnetic moment of an electron in orbit is as follows:

$$\mu = \pi r^2 \left(\frac{ev}{2\pi r}\right) = \frac{evr}{2} \qquad (2.1)$$

The equation involves the orbit radius (r), electron charge (e), and velocity (v).

The angular momentum of an electron must be an integer multiple of Planck's constant, which is written as:

$$mvr = \frac{nh}{2\pi} \qquad (2.2)$$

In this equation, m represents the mass of the electron, and h represents Planck's constant. The first orbit of an electron has n equal to 1. Accordingly, an electron's orbital magnetic moment can be calculated as follows:

$$\mu = \frac{eh}{4\pi m} \tag{2.3}$$

In physics, this is a Bohr magneton, the least possible magnetic moment of an orbit [60].

2.2.2. Spin magnetic moment

Similarly, the electron's shortest spin magnetic moment is

$$\mu = \frac{eh}{4\pi m}$$

Quantum theory states that the spin of an electron has solely two possibilities $+\left(\frac{1}{2}\right)\left(\frac{h}{2\pi}\right)$ or $-\left(\frac{1}{2}\right)\left(\frac{h}{2\pi}\right)$.

We can express it in the same format as equation (2.3), which is:

$$\mu = \left(\frac{e}{2m}\right) S \tag{2.4}$$

In this case, S represents the spin quantum number.

In short,

$$\mu = g\left(\frac{e}{2m}\right) S \tag{2.5}$$

The letter "g" in this context stands for the gyromagnetic ratio. When g is equal to 2, a contribution from the spin is visible. On the other hand, when g equals 1, an orbital contribution is observed. The magnetic moment of a nucleus is negligible compared to that of an electron due to its massive size. The gyromagnetic ratio is proportional to the g-factor, which results from the precession of electrons in a gravitational field. The value of g determines whether the magnetic moment is caused by spin or electron orbital motion[61].

2.3. Basic Concepts of Magnetism

When electric charges move, they create electric currents that generate magnetic fields. These magnetic fields are represented by magnetic dipoles, which are essentially flat current loops. The magnetic moment of a dipole (m) is calculated by multiplying the current (I) with the area (A) (m = IA). Magnetic fields are formed by the movement and spinning of electrons within atoms, creating small current loops. Bohr's magneton (μ_B) is the fundamental magnetic dipole moment, with a magnitude of 9.27×10^{-24} Am^2. An electron in an atom has a spin magnetic moment of $\pm\mu_B$ (the plus sign is for spinning up, and the minus sign is for spinning down). The electron's magnetic quantum number is labeled m_l, and its impact on orbital magnetism is demonstrated as $m_l\mu_B$[61–63].

The material magnetization vector **M** represents the magnetic moment per unit volume. As a result of external magnetic fields, magnetic moments within the material align either parallel or antiparallel with the field, which changes it. The magnetic field intensity, represented by the vector **H**, is expressed in Amperes per meter (A/m). On the other hand, B represents the magnetic flux density measured in Weber per square meter (Wb/m^2) or tesla. There is a linear relationship between **M** and **H**, which is

$$\boldsymbol{M} = \chi \boldsymbol{H} \tag{2.6}$$

where χ is the magnetic susceptibility which depends on the magnetic materials[60–65]. Another relationship between **M** and **H** also implies the following:

$$\boldsymbol{B} = \mu_0 \boldsymbol{M} + \mu_0 \boldsymbol{H}$$
$$\boldsymbol{B} = \mu_0 \chi \boldsymbol{H} + \mu_0 \boldsymbol{H}$$
$$\boldsymbol{B} = \mu_0 (1 + \chi) \boldsymbol{H}$$
$$\boldsymbol{B} = \mu \boldsymbol{H} (when\ \mu = \mu_0 (1 + \chi)\ or\ \frac{\mu}{\mu_0} = 1 + \chi \tag{2.7}$$

Magnetic permeability (μ) is a characteristic of the medium through which the magnetic field (**H**) flows and where the magnetic flux density (**B**) is measured. Weber per ampere meter

(Wb/A.m) or Henry per meter (H/m) are used to measure it. Materials are categorized into five groups based on their magnetic properties, which are:

2.3.1. Diamagnetism

Diamagnetic materials like bismuth or silver do not have a permanent magnetic dipole moment. However, they exhibit weak magnetic dipole moments in an external magnetic field. It is due to their negative magnetization, resulting in a negative susceptibility ($\chi < 0$) consistent with Lenz's law. Additionally, the susceptibility of diamagnetic particles is not dependent on temperature. In diamagnetic materials, an orbiting electron produces a weak repelling force when there is a magnetic field[61–63].

2.3.2. Paramagnetism

In paramagnetic materials, the unpaired electrons' spin and orbital magnetic moments are not entirely balanced, which means they do not have a permanent dipole moment. Without a magnetic field, the randomly oriented dipole moments do not create any macroscopic magnetization. When a magnetic field is present, the moments align with its direction, causing a positive susceptibility ($\chi > 0$). Nowadays, only a few paramagnetic substances like Mn and Cr exist[64,66].

2.3.3. Ferromagnetism

Compared to other magnetic materials, atoms of ferromagnetic materials have powerful permanent magnetic moments. Consequently, this permanent magnetic moment can easily align with a magnetic field, which strengthens the magnetic field's pull. Ferromagnetic materials are known as magnetic materials.

The interaction of magnetic moments among neighboring atoms selected its magnetic characteristics. Heisenberg[67] developed a Hamiltonian, H, to illustrate the interaction of two neighboring particles using Pauli's exclusion principle:

$$H = -2J\vec{S}_i.\vec{S}_j \quad (2.8)$$

where J, exchange integral, $\vec{S}_i$, the spin angular momentum of the i^{th} atom, and $\vec{S}_j$, the spin angular momentum of the j^{th} atom. When the exchange integral is positive, the spin magnetic moment of the i^{th} and j^{th} atoms must be parallel to minimize the total energy. Therefore the magnetic moments are arranged parallelly to form ferromagnetic materials. Ferromagnetic materials include the domain of minimizing demagnetizing energy. The magnetic moment inside the domain sets parallelly, and the domains are organized randomly to make zero net magnetization without magnetic fields. Iron, nickels, cobalt, gadolinium, and some alloys are ferromagnetic materials[64,66,68].

2.3.4. Antiferromagnetism

Again, when the exchange integral is negative, the magnetic moment of the ith and jth atom is oriented anti-parallelly for energy minimization. These kinds of materials are called anti-ferromagnetic materials. In anti-ferromagnetic materials, the magnetic moment of the i^{th} and j^{th} sublattices are equal and opposite. Like ferromagnetic materials, they also form domains. The frequent examples of antiferromagnetic materials with ordering consist of MnO, CoO, FeO, and NiO[64,66].

2.3.5. Ferrimagnetism

Ferrimagnetic materials are similar to antiferromagnetic materials in their arrangement of magnetic moments but differ in the degree of magnetic moment in different directions. It results in a net magnetic moment even without an external magnetic field. Ionic compounds like oxides

can exhibit many types of magnetic ordering because of their crystal structure. The oxygen anions mediate the exchange contacts between the magnetic structure's magnetic sublattices (A and B). The most significant of these exchanges, indirect or superexchange interactions, causes an antiparallel spin arrangement between the A and B sublattices. Compared to ferromagnetism, ferrimagnets have a net magnetic moment that differs in the A and B sublattices. The ferromagnetic behavior's properties, including spontaneous magnetization, can be seen in ferrimagnetism[64,66,68].

2.4. Magnetic Domain

Magnetic materials have regions called magnetic domains where the magnetization of atoms aligns in the same direction. When ferromagnetic materials are cooled below the Curie temperature, their magnetization separates into small areas called magnetic domains. The magnetization within each domain points in the same direction, but different domains may point in different directions. The arrangement of magnetic domains determines the magnetic behavior of ferromagnetic particles (such as iron, nickel, and cobalt and their alloys) and ferrimagnetic materials (like ferrite), including the building of magnets and their attraction to a magnetic field. The areas that separate magnetic domains are called domain walls, where the direction of magnetization changes smoothly from one domain to the next. The study of magnetic domains is known as micromagnetics[69,70].

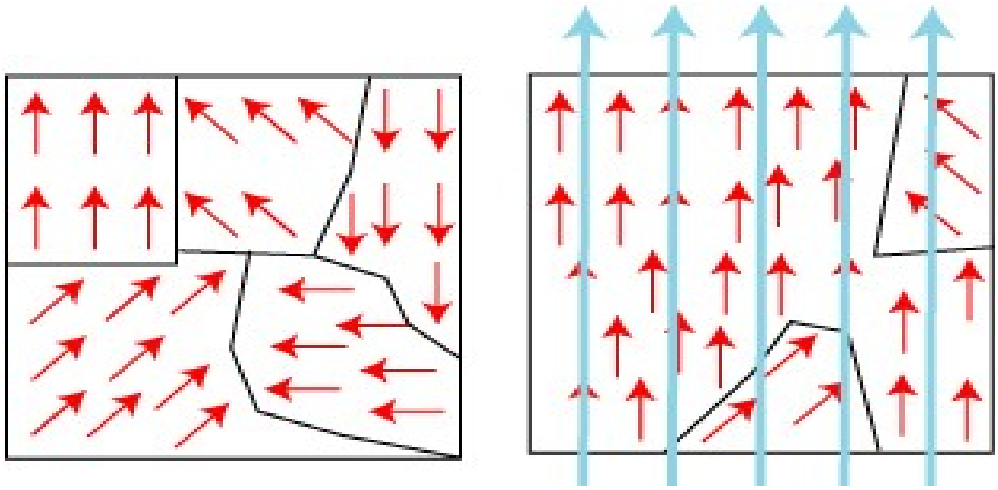

No field Strong field

Figure 2.2: Magnetic domain with no field and strong field.

2.5. Hysteresis

Understanding magnetic hysteresis is crucial as it relates to the irreversible process of magnetization and demagnetization. The Hysteresis loop provides various information about magnetic materials. The B-H loop illustrates the relationship between magnetizing force (H), induced magnetic flux density (B), and magnetization (M) for a ferromagnetic particle. We adjust the magnetizing force while measuring the magnetic flux to create the loop. Initially, an un-magnetized or demagnetized particle like iron follows the dashed line as the magnetizing force increases. As the magnetic field (**H**+) increases, the magnetic flux density (**B**+) strengthens. At point "a" in Figure 2.3, most magnetic domains align in parallel, resulting in a slight magnetic flux increase with further magnetizing force increases. This point indicates magnetic saturation. When H returns to zero, the curve moves from point "a" to point "b," where some magnetic flux remains in the material despite zero magnetizing energy. This point is called retentivity and shows the level of remanence on the graph[71–73]. The coercive force, or coercivity, refers to the force needed to eliminate any remaining magnetism in a material. Figure 2.3 is an illustration of a hysteresis loop as an example.

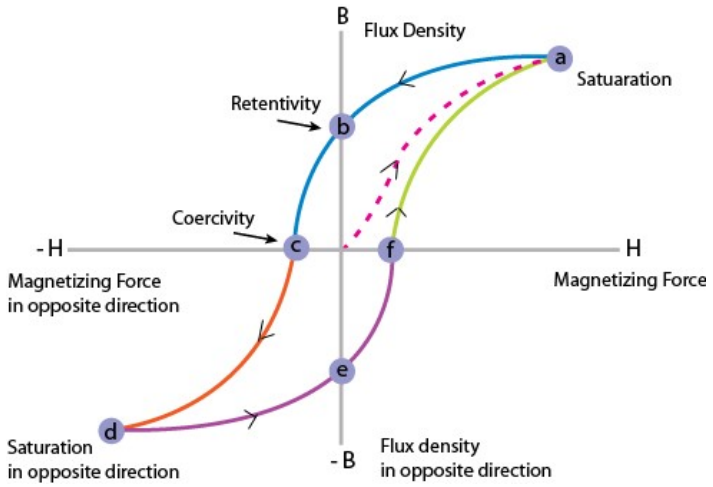

Figure 2.3: Typical hysteresis loop of ferromagnetic materials.

At point "d" on the negative path, the material becomes magnetically saturated again when the magnetizing energy increases in the opposite direction. Lessening H to zero leads to point "e," where residual magnetism is no different from the other direction. B returns to zero when H is increased in a positive direction. There is, however, a residual magnetic field that prevents the curve from returning to the origin. Upon reaching saturation point, the curve follows a distinct route back to point "f." By measuring the hysteresis loop, we can determine several critical magnetic properties.

2.5.1. Retentivity

Retentivity measures the magnetic field in a sample after the magnetizing power has been removed from the saturation level. It is similar to the saturation induction of a magnetic material. The retentivity of the sample is represented by the value of B at point b on the hysteresis loop[71].

2.5.2. Residual Magnetism or Residual Flux

Residual magnetism is the magnetic flux density that persists in a material even without a magnetizing field. It is significant to remember that when the magnetization achieves saturation,

a sample's residual magnetism and retentivity are identical. However, if the magnetizing energy is insufficient to attain the saturation level, the intensity of residual magnetism may be lower than the retentivity value[71].

2.5.3. Coercive Force

The coercive force is the magnetic field required to reset the magnetic flux to zero. H represents the magnetic material's coercive force at point c on the hysteresis loop[71].

2.5.4. Permeability

Material permeability refers to its ease in establishing an element's magnetic flux. Higher permeability ensures a higher number of force lines inside a sample[74].

2.5.5. Reluctance

Reluctance is a ferromagnetic material's resistance to an applied magnetic field. The reluctance is similar to electrical circuit resistance[75]. Figure 2.3's B vs. H hysteresis loop area shows the energy lost per unit volume per cycle of applied field fluctuation cycle. This energy loss for magnetization and demagnetization is the hysteresis loss. It dissipates in the setting as thermal energy, which is used in magnetic hyperthermia[76].

2.6. Ferrite's Structure

According to the crystal structure, there are four types of ferrite. These are

i) Spinel ferrite,

ii) Hexagonal ferrite,

iii) Garnet ferrite, and

iv) Ortho ferrite.

Our investigated samples are spinel ferrites. So we focus on spinel ferrite in this section.

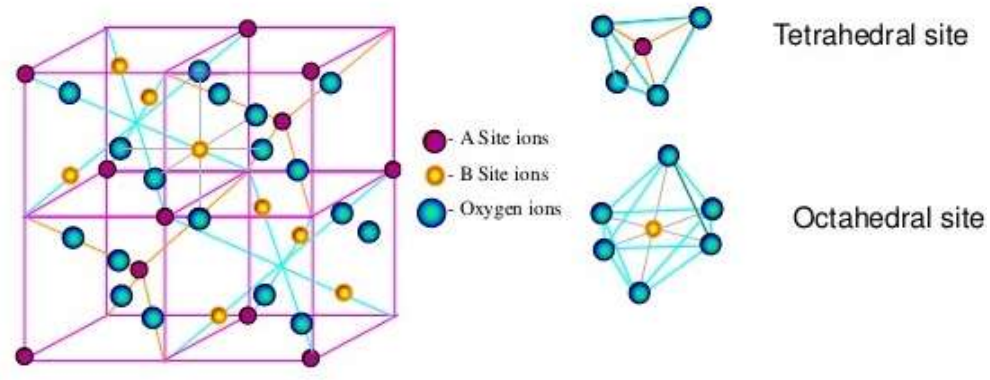

Figure 2.3 (a): Crystal structure of Spinel ferrite.

Spinel ferrites are magnetically soft and exhibit high electrical resistivity and low magnetic losses. Spinel ferrites are depicted by the chemical formula MFe_2O_4, where M is divalent metal ions like Cu, Ni, Mg, Mn, Co, Zn, Cd, etc. Generally, Fe^{3+} can be substituted by further trivalent ions like Al, Cr, Ga, In, etc. Thirty-two oxygen ions create a cubic shape within a closely packed face-centered cubic arrangement. These ions occupy two interstitial sites between the anions. At site A, four neighboring oxygen atoms surround a tetrahedral coordinate (A). Meanwhile, six oxygen atoms from the nearest neighbors at site B encompass an octahedral coordinate (B). One unit cell is composed of 64 A sites and 32 B sites. 8 A sites and 16 B sites are filled by cations[77–82]. There are three types of spinel Ferrites. These are

i) Normal spinel ferrite,

ii) Inverse spinel ferrite, and

iii) Mixed spinel ferrite.

i) Normal spinel ferrite: In a normal spinel ferrite, divalent ions occupy the A sites, whereas the trivalent ions occupy the B sites. For example, bulk Mn_3O_4, $ZnFe_2O_4$, $FeCr_2O_4$, etc, are normal spinel Ferrites.

ii) Inverse spinel ferrite: In an inverse spinel ferrite, the B sites are occupied by divalent ions, while trivalent ions occupy the A sites. For example, bulk Fe_3O_4, $CoFe_2O_4$, $NiFe_2O_4$, etc., ferrites are inverse spinel ferrites.

iii) Mixed spinel ferrite: In the mixed spinel ferrite, divalent and trivalent ions can be found in the A and B sites. For example, bulk $CuFe_2O_4$ ferrite is a mixed spinel ferrite.

2.7. Theory of Magnetization in Spinel Ferrite

Ferrite nanoparticles usually form by a suitable ferric oxide (Fe_2O_3) reaction and other divalent metal oxides. The spinel structure comprises a network of positively-charged metal ions (Fe^{3+}, M^{2+}) and negatively charged divalent oxygen ions (O^{2-}). Its formula is $MOFe_2O_3$ or MFe_2O_4, where M represents the divalent metal ion. Ferrites can also contain iron oxide based on elements such as Cr and Mn. Although Mn and Cr are not ferromagnetic elements, they can act as magnetic ions when combined with other elements in ferrite. Magnetic spinels can have various divalent ions substituted for M^{2+}, including Mn^{2+}, Ni^{2+}, Cu^{2+}, Co^{2+}, Fe^{2+}, Li^{2+}, Zn^{2+}, Mg^{2+}, or combinations of these ions. Fe^{3+}, Fe^{2+}, Ni^{2+}, Co^{2+}, and Mn^{2+} can provide unpaired electron spins and part of the magnetic moment in a spinel. Other divalent ions, such as Mg^{2+} or Zn^{2+}, aim to raise or deliver the magnetic moment by displacing Fe^{3+} ions on crystal lattice sites, even though they are not magnetic[83,84].

Magnetic nanoparticles have numerous benefits as relevancy at higher corrosion resistance, higher heat resistance, lower price, and higher frequency due to maintaining lower saturation magnetization of ferrites than ferromagnetic alloys. The magnetic behavior of ferrites depends on the arrangement and distribution of ions in the sublattice. Therefore, several practical applications of ferrites have been developed by completely employing these advantages. The superparamagnetic or ferromagnetic character is more favorable for biomedical applications. Ferrimagnetic materials contain atoms with varying magnetic moments, similar to antiferromagnetism. However, the opposing magnetic moments are unequal in ferrimagnetic materials, resulting in spontaneous magnetization. It occurs when different materials or ions are present, such as Fe^{2+} and Fe^{3+}. Examples of ferrimagnetic materials include ferrites and magnetic garnets. Magnetite, the ancient and well-known magnetic substance, is also a ferrimagnet. It was initially thought to be a ferromagnet before the discovery of ferrimagnetism and antiferromagnetism by Néel in 1948.

Cubic ferrites comprise iron oxides and other elements like aluminum, manganese, cobalt, nickel, iron, and zinc. On the other hand, hexagonal ferrites such as $BaFe_{12}O_{19}$, $PbFe_{12}O_{19}$, and pyrrhotite, $Fe_{1-x}S$.

According to Hund's rule, the spontaneous magnetization of magnetic particles arises from the non-zero net magnetic moments when filling up the 3d orbital. In the case of ferromagnetic or superparamagnetic ferrite nanoparticles, divalent ions occupy the A-sites, while trivalent ions occupy the B-sites, creating a normal spinel structure. However, if trivalent ions occupy the octahedral position and divalent ions occupy the tetrahedral position within a unit cell of cubic ferrite, this is called the inverse spinel structure. Fe^{3+} ions cancel each other out in this structure due to their equal and opposite magnetic moments. In addition, both the trivalent and divalent

ions occupy tetrahedral and octahedral positions in a mixed spinel structure. Fe^{3+} ions are evenly allocated across both A and B sites to cancel out the net magnetic moment in magnetic ferrite nanoparticles. The electron arrangement of magnetic nanoparticles is $3p^6 4s^2$, and two electrons are taken away from $4s^2$ to form 2+ ions. Magnetic moment, curie temperature, and the crystal structure of ferrite nanoparticles are selected for magnetic hyperthermia over other metal nanoparticles to avoid extra heating due to eddy current losses. Because of their high anisotropy, minimum coercivity, minimum remanence, maximum saturation magnetization, thin deadline, and high resistivity, magnetic nanoparticles are crucial contrast agents during MR imaging[7,79,85].

2.8. Superparamagnetic Behavior of Ferrite Nanoparticles

Superparamagnetism is the magnetic activities related to magnetic nanoparticles, usually of ferromagnetic materials analogous to a single magnetic domain and a high magnetic moment. When ferromagnetic or ferrimagnetic particles are small enough, their magnetization is subject to thermal fluctuations. Assume that the Néel relaxation time—a period between two such fluctuations—is shorter than the time required to determine the magnetization of the particles in the absence of an external magnetic field. The magnetization of the particles will then typically appear to be zero in that situation. This phenomenon is known as superparamagnetism. If the nanoparticles are too small, their magnetization can arbitrarily flip under temperature pressure, with the Néel relaxation time being the characteristic time between two flips. The average magnetization of the nanoparticles will appear to be zero if the measurement duration is substantially longer than the Néel relaxation time and there is no external magnetic field. It is known as the superparamagnetic state, and an external magnetic field can manipulate it[45,86,87]. Superparamagnetic materials contain a large saturation magnetization and zero coercivity and

remanence, making it to be notable from ferromagnetism and paramagnetism as illustrated below:

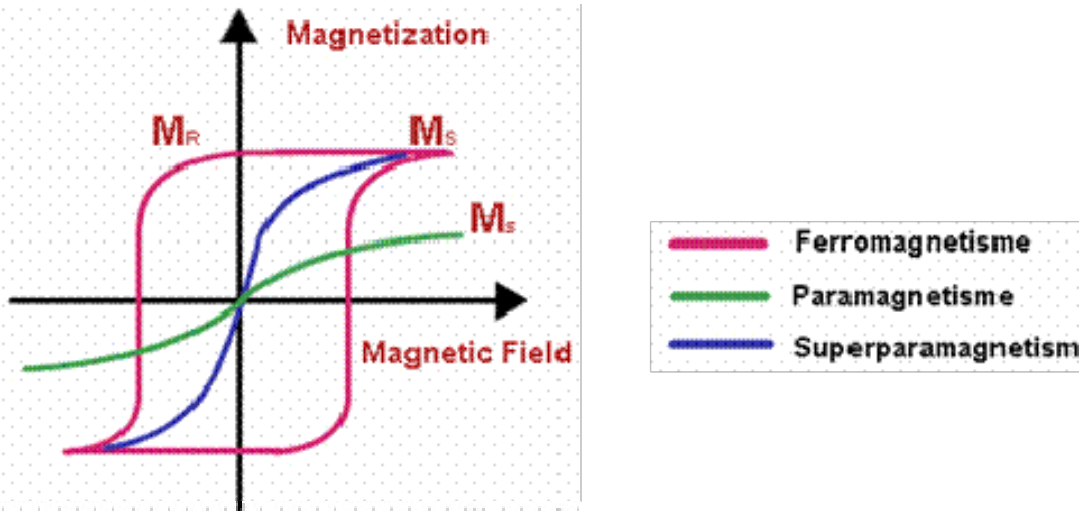

Figure 2.4: Hysteresis loops of ferromagnetic, paramagnetic and superparamagnetic materials.

Superparamagnetism is a consequence of ferromagnetism, where the material's surface dominates to fix its magnetic characteristics. Figure 2.5 depicts the magnetic particle size's influence on magnetic properties. The coercivity changes with the particle dimension, and at a small enough size, the coercivity becomes zero, as exposed in the following figure:

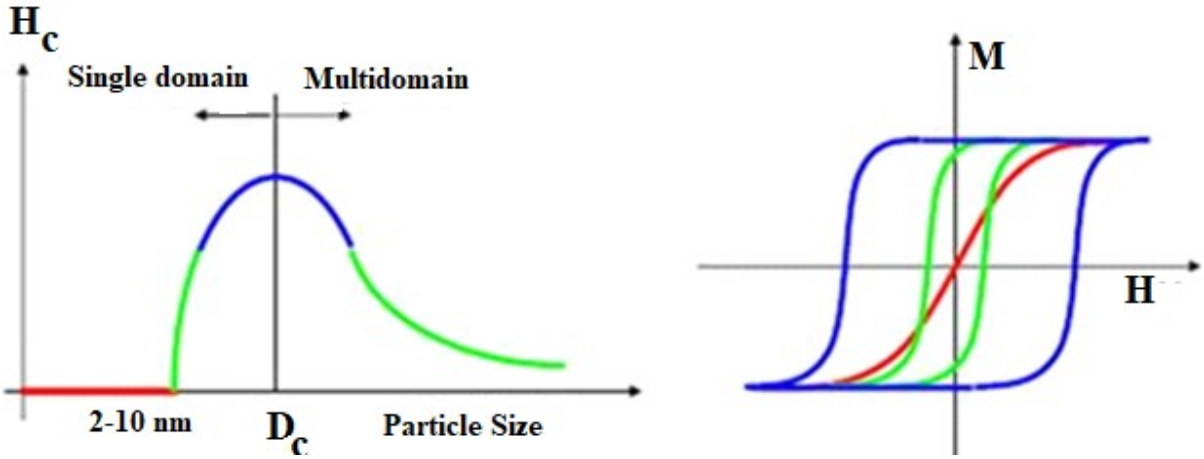

Figure 2.5: Size effects of particles on magnetic properties.

2.9. Magnetic hyperthermia for cancer treatment

Hyperthermia is a method of destroying tumor cells without invasive procedures by subjecting them to high temperatures. However, there is a risk of harming healthy tissues if too much heat is delivered. To avoid this, magnetic nanoparticles (MNPs) induce heat in specific areas like tissues or cells using an alternating magnetic field (AMF). This approach is beneficial since it is non-invasive and localized, ensuring that healthy cells are unaffected[88]. Several requirements need to be met to implement MNPs in tumor treatment successfully. The MNPs must, first and foremost, be biocompatible, biodegradable, and of sufficient colloidal strength. Second, they should be delivered to the tumor cells efficiently in small doses, necessitating MNPs with substantial heat production capabilities.

Additionally, the frequency and amplitude ranges of the AMF utilized to heat the MNPs must adhere to safety standards. It is crucial to monitor cellular temperature variations utilizing natural and non-invasive techniques. Furthermore, it is critical to comprehend the elements that influence heat transfer from MNPs to cells and the effects of temperature on cellular biological processes[89–91].

The AMF is written as

$$\boldsymbol{H(t) = H_0 e^{i2\pi ft}} \tag{2.9}$$

Where H_0, is the maximum value of AMF, and f is the frequency of the wave.

Hyperthermia, a treatment method that uses heat to cure diseases, has been practiced since ancient times. When exposed to temperatures above 41^{o}C, it can have a variety of effects on both the cell membrane and interior. The cell membrane becomes more permeable and fluid, which inhibits protein and nucleic acid production, results in protein denaturation and aggregation, and damages the blood vessels in the malignant area, reducing blood flow. Hyperthermia is classified

into three categories depending on the area affected: whole-body, regional, and local hyperthermia. Whole-body hyperthermia involves heating the body with hot water or an electric blanket. Regional hyperthermia involves heating an entire organ or a specific body part using external applicators and local perfusion. Local hyperthermia involves applying heat to small tumor areas using electromagnetic signals like ultrasound, microwaves, and radio waves[88,92].

When treating cancer with local hyperthermia, it is essential to have precise control over the affected area and ensure that the heat is distributed evenly. This method only reaches a few centimeters and is invasive for deep cancer locations. Nanotechnology overcomes these difficulties by using magnetic nanoparticles delivered directly to cancer cells and heated externally with an alternating magnetic field. This method enables targeting deep cancer cells while minimizing adverse effects. It is crucial to ensure the nanoparticles have a precise and uniform size distribution for practical purposes. If the particles have vastly different dimensions, tissue may not heat evenly and could cause harmful side effects. When testing this method in living organisms, it is crucial to consider these factors[88,93–95].

When magnetic moments in magnetic materials align in a specific direction, known as the easy direction, this phenomenon is known as magnetocrystalline anisotropy. The atomic spin and orbital angular moments are intimately related when the magnetocrystalline anisotropy is strong, aligning the magnetic moment in a straightforward direction. To change the direction of magnetization, energy is needed, which is equal to the anisotropy energy (except for insignificant higher order). Hence, the anisotropy is written as:

$$E = KV\sin^2\theta \tag{2.9a}$$

The anisotropy constant (K) is a unit of measurement that considers all sources of anisotropy and is measured in J/m^3. The anisotropy energy is determined by the magnetic volume of a particle

(V) and the angle (θ) between the particle's magnetization and the easy magnetization axis. When particles are exposed to an alternating magnetic field (AMF), heat is produced as they receive energy and work against the anisotropy energy. Upon removal of the AMF, the magnetic moments align with the easy axis of magnetization, resulting in relaxation. This alignment and relaxation of moments continuously generate heat from the AMF. The amount of anisotropy energy depends on the particle size and anisotropy constant[88,96,97].

If a particle cannot change its orientation while its magnetic moment is flipped, then the relaxation time of the moment is known as the Néel relaxation time (τ_N) and is expressed as:

$$\tau_N = \tau_0 e^{\frac{KV}{k_B T}} \tag{2.10}$$

The equation for magnetic susceptibility considers several factors, such as the magnetic particles' anisotropy constant (K), volume, the Boltzmann constant, and temperature. Notably, an increase in the concentration of magnetic nanoparticles in the solution leads to a rise in magnetic susceptibility due to Brownian relaxation[47,98,99]. The size and anisotropy of nanoparticles determine Brownian relaxation. The Brownian relaxation time[47,99] is written as:

$$\tau_B = \frac{3\eta V_H}{k_B T} \tag{2.11}$$

The formula is as follows: η represents the dynamic viscosity of the carrier liquid, V_H stands for the hydrodynamic volume of the particles, k_B represents the Boltzmann constant, and T represents the temperature. The effective relaxation time is expressed as follows:

$$\frac{1}{\tau_{eff}} = \frac{1}{\tau_N} + \frac{1}{\tau_B} \tag{2.12}$$

To determine the effective relaxation time (τ_{eff}) of magnetic nanoparticles (MNPs), we use equation (2.12) with either the Néel relaxation tool for smaller particles in highly viscous

mediums or the Brownian relaxation tool for larger particles in less viscous mediums. If the MNPs are less than 15 nm in size, τ_N is shorter than τ_B, and τ_{eff} is mainly influenced by τ_N. Conversely, if the MNPs are larger than 15 nm, τ_B is shorter than τ_N, and τ_{eff} is mainly determined by τ_B. Equations (2.11) and (2.12) were developed for non-interacting particles with similar characteristics, and they are employed in in-vivo MH experiments to generate heat.

Meeting specific criteria for the Specific Absorption Rate (SAR) is crucial to successfully studying magnetic hyperthermia in living organisms. Safety is of utmost importance, which means that the lowest possible dose of magnetic nanoparticles (MNPs) should be used, and any associated alternating magnetic field (AMF) must not harm living tissue. Optimal magnetic results (magnetic moment, coercive force, anisotropy constant) can be achieved by generating significant heat at lower concentrations of MNPs. To attain this, a single MNP with a biocompatible shell can maximize magnetic saturation and effective magnetic anisotropy by controlling particle size, shape, composition, and interparticle exchanges. Using an AMF with a well-defined intensity range and frequency is also essential[88,100,101]. When using an adiabatic approach, a magnetic system has an internal energy equal to its magnetic work. It can be expressed as:

$$U = \mu_0 \oint M dH \tag{2.13}$$

During several magnetic field cycles, the power dissipation in the magnetic strategy depends on the frequency multiplied by internal energy given by:

$$P = U f \tag{2.14}$$

To apply an AMF of maximum strength Ho and frequency f ($\omega = 2\pi f$), the power dispersed in superparamagnetic NPs relies on magnetic moment relaxations, which is expressed as:

$$P(f, H) = \pi \mu_0 \chi'' H_0^2 f \quad (2.15)$$

The formula for calculating the permeability of free space is denoted by "μ_0" while the imaginary part of the susceptibility is represented by "χ''". According to linear response theory (LRT), there exists a linear relationship between magnetization (M) and magnetic field (H). It means that as H increases, M remains constant ($M = \chi H$). The LRT applies in small magnetic fields and is accurate in the superparamagnetic regime where $H_{max} < k_B T/\mu_0 M_s V$ and when the magnetization of MNPs is linearly proportional to the dynamic magnetic field. For the LRT to be effective, the magnetic field should be much less than the saturation field of the MNPs, where H_{max} represents the amplitude of the AMF. If the LRT is accepted, the real part of the magnetic susceptibility χ', can be calculated as follows[88]:

$$\chi' = \chi_0 \frac{1}{1+(2\pi f \tau_{eff})^2} \quad (2.16)$$

where χ_0 is the initial susceptibility constant[88]. The out-of-phase component of the susceptibility, represented by χ'', is determined by its imaginary part as follows[88]:

$$\chi'' = \frac{\chi_0 2\pi f \tau_{eff}}{1+(2\pi f \tau_{eff})^2} \quad (2.17)$$

The initial susceptibility constant χ_0 is given by[88]:

$$\chi_0 = \frac{\mu_0 M_S^2 V}{k_B T} \quad (2.18)$$

where V is the volume of the particle. The usual way to measure heating efficiency in this context is specific loss power (SAR). SAR measurements are expressed in watts per gram and written as[88]:

$$SAR(f,H) = \frac{P(f,H)}{\rho} = \frac{\pi\mu_0\chi''H^2f}{\rho} \quad (2.19)$$

The symbol represents the mass density of the magnetic material ρ. Two important factors should be considered for the safe usage of MNPs in mental health: (a) MNPs should be used in small concentrations to ensure safety, and (b) when applied near cells in living organs, water-based media absorbs a significant amount of the heat produced by the MNPs. In the case of living organs, the power and frequency of an AMF should not matter because eddy currents are generated in a conductor, resulting in heat transfer[88,91,92,100,101].

During calorimetric investigations, the sample of MNPs is subjected to an AMF, and the temperature is measured over time using the following equation:

$$SAR\left(\frac{W}{g}\right) = \frac{C}{m_{MNP}}\frac{dT}{dt} \quad (2.20)$$

To calculate the heat capacity of a sample, the mass of the magnetic nanoparticles (MNPs) in the solution is multiplied by the initial slope of the temperature-time curve ($\frac{dT}{dt}$). Then multiply the total mass of all the sample's constituents by the specific heat. It will give the sample's heat capacity, represented by the letter C[47,99].

To achieve the necessary temperature increase for specific applications, magnetic nanoparticles (MNPs) must have a high specific loss power (SLP). This is because temperature enhancement in MNPs occurs when there are losses in alternating magnetic fields (AMF) during the dephasing of magnetic moments. Low doses of nanoparticles can be beneficial for this purpose.

When a continuous suspension of MNPs is subjected to high frequency, heat is induced due to Néel-Brownian relaxation, hysteresis loss, and other magnetic losses. However, eddy current loss

does not generate heat in magnetic hyperthermia. This is because the size of the particles and the low AMF does not cause substantial eddy currents.

Heating tumor cells with MNPs based on Néel and Brownian relaxations is how magnetic hyperthermia works. A phase lag exists between the direction of the magnetic moments and the applied magnetic field because the magnetic moments of the nanoparticles rotate and relax in an external magnetic field.

2.10. Magnetic Resonance Imaging (MRI)

2.10.1. Fundamental Principles of MRI

Using magnetic fields and radio waves without intrusive procedures, MRI is a medical technology that produces precise images of the inside structures of the body. It is a preferred method due to its ability to generate high-quality images of soft tissues. MRI uses several parameters to create contrast based on density, resulting in excellent tissue differentiation. MRI is a versatile tool that can be tailored to specific needs. Advances in digital image processing and computer technology have expanded its capabilities even further. Although it is a mature technology, ongoing research promises to improve the healthcare field in the future[102,103].

2.10.2. Spin Physics

In MR imaging physics, the central concept is "spin." It refers to the magnetic moment produced by a spinning charged particle's current loop, with the charge located on the particle's exterior shell. This current can be measured as[104,105]:

$$I = \frac{q \times v}{2\pi r} \tag{2.21}$$

This formula calculates the tangential velocity of a point on the exterior of a particle based on its charge (q), radius (r), and the symbol "v." In medical MR imaging, the spin of a water proton is commonly used. The magnetic dipole moment (a vector with a direction parallel to the spinning particle's angular momentum) is determined by multiplying the particle's area by the current. The equation of dipole moment, μ is written as[104,105]:

$$\mu = \frac{q}{2m} \times J \tag{2.22}$$

The formula for a particle's behavior in a magnetic field includes the variables J for angular momentum, q for charge, and m for mass. The particles' spins align with external magnetic fields, similar to how iron filings align in free space. This alignment takes place in the applied field's direction. Even though there is not much energy difference in the up and down directions, many spins' energy states can be predicted based on their alignment. According to the direction of the applied field, it should be oriented either "up" or "down". Thus, we can depict a system of many spins using the difference in energy between the two orientations. Spins align to a lower energy state or equilibrium when exposed to an external field. It is determined by assigning them the up or down state. In the case of a more intense field, the polarization between the two states will be more powerful. Therefore, the spins will settle into their adjusted equilibrium state with the external field changes. When multiple spins are considered a system, they produce the same effect as a single magnetic moment. This effect can be observed in three dimensions.

Hence, to learn about the relevant spins, MR imaging techniques exploit the power transfer mechanisms that underlie this effect. When a constant magnetic field polarizes or aligns spins, they can be excited as a group using radiofrequency energy. It is possible to detect the effects if there and enough spins. External field strength also affects the size of the collection required for

detection. One of the basic principles of MR imaging is that a more extensive sample generates a stronger signal. A more powerful magnet will also produce a stronger signal, assuming all other factors are equal. When strong magnetic fields (B_0) exist, their nuclear magnetic moment precesses around the axis of B_0 with the Larmor frequency (ω_0), which is written as[104,105]:

$$\omega_0 = \gamma B_0 \tag{2.23}$$

where γ is the gyromagnetic ratio. When energy is used at a resonance frequency to stimulate a spin system, it exposes a modified magnetic field perpendicular to the applied external field. It causes the spins to relax towards an equilibrium state, settling or moving towards an axis anti-parallel to the gigantic stationary field. Understanding the movement of the vector presentation of a spin ensemble toward a balanced position is crucial to comprehending the origin of MR imaging. By applying resonance radio frequency irradiation of a virtually modified field, a spin system aligned with the primary magnetic field will rotate around the effective field axis instead of the external field axis. After removing the resonance excitation, it will return to its equilibrium position. Bloch and Purcell explained the motions of spins, or ensembles of spins, with Bloch equations consisting of coupled differential equations[104,105].

2.10.3. MRI Instruments

An MR imaging procedure consists of a central magnet, gradient magnets, radiofrequency coils for transferring or accepting the MR imaging signal, and a signal processing kit. In modern clinical MR imaging approaches, a strong static magnetic field is delivered by a superconducting magnet. Magnets are crucial in generating steady, spatially homogeneous magnetic fields over specified volumes that the Earth's magnetic field can approximate. Cryogens (such as liquid helium) are used to cool superconducting magnets, which require no electric power after

establishing a static magnetic force. Installation of a magnet system requires consideration of several factors, including price, weight, and placement. From the point of view of signal-to-noise ratio (SNR) (signal quality), advanced field strength is beneficial. Despite this, it continues to suffer from rising costs due to the need for an additional wire to carry the high current and the increased size of the cryostat.

Moreover, fringe fields must be considered, and the machine's footprint may be large and close to various imaging equipment. The main magnet is expected to have the capability of making slight modifications to the magnetic field to ensure that the homogeneity required for MRI is achieved. Secondary magnetic fields, or shims, can be added to the central energy spatially inhomogeneously to correct errors and compensate for engineering factors. In magnetic resonance imaging, gradients are another type of secondary magnetic field. The gradient coil is an electromagnet installed along an axis to produce a predictable disturbance in the central magnetic field[106,107]. In the z-direction, the practical field (net) with a gradient can be expressed as:

$$B_{net} = B_0 + \Delta B_0 = B_0 + G_Z Z \tag{2.24}$$

In MRI, B_0 is the main magnetic field strength, ΔB_0 is the additional force assisting the effective field from the gradient, G_z is the gradient force in the z-direction, and Z is the distance along the z-axis. The Larmor equation (2.23) shows that with a gradient, the resonance frequency linked to the susceptible volume of the main magnet varies along the gradient axis. The frequency variation will also be linear if the field deviation is linear along that axis. This comment will lay the foundation for the MR imaging processes discussed below. At least three gradients must be present for constructing three-dimensional images. A further practical necessity is that they must

be easily switched on and off. It is recommended that three gradient isocenters be located at the exact location of the primary magnet isocenter coils employed to energize and measure a specific portion of tissue or material during MR imaging. This process also captures the resulting MRI signal. Generally, the same coil can transmit and receive signals. Other applications need separate loops for doing the same job. The RF coil must generate the resonance frequency of the spins, which energizes spin systems. The coils have different shapes that can be customized for specific uses. Customizing the coil's dimensions for investigating tissue is beneficial because the picture's signal should originate exclusively from the tissue under investigation. However, any noise in the image is generated by the entire coil. Since image quality depends on SNR, an optimal size loop will produce the highest quality image for the tissue of interest. MR imaging techniques permit both quality and speed during trading where acceptable grade exists in the acquisition where image can generate more instantaneously by sacrificing a predictable portion of grade as SNR. During imaging, loops sequentially use unique coils. This approach can enhance the quality of data acquisition by repeatedly obtaining data or by expanding the range of an area by using a collection of loops with a principal linear dimension, such as imaging the spine. This technique helps increase SNR, which can improve image quality or acquisition speed. When the coil induces a voltage, the signal is amplified by a receiver and transmitted to a computer via a signal processing train for storage. Adequate data allows the computer to reconstruct an image. To use phased coil exhibitions should connect each coil to its channel for signal processing[104,105].

2.10.4. Relaxation and the MR signal

It is possible to describe a spin system's state by its longitudinal (z-direction) and transverse (x-y direction) magnetization. The magnetization is considered balanced when it aligns with the z-

axis. Applying energy to the spins allows the magnetization to be "tipped" or "reversed," resulting in an x-y component. It is possible to achieve the greatest transverse magnetization by tilting the spins 90 degrees. Two vectors can depict the spin state, one along the z-axis and the other showing the magnetization projected in the x-y plane. The Bloch equations predict that a spin system will tend to relax to equilibrium if it is not at balance energy. Two exponential relaxation constants, T_1 and T_2, contribute to this relaxation. When the z-magnetization vector returns to its balanced state, it is known as spin-lattice relaxation or longitudinal relaxation which is denoted by T_1. Spin-lattice relaxation, T_1, measures how quickly a net magnetization vector returns to its ground state in the direction of a static magnetic field, B_0. It can be calculated using the formula

$$M_z = M_0(1 - e^{\frac{t}{T_1}}) \tag{2.24a}$$

At time t after the 90° pulse, magnetization is M_z and M_0 is the maximum magnetization at full recovery.

As a result of differences in resonance frequency caused by factors such as spatial surroundings, chemical atmospheres, and random processes, T_2 relaxation may lose synchronization when spins are tilted into the transverse plane. The spins cancel each other in the transverse plane, decreasing the transverse vector. It is known as spin-spin relaxation, which has a T_2 time constant. The T_2 relaxation process, also known as spin-spin relaxation or transverse relaxation, refers to the gradual loss of coherence among spinning dipoles, leading to a decay in magnetization in the transverse plane (M_{xy}). When a radiofrequency pulse is applied, this type of relaxation happens with the time constant T_2. T_2 is the time required for the transverse

magnetization vector to decay to 1/e or 37% of its initial magnitude after applying the radiofrequency pulse. The T_2 relaxation time can be calculated using the formula

$$M_{xy} = M_0 e^{\frac{-t}{T_2}} \quad (2.24b)$$

The presence of transverse magnetization leads to a coil voltage, thanks to Faraday's Law. Coils serve as conductors while spin approaches serve as magnetic fields, and as the transverse magnetization moves, flux lines associated with the spin magnetization pass through the coil's conductor. This process generates power.

It has been discussed previously that the spins lose synchronization due to either random (or irreversible) or nonrandom (possibly reversible) processes and that the extent of signaling is directly related to the amount of dephasing. A gradient can be applied on one axis to cause spin dephasing. Due to the Larmor relationship, the spin frequency changes proportionately to the shift in the local applied field relative to the static field. As a result, the spins lose alignment, leading to a phase difference or dephasing. The gradient amplitude is eventually reversed to rephase the spins. It causes the frequency differences between spins to change, achieving phase in the opposite direction. The spins are rephased, resulting in a maximum signal buildup followed by a decrease in magnitude. The timing of the gradient application determines when this "gradient echo" occurs.

A different dephasing/rephasing technique is developed from tiny inhomogeneities in the stationary field. The gradients do not follow axis-like divisions but are spatially consistent. Applying a radiofrequency pulse corresponding to an angle of 180 degrees allows this dephasing to be switched off naturally following excitation. A spin echo (also known as a Hahn echo after

the effect's discoverer, Erwin Hahn) results from this effect. It builds up and decays again to the pattern above after a time called TE (echo time) is substituted from the initial excitation. As a result, the signal disappears for a while in a scenario with many spins. After the spin echo occurs, it reappears[108].

According to Keonig and Keller[21], spin-spin relaxation is written as

$$R_2 = \frac{1}{T_2} = \frac{a}{d_{NP}D}\gamma^2\mu^2 C_{NP} J(\omega, \tau_D) \quad (2.25)$$

In this equation, a stands for a constant, "d_{NP}" stands for the nanoparticle diameter, "D" stands for the diffusion coefficient, "C_{NP}" stands for the concentration of the nanoparticles, "J" stands for the spectral density function, and " μ " stands for the magnetic moment of the nanoparticles.

The spin-spin relaxation $1/T_2$ was found from the first-order exponential fitting, which is written as

$$\mathbf{I(t) = P^{*} exp\ (-\frac{t}{T_2})} \quad (2.26)$$

In this spin-spin relaxation measuring equation, t stands for the decay time, P^* represents the initial intensity, $I(t)$ is the peak intensity. For a concentration (C) of the solution of contrast agents, $R_2=\frac{1}{T_2}$, relaxation rate was found from the exponential fitting of equation (2.26). Nuclear spin relaxivities of magnetic nanoparticles in aqueous solutions can be calculated using the following:

$$\frac{1}{T_i} = \frac{1}{T_i^0} + r_i.C \quad (2.27)$$

In this relaxivity measuring equation, i stands for 1 or 2, $\frac{1}{T_i^0}$ represents the relaxation rate of the control, and r_i represents the relaxivity of nuclear spins of nanoparticles. The $\mathbf{r_2}$ relaxivities were calculated from the slope of the concentration vs relaxation rates curve [15,17,19,21].

In MRI, the contrast describes the signal differences between neighbouring areas, such as tissue and tissue, vessel and tissue, and bone and tissue. Contrasting agents are developed based on relaxation mechanisms: T_1 and T_2.

2.10.5. Gradient echo imaging

When field gradients are applied in MRI, they can alter the magnetic field of individual points in the device. By manipulating the gradients in all three dimensions, it is possible to specify a single point in the magnet with a different one. This imaging process is called the "sensitive point" strategy. However, it is not commonly used for clinical imaging due to the time required for data acquisition.

Current imaging techniques use field gradients to encode spatial knowledge, and the Fourier transform allows for the simultaneous acquisition of data from many points along an axis. To build a 2D magnetic resonance picture, a piece of tissue is "chosen" by establishing a gradient in one direction and involving a pulse that counts energy to the spins. The frequency of this pulse is adjusted so that only spins in the specified slice will undergo the resonance effect. Applying a field gradient along an axis proves a likeness between frequency and spatial position. By documenting the signal in the coil during the gradient application, the spins along the gradient axis will rotate with distinct frequencies that reflect their place.

Constructing and recovering a gradient echo can be duplicated after applying an orthogonal gradient demonstrating a phase association along the remaining axis. The mathematics concerned with reconstructing this information involves a two-dimensional Fourier transformation. Gradient echo imaging is more challenging concerning the scanner than spin-echo strategies because the dephasing that results from inhomogeneities within the stationary field needs to be rephrased. However, progress in magnet configuration and construction has made it attainable to achieve good-quality gradient echo images, which can be the most suitable choice for higher fields[104,105].

2.10.6. Spin echo imaging

MR imaging relies heavily on pulse sequencers for spin echo imaging. Signal performance is excellent when reversible dephasing is appropriately rephrased. As a result of static magnetic field inhomogeneities, all dephasing associated with them is rephased during the spin echo period. As described above, a gradient echo encodes gradients at a particular frequency. An inversion pulse generating a spin echo at time TE is almost analogous to a gradient echo pulse. Gradient echo selects slices, encodes frequency and phase, and reconstructs the image. Another gradient may be encoded with a degree instead of slice selection in the pulse sequence. Fourier three-dimensional transforms were used for the reconstruction of images. As a result of such a procedure, three-dimensional MR imaging is possible, offering many advantages, including acquiring smaller tissue slices. It provides higher-resolution images, improving diagnostic accuracy and allowing for better anatomy visualization. It also reduces imaging time, making it more efficient and cost-effective. Additionally, three-dimensional MR imaging benefits complex anatomy, such as the brain, heart, and spine, enabling more accurate diagnosis and treatment of diseases[104,105].

2.10.7. MRI Contrast

Two significant timing variables in spin echo pulse sequences are repetition time (TR) and echo time (TE). As an alternative and equivalent concept, TR can be viewed as the time interval between pulses encoded with phases or as the time for one pulse train to play out fully. The TE measures the time difference between when the excitation occurs and when the signal is acquired. Inhomogeneities in magnetic fields that cause spatially invariant spins to be dephased can be rephased by the spin echo methodology. There are other ways in which dephasing can occur that are spontaneous and irreversible. The T_2 time constant represents the loss of signal caused by irreversible dephasing. As a result of the combination of reversible dephasing and T_2 processes, Spin Echo can produce a composite time constant called T_2^*. So T_2 decay tends to be slower than T_2^* decay. The decay of an FID can be analyzed as it reflects T_2^* to gain a deeper understanding of T_2 and T_2^* effects.

If there is a difference in signal force between spin echo acquisitions with various TE, it indicates T_2. A spin system with equal balance magnetization but differing T_1 decay constants can be examined to determine the effects of changing TR. For example, the brain's lateral ventricles have longer T_1 values than the brain parenchyma, which has shorter T_1 values. A 90-degree pulse can be used to stimulate both tissues and after allowing them to return to equilibrium, the process can be repeated. The short and long T_1 signals are identical after each excitation since magnetization has reached its maximum value. If the equilibrium magnetizations of the spin approaches differ, then an individual's signal will reflect the number or density of spins in the system. Proton-density images are similar to x-ray images in MR imaging, which reflects these differences. There are some instances where proton-density images are preferred over relaxation-time-weighted images. As a result of a shortened TR, one spin system may relax

to equilibrium, whereas another with a longer decay time may not. To achieve complete transverse magnetization, the successive excitation pulses will induce the fully relaxed spin method. Despite this, the partially flexible design will gain less than the total transverse magnetization. In simpler terms, some molecules in our body have a short T_1 relaxation time, and others have a long T_1 relaxation time. It means that when they are excited, the short T_1 molecules have a stronger magnetic signal than the long T_1 molecules. When we take an image, the machine can detect these differences and create a T_1-weighted image which is excellent for showing the body's structure. However, the long T_1 molecules may appear darker in the image due to their weaker magnetic signal. It is known as partial saturation. Overall, T_1-weighted imaging is the preferred method for displaying anatomy.

The maximum transverse magnetization that may be achieved before the excitation pulse does not directly reflect the longitudinal magnetization, even though longitudinal magnetization cannot be directly detected. As a result, it offers an additional imaging opportunity known as inversion recovery. At equilibrium, a spin system's longitudinal magnetization reaches a maximum value called M_0. A spin along the z-axis with magnitude M_0 can be rotated to any degree around any axis using the appropriate excitation pulse. It allows for a composite spin to be manipulated in various ways. Practically it will transform all the longitudinal magnetizations into signal-producing transverse magnetizations by ninety degrees of rotation. The transverse and longitudinal magnetization values are equal when the longitudinal magnetization is rotated 45 degrees. Increasing the spin vector rotation by 90 degrees produces more transverse and less longitudinal magnetization. Suppose the spin vector is rotated more than ninety degrees. In that case, the amount of transverse magnetization decreases as the rotation increases, but the longitudinal magnetization remains far from equilibrium after excitation up to 180 degrees. At

the end of the excitation, the longitudinal magnetization equals M_0, and the transverse magnetization equals zero. The spin strategy has been inverted. A transverse magnetization does not develop as a result of relaxation.

As a result, a second excitation pulse can be applied at any time to change the current state of longitudinal magnetization to transverse magnetization, resulting in a signal. In passing through the impartial state, when the spins associated with the tissue or essence of interest (most commonly fat or water) undergo z-magnetization, a second excitation pulse occurs that is particularly beneficial. A signal is generated when the remaining tissue (having different T_1) produces transverse magnetization. However, the tissue that has passed through the null will not generate a pulse. In the reconstruction of this picture, the void tissue will have dimensions of zero intensity. When the arrangement is designed to void water (including cerebrospinal fluid), it is known as Fluid Attenuated Inversion Recovery (FLAIR). The potential outcomes of changing the TE can be examined when the TR is replaced with a value that minimizes T_1-weighting. As a result of increasing the TE, spin systems can completely dephase before being acquired. Therefore, there is no signal upon acquisition.

In contrast, other spin systems (with long T_2) will exhibit significant pulses upon accession. When the imaging is complete, areas with long T_2 will appear brighter, while regions with short T_2 will also appear more luminous. T_1-weighted data for the specific analyzed tissue will be obtained if the TR is short and the TE is fast. A proton density distribution can be constructed when the TR is relatively large. To obtain a T_2-weighted image, a long TR is combined with a relatively long TE. It is essential to optimize TR and TE to design specific contrasts appropriate for the tissue under consideration. In clinical imaging, the development time of an image is

determined by the repetition time and the number of repetitions. The number mentioned here represents the number of phases encoded in the image. In clinical imaging, this sequence is repeated 256 times. The use of 512 repetitions is not uncommon, and inspections can also be run up using 128 or fewer repetitions[104,105].

2.10.8. Fast spin-echo imaging in k-space

MRI has challenged scientists to obtain higher-quality and faster images since its development. Current MR imaging scanners possess significantly advanced capabilities due to simultaneous advances in computing, mechanical design, and construction since then. The limitation of T_2-weighted diagnostic scanning was the requirement for long TR periods to avoid saturating spin approaches, resulting in the addition of pure T_1 contrast when the contrast was anticipated to be pure T_2. The T_2-weighted imaging was also inadequate since most of the pulse sequence's duration was spent waiting for relaxation. Spins can be refocused within a specific TR period in a spin echo technique to create multiple spin echoes simultaneously. It is possible to reconstruct images corresponding to different TEs within the same TR by acquiring and storing multiple echo signals within the same TR. A rapid method for obtaining T_2-weighted diagnostic images has been developed by utilizing the natural evolution of this technique.

Understanding k-space is crucial to understanding modern MR imaging procedures. In an MR imaging sequence, the signal acquired is recorded over time. To create an image using magnetic resonance imaging (MRI), spin echoes or gradient echoes need a specific amount of time to play out in the receiver coil. The computer then records these echoes and combines them with the rest of the pulse sequence. Finally, the Fourier transform converts the echo data into an image. A crucial mathematical tool is the Fourier transformation, which can decompose complex signals

into components, each with its characteristic frequency and magnitude. In MRI, gradient magnetic fields are crucial as they relate frequency to spatial position encoded in the signal. The coil receives a signal that is made up of multiple frequencies. Time-domain signals are those that record the strength of a signal over some time. Using the Fourier transform, this signal is transformed into frequencies and magnitudes. An ordinate would be labeled through the frequency if this effect were plotted on a graph. As a result, the curve represents a frequency domain. Because the frequency is connected to space (again, through gradients), the frequency domain is comparable to the spatial domain in MR imaging. Therefore, the Fourier transformation effectively reveals the source's position for each signal segment (along the gradient axis). In the magnitude of the signal, the number of spins at that zone is maintained. An image is merely a matrix of numbers, each corresponding to a level of intensity on the scale of black to white, as viewed by a mathematician. There is a spatial relationship between each intensity number in the course. The first spin echo is characterized as a row in a matrix formed by piling the intensity values from the receiver loop. Rows are formed by successive spin echos (each with a different phase encoding gradient applied). The intensity values in these matrices (or k-space matrices) correspond to places in time at which the coil receives a signal. Using the Fourier transformation, the spatial dimensions are transformed into time dimensions, thus completing the theoretical framework.

A one-dimensional image can be viewed in two dimensions or three dimensions. Creating an image from a k-space matrix involves converting the matrix into the frequency or spatial domain. Both the k-space and image space matrices have identical dimensions. The k-space needs data points corresponding to the number of segments in the ultimate image to produce an entire image. However, it is essential to note that the signal gained at a specific time in k-space does

not instantly translate into the intensity of a single point in image space. Instead, each point in k-space contributes to all points in image space. Therefore, the central region of the k-space is crucial for the overall contrast of the image.

In contrast, the boundary of k-space determines the image's edge definition and fine structural quality. The signal's strength in the k-space's centre determines the image's contrast. It can be understood when gradients are enabled. To prepare for the next row in a k-space matrix, the frequency encoding gradient moves from left to right, while the phase encoding gradient moves up and down. A fast spin echo image (FSE) is created with multiple excitation pulses within a single TR period. This way, a picture can be filled four times faster than a conventional acquisition method. The discrepancy in the k-space central region causes the discrepancy in an FSE image. In this image, the contrast will be comparable to the difference between a conventional and effective acquisition with a single TE. During repeat cycles, the number of spin echoes determines the period during which an FSE sequence is acquired. Increasing this number will increase speed[104,105].

2.10.9. Other rapid imaging techniques

The FLASH10 technique was one of the first to be introduced for rapid imaging. An initial pulse lower than ninety degrees could recover sufficient longitudinal magnetization much faster. Echo-planar imaging (EPI) is a family of gradient echo imaging techniques recently developed for rapid imaging. Following a single excitation pulse, EPI uses rapidly changing gradients to cover K-space completely. Performing hybrid MR imaging, incorporating gradient and spin echo techniques, is becoming increasingly common. An array of coils can be used to conduct multiple imaging experiments simultaneously. It allows for increased coverage of the same area, which

results in higher-resolution images. Furthermore, hybrid MR imaging reduces the time required for imaging, enabling faster scans with higher accuracy[104,105].

2.10.10. MR Angiography (MRA)

The foundation for MRA is the exploitation of blood flow enhancement. There are two methods for capturing images of vascular anatomy: time-of-flight angiography and phase contrast angiography.

The time-of-flight technique relies on proton saturation, inversion, or relaxation to modify the longitudinal magnetization of moving blood. It differentiates moving blood from the surrounding immobile tissues and allows for the visualization of extended vessels in a two-dimensional stack of slices. Often used for two-dimensional stationary anatomy, window thresholding, and subtracting non-contrast maximum intensity projection (MIP) from contrast MIP reduces background signals. Phase Contrast Angiography relies on the phase change in moving protons such as blood. By applying a bipolar gradient, the phase change is induced, and image information is provided by subtracting the second excitation from the first. MRA uses a bipolar gradient to measure blood flow. The degree of phase shift is directly related to the protons' velocity within the excited volume[108].

CHAPTER 3: MATERIALS AND METHOD

3.1. Materials

Materials used in this investigation are as follows:

Ferric chloride

- Chemical formula: $FeCl_3$
- Molecular weight: 162.21 g/mol
- Reagent grade: 99%
- Company: Loba chemic pvt ltd, Mumbai
- Country: India

Magnesium nitrate hexahydrate

- Chemical formula: $MgSO_4.6H_2O$
- Molecular weight:256.41 g/mol
- Reagent grade: 99%
- Company: Merck
- Country: Germany

Cobalt (II) chloride

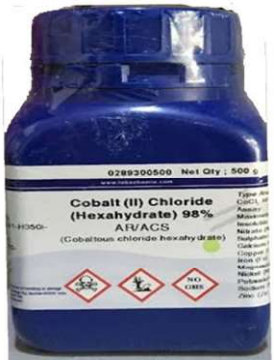

- Chemical formula: $CoCl_2.6H_2O$
- Molecular weight: 237.93 g/mol
- Reagent grade:98%
- Company: Loba chemic pvt ltd, Mumbai,
- Country: India.

Sodium hydroxide

- Chemical formula: NaOH
- Molecular weight: 40 g/mol
- Reagent grade: 99%
- Company: Merck, KGaA
- Country: Germany.

Chitosan

- Chemical formula: $(C_6H_{11}NO_4)_n$
- Molecular weight: low molecular weight (1536/1538),
- Reagent grade:(60-100)% deacetylated
- Viscosity: Brookfield 1% solution in 1% acetic acid
- Company: Sigma-Aldrich,
- Country: USA.

Acetic acid

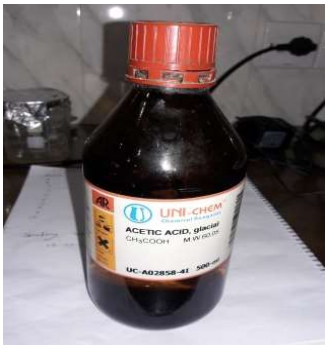

- Chemical formula: CH_3COOH
- Molecular weight:60.05 g/mol
- Reagent grade:100% (glacial)
- Company: Merck, KGaA,
- Country: Germany.

Polyethylene glycol (PEG.)

- Chemical formula: $C_{2n}H_{4n+2}O_{n+1}$
- Molecular weight: 6000 g/mol; 8000 U.S.A
- Reagent grade:100%
- Company: Merck chemical private limited, Mumbai,
- Country: India.

Dextran

- Chemical formula: $(C_6H_{10}O_5)_n$
- Molecular weight: 4000 g/mol
- Reagent grade:100%
- Company: Merck, Sigma-Aldrich
- Country: Germany.

Acetone

- Chemical formula: C_3H_6O
- Molecular weight: 58.08 g/mol
- Reagent grade:98%
- Company: Merck KGaA
- Country: Germany.

Ethanol

- Chemical formula: C_2H_5OH
- Molecular weight: 46.07 g/mol
- Reagent grade:98%
- Company: Merck KGaA
- Country: Germany.

Ammonia solution

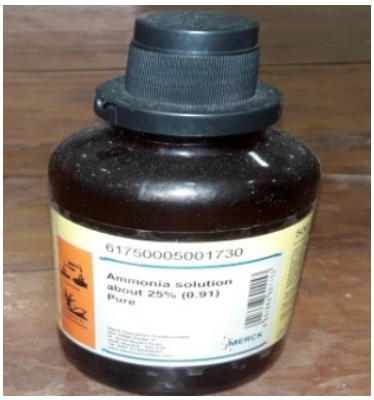

- Chemical formula: NH_3
- Molecular weight: 17.03 g/mol
- Reagent grade:(25%; 0.98)
- Company: Merck SpecialtiesPvt. Ltd., Mumbai,
- Country: India.

Ammonium hydroxide

- Chemical formula: NH_4OH
- Molecular weight: 35 g/mol
- Reagent grade:99%
- Company: Merck Specialties Pvt. Ltd., Mumbai,
- Country: India.

Silver nitrate

- Chemical formula: $Ag(NO_3)$
- Molecular weight: 169.87 g/mol
- Reagent grade:99.99%
- Company: New York City: D. Van Nostrand Company.
- Country: USA.

3.2. Materials Synthesis Technique

The size, shape, and properties of nanoparticles are susceptible to their preparation technique. Various synthesis methods can be used to create nanoparticles, including (a) solid-state reactions, (b) high-energy ball milling, (c) sol-gel, (d) chemical co-precipitation, (e) microwave sintering, (f) auto combustion, etc.

In this study, chemical co-precipitation was used to synthesize nanoparticles. The process of chemical co-precipitation is simple and inexpensive. The relative nucleation and growth rate are controlled during synthesis to control particle size and size distribution[53,109–113]. A series of MCFO were synthesized by wet chemical co-precipitation method using NaOH co-precipitating agent. Analytical grades of $Mg(NO_3)_2 \cdot 6H_2O$, $CoCl_2.6H_2O$, and $FeCl_3$ were incorporated in the needed molar proportion. Then 8 M of NaOH solution was added continuously through a magnetic stirrer at a speed of 400 rpm. Once the co-precipitation was formed, 8 M NaOH was added dropwise, and the solution was allowed to stabilize. After that, an additional 6 M NaOH was added dropwise to the solution to keep the pH between 11 and 13. For better co-precipitation, the solution was heated to 353 K for an hour and cooled at ambient temperature. After reaching room temperature, extra NaOH and salts were removed from the mixture using centrifugation at 13000 rpm for 20 min, and the process was repeated several times. The $AgNO_3$ test verified the separation of NaOH. The MCFO nanoparticles were then incubated at 343 K for 72 hours to fully ferritize them. The schematic diagram of the synthesis process is as follows:

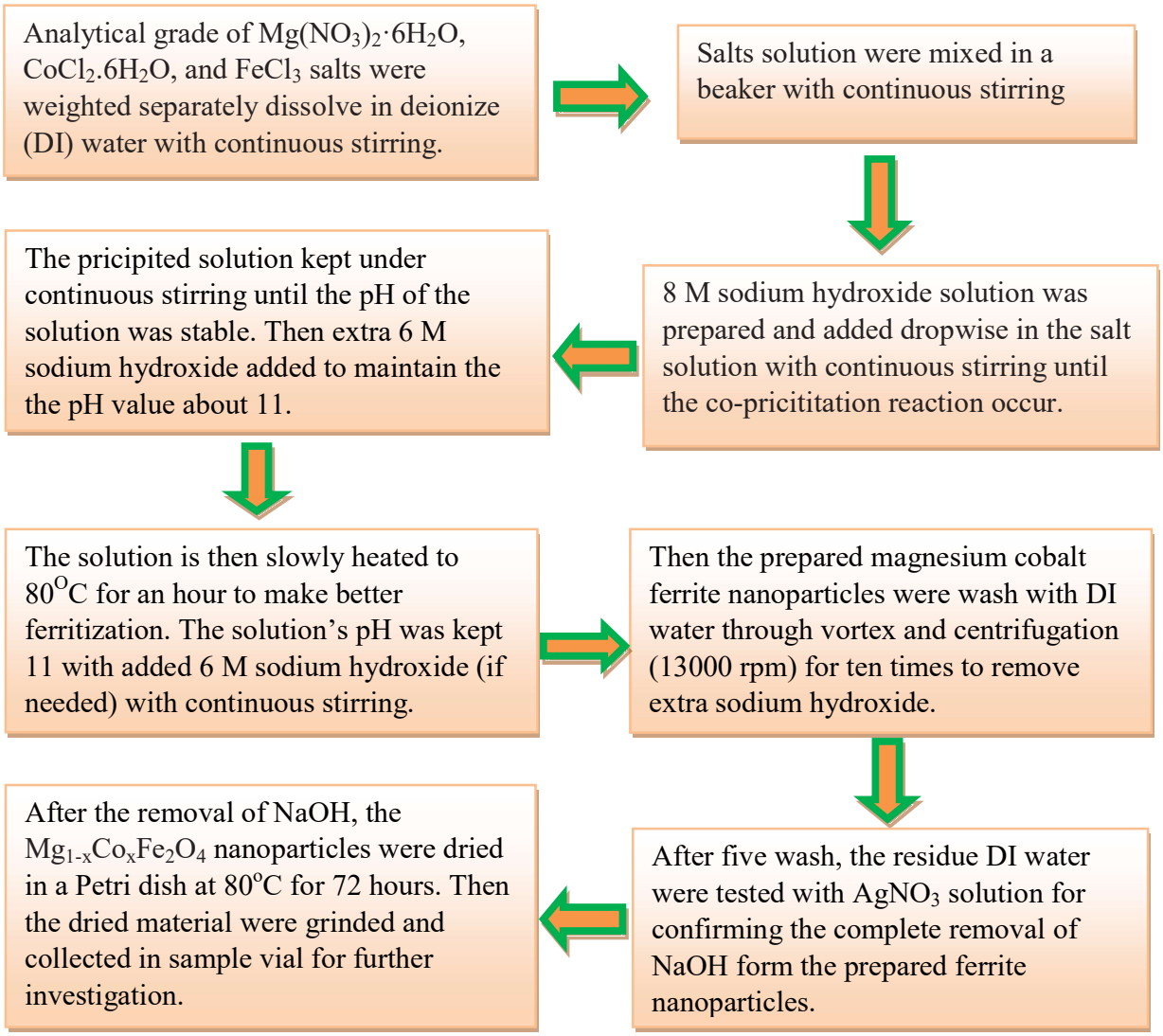

Figure – 3.1: The schematic diagram of the synthesis method $Mg_{1-x}Co_xFe_2O_4$ nanoparticles in the co-precipitation method.

Chemical reactions of the prepared $Mg_{1-x}Co_xFe_2O_4$ nanoparticles are as follows:

1. $Mg(NO_3)_2.6H_2O + 2FeCl_3 + 8NaOH = MgFe_2O_4 + 2NaNO_3 + 6NaCl + 10H_2O$
2. $0.9Mg(NO_3)_2.6H_2O + 0.1CoCl_2.6H_2O + 2FeCl_3 + 8NaOH = Mg_{0.9}Co_{0.1}Fe_2O_4 + 1.8NaNO_3 + 6.2NaCl + 10H_2O$
3. $0.8Mg(NO_3)_2.6H_2O + 0.2CoCl_2.6H_2O + 2FeCl_3 + 8NaOH = Mg_{0.8}Co_{0.2}Fe_2O_4 + 1.6NaNO_3 + 6.4NaCl + 10H_2O$

4. $0.7Mg(NO_3)_2.6H_2O + 0.3CoCl_2.6H_2O + 2FeCl_3 + 8NaOH = Mg_{0.7}Co_{0.3}Fe_2O_4 + 1.4NaNO_3 + 6.6NaCl + 10H_2O$
5. $0.6Mg(NO_3)_2.6H_2O + 0.4CoCl_2.6H_2O + 2FeCl_3 + 8NaOH = Mg_{0.6}Co_{0.4}Fe_2O_4 + 1.2NaNO_3 + 6.8NaCl + 10H_2O$
6. $0.5Mg(NO_3)_2.6H_2O + 0.5CoCl_2.6H_2O + 2FeCl_3 + 8NaOH = Mg_{0.5}Co_{0.5}Fe_2O_4 + NaNO_3 + 7NaCl + 10H_2O$
7. $0.4Mg(NO_3)_2.6H_2O + 0.6CoCl_2.6H_2O + 2FeCl_3 + 8NaOH = Mg_{0.4}Co_{0.6}Fe_2O_4 + 0.8NaNO_3 + 7.2NaCl + 10H_2O$
8. $0.3Mg(NO_3)_2.6H_2O + 0.7CoCl_2.6H_2O + 2FeCl_3 + 8NaOH = Mg_{0.3}Co_{0.7}Fe_2O_4 + 0.6NaNO_3 + 7.4NaCl + 10H_2O$
9. $0.2Mg(NO_3)_2.6H_2O + 0.8CoCl_2.6H_2O + 2FeCl_3 + 8NaOH = Mg_{0.2}Co_{0.8}Fe_2O_4 + 0.4NaNO_3 + 7.6NaCl + 10H_2O$
10. $0.1Mg(NO_3)_2.6H_2O + 0.9CoCl_2.6H_2O + 2FeCl_3 + 8NaOH = Mg_{0.1}Co_{0.9}Fe_2O_4 + 0.2NaNO_3 + 7.8NaCl + 10H_2O$
11. $CoCl_2.6H_2O + 2FeCl_3 + 8NaOH = Mg_{0.9}Co_{0.1}Fe_2O_4 + 8NaCl + 10H_2O$

The dried MCFO ferrite nanoparticles were collected from a Petri dish. Then the as-dried magnesium cobalt nanoparticles were pelletized and annealed at 200oC, 400oC, 600oC, and 800oC, respectively, to vary their particle size.

3.3. Surface Coating

The coating method should be used for surface modification of nanoparticles to increase the biocompatibility and biodegradation of these samples. Bare particles tend to agglomerate, but after coating with some nonmagnetic material to be highly dispersive, their high surface-to-volume ratio is also reduced per unit[114–116]. In this study, Chitosan, PEG, and Dextran can be used as a coating material because:

- They are biodegradable, biocompatible, antibacterial, and non-toxic.
- They are unique cationic, hydrophilic polymers.
- They have low immunogenicity.
- The functional groups on their surface can be used to functionalize the particle[117–120].

The coating protocols of Chitosan, PEG, and Dextran are discussed in the next section.

3.3.1. Coating with 2 % Chitosan Solution

The samples were coated with a 2% chitosan solution that was made by combining 2 grams of chitosan with 100 ml of deionized (DI) water at 400 revolutions per minute and stirring continuously for 72 hours. The mixture was combined with acetic acid to dissolve chitosan in water after 12 hours of mixing. After that, the solution was spun twice at 13000 rpm to remove any leftovers. Secondly, 20 mg of magnesium cobalt ferrite was added to 1 ml 2 % chitosan solution, then vortexed on and repeatedly sonicated to prepare 20 mg/ml chitosan-coated stock solution. Extra Chitosan was removed by centrifugation at 20000 rpm for 20 minutes. The stock solution was then diluted to create solutions with different concentrations[121–123].

3.3.2. Coating with 25% PEG Solution

Twenty-five grams of polyethylene glycol (PEG) was dissolved into 100 ml distilled water through continuous stirring at 400 rpm for 2 hours to form a homogeneous 25% PEG solution. After that, we added 20 mg of magnesium cobalt ferrite to 1 ml of 25% PEG solution, vortexed it, and repeatedly sonicated it. Extra PEG was taken out, and DI water was added to keep the solution's concentration at a certain level. Finally, we kept vortex and sonication until the sedimentation was found, and the solution was kept as the stock solution. Other engagements were prepared for further study to dilute the stock solution[124–126].

3.3.3. Coating with 20 % Dextran Solution

Twenty grams of Dextran was dissolved into 100 ml distilled water through continuous stirring at 400 rpm for 2 hours to form a homogeneous 20% Dextran solution. Then, we added 20 mg of magnesium cobalt ferrite to 1 ml 20 % Dextran solution and heated it to 393 K for 20 minutes, followed by vortex and sonications several times. Extra Dextran was removed by centrifugation at 20000 rpm for 20 minutes. Finally, we kept vortex and sonication until the sedimentation was found, and the solution was kept as the stock solution. Other concentrations were prepared for further study to dilute the stock solution[127,128].

.

The MNPs were coated to form a homogeneous suspension called ferrofluids, colloidal liquids in the range of nano dimension and superparamagnetic or ferromagnetic. Since nanoparticles have a weak magnetic attraction, every particle is thoroughly coated with surfactants to inhibit aggregation. The van der Waals force of the surfactant becomes sufficient to prevent accumulation[118,129]. From the initial concentration, 20 mg/ml, the different concentrations, such as 0.5mg/ml, 1 mg/ml, 2 mg/ml, 3 mg/ml, 4mg/ml, and 6 mg/ml, were prepared for as dried and calcinated magnesium cobalt ferrites. These concentrations were used in FTIR, DLS, magnetization, cytotoxicity, and hyperthermia measurements. Moreover, 0.01mg/ml, 0.025 mg/ml, 0.05 mg/ml, 0.75 mg/ml, 0.10 mg/ml, 0.12 mg/ml, and 4 mg/ml concentrations of magnesium cobalt ferrites nanoparticles were prepared to test the efficiency as MRI contrast agent.

3.4. Characterization

Magnesium cobalt ferrite nanoparticles' structural characterization was done using an X-ray diffractometer (XRD), model: Philips PW 3040-X'Pert PRO Panalytical, Netherlands, and a transmission electron microscope (TEM), model: TALOS F200 G2, FEI Company, USA. The XRD scan was carried out at a 2θ angle ranging from 15-70 degrees at 40 kV and 30 mA using CuKα radiation (where λ=1.54059 A0) using a scan step size of 0.0167º for a powder sample. TEM operated at 200 kV. For TEM analysis, the samples were dispersed in ethanol through sonication for 15 minutes and drop-casting on an electron-transparent Cu grid coated with carbon and dried. The FTIR spectroscopic measurements were performed using the Jupiter, UK, STA, 449 F3 model. Chitosan, bare magnesium cobalt ferrite nanoparticles, and chitosan-coated magnesium cobalt ferrite nanoparticles all had FTIR spectra in the 350–4000 cm^{-1} range. Raman Spectroscopy measurements were performed using S & I Spectroscopy & Imaging, CRS+ 500/BX53, MonoVista GmbH, Germany. The filter was cleaned up with a length of 60 cm^{-1} using a diode laser system operating at 785 nm. It supplied a power output of 100 mW. The Raman spectroscopy of dried magnesium cobalt ferrite nanoparticles was taken between 200 and 4000 cm^{-1} as pelletized. A dynamic light scattering (DLS) device, model: ZEN 3600, from Zetasizer, Malvern, UK, was used to examine the samples' hydrodynamic size and zeta potential. At 25°C, 37°C, and 44°C, respectively, the hydrodynamic size of MCFO magnetic nanoparticles coated with chitosan at various concentrations was studied. The magnetic moment of all samples was measured at room temperature with the Physical Property Measurement System (PPMS), model Inc.10307, Quantum, USA. The magnetic moment of all the investigated samples (coated and bare) was measured from -5 to +5 tesla. Magnetic status was also studied using Mössbauer spectroscopy, model: W302, web research company, USA. A resonant transmission gamma-ray

spectrometer with a transducer velocity of 11 mm/s and a constant acceleration mode was used to capture Mössbauer spectra. Before measurement, the spectrometer was calibrated using a sample of metallic iron foil, and the centroid of the Mössbauer spectrum was determined to be zero velocity. At ambient temperature and without magnetic fields, 72 hours were required for Mössbauer data gathering. The temperature profiles of the investigated nanoparticles were measured using a hyperthermia apparatus made by Ambrell, USA, dubbed EASY HEAT 5060LI. It consists of an eight-turn coil with a 4 cm diameter. The coil's current was fixed at 283 A and its signal frequency at 343 kHz for the hyperthermia tests, creating a magnetic field of 26 mT in the sample coil. The magnesium cobalt ferrite nanoparticles in a 600 µL chitosan-coated solution were placed in an Eppendorf tube for heating at a 26 mT magnetic field for different time intervals[3,48,99]. After removing the magnetic field, a digital thermometer measured the sample's temperature.

All T_2 W FSE and T_2 map MR images were captured using an MRI machine with the following model number: MRS7017, MR Solution, United Kingdom. TR was 4000 ms, TE was 45 ms, THK was 1.0 mm, and FOV was 40 during T2 W FSE imaging. When doing T2 mapping, the following parameters were used: TR = 4000 ms, TE = 7, 14, 21, 28, 35, 42, 49, 56, 63, 70, 77, 84, 91, 98, 105, and 112 ms, THK = 1.0 mm, and FOV = 40. MCFO magnetic nanoparticles coated in chitosan were used to capture phantom images. Five concentrations of tiny Eppendorf tubings were used to create the phantom for each sample. A mouse body coil was used to house the ghost. The coil with the sample was placed at the homogeneous MRI magnet center with B_0 = 7 T. The B was obtained by applying a perturbation field with the Larmour frequency of 2048 Hz. MRA of rat head was performed using T_2 W FSE imaging and time-of-flight (TOF) magnetic resonance imaging (MRI) techniques to inquire about the contrast efficacy of

investigated PEG-coated, chitosan-coated, and dextran-coated MCFO ferrite nanoparticles. In this study, forty Albino Wister male healthy rats of body weight 250 to 300 g were used. Throughout the TOF experiment, the rats were unconscious by injecting the prescribed ketamine (0.6 ml) dose into the muscle[9]. The unconscious rat was placed in a horizontal bed. Its neck was placed in the centre of the radio frequency (RF) coil, which was positioned at the centre of the nuclear magnetic resonance (NMR) coil, which was the homogeneous centre of the static magnetic field (7 T). With a flip angle (FA) of 35°, repletion time (TR) of 22 ms, echo time (TE) of 3 ms, a field of view (FOV) of 3.6 * 3.6 mm, and an image matrix of 256 * 256, TOF pictures of the entire rat brain were first collected without the use of a contrast agent. Because brain tissues were thoroughly saturated and the low flow velocity nearly inhibited the venous system, a repetition period of 22 ms was chosen[130–133].

Animal research reports were maintained according to ARRIVE Guidelines. Guide for the Care and Use of Laboratory Animals (1996) was followed when handling the animals. Atomic Energy Centre Dhaka's Ethical Review Committee for Animal Experiments approved the protocol with Memo No: AECD/ROD/EC/21/202 to minimize the suffering of experimental animals.

A hemocytometer (Optika, Italy), a CO_2 incubator (Nuaire, U.S.A.), an inverted light microscope, and a biosafety cabinet (Model NU-400-E, Nuaire, U.S.A.) were used to conduct the cytotoxicity test on the Hela (a human cervical carcinoma cancer cell) cell line. In the current investigation, HeLa cells were kept alive in DMEM (Dulbecco's Modified Eagles' Medium), which contained 10% fetal bovine serum, 0.2% gentamycin, and 0.1% penicillin-streptomycin. HeLa cells ($4x10^5$/200 μL) were seeded into 96-well plates and cultured for 24 hours in a CO_2 incubator at 37°C and 5% CO_2. In each well, 50 μL of MCFO nanoparticles with 4 mg/ml concentration were filtered (filtered through a 0.45 μm syringe filter). Each sample was

contained in a duplicate well. Approximately 48 hours after incubation, the insoluble samples were washed out seven times with media, and the survival of HeLa cells was examined under an inverted light microscope[134–136].

3.5. Equipment Used for the Synthesis of Nanoparticles

3.5.1. Magnetic stirrer with a hot plate

A magnetic stirrer with a hot plate performed the heating and stirring operation. During the synthesis process, the stirring speed was maintained at 400 rpm.

Figure 3.2: Magnetic stirrer with a hot plate of model no. TS-18Q, Lab Tech, DAIHAN LABTECH CO. LTD., U.S.A.

3.5.2. pH meter

The pH meter was used to determine the pH of the synthesis solution at different stages of the synthesis process. Temperatures of other measurements were taken using a temperature probe of this pH meter.

Figure 3.3: The pH meter of the model was HI 2211, HANNA Instruments, Europe, Romania. Model no of the pH probe was HI 7662, HANNA, Romania.

3.5.3. Balance meter

A balance meter was utilized to determine the sample's weight at different stages of the synthesis technique.

Figure 3.4: Balance meter of model SP250, SCIENTECH BOULDER CO, U.S.A.

3.5.4. Fume hood

A fume hood continuously delivers harmful gas or volatile chemicals away from the user. In this work, a fume hood was used to release high CO2, N2, and water vapour, which was produced considerably.

Figure 3.5: Fume hood of model FH 1200(E), JINAN BIOBASE BIOTECH CO.LTD., China.

3.5.5. Oven

The drying and annealing were performed by using an oven.

Figure 3.6: Oven for sample heat treatment of Model L3/12/C6, Lilienthal, Germany.

3.5.6. Centrifuge

Figure 3.7: Centrifuge machine of Model: Sigma 2-16 P, Speed: 15000 rpm (max), Company: SIGMA Laborzentrifugen, Country: Germany, situated in Atomic Energy Centre Dhaka.

Centrifuges rotate objects around fixed axes, involving a powerful force parallel to the spin axis (outward). Centrifuges work on the sedimentation principle, where denser substances move outward in a radial direction due to centripetal acceleration. As a result, less dense entities are displaced and move toward the centre. Nanoparticles settle to the bottom of a laboratory centrifuge that uses sample tubes, while low-density particles rise to the top[137]. In this thesis work, the following centrifuge is used.

3.5.7. Vortex mixer:

Vortex mixers were employed to mix magnetic nanoparticles with distilled water and coating materials homogeneously.

Figure 3.8: Vortex-1 for homogeneous mixing, Model: VM-1000, Input Voltage: 220 AC, Frequency: 50 Hz, Company: Digisystem Laboratory Instruments Inc, Country: Taiwan. Speed: 3000 rpm

3.5.8. Ultrasonic sonicator

Sonication uses sound energy to stir particles in a sample for various purposes. *Ultrasonication* is a process guided by ultrasonic frequencies (>20 KHz). Sonication contains considerable effects, both chemical and physical. Ultrasound involves sonic waves on chemical systems, which is called sonochemistry. In addition to wastewater purification, degassing, extracting plant oils, extracting antioxidants and anthocyanins, producing biofuels, desulphurizing crude oil, rupturing cells, processing polymers and epoxy, thinning adhesives, and many other processes, sonication can produce a variety of nanoparticles, including nanoemulsions, nanocrystals, liposomes, and wax emulsions. By stopping intermolecular exchanges, sonication can be used to hasten breakdown. When stirring the sample is not possible, as with NMR tubes, it is functional. In nanotechnology, sonication is frequently used to distribute nanoparticles in fluids equally[138].

Figure 3.9: Ultrasoniccator of Model no Power sonic 510, Hwa Shin Technology, SEOUL, KOREA, having frequency- 50 Hz, Input voltage- 230AC, Output power-500W.

3.6 Equipment Used for Characterizations

3.6.1. X-Ray Diffraction (XRD)

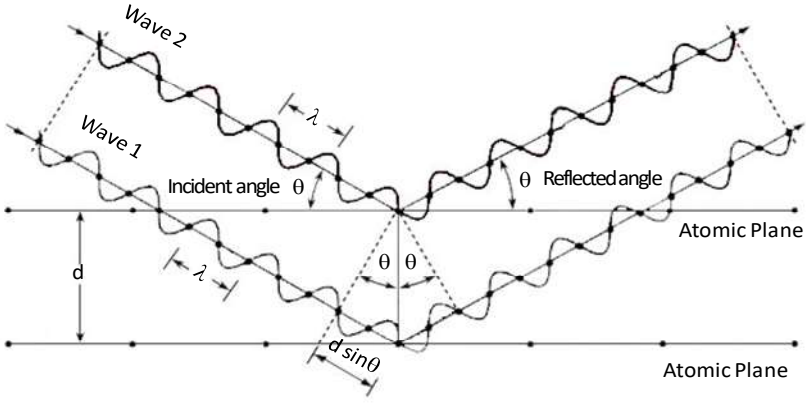

(A) (B)

Figure 3.10: (A) Philips PhilipsX'Pert Pro X-ray diffraction machine; (B) The X-ray beam incident and diffracted from a plane of a crystal with the same angle complying with Bragg's Law.

XRD is a universal non-destructive approach for structure investigation and phase identification of various materials, such as metals and composites, polymers and biological materials, and electronic and optoelectronic components. X-rays are electromagnetic radiation with wavelengths ranging from 100 to 0.1 Å and frequencies of 3×10^{16} Hz to 3×10^{19} Hz. They can penetrate materials and provide information about their bulk structure. Short wavelength X-rays, often known as hard X-rays, have a wavelength between a few angstroms and 0.1 (1 keV-120 keV) and are frequently employed for diffraction applications. They are perfect for examining the structural organization of atoms and molecules in various materials because their wavelength is comparable in size to atoms[139].

Photons of an X-ray beam interact primarily with electrons in particles when they are incident on a material. The exchange of reflected waves between various particles can strongly modulate the intensity distributions of diffracted waves. Suppose the atoms are placed periodically, as in crystals. As a result, the acute interference maximum in the diffracted waves will be symmetrical with the distribution of atoms in the material. The spacing between atoms is known to correspond to the peaks in an X-ray diffraction pattern. In XRD diffraction experiments[146], only X-rays diffracted by elastic scattering are counted[140].

A programmable divergence slit was used to control the area irradiated by the rays, and a programmable receiving slit was used to control the intensity of the output. X'Pert High Score was used to analyze powder diffraction data. A scan of standard Si was conducted to determine the instrumental broadening of the system. It was found that the instrumental broadening was 0.07 degrees at the position of the peak of the reflection (110) in the reflection. By subtracting this value from the pattern, the instrumental broadening is calculated. The lattice constant (a) and the X-ray densities were computed based on the XRD data. Peak locations, intensities, widths, and forms determine the material structure. A Philips X'Pert Pro multipurpose X-ray diffractometer, Model: PW3040, X'Pert Pro, PANalytical, Philips, Netherlands, is shown in Figure 3.10 (A) and was used for this study at the Atomic Energy Centre in Dhaka.

Fig. 3.10 (B) shows the X-ray beam incident and diffracted from a plane of a crystal at an angle that complies with Bragg's Law. One can easily find the crystal structure from the XRD curve's peak. According to Bragg's[141] law, we can write –

$$d_{hkl} sin\theta = n\lambda \tag{3.1}$$

where θ is the X-ray beam's incidence angle, d_{hkl} is the separation between two succeeding planes, h, k, and l are its Miller indices, λ is its wavelength, and n is an integer. The observed lattice parameter, a for each plane, was calculated using Bragg's law for the cubic structure, which is written as

$$a = d_{hkl}\sqrt{h^2 + k^2 + l^2} \tag{3.2}$$

where a is the lattice parameter, and. The lattice parameter was calculated using the equation (2.22). The actual values of a were obtained using the Nelson–Riley[142] function,

$$F(\theta) = \frac{1}{2}\left(\frac{cos^2\theta}{sin\theta} + \frac{cos^2\theta}{\theta}\right) \tag{3.3}$$

The average particle size of each composition was calculated using Debye–Scherrer's[143] formula:

$$D_p = \frac{0.94\lambda}{\beta cos\theta} \tag{3.4}$$

where, D_p represents the average crystallite size, β is the full width at half the maximum of the highest intensity (311) peak.

The X-ray density (d_x) of spinel ferrite nanoparticles can be written as

$$d_x = \frac{8M}{N_0 a^3} \tag{3.5}$$

This equation uses M for molecular weight, No for Avogadro's number (6.0225 x 10^{23} particles/mole), and a for lattice parameters[144].

The specific surface area of the particles (S), the radius of the A-site (r_A), the radius of the B-site (r_B), the theoretical lattice parameter (a_{th}), the hopping length for the A-site (d_A), hopping distance for the B-site (d_B), the tetrahedral and the octahedral bond length ($d_{A\times}$and $d_{B\times}$), the tetrahedral edge ($d_{A\times E}$), the shared and unshared octahedral edge ($d_{B\times E}$ and $d_{B\times EU}$) for cubic spinel ferrite nanoparticles can be written as[145,146]

$$S = \frac{6}{D \times d_x} \tag{3.6}$$

$$r_A = (u - 0.25)a\sqrt{3} - R_0 \tag{3.7}$$

$$r_B = (0.625 - u)a - R_0 \tag{3.8}$$

$$a_{th} = \frac{8}{3\sqrt{3}}[(r_A - R_0) + (r_B - R_0)] \tag{3.9}$$

$$d_A = 0.25a\sqrt{3} \tag{3.10}$$

$$d_B = 0.25a\sqrt{2} \tag{3.11}$$

$$d_{AX} = a\sqrt{3}\left(u - \frac{1}{4}\right) \tag{3.12}$$

$$d_{BX} = a\left[3u^2 - \left(\frac{11}{4}\right)u + \left(\frac{43}{64}\right)\right]^{\frac{1}{2}} \tag{3.13}$$

$$d_{AXE} = a\sqrt{2}\left(2u - \frac{1}{2}\right) \tag{3.14}$$

$$d_{BXE} = a\sqrt{2}(1 - 2u) \tag{3.15}$$

$$d_{BXEU} = a\left[4u^2 - 3u + \left(\frac{11}{16}\right)\right]^{\frac{1}{2}} \tag{3.16}$$

where u (0.381) is the oxygen positional parameter, a is the lattice constant, and R_0 (1.32 Å) is the oxygen ion radius.

The interionic distances between cations $b, c, d, e,$ and f were obtained by the equations, which are written as

$$b = (a\ /\ 4)\ \sqrt{2} \tag{3.17}$$

$$c = (a/8)\sqrt{11} \tag{3.18}$$

$$d = (a/4)\sqrt{3} \tag{3.19}$$

$$e = (3a/8)\sqrt{3} \tag{3.20}$$

$$f = (a/4)\sqrt{3} \tag{3.21}$$

The distances between cations and anions $p,\ q,\ r,$ and s were found using the relations.

$$p = a\left(1/2 - u^{\bar{3}m}\right) \tag{3.22}$$

$$q = a\left(u^{\bar{3}m} - 1/8\right)\sqrt{3} \tag{3.23}$$

$$r = a\left(u^{\bar{3}m} - 1/8\right)\sqrt{11} \tag{3.24}$$

$$s = a_{exp}/3\left(u^{\bar{3}m} - 1/2\right)\sqrt{3} \tag{3.25}$$

The bond angles were computed by utilizing the relations

$$\theta_1 = cos^{-1}((p^2 + q^2 - c^2)/2pq) \tag{3.26}$$

$$\theta_2 = cos^{-1}((p^2 + r^2 - e^2)/2pr) \tag{3.27}$$

$$\theta_3 = cos^{-1}((2p^2 - b^2)/2pr) \tag{3.28}$$

$$\theta_4 = cos^{-1}((p^2 + s^2 - f^2)/2ps) \tag{3.29}$$

$$\theta_5 = cos^{-1}((r^2 + q^2 - d^2)/2rq) \tag{3.30}$$

3.6.2 Transmission Electron Microscope (TEM.)

With a data resolution limit of 0.14 nm, the FEI Tecnai F30 transmission electron microscope offers high-resolution imaging. It uses a Schottky field-emission electron gun to deliver a small electron wavelength through a high accelerating voltage of 300 kV. The "super twin" objective

lens, high illumination FEG, and high mechanical and electrical equilibrium of the microscope enable microanalysis at improved spatial resolution and high probe current. For obtaining high signal-to-noise ratios, it is essential. A scanning unit is also a part of the apparatus, capable of acquiring images and analytical data by scanning a sample with a narrow electron probe with a diameter as small as 0.17 nm. The FEI Tecnai F30 is ideal for analyzing materials' structure and local chemical composition on a nanoscale level. Its different powerful analytical and high-resolution TEM techniques enhance the capability of SCSAM, especially for nanotechnology research[147–149]. The Tecnai F30 TEM is shown in Figure 3.11.

The STEM method uses a high-angle annular dark-field (HAADF) detector to detect electrons scattered during "Z-contrast" imaging. It results in high-resolution images with fewer interpretation issues than traditional HRTEM imaging. With coherent imaging states and digital image processing at different focus levels, the Tecnai F30 can achieve quantitative HRTEM with 0.14 nm resolution. Additionally, the Tecnai F30 is equipped with an EDAX XEDS technique, which utilizes a Li-drifted Si detector with an energy resolution of 130 eV. The system's post-column imaging energy filter, provided by Gatan, directs electrons on an energy-dispersive path, allowing for advanced microanalysis processes[147–149].

Electron energy-loss spectroscopy (EELS) is a crucial technique in scientific research. When viewed on a CCD camera, the energy-dispersive plane of the filter shows the electron energy-loss spectrum of the area being studied. This spectrum includes absorption edges specific to the sample's elements. Researchers can use a CCD camera to investigate the sample's chemical composition in detail by measuring the electron intensity in the energy-dispersive plane. This method is handy for analyzing light elements.

The local electrical configuration and particle coordination can be learned from electron energy-loss spectra. By looking at the intricate structure of energy-loss spectra at absorption edges, researchers can examine the energy-loss near-edge structure (ELNES) to learn about the electronic form. A focused electron probe and an EELS spectrometer with parallel data processing are typically used for this examination.

The imaging energy filter has a significant application called "zero-loss imaging." In order to accomplish this, a narrow opening is placed in the path of the electrons that are being dispersed. Only electrons with a specific energy or energy loss can flow through this aperture. Only

electrons that lost no energy in the sample can pass through the filter using the "zero-loss filtering" technique, and only elastically scattered electrons can reach the detector. Quantitative electron diffraction and imaging of dense materials are crucial for this filtering technology. The imaging energy filter also enables electron-spectroscopic imaging, which uses the energy filter to record images of electrons that have lost a particular quantity of element-specific kinetic energy in the sample[147–149].

Figure 3.11: Transmission electron microscope of Model: Tecnai F30, Company: Field Electron and Ion (FEI.), Country: USA, situated in Atomic Energy Centre Dhaka.

3.6.3 Vibrating Sample Magnetometer (VSM.)

The VSM is a scientific device used to investigate the magnetic effects of samples. It contains coils linked in series with a pole diameter of 150mm and a pole gap of 0.96mm. To magnetize an element, a sample must be placed inside a consistent magnetic field. A piezoelectric substance is used to vibrate the piece sinusoidally physically. The magnetic moment of a sample determines the pickup coil's induced voltage, which is independent of the magnetic field's intensity. A specific design estimates the induced voltage using the piezoelectric reference signal. The

hysteresis curve of a material can be determined by calculating it in the field of an external electromagnet. An ac electrical signal is generated by altering the dipole field of a tiny sample of magnetic material positioned in an external magnetizing field to estimate the material's magnetization[150]. The picture of VSM is shown in Figure 3.12.

Figure 3.12: Vibrating sample magnetometer of Model: EV-9 (3473-70 electromagnet), Temperature range: -170^{0}C - 700^0 C, Magnetic field: 2.1 Tesla, Max.), Company: Microsense L.L.C., Country: USA situated in Atomic Energy Centre Dhaka.

In order to perform the primary measurement, the piece oscillates near a detection (pickup) coil, and the voltage induced by the oscillation is synchronously captured. This system utilizes a consolidated gradiometer pickup coil arrangement with a frequency of 40 Hz and a relatively large oscillation amplitude of 1-3 mm peak. At a rate of 1 Hz, it can precisely detect magnetization shifts of less than 10-6 emu. The VSM option for PPMS comprises a linear motor device (head) for oscillating the sample, a coil cluster puck for detecting the response, and electronics for managing the linear motor transport and the pickup coil response. For automation and management, the MultiVu software program is also necessary. A sample rod's end conducts a sinusoidal current through the sample. The vibration center is in the middle of a vertical arrangement of gradiometer

pickup coils. Utilizing a readback of the optical linear encoder data from the linear motor transport of the VSM motor module, the exact position and magnitude of the oscillation are retained. The VSM detection module amplifies the voltage created in the pickup coil during lock-in. The position encoder signal is a reference for synchronous detection in the VSM detection module. The encoder signals that linear motor transporters send to VSM motor modules are used by the VSM motor module for troubleshooting. The VSM detection module detects an enhanced voltage when it receives in-phase and quadrature-phase signals from the encoder and pickup coil. These signals are averaged, and the outcomes are sent to the VSM application operating on the PC over the CAN bus. The magnet and power source constrain the magnetic field ramp rate. In contrast, the temperature and magnetic field could alter during the measurement[151]. In this research, VSM measurements were obtained by PPMS, as shown in Figure 3.13.

Figure 3.13: PPMS of Model: P525, Temperature range: 1.2 K - 1200 K, Magnetic field: 9 Tesla (Max.), Company: Quantum Design, Country: UK situated in Atomic Energy Centre Dhaka

3.6.4 MössbauerSpectroscopy

Figure 3.14: Mössbauer spectroscopy of Resonant Gamma-Ray Spectrometer, Model: W302, Company: WEB RESEARCH CO, Country: USA.

A solid sample is exposed to a gamma radiation beam in Mössbauer absorption spectroscopy, its most common variation. It measures the beam's strength when it passes the detector. The atoms in the source of the rays must share the same isotope as the atoms in the item for gamma rays to be efficiently absorbed by the object. The nuclear shift energies would be the same if the emitting and absorbing nuclei were in comparable chemical environments, and resonant absorption would occur with both materials at rest. However, as discussed below, numerous modifications to nuclear energy levels result from changes in chemical circumstances. The modest energy shifts that result in noticeable changes in absorbance are caused by the radionuclides' narrow gamma-ray spectral line widths, even though these energy shifts are often less than a micro-electronvolt. To bring the two nuclei back into resonance, it is essential to adjust the gamma ray's energy negligibly. The Doppler Effect is frequently used in practice to do this. The gamma-ray energy is scanned across a specific field using the Mössbauer absorption spectroscopy technique, which includes accelerating the source at various speeds to produce a Doppler effect. For example, the speed range for ^{57}Fe is specifically 11 mm/s, which is equivalent to 48.075 meV per 1 mm/s. Gamma-ray intensity is displayed as a function of source speed in the resulting spectra. A portion of the gamma-ray is absorbed at speeds that are close to the resonant energy levels of the sample, which causes a decrease in the measured intensity and a corresponding dip in the spectrum[152]. This equipment can use dips (also known as peaks; dips in transmitted intensity are peaks in absorbance; dips in transmitted intensity are peaks in

absorbance) to determine the sample's characteristics. Isomer shift (δ) is a comparative measure describing a change in the resonance energy of a nucleus for the shift of electrons within its *s* orbitals. The electrical interaction between the non-zero probability s orbital electrons and the non-zero volume nucleus they orbit changes, causing this transformation. Depending on the density of s electrons in the core, the entire spectrum is either moved in a favourable or unfavourable direction. The probability of an electron in the nucleus is only non-zero for electrons in s orbitals. Through a screening effect, p, d, and f electrons can modify the density of s electrons. Isomer shift can be represented as:

$$CS = K\left(\langle R_e^2\rangle - \langle R_g^2\rangle\right)(|\psi_s^2(0)|_b - |\psi_s^2(0)|_a) \quad (3.31)$$

where K is a nuclear constant, $\langle R_e^2\rangle$ is the effective nuclear charge radius of the excited state, and $\langle R_g^2\rangle$ is the effective nuclear charge radius of the ground state, $|\psi_s^2(0)|_b$ is the electron density of the sample, and $|\psi_s^2(0)|_a$ is the electron density of the source.

Examples can be used to clarify the meaning of equation (2.91) in terms of physics:

1. A increase in s-electron density in ^{119}Sn results in a favourable alteration because of a positive shift in overall nuclear charge (Re > Rg), but the gain in s-electron density in the ^{57}Fe spectrum presents an adverse shift because the transformation in the effective nuclear charge is unfavourable (Re<Rg).

2. Because oxidized ferric ions (Fe^{3+}) have a higher s-electron density at their cores and a less screening effect from d electrons, they undergo fewer isomer transitions than ferrous ions (Fe^{2+}). The isomer shift determines the oxidation state, electron shielding, valency states, and electron-drawing ability of electronegative groups[153–156].

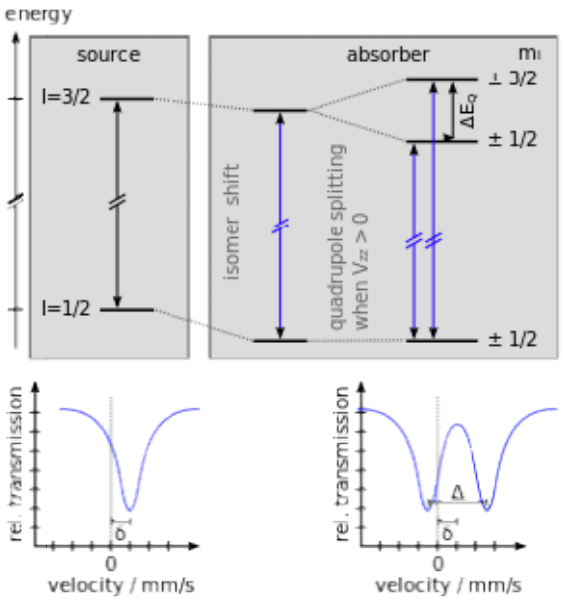

Figure 3.15: The splitting of the quadrupole occurs as a result of the exchange between nuclear energy levels and the gradient of the electric field around them

Quadrupole splitting

The interaction between the nuclear energy levels and the gradient of the external electric field causes quadrupole splitting. Nuclei having a spin quantum number (l) larger than 1/2, or cores with non-spherical charge distributions, may have a nuclear quadrupole moment. In this case, an asymmetric electric field separates the nuclear energy levels. The excited state of an isotope having l= 3/2 excited states, like ^{57}Fe or ^{119}Sn, is split into two substates: $m_l = \pm 1/2$ and $m_l = \pm 3/2$. The change from the ground state to the excited state manifests as two separate peaks in the spectrum, often known as a "doublet." The split between these two peaks, known as quadrupole splitting, describes the electric field at the nucleus. The oxidation state, site symmetry, spin state, and structure of ligands are chosen via quadrupole splitting[157,158].

Magnetic hyperfine splitting

The Zeeman effect illustrates how the nucleus and any nearby magnetic field interact to produce magnetic hyperfine splitting. A nucleus with spin l splits into 2l + 1 sub-energy levels in a magnetic field. The ^{57}Fe nucleus will split into four non-degenerate substates with ml values of +3/2, +1/2, -1/2, and -3/2 as the first excited state with spin state l = 3/2. The separations are described as being on the order of 10^{-7} eV hyperfine and evenly spaced. According to the selection rule for magnetic dipole shifts, transitions from the excited to the ground state can occur whenever ml shifts by 0 or 1, or -1. It provides six plausible transitions between the 1/2 and the 3/2 states. Like many iron compounds, the natural inner magnetic fields are relatively strong in ferromagnetic materials, and their effects predominate the spectra. The strength of the magnetic field at the core, which in turn depends on how the nucleus allocates its electrons, determines how much splitting occurs. A sample foil between an oscillating source and a photon detector, which produces an absorption spectrum, can measure the splitting[159].

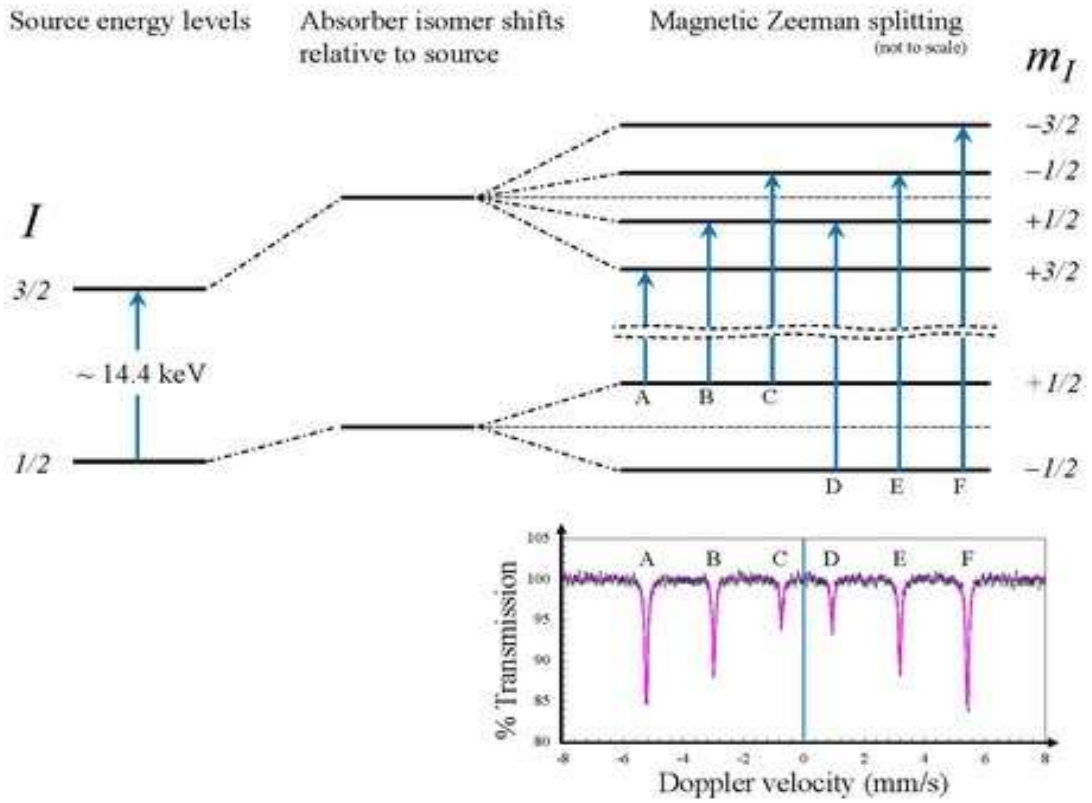

Figure 3.16: Magnetic hyperfine splitting due to the exchange between the nucleus and any surrounding magnetic field

3.6.5 Fourier Transforms Infrared Spectroscopy (FTIR)

The FTIR measures the absorption or emission of solids, liquids, or gases in the infrared spectrum. With the help of FTIR spectrometers, an extensive range of spectral resolution data can be simultaneously analyzed. Figure 3.16 shows FTIR spectroscopy. The spectrum of a sample can be determined by passing an infrared beam through it. Because of the way molecules are built, they absorb frequencies. The fact that these absorptions are at resonance frequencies is crucial. It implies that the vibrational frequency determines the frequency of the absorbed radiation. Absorption occurs when the vibrational frequency of a bond or group of bonds and the frequency of the IR coincide. To ascertain how much energy has been absorbed in each frequency or wavelength, it is required to examine the transmitted light. This measurement can be made using a monochromator to scan the wavelength range. Alternately, the whole

wavelength range can be calculated using a Fourier transform instrument, and a transmittance or absorbance spectrum can then be developed appropriately[160].

Figure 3.17: FTIR spectroscopy of model: STA, 449 F3, Jupiter, UK.

FTIR is a broadly habituated method to recognize the functional groups in the materials by utilizing the beam of infrared (IR) radiation. It determined how much IR radiation each bond in the molecule absorbed and provided a spectrum often shown as % transmittance vs wavenumber (cm^{-1}). The infrared area is between the visible and microwave portions of the electromagnetic spectrum. Near-IR (14000–4000 cm^{-1}), mid-IR (400–4000 cm^{-1}), and far-IR (400–40 cm^{-1}) are the three primary components. IR spectroscopy is a modern technique that uses IR radiation to illuminate a sample to analyze its structural chemistry. The energy of the IR region is lower than the energy of the UV-visible light and higher than microwave radiation. Various materials (with the covalent bond) absorbed electromagnetic IR radiations. The FTIR provides the fingerprint of the functional group of IR active materials[161,162].

A molecule that is IR active possesses a dipole moment. The covalent bond oscillates back and forth as the IR functional materials come into contact with IR radiation, absorbing its energy. As

a result, IR light should be absorbed by the oscillation that changes the molecule's net dipole moment. Because they have zero dipole moments, a single atom and symmetrical molecules do not absorb IR light. Because each bond has a unique natural vibrational frequency, we noticed that a specific covalent molecular link would absorb a specific IR radiation (frequency). All bonds, therefore, absorb light at a consistent wavelength and are unaffected by other bonds. So even if some frequencies may be the same, two molecules with different structures do not have the same infrared spectrum[163,164]. The absorbance of IR absorbance spectra of a sample is figured out from the following relation:

$$A = \log\left(\frac{I_0}{I}\right) \tag{3.32}$$

where I_0 represents the intensity of the background spectrum, I represent the intensity of the sample spectrum, and A stands for absorbance. The absorbance can also be calculated with the concentration of molecules in a sample using Beer's law which is written an

$$A = \varepsilon lc \tag{3.33}$$

A is for absorbance, m for molar absorptivity, l for path length, and c for sample concentration. The height or size of the matching peak in an absorbance spectrum, which corresponds to the concentration of the molecule, is proportionate. Therefore using Beer's[165] law, we can obtain the concentrations of molecules in samples. On the other hand, the percent transmittance (% T), which calculates the percentage of light transmitted by the mixture and can be found as follows

$$\%T = 100 \times \left(\frac{I}{I_0}\right) \tag{3.34}$$

where I_0 is intensity in the background spectrum, I is intensity in the sample spectrum, and %T is the transmittance percentage. Except for the material's peaks being overlaid upon the instrumental and atmospheric bands, the sample's single-beam FTIR spectrum, obtained following Fourier's interferogram transformation, looks exactly like the background spectrum. The resulting IR range of the sample must be normalized against the background spectrum to eliminate background contribution. Accordingly, an FTIR transmittance spectrum is written as

$$\%T = \frac{I}{I_0} \tag{3.35}$$

where %T is percentage transmittance, I is the intensity of the measured sample, and $I_{0\ is}$ the intensity of the background spectrum. The absorbance spectrum of FTIR can be figured out from the transmittance spectrum as

$$A = -\log_{10} T \tag{3.36}$$

Using FTIR software, the mathematical relationships between the transmittance and absorbtance percentages can be converted. Stretching and bending are the two vibrational modes the molecules' bonds display when the IR active molecules absorb IR light. Triatomic molecules generally exhibit bending beat, while linear molecules favour stretching vibration. However, IR active molecules also exhibited additional intricate stretching and bending vibrations. Stretching vibrations include symmetric and asymmetric vibrations, whereas bending vibrations include wagging, rocking, twisting, and scissoring. Stretching that is asymmetric requires more energy than symmetric stretching. Others are out-of-plane bending vibrations, whereas scissoring and rocking are in-plane vibrations[8].

3.6.6 Dynamic Light Scattering (DLS.)

Figure 3.18. Dynamic light scattering instrument of model: ZEN3600, RatedVoltage: AC 100-240 V, Rated frequency: 50/60 Hz, Rated Input Power: 250 V, Company: MALVERN INSTRUMENTS LTD, Country: UK.

Dynamic light scattering (DLS) is a physics approach to determining a nanoparticle's hydrodynamic size distribution profile in a solution. The intensity or photon auto-correlation function, or photon correlation spectroscopy (PCS) or quasi-elastic light scattering, is typically used in the DLS measurement to examine material variations. This method works in Brownian motion, where particles move randomly in gas or liquid. The DLS approach measures Brownian activity and associates this with particle size. If the particle is large, the Brownian movement will be slower. The solvent molecules also "kick" the smaller particles, which drive more quickly. Therefore, faster action generates smaller particles, and slower movement causes large particles. The DLS is demonstrated in Figure 3.18. The interaction of light with a particle in solution

causes the physical phenomena known as the principle of light scattering. The light that strikes a particle in solution causes the electrons nearby to vibrate in time with the incident light's energy. As a result, the particle develops an oscillating dipole from the incident light. The strength of the incident light directly correlates with the power of this dipole moment. To understand light scattering, we must consider several factors. Specifically, the energy-scattering light in all directions at the same wavelength as an oscillating dipole produces the incident light. These include particle size, wavelength dependency, the duration of the light scattering measurement, particle concentration, and molecular weight.

The size of the particle interacting with the incident light is a crucial factor in understanding light scattering. The fundamental particle is simultaneously exposed to the same energy field strength as the particle, which is ten times smaller than the wavelength of the incident light. The wavelengths of the resulting dispersed light are all in phase and work in concert. The wavelengths of the scattered light are no longer entirely in a phase when the particle is more significant than the wavelength of the incident light, which causes reinforcement in some directions and destructive interference in others. The particle's size and form affect big particles' scattering patterns. These problems significantly impact how light scattering measurement instruments are set up. The light is scattered forward, backward, and 90 degrees away from the incident light. The light scatter pattern shifts to a more forward direction and less in the backward and 90° directions as the particle size grows ($>\lambda/10$). A polarizer is used to fire a 630 nm He-Ne laser, which is a monochromatic light source, into a sample. The image is then projected onto a screen after the scattered light passes through a second polarizer, where a photomultiplier captures it. It has the name "speckle pattern." There are two possible geometric configurations for the polarizer placement. One type of geometry, vertically vertical (VV)

geometry, allows light to pass through both polarizers in the same direction. The second polarizer does not guide light in the same direction as the incident light in vertical or horizontal (VH) geometry. Light is shot at the molecules in the solution, and the molecules differ in all directions from the light. All molecules can cause their diffracted light to interfere with areas of light or darkness. Rapid time gaps are used to repeat this process. The resulting speckle patterns are examined using an autocorrelation to approximate the light intensity at each point over time. With the diffusion of the particles in the dispersed solution due to Brownian motion brought on by changes in light intensity (intensity of scattered light) to vary as a function of time, the autocorrelation function (ACF) is an important parameter to estimate the hydrodynamic size and polydispersity index. The autocorrelation function of the scattered light intensity is produced by the correlator in photon correlation spectroscopy (PCS) equipment. The correlation function, an exponentially decaying function of the correlator time delay, or the autocorrelation function, typically deteriorates starting from zero delay time for many monodisperse particles in Brownian motion. Faster dynamics brought on by smaller particles cause faster decorrelation of the scattered intensity trace. To extract the size from the correlation function, several approaches are used. Two methods are used to determine the mean size or z-average diameter and the polydispersity index through Cumulants analysis: (1) fitting an exponential function to the correlation function and (2) fitting multiple exponentials to the correlation function to obtain the distribution of particle sizes. The particle size of spherical, smooth particles that diffuse at the same rate as the sample particles is called the hydrodynamic diameter. When the findings of DLS measurements are approximated using other techniques that point to distinct physical properties of the sample, they must be preserved. The polydispersity index is used to measure the range of particle sizes in a sample. The polydispersity index is also calculated using the cumulant method.

If the percentage is less than 10%, the sample is monodisperse, and the sizes of all the particles detected are consistent. However, the polydispersity index does not reveal details about the size distribution's shape or the proportion of the two-particle divisions[166].

Dynamic Light Scattering (DLS) is a Photon Correlation Spectroscopy known for selecting particle size. When a monochromatic laser beam enters a fluid containing spherical particles moving with Brownian motion, the light undergoes a Doppler shift, which changes the wavelength of the light. This change is related to the particle's hydrodynamic size. The Brownian motion of particles caused by bombardment by the solvent molecules around them is measured by DLS, and this motion is correlated to the size of the particles in the solution[167]. The Stokes-Einstein equation is used to determine the hydrodynamic size of a particle based on the translational diffusion coefficient[167], which is written as

$$d(H) = \frac{kT}{3\pi\eta D} \tag{3.37}$$

where $d(H)$ is the hydrodynamic diameter, D is the translational diffusion coefficient, k is Boltzmann's constant, T is the absolute temperature, and η is the solution's viscosity.

According to Derjaguin, Verwey, Landau, and Overbeek's (DVLO) theory[168], the stability of a particle is dependent upon its total potential energy function V_T, which is written as

$$V_T = V_A + V_R + V \tag{3.38}$$

Within a few nanometers of separation, VS is the potential energy due to the solvent, which typically marginalizes the total potential energy. V_A is the contribution of the attractive force, and V_B is the contribution of the repulsive force. The attractive potential function, which operates over a much larger distance, is written as[167,168]:

$$V_A = \frac{-A}{12\pi D^2} \tag{3.39}$$

where A is the Hamaker constant, and D is the particle separation. The repulsive potential function is the more complex one, which is written as[167,168]:

$$V_R = 2\pi\epsilon a\zeta^2 \exp(-\kappa D) \tag{3.40}$$

In this equation, the terms a and stand for the particle radius, solvent permeability, ionic composition, and zeta potential. The stability of a colloidal system, according to the DVLO theory, depends on the total of the Van Der Waals attractive and electrical double-layer repulsive forces traveling in opposite directions when Brownian motion takes place. As a result, the repulsive force creates an energy barrier that prevents two particles from coming together and attaching. However, if the repulsive force weakens, the particles collide with sufficient energy during Brownian motion. The attractive force pulls them into contact, which results in a sizeable hydrodynamic diameter by flocculation and agglomeration. Therefore, for the colloidal system's stability, a sufficiently high repulsive force is necessary for resisting flocculation and agglomeration.

The zeta potential in colloidal suspension is the electrokinetic potential that develops from the electrical potential in the dual interfacial layer at the site of the sliding plane in comparison to a point in the bulk fluid away from the interface. The Henry[169] equation connects the zeta potential and electrophoretic mobility, which is written as follows:

$$U_E = \frac{2\varepsilon_r\varepsilon_0\zeta F(\kappa a)}{3\eta} \tag{3.41}$$

where U_E is electrophoretic mobility, ε_r it is the dielectric constant, ε_0 is the permittivity of vacuum, ζ is zeta potential, $F(\kappa\alpha)$ is Henry's function, and η is the viscosity of the solution at

experimental temperature. It depends on the solution's particle concentration, viscosity, and pH.

3.6.7 Raman spectroscopy

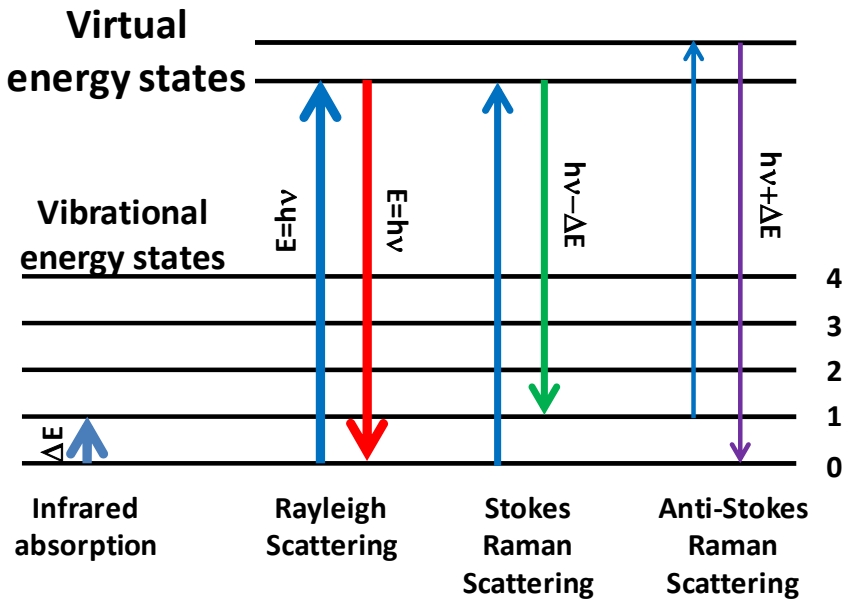

Figure 3.19: Stokes line and anti-Stokes line of Raman scattering.

Raman spectroscopy is molecular spectroscopy followed by inelastically scattered light, permitting the interrogation and designation of molecule vibrational (phonon) states. It delivers a valuable analytical device for molecular fingerprinting and observing transformations in molecular bond structure. Consequently, it provides information about product formation, state changes, stresses and strains of covalent bonds, crystalline form, and crystallinity. Raman has several significant advantages corresponding to other vibrational spectroscopy methods. Instead of the light being absorbed by a sample, the Raman effect manifests itself in the reflected light. It makes it imperceptible to aqueous absorption bands and requires little to no sample preparation. This Raman effect encourages the direct exploration of solids, liquids, and gases through a

transparent holder made of glass, quartz, or plastic. Raman spectra of various materials are differentiable, even to the untrained eye. Therefore it can be employed for material identification and confirmation. The most effective way to detect Raman scattering is as a slight shift in frequency for a monochromatic ray's intensity due to the interaction between the incident radiation and molecules' vibrational energy levels. When the polarizability of the molecule in a vibrational mode changes, it becomes Raman active[170].

A transparent substance distributes a small amount of monochromatic light in all directions. When a spectroscope examines the dispersed light, it reveals numerous new, faint frequencies and a solid line with the same frequency as the incident light. For example, if a substance is illuminated with light of frequency v and the scattered light is analyzed, several new frequencies will be seen $v - v_1$, $v - v_2$, $v - v_3$, etc., of lower energy named Stokes lines, and $v + v_1$, $v + v_2$, $v + v_3$, etc., of higher energy called anti-Stokes lines. These lines are symmetrically disposed near the stimulating frequency and the values of v_1, v_2 are often seen to overlap with empirical infrared frequencies. The Stokes lines are found to be broadly better intense than the anti-Stokes lines, and if the exciting frequency v is modified, the values of v shift, but the frequency changes (v_1, v_2, v_3, etc.) remain unaffected. The power of the Raman line is proportional to the intensity of the frequency of the stimulating light, so blue light provides much better intense Raman lines than red light[171].

If an incident light of energy $E = hv$ strikes a molecule, it can be scattered inelastically, where power is given up or received from the molecule. The lights' quantum can offer or accept energy from the approach simply in amounts identical to the energy difference between the fixed states of the system. Suppose the illuminating incident light scatters a molecule in the ground state; it

moves to a short-lived virtual energy state and immediately gets back to a vibrational state by releasing energy $h\nu - \Delta E$, where ΔE represents the energy difference between the ground state and vibrational state. In this case, we obtain the Stokes line. When the incident light is scattered with the molecule of vibrational states, it also moves to the virtual state and immediately back to the ground state by emitting energy $h\nu - \Delta E$. In this case, we obtain the Anti-Stokes line[170,171].

The CRS+ 500/BX53, MonoVista, S & I Spectroscopy & Imaging, Germany, was used for the Raman Spectroscopy measurements. The laser line was cleaned with an edge filter width of approximately 60 cm^{-1} and a diode laser system operating at 785 nm, powered internally by 100 mW. For pelletized materials with diameters ranging from 200 to 3500 cm^{-1}, Raman spectra were recorded.

Figure 3.20: Raman spectroscope, model no CRS+ 500/BX53, MonoVista, S & I Spectroscopy & Imaging, Germany.

3.6.8 Hyperthermia Set-up

An AMF is used in induction heating, a non-contact method of heating conductive objects. *Hyperthermia setup* is a vital tool used in all induction heating forms. An induction

heater typically operates in medium frequency (MF) or radio frequency (RF) frequencies. Induction heaters with instantaneously fed coils from the power source and supply frequencies of 50 Hz or 60 Hz are typically used in industrial settings requiring lower surface temperatures. Some specialized induction heaters operate at 400 Hz, the frequency of aerospace power. Operating frequencies for induction generators range from 100 kHz to 10 MHz. Most induction heating devices (with induction frequency control) have an operational voltage range of 2.5 kW to 40 kW and a frequency range of 100 Hz to 200 kHz. MF induction generators operate between 1 and 10 kHz. 50 kW to 500 kW are commonly included in the output range. Induction heaters are used on medium to more significant components within these ranges. By using the Neel and Brownian effects in the presence of magnetic nanoparticles, the induction heater is a simple way to generate heat. Figure 3.18 shows how the hyperthermia setup is set up. Induction coils with eight turns and a 4 mm diameter are used in the hyperthermia setup, producing a 20 mT applied field while measuring 200 A current, 342 kHz frequency, and 1.5 kW power[3,10,10,99,172–175].

Figure 3.21: Hyperthermia Set-up Material Science Division, Atomic Energy Centre, Dhaka, Model: EASY HEAT 5060LI, Input voltage: 187-265 AC, Frequency: 150-400 Hz, In-Out power: 3 Kw-60 Kw, Company: Ambrell, USA.

3.6.9 MRI

MRI is a high-imaging technique used in radiology to create images of the physiological and anatomical functions of the body. MRI scanners used strong magnetic fields, magnetic field gradients, and radio waves to create images of the body parts depicted in Figure 3.19. Unlike CT, CAT, and PET scans, MRI does not use X-rays or ionizing radiation. MRI scan may even be a more suitable option than a CT scan. MRI is widely utilized in hospitals and clinics for medical diagnosis, producing disease, and follow-up without disclosing the body to radiation. MRI is established in the base of nuclear magnetic resonance (NMR). When positioned in an external magnetic field that produces MR pictures via a pair of relaxations, many atomic nuclei can absorb and emit radio frequency energy. In MRI, hydrogen atoms are typically used to create a strong radio frequency signal that the antenna picks up close to the scanned object being studied. People and other living things have many hydrogen atoms, particularly in water and fat. For clinical and research purposes, MRI procedures are often performed. The movement in space is localized by magnetic field gradients after the radio wave pulses ignite the nuclear spin energy shift. According to this reasoning, most MRI scans practically map where the body's water and fat are located. Based on the relaxation characteristics of the hydrogen atoms, altering the pulse sequence parameters may provide various contrasts between tissues. A contrast agent's capacity to increase the proton relaxation rate in a homogenous medium. The relaxivity proportionality constant measures how much the proton relaxation rate of the contrast agent is increased per unit concentration and measures it in millimoles per second. Increasing the T_1 relaxation rate tends to enhance the MR signal intensity, whereas increasing the T_2 relaxation rate tends to decrease the signal intensity. Once the electromagnetic field is switched off, the nuclei will resume their initial precession around the external magnetic field. Removing magnetic moments to their

original orientation is referred to as T_1 relaxation. The phase loss in nuclear precession following the electromagnetic field is called T_2 relaxation.

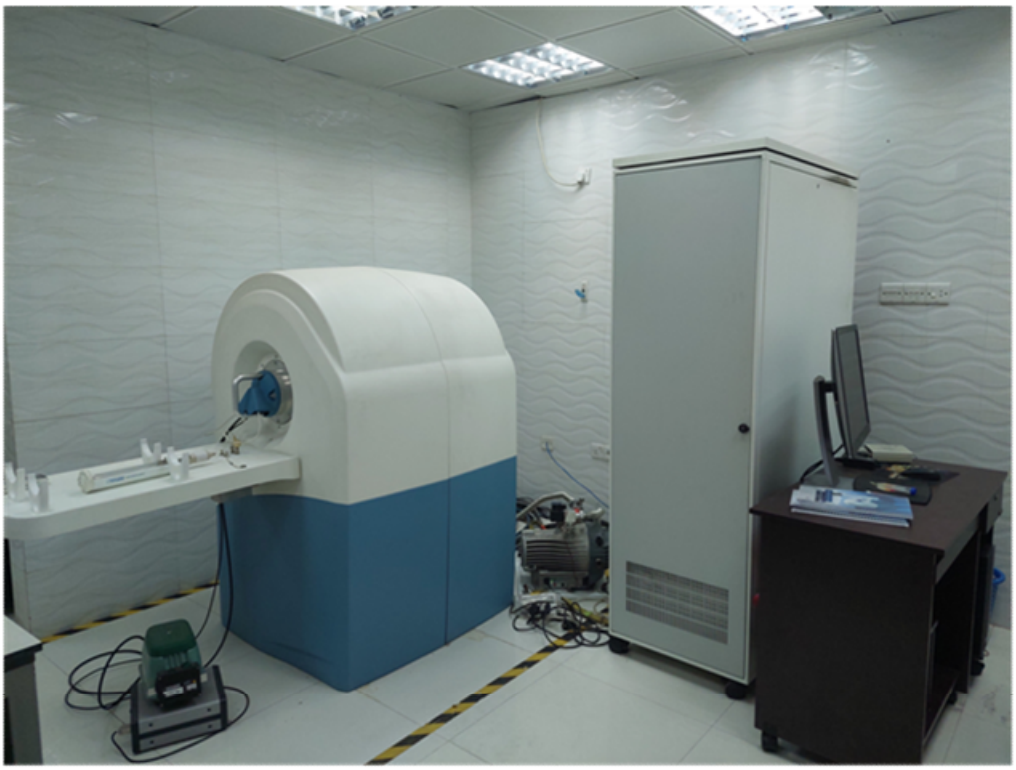

Figure 3.22: Laboratory Research MRI of Model: MRS7017, Company: MR Solution, Country: UK situated at Materials Science Division, Atomic Energy Centre, Dhaka

3.6.10. Cytotoxicity

A Bio Safety Cabinet, Model: NU-400 E, Nuaire, U.S.A., CO_2 Incubator, Hemocytometer, Optika, Italy, and an inverted light microscope were used to conduct the cytotoxic assay on the HeLa cell line. The material employed was DMEM (Dulbecco's Modified Eagles' Medium), which contained 10% fetal bovine serum (FBS), 0.2% gentamycin, and 1% penicillin-streptomycin. HeLa cells (4×10^5 per 200 mL) were seeded in 96-well plates and incubated in a CO_2 incubator for 24 hours containing 37^{o}C temperature and 5% CO_2. A 0.45 mm syringe filter was then used to filter them. Each well received 50 mL of coated and uncoated MCFO

nanoparticles at a concentration of 4 mg mL^{-1}. Each sample was placed in a different set of wells. Insoluble samples were removed from the incubation solution with media numerous times after 48 hours.

Figure 3.23: Co_2 Incubator (Nuaire, U.S.A) in the cell culture lab

Cytotoxicity measurement is crucial for MNPs before in-vivo biomedical application. The toxicity of MNPs can be measured in cell lines or animal models. In the cell lines model, the cell viability of living cells or cancer cells was measured to calculate the cytotoxicity of MNPs.

Cell viability was studied manually by a hemocytometer which is written as

% cell viability = [Total Viable cells (Unstained) / Total cells (Viable +Dead) × 100 (3.42)

where, Viable cells (/ ml) = Average viable cell count per square x Dilution Factor x 10^4; Average Viable cell (count per square) = Total number of viable cells in 4 squares / 4; Dilution Factor = Total Volume (Volume of sample + Volume of diluting liquid / Volume of the sample)[176–178].

CHAPTER 4: STUDY OF COMPOSITION DEPENDENCE HYPERTHERMIA AND IN-VIVO MRI PROPERTIES OF SURFACE-FUNCTIONALIZED MCFO

The composition of MCFO changed with different levels of cobalt content. After that, chitosan was used to coat the prepared MCFO materials. The structural and magnetic properties of these materials were then investigated. The objective was to find the appropriate combination of composition for the hyperthermia treatment and MRI contrast agents. Finally, the hyperthermia and MRI properties of the chitosan-coated MCFO materials were studied.

4.1. Structural Characterizations

4.1.1. X-ray diffraction (XRD)

As-dried XRD patterns of MCFO are shown in Figure 4.1 (a-b) for structural characterization. XRD spectra did not show a different peak within the resolution level of the XRD machine[44,46,179]. Spinel is the structure of the samples, which belong to the Fd3m space group. A broad diffuse peak pattern can be seen in Figure 4.1(a) for Mg-rich compositions up to x=0.4. As the Co amount increases, the peak pattern narrows. Figure 4.1(a-b) shows that while the intensity of the peaks sharpens, their positions shift towards the lower value with an increase in cobalt content x. $CoFe_2O_4$ has a higher crystallinity than $MgFe_2O_4$, and NaOH is a co-precipitant. Lodhi et al.[179] also found that particle size increased with increased cobalt content, x of MCFO, prepared by the micro-emulsion method. Bragg's law calculated the lattice parameters, and the Nelson-Riley function was used to determine the absolute lattice parameters.

According to Figure 4.1(c), lattice parameters for each composition are determined from plots of the lattice constants, ao. Cobalt content x increases the lattice parameter because Mg^{2+} (0.065 nm) has a smaller ionic radius than Co^{2+} (0.072 nm) [180,181]. Fig. 4.1 (c) illustrates a linear relationship between lattice parameters and composition as predicted by Vegard's Law. The lattice parameter of spinel MCFO nanocomposites increases with increased cobalt content, as reported by Abraham[182] et al. The value of the lattice constant is 8.303Å for $MgFe_2O_4$, which is close to our finding. A chemical co-precipitation method was used by Stein et al.[183] to synthesize $CoFe_2O_4$ nanoparticles with a lattice parameter of 8.358 Å. According to this study, $MgFe_2O_4$ and $CoFe_2O_4$ have lattice parameters of 8.301 and 8.351, respectively. Using Debye-Scherrer's formula in equation (2.34), we can determine the grain sizes of the compositions.

Figure 4.1 (c) presents the variations in grain size with x. The grain size at x=0 was 3.8 nm, and at x=1 was 7.3 nm. There is almost a linear relationship between grain size and x. Highscore Software was used to estimate peak width.

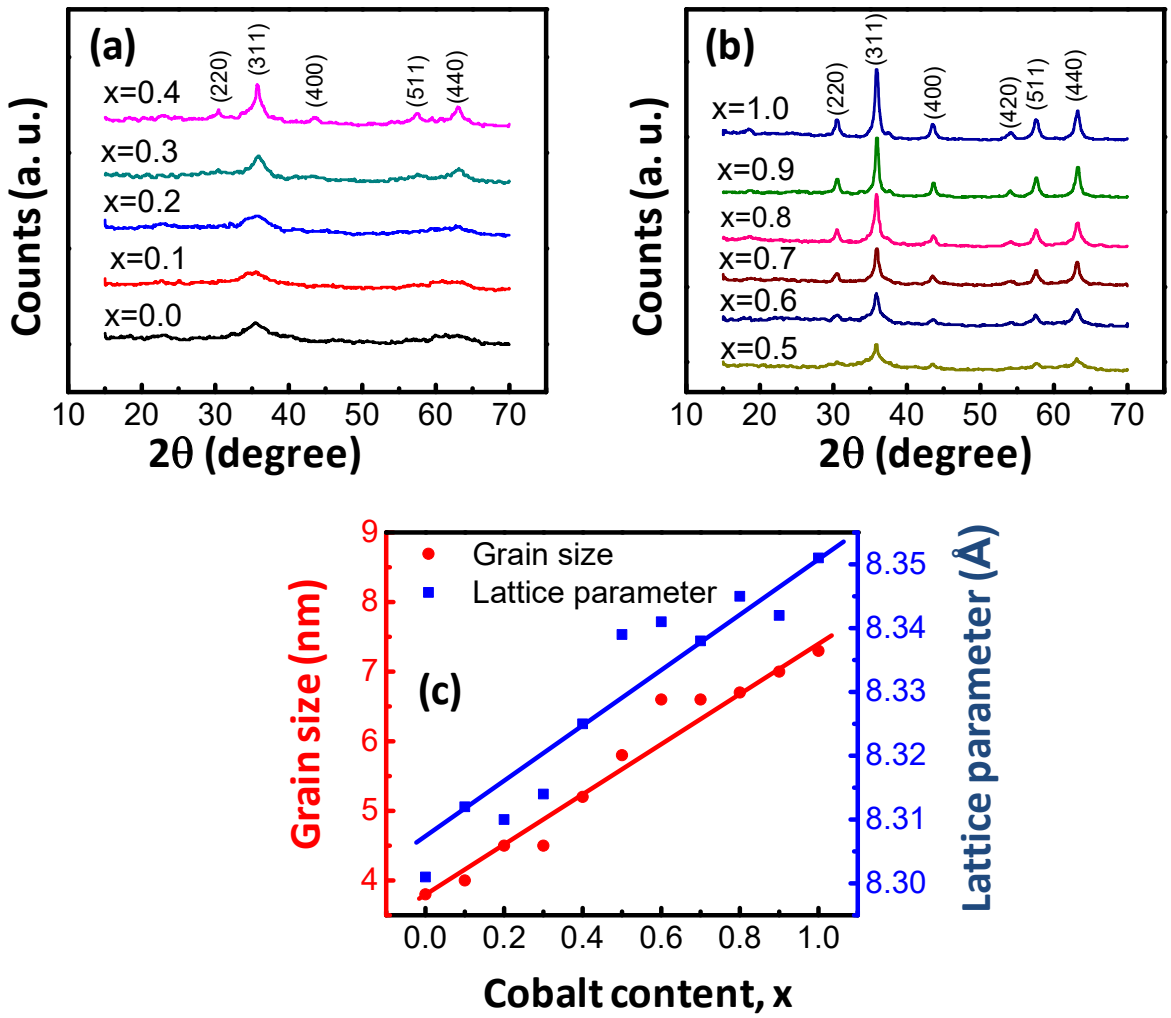

Fig. 4.1 (a-b) X-ray diffraction pattern of $Mg_{1-x}Co_xFe_2O_4$ magnetic material at the as-synthesized condition, (c) variations of lattice parameter and grain size with the cobalt content x.

4.1.2. Transmission electron microscopy (TEM)

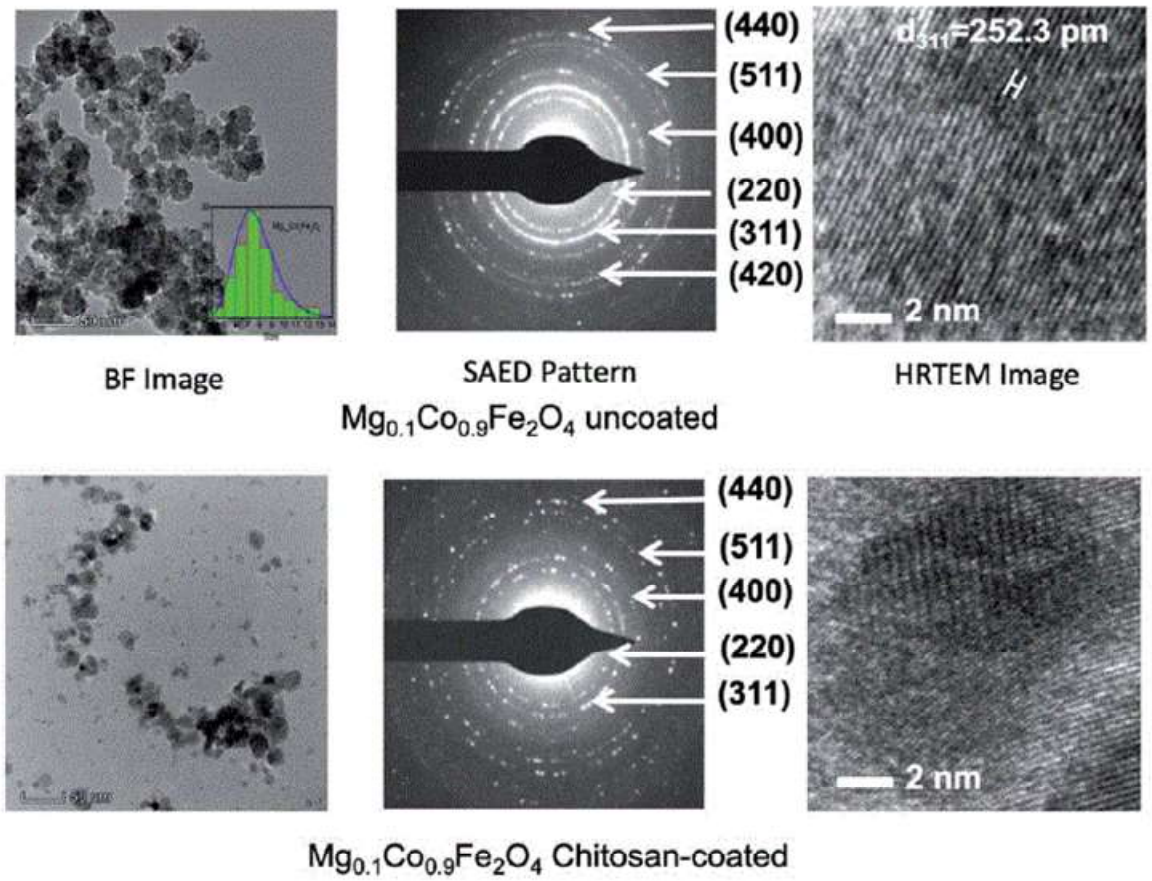

Fig. 4.2: TEM images of uncoated and chitosan-coated $Mg_{0.1}Co_{0.9}Fe_2O_4$ nanoparticles. In this figure, representative TEM images of the $Mg_{1-x}Co_xFe_2O_4$ series are presented. Uncoated nanoparticle BF images, SAED patterns, and HRTEM images are shown in the upper panel. Chitosan-coated nanoparticle BF images, SAED patterns, and HRTEM images are shown in the bottom panel. Uncoated nanoparticles are agglomerated in the figure, while coated nanoparticles are dispersed. Because coated nanoparticles are more dispersed than uncoated nanoparticles, the lines appear more intense on the SAED patterns for uncoated samples. As-dried HRTEM images of the uncoated and coated nanoparticles demonstrate good crystallinity.

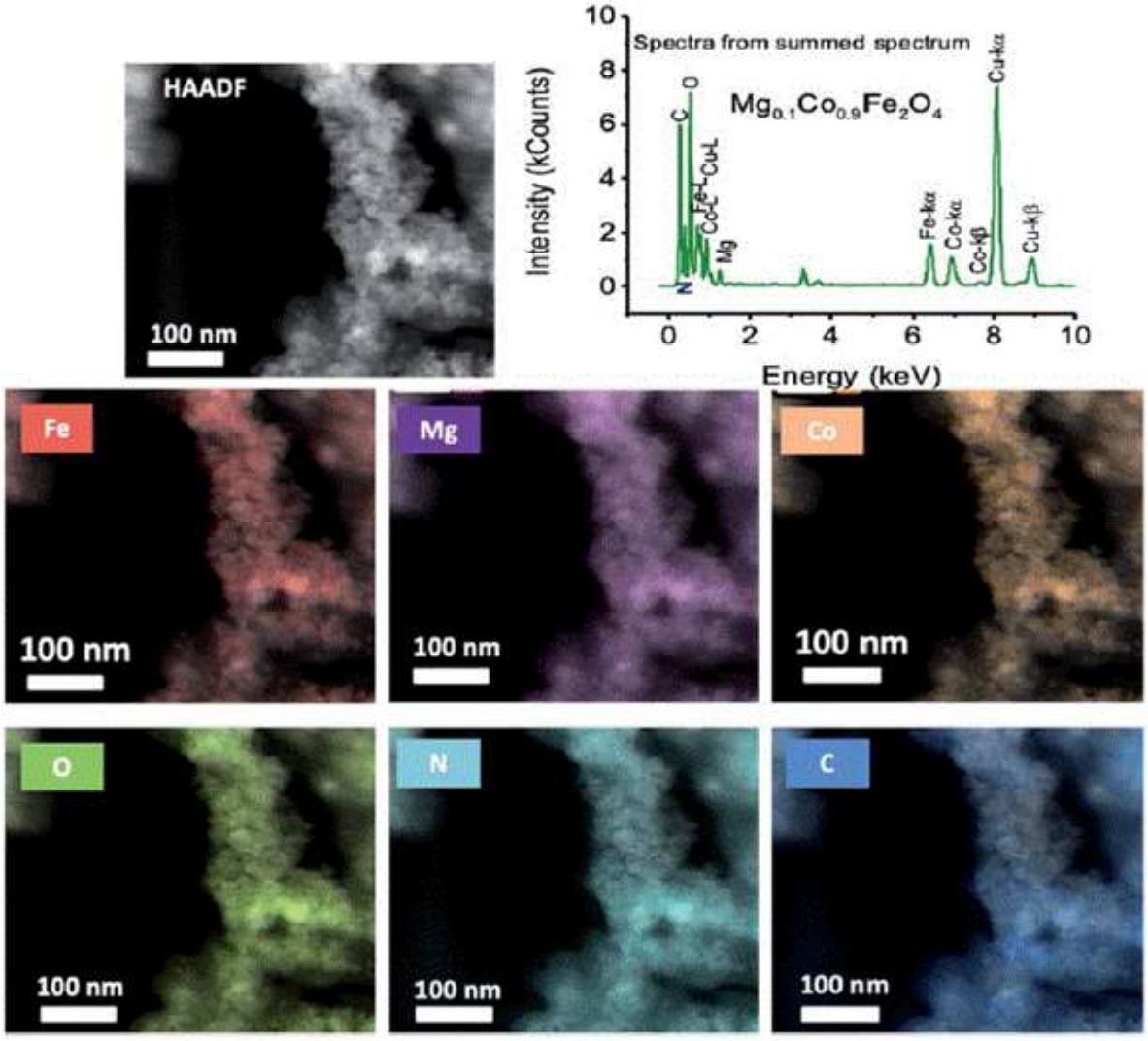

Figure 4.3: An electron diffraction spectroscopy (EDS) mapping of Fe, Mg, Co, and O after scanning transmission electron microscopy (STEM) of chitosan-coated $Mg_{0.1}Co_{0.9}Fe_2O_4$ nanoparticles using the HAADF detector. Chitosan atoms such as carbon (C) and nitrogen (N) are also mapped. The figure shows the EDS spectrum of $Mg_{0.1}Co_{0.9}Fe_2O_4$ particles coated with chitosan.

A representative TEM image of bare and chitosan-coated $Mg_{0.1}Co_{0.9}Fe_2O_4$ nanoparticles from the MCFO series is shown in Figure 4.2. Ferrite nanoparticles cluster due to magnetic dipole interactions[184]. After coating with Chitosan, dipole interactions are decreased, and particles are dispersed. The size distribution is shown as an inset in the BF image. BF images of $Mg_{0.1}Co_{0.9}Fe_2O_4$ show an average nanoparticle size of 7.4 nm, consistent with the XRD value of 7.2 nm. Figure 4.2 shows selected area electron diffraction patterns of bare and chitosan-coated $Mg_{0.1}Co_{0.9}Fe_2O_4$ nanoparticles. According to the SAED patterns, (311) is the plane with the highest intensity, followed by (220), (400), (420), (511), and (440). Diffractograms were indexed based on the SAED d values as determined by the Velox software. SAED patterns support the noncrystalline structure reported in the literature[185–187]. Debye circles are more intense for uncoated nanoparticles due to the higher level of dispersion in coated particles. In addition, figure 4.2 displays images of bare and chitosan-coated particles captured by high-resolution transmission electron microscopy (HRTEM). Figure 4.2 shows that uncoated and chitosan-coated particles have excellent crystallinity based on their lattice fringes. According to the HRTEM image, the (311) plane had a d value of 252 pm. Fig. 4.2 shows HRTEM images of as-synthesized $Mg_{0.1}Co_{0.9}Fe_2O_4$ compositions. Based on HRTEM images, all nanoparticles are crystalline, with the degree of crystallinity increasing with increasing cobalt concentration x. Higher cobalt concentrations result in more prominent fringes in HRTEM images. It is because of the higher crystallinity degree with the rising Co. In the as-synthesized conditions, the particle size of MCFO increases with increasing cobalt content. STEM images, electron diffraction spectra, and elemental mapping of chitosan-coated $Mg_{0.1}Co_{0.9}Fe_2O_4$ nanoparticles are presented in Figure 4.3. Atomic maps of the carbon (C) and nitrogen (N) in chitosan are also offered. According to STEM-EDS mapping, ferrite nanoparticles are chemically homogeneous. It is

remarkable to see that C and N atoms are distributed uniformly on chitosan-coated ferrite nanoparticles. The coating of chitosan is thin and exclusively applied to the nanoparticles. According to the STEM EDS mapping, Mg, Co, Fe, and O have respective atomic percents of 4.11% (0.86), 8.6%5 (1.31), 12.86% (1.94), and 74.39% (5.36) and mass percents of 3.96% (0.81), 20.25% (2.87), 28.52 (4.03), and 47.27% (2.31). From the EDS spectra of chitosan-coated $Mg_{0.1}Co_{0.9}Fe_2O_4$ particles, the N (0.39 keV), C (0.28keV), Fe-L (0.71 keV), O (0.53 keV), Cu-L (0.79 keV), Co-L (0.93 keV), Mg (1.27 keV), Fe-ka (6.42 keV), Co-ka (6.96keV), Co-kb (7.68 keV), Cu-ka (8.07 keV), and Cu-kb (8.91 keV) peaks were observed. The C and Cu peaks in the EDS spectrum are highly intense due to the carbon-coated copper grid. Additionally, there are no impurity peaks.

Table 4.1: Value of lattice parameter and grain size of studied $Co_xMg_{1-x}Fe_2O_4$ ferrite nanoparticles.

Name of the sample	Grain size in (nm) of the as-dried particle measured by XRD	Grain size in (nm) of the as-dried particle measured by TEM	Lattice parameter a (Å)
$MgFe_2O_4$	3.81	3.84	8.301
$Mg_{0.9}Co_{0.1}Fe_2O_4$	4.02	4.0	8.314
$Mg_{0.8}Co_{0.2}Fe_2O_4$	4.47	4.5	8.312
$Mg_{0.7}Co_{0.3}Fe_2O_4$	4.5	4.52	8.304
$Mg_{0.6}Co_{0.4}Fe_2O_4$	5.21	5.19	8.325
$Mg_{0.5}Co_{0.5}Fe_2O_4$	5.84	5.9	8.339
$Mg_{0.4}Co_{0.6}Fe_2O_4$	6.57	6.7	8.341
$Mg_{0.3}Co_{0.7}Fe_2O_4$	6.57	6.68	8.335
$Mg_{0.2}Co_{0.8}Fe_2O_4$	6.69	6.7	8.334
$Mg_{0.1}Co_{0.9}Fe_2O_4$	7.02	7.21	8.337
$CoFe_2O_4$	7.32	7.41	8.349

4.1.3. Mössbauer spectroscopy

Figure 4.4 shows Mössbauer spectroscopy of MCFO at room temperature in the as-dried condition. The spectrum was analyzed using the WMOSS 4R program. Hyperfine parameters of isomer shift, quadrupole splitting, and hyperfine magnetic field with x are presented in Table 4.2. These parameters were obtained by model-fitting the experimental data. The goodness of fit, $\chi 2$, ranges from 0.64 to 3.112, within acceptable limits[188,189]. Manova et al.[190] showed that a Fe^{3+} sub-spectrum with a more significant isomer shift represents octahedral B-sites. In contrast, a Fe^{3+} sub-spectrum with a lower isomer shift represents tetrahedral A-sites. B-sites have a stronger covalent bond than A-sites due to the smaller orbital overlap at B-sites and the greater internuclear separation between ferric and oxygen ions[191].

Because of the short-range order of the ferric ions surrounded by the nonmagnetic ions, zero-field measurements cannot be used to determine the site occupancy for this spinel series. There is a decrease in the doublet area and an increase in the sextet area. Lin et al.[192] observed a reduction in the hyperfine field on the A and B sites of $CoAl_xFe_{2-x}O_4$ ferrite nanoparticles, increasing nonmagnetic Al^{3+} content. Low cobalt content spectra ($0 \leq x \leq 0.3$) showed two distinct doublets. These samples contain nonmagnetic Mg^{2+} ions surrounding magnetically short-range ordered Fe^{3+} ions, which reduces their magnetic moment, resulting in fast relaxation[193]. Model fitting was successful for spectra with a more significant cobalt content ($0.4 \leq x \leq 1.0$) when considering one doublet and one sextet subspectra, which exhibit mixed relaxation. The quadruple splitting is higher for the doublet subspectra than the sextet subspectra[194]. The region of the subspectra with the most considerable ferrimagnetic contribution to slow relaxation was cobalt ferrite. The isomer shifts fall within the 0.250–0.338 range, consistent with

the literature[195]. According to the isomer shift values, only the trivalent state of iron (Fe^{3+}), which falls within the range of 0.1-0.5, exists; no Fe^{2+} has an isomer shift greater than>0.5. Because of the ferrimagnetic to superparamagnetic transition, the areas of the subspectra that represent the sextet in Table 4.2 decrease as cobalt levels rise, consistent with the findings of the physical property measuring system (PPMS) that are described subsequently[190,191,193,195,196].

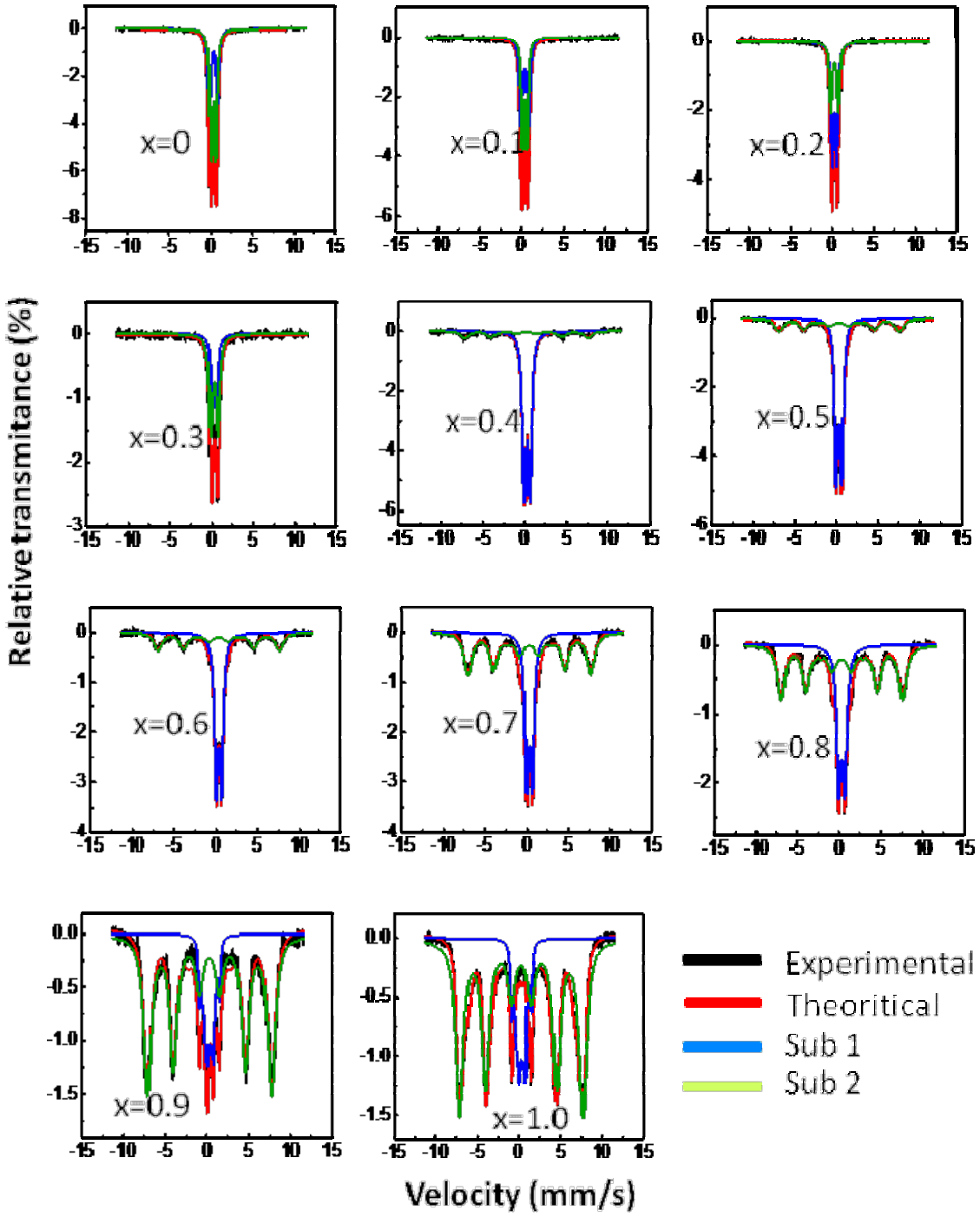

Figure 4.4: Mossbauer spectra of $Mg_{1-x}Co_xFe_2O_4$ at room temperature in the as-dried state. The spectra were collected without using an applied field at room temperature. The black lines in the picture represent the experimental data, while the red lines show the model fitting. The contributions of subspectra 1 and 2, estimated by model fit using the WMOSS 4R program, are represented by the blue and green lines, respectively.

Table 4.2: Hyperfine Mossbauer spectroscopic characteristics data recorded under zero-field and room temperature

Sample name	Position of Fe^{3+}	IS	QS	Hyperfine field (kG)	fwhm	Area
		(mm s^{-1})	(mm s^{-1})		mm/s	
$CoFe_2O_4$ Reduced $\chi 2$ = 3.112	A	0.304	2.2	18	0.2	0.997
	B	0.299	0.534	448	1.23	0.055
$Mg_{0.1}Co_{0.9}Fe_2O_4$ Reduced $\chi 2$ = 2.318	A	0.276	0.674	65	0.27	0.207
	B	0.295	0.27	462	1.08	0.895
$Mg_{0.2}Co_{0.8}Fe_2O_4$ Reduced $\chi 2$ = 2.327	A	0.325	0.669	0.18	0.59	0.418
	B	0.293	0.047	554	1.11	0.73
$Mg_{0.3}Co_{0.7}Fe_2O_4$ Reduced $\chi 2$ = 1.752	A	0.326	0.656	0.06	0.54	0.453
	B	0.3	0.014	456	1.12	0.688
$Mg_{0.4}Co_{0.6}Fe_2O_4$ Reduced $\chi 2$ = 0.939	A	0.329	0.650	2	0.516	0.652
	B	0.303	0.06	453	1.17	0.43
$Mg_{0.5}Co_{0.5}Fe_2O_4$ Reduced $\chi 2$ = 0.774	A	0.325	0.663	13	0.41	0.862
	B	0.25	0.169	457	1.15	0.202
$Mg_{0.6}Co_{0.4}Fe_2O_4$ Reduced $\chi 2$ = 1.04	A	0.332	0.631	10	0.42	0.651
	B	0.327	0.022	449	1.28	0.405
$Mg_{0.7}Co_{0.3}Fe_2O_4$ Reduced $\chi 2$ = 0.641	Doublet	0.323	0.532	354	0.37	0.348
	Doublet	0.32	0.871	352	0.5	0.596
$Mg_{0.8}Co_{0.2}Fe_2O_4$ Reduced $\chi 2$ = 0.906	Doublet	0.335	0.506	287	0.33	0.473
	Doublet	0.334	0.864	335	0.41	0.48
$Mg_{0.9}Co_{0.1}Fe_2O_4$ Reduced $\chi 2$ = 0.841	Doublet	0.337	0.531	355	0.35	0.67
	Doublet	0.338	0.903	352	0.38	0.431

4.1.4. FTIR spectroscopy

The FTIR spectrum of bare, uncoated, and chitosan-coated MCFO nanoparticles is shown in Figure 4.5. Chitosan is known for its peaks at 890, 1402, 1638, 2896, and 3482 cm^{-1}. The stretching vibration of the O-H and -CH_2 pyranose rings, respectively, were responsible for the absorption peaks at 3482 cm^{-1} and 2896 cm^{-1}. Because of the amino (-NH_2) group's N-H bending vibration, there were absorption peaks at 1638 cm^{-1}. Alkyl group C-H bending vibration is represented by an absorption peak at 1402 cm^{-1}. The antisymmetric stretching vibration of the C-O-C bridges of the glucopyranose ring in the chitosan matrix is shown by the absorption peaks at 1058 and 890 cm^{-1} [185,187]. Two peaks are observed at the lower frequency region, the characteristic peaks of the cubic spinel structure [46,179,182,197]. A higher frequency absorption band (v_2) is seen in the 580 to 592 cm^{-1} range, whereas a lower frequency absorption band (v_1) is seen in the 390 to 418 cm^{-1} range. A metal-oxide bond at the A-site is stretched, vibrating in the higher frequency band (v_2). The stretching vibration of a metal-oxide bond at the B-site is represented by the lower frequency band (v_1) simultaneously. Due to the A-site's shorter bond length, the typical mode of vibration at the A-site is higher than B-site [43,198,199]. With the increase in x, the occupation of Co^{2+} ions at the octahedral sites increases, thus reducing the bond length at this site. The preference of Mg^{2+} ions is for the tetrahedral sites. Therefore, with the increase in x, the bond length at the octahedral sites increases with a corresponding reduction in the bond length at the tetrahedral sites, for which v_1 increases, and v_2 decreases with cobalt content x. Figures 4.6(c) and (d) show the variations of $v_1$and $v_2$of bare and coated nanoparticles. For coated $Mg_{1-x}Co_xFe_2O_4$ nanoparticles, the v_1 and v_2 shift towards the higher wavenumber than the as-dried nanoparticles, which ensures the bonding of ferrite with chitosan [200]. When other nuclei are considered to be in their

equilibrium positions, the force constant informs us of the stiffness of the Fe^{3+} ions to vibrational displacement. The length of the Fe^{3+} and nearest neighbour ions' bonds is inversely correlated with the force constants. We obtained the force constants (F_C) for the A-site (F_{CT}) and B- site (F_{CO}) by the following relation,

$$F_c = 4\pi^2 C^2 v^2 m \tag{4.1}$$

In the above equation, c is the speed of light~2.99×10^{10} cms^{-1}, v is the vibrational frequency of the ions at A and B sites, m is the reduced mass for the Fe^{2+} and the O^{2-} ions which are 2.061×10^{-23}g. Figure 4.6(b) shows that the value of F_{CO} is lower than F_{CT} because of the higher orbital overlap at the A-site. However, F_{CO} increases, and F_{CT} decreases with increasing cobalt content x, indicating that the B-site's bond lengths reduce and the A-site increases with x[201].

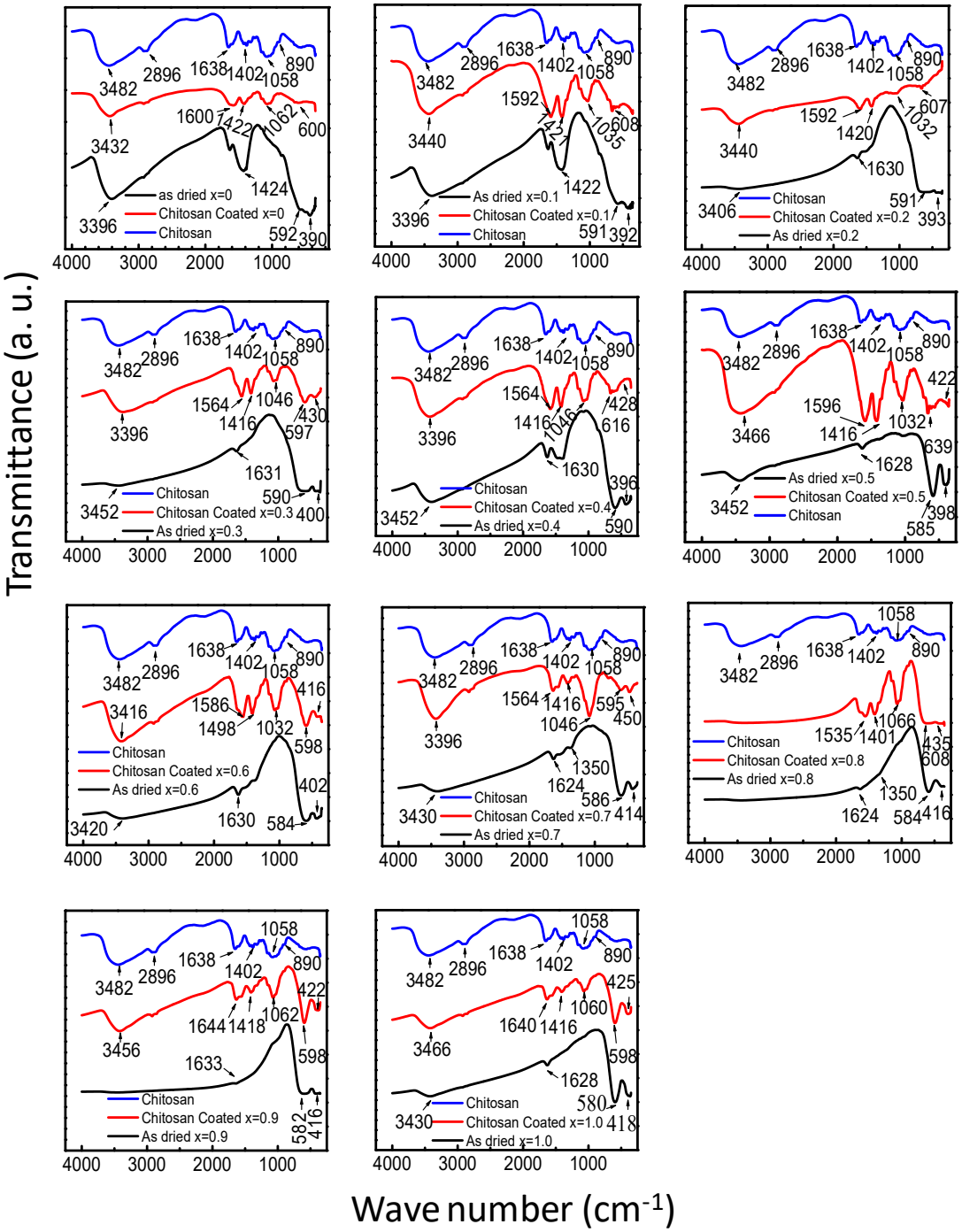

Figure 4.5: FTIR spectrum of Chitosan, as dried $Mg_{1-x}Co_xFe_2O_4$ and chitosan-coated $Mg_{1-x}Co_xFe_2O_4$ ferrite nanoparticle.

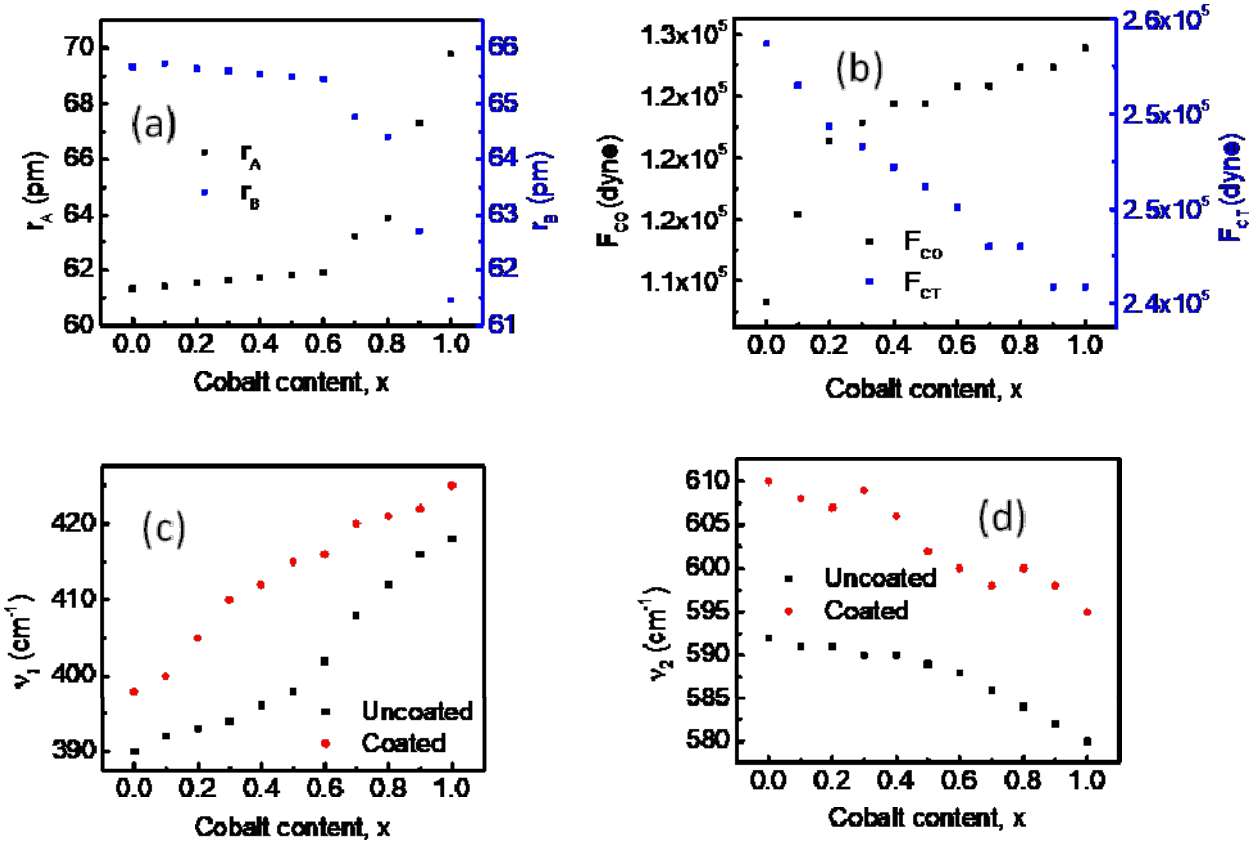

Figure 4.6: (a) Variation of the ionic radius of A site (r_A) and B site (r_B), (b) Variation of the force constants of A site (F_{CT}) and B site (F_{CO}), (c) variation of lower frequency absorption band (ν_1), and (d) variation of higher frequency absorption band (ν_2) with cobalt content, x of $Mg_{1-x}Co_xFe_2O_4$ ferrite nanoparticle.

4.1.5. Raman spectroscopy

Nanoparticle structure is further investigated using Raman spectroscopy by identifying several vibrational modes[202–205]. Figure 4.7 illustrates room temperature Raman spectra of MCFO nanoparticles in the 190–1000 cm^{-1}. It has already been shown that MCFO ferrites have a partially inverse spinel structure associated with spacegroups (Fd3m) [42,203,206–208]. This space group has vibrational modes A_{1g}(R), E_g(R), F_{1g}, $3F_{2g}$(R), $2A_{2u}$, $2E_u$, $4F_{1u}$(IR), $2F_{2u}$. The others are silent modes, while R denotes Raman-active vibrational modes and IR denotes infrared-active vibrational modes. Five Raman active modes, A_{1g}, E_g, F_{2g}(3), F_{2g}(2), and F_{2g}(1), are therefore anticipated to be seen in Raman spectra. The examined samples exhibit observable Raman modes, as shown in Figure 4.7 (b). Symmetric stretching of MeO_4 (Me represents Co and/or Mg) and stretching of FeO_4 at the A-site are linked to A_{1g} modes. E_g modes represent oxygen bending concerning Fe at the B site. The asymmetric bending of oxygen for Fe is represented by an F_{2g}(3) mode, the asymmetric stretching of Fe and O is represented by an F_{2g}(2) mode, and the complete translation of Fe and O is represented by an F_{2g}(1) mode[203,207]. 660 to 720 cm^{-1} and 460 to 660 cm^{-1} can be assumed to be Raman peaks corresponding to the A-site of ferrites and the B-site of ferrites, respectively[209]. Raman modes A_{1g}, E_g, F_{2g}(1), F_{2g}(2), and F_{2g}(3) of MCFO are presented in Table 4.3. A_{1g} vibrational modes are reduced with increasing cobalt content x since Co (58.9332 amu) ions have a higher atomic mass than Mg ions (24.3050 amu). Mund et al.[204] also establish a rise in the vibrational mode (blue shift) when Mg is increased in magnesium cobalt ferrite prepared by the sol-gel auto-combustion technique because of the lower atomic mass Mg than Co. The different Raman peak at 402-415 cm^{-1} is related to the A-site way that exhibits the local lattice effect in the B-site of MCFO[209].

Based on the Gaussian fitting of the Raman spectra, Figure 4.8 depicts variations in area integrals with the cobalt concentration x. Following background subtraction and deconvolution, the Gaussian function produced the best fit for the experimental and theoretical data. In Figure 4.8, the area integral for A_{1g}, i.e., the peaks describing the tetrahedral sites for both Me–O and Fe–O, is the highest, demonstrating that the cation occupancy at the A-site is the highest (where Me represents Mg and Co and Fe for iron). Figure 4.8 depicts the area integral of A_{1g} for Me–O and Fe–O, illustrating that as x increases, the occupancy of Me and Fe ions decreases. As x increases, the integral area of E_g, $F_{2g}(2)$, and $F_{2g}(3)$ increases, indicating a more incredible inverse spinel structure at the B-site. Cobalt prefers to occupy the B-sites, while magnesium prefers the A-sites. The area integral of the peaks of A_{1g} decreases with increasing cobalt concentration x, which leads to the emergence of lower modes, such as E_g and F_{2g}[210].

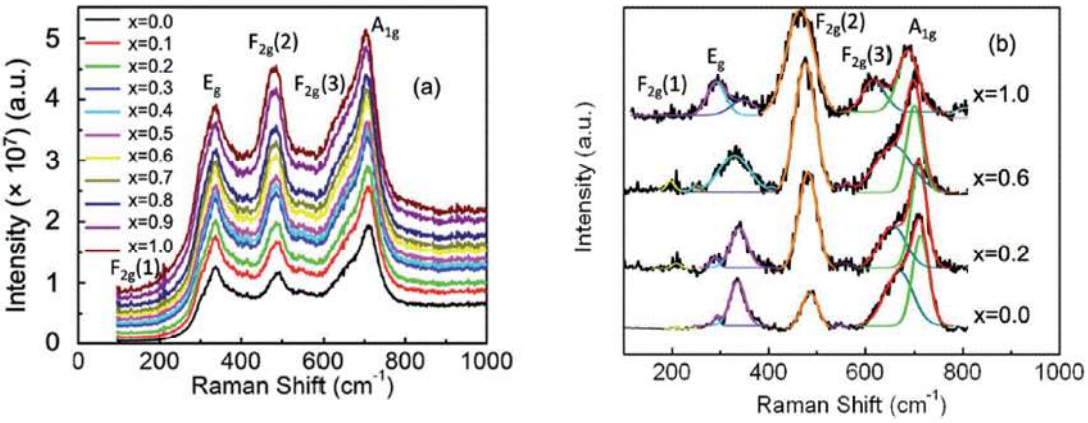

Figure 4.7 (a) Room temperature Raman spectra of $Mg_{1-x}Co_xFe_2O_4$ nanoparticles in the range of 190–1000 cm^{-1} using the pelletized solid samples. Five Raman active modes A_{1g}, E_g, $F_{2g}(1)$, $F_{2g}(2)$, and $F_{2g}(3)$ are assigned in the Raman spectra. (b) Representative best fitting of the Raman spectra using the Gaussian function after background subtraction and deconvolution.

Table 4.3: Data of Raman modes of $Mg_{1-x}Co_xFe_2O_4$ ferrite nanoparticles.

Value of x	Main Raman mode peak energy (cm^{-1})				
	F_{2g} (1)	E_g	F_{2g} (2)	F_{2g} (3)	A_{1g}
0	-	337	491	550	712
0.1	216	336	481	549	707
0.2	216	336	481	561	705
0.3	216	336	479	564	705
0.4	213	335	480	569	643, 704
0.5	213	325	480	567	642, 700
0.6	208	329	465	563	627 , 697
0.7	213	323	475	573	637, 694
0.8	212	318	479	567	632, 694
0.9	-	315	470	-	620, 689
1.0	-	311	472	569	613, 687

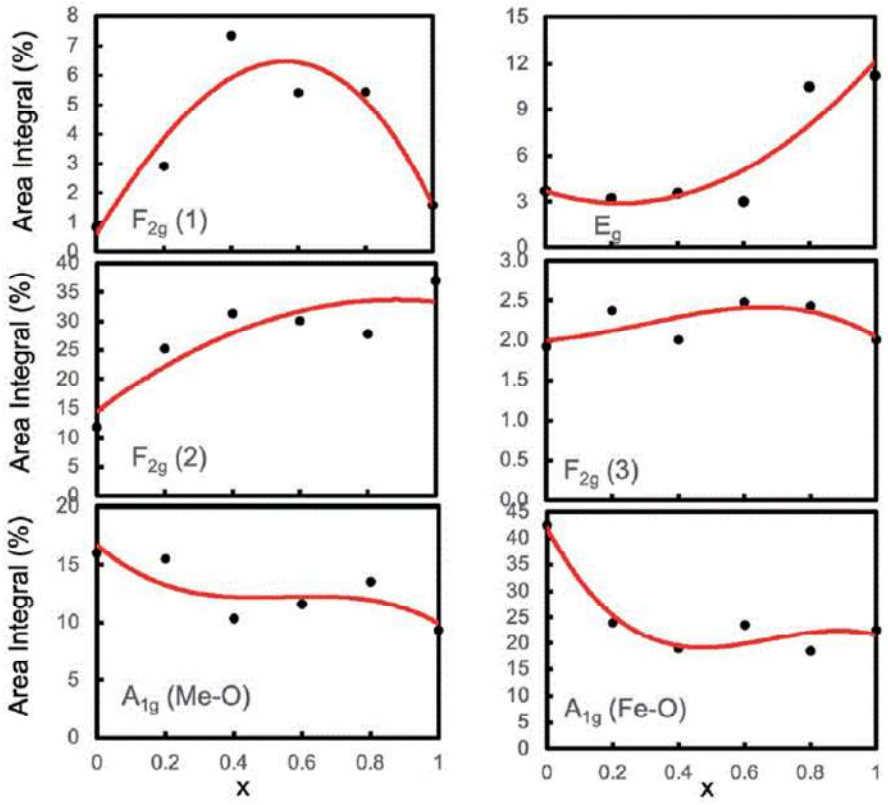

Figure 4.8 Variation of area integral with Co concentration x of the A_{1g}, E_g, $F_{2g}(1)$, $F_{2g}(2)$, and $F_{2g}(3)$ peaks assigned to the Raman spectra of the $Mg_{1-x}Co_xFe_2O_4$ nanoparticles obtained by Gaussian fitting and deconvolution.

4.1.6. Hydrodynamic diameter and Zeta potential

Figures 4.9(a-d) and 4.10 (a-d) present the hydrodynamic diameter of chitosan-coated MCFO nanoparticles in water at different concentrations and temperatures determined by dynamic light scattering. Dynamic light scattering (DLS) measures Brownian motion, the arbitrary movement of particles due to the interactions with the neighbouring solvent molecules, correlating to the particle size in the solution by the Stokes-Einstein equation[167]. Nanoparticles without coatings exhibited massive hydrodynamic diameters ranging from 2000 to 8000 nm at 4 mg/ml. Uncoated nanoparticles had polydispersity indices ranging from 0.152 to 1. As-dried particles tend to agglomerate, resulting in sedimentation in water [167]. In Figure 4.2(a–c), TEM images confirm the accumulation of uncoated samples. Nanoparticles coated with chitosan and diluted to 4 mg/ml were 145 to 165 nm in hydrodynamic size. The corresponding poly-dispersity indexes were 0.115 to 0.291. It can be seen from Figure 4.9(a) that the curves are symmetrical. Figure 4.9(b) shows nanoparticle hydrodynamic diameters increase as solution concentration rises. Figs. 4.9(c) and (d) show the hydrodynamic diameters of coated nanoparticles at 4 mg/ml and 2 mg/ml, respectively, as a function of temperature. Temperature decreases hydrodynamic diameter at both concentrations. When the concentration of the solution decreases, and the temperature increases, the hydrodynamic size decreases. Therefore, chitosan-coated MCFO nanoparticles should not aggregate at physiological temperatures of 37°C or 42-46°C for hyperthermia applications. As shown in Figure 4.10 (e), chitosan-coated MCFO particles exhibited a greater zeta potential at pH 2.5 to 5, indicating stability in that range. The solution's isoelectric zeta potentials were found at pH 9 to 10.5. Uncoated MCFO particles at 4 mg/ml had zeta potentials of -2mV to 6.45mV, and their pH ranged from 6.25 to 6.70, indicating that the particles were unstable. Figure 4.10 (e) shows that the pH of the chitosan-coated MCFO

particles was 3.45 to 4.55, and their zeta potential was 30 to 50 mV. Zahraei et al. [41] observed the highest zeta potential value of chitosan-coated manganese zinc ferrite at pH 3, close to our findings. Arakha et al. [211] determined the zeta potential of chitosan-coated iron oxide nanoparticles, resulting in a stable suspension of 36.3 mV. Nevertheless, in this pH region, the solution is durable because the zeta potential of the coated particles is higher than 30 mV. It was evident that the samples were well-coated and dispersed. Even after one year, no precipitation or aggregation occurred in the solution's vial. Therefore, electrostatic stability occurs in pH>2.5 and pH<5.5. The isoelectric zeta potentials of the investigated solution were in the pH range of 7 to 8.5. Zahraei et al. [41] found that the isoelectric point of chitosan-coated manganese zinc ferrite is 8.5, which supported our measured data. For the higher pH, zeta potential decreases slowly, and particles may settle down due to flocculation, aggregation, and coagulation[169]. There is a direct correlation between particle concentration, viscosity, and pH of the solution and the zeta potential of the solution[210].

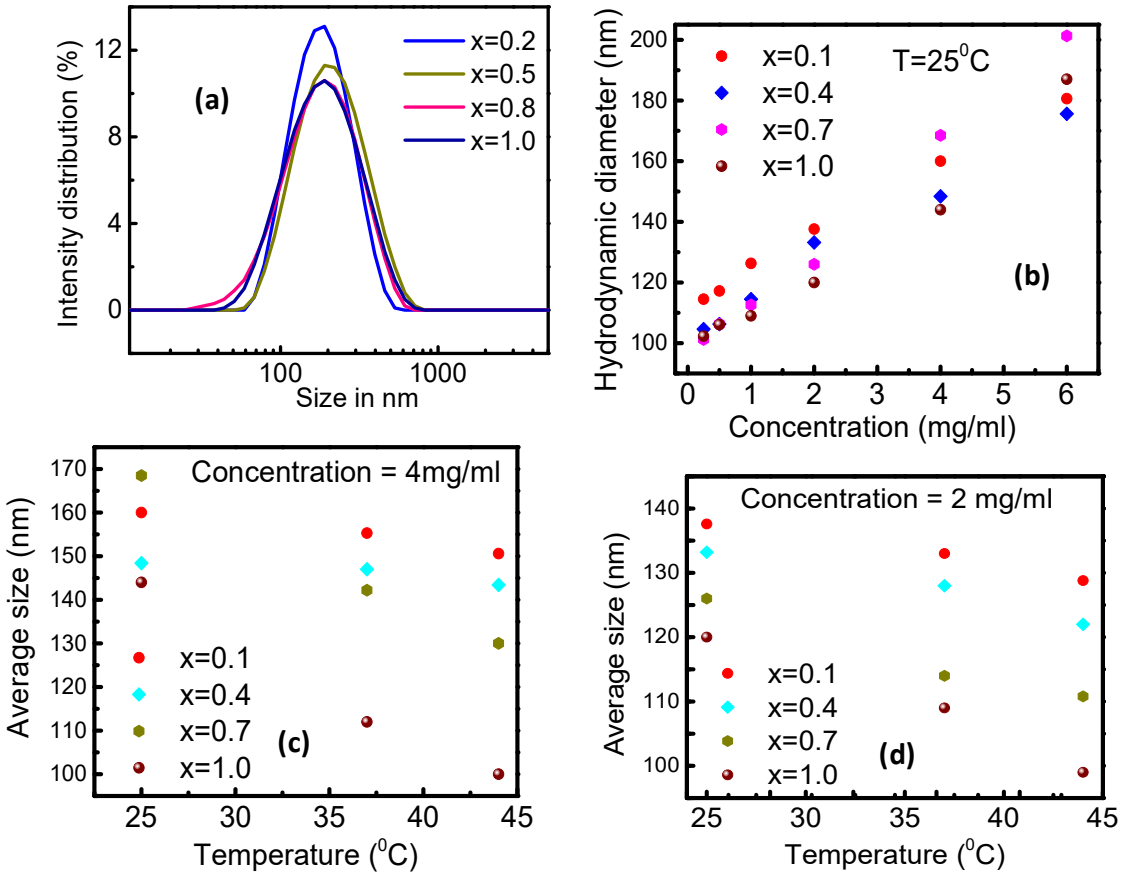

Figure 4.9: Hydrodynamic size distribution of Chitosan coated $Mg_{1-x}Co_xFe_2O_4$ nanoparticles at 25^{o}C temperature, (b) Variation of hydrodynamic size with the concentration of the solution of chitosan-coated $Mg_{1-x}Co_xFe_2O_4$ nanoparticles, (c) Variation of average hydrodynamic size with the temperature at the concentration of 4 mg/ml chitosan coated $Mg_{1-x}Co_xFe_2O_4$ nanoparticles, (d) variation of average hydrodynamic size with the temperature of 2 mg/ml chitosan-coated $Mg_{1-x}Co_xFe_2O_4$ nanoparticles.

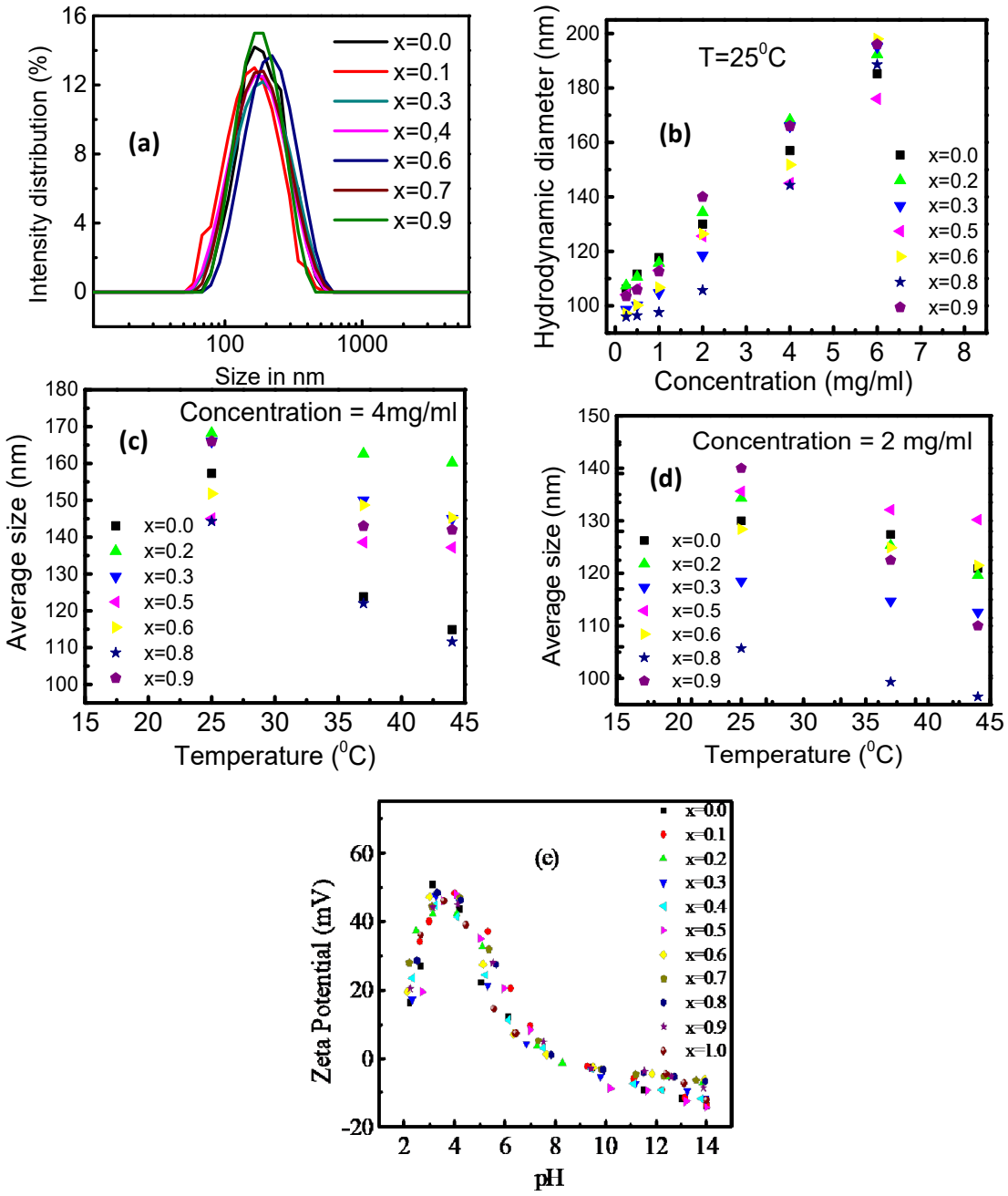

Figure 4.10: (a) Hydrodynamic size distribution of Chitosan coated $Mg_{1-x}Co_xFe_2O_4$ nanoparticles at 25°C temperature, (b) Variation of hydrodynamic size with the concentration of the solution of chitosan-coated $Mg_{1-x}Co_xFe_2O_4$ nanoparticles, (c) Variation of average hydrodynamic size with the temperature at the concentration of 4 mg/ml chitosan coated $Mg_{1-x}Co_xFe_2O_4$ nanoparticles, (d) variation of average hydrodynamic size with the temperature of 2 mg/ml chitosan-coated $Mg_{1-x}Co_xFe_2O_4$ nanoparticles, (e) Variation of zeta potential with pH of the solution of chitosan-coated $Mg_{1-x}Co_xFe_2O_4$ nanoparticles at 25^{0}C temperature.

4.2. Magnetic measurements

Figures 4.11 and 4.12 show variations in magnetization with a magnetic field of 5 Tesla for bare and chitosan-coated MCFO nanoparticles. M-H curves exhibit interesting composition variations and differences between bare and coated conditions. The M-H curves of uncoated and coated samples show a significant difference, demonstrating the surface functionalization of nanoparticles. $MgFe_2O_4$ (x=0) particles, whether uncoated or coated, are superparamagnetic. According to Mössbauer spectroscopy, superparamagnetic relaxation occurs as x increases, followed by a mixed slow and fast relaxation. Hysteresis loop shapes differ significantly between bare and coated particles at x=0, possibly because of clustering effects[210,212]. Since nanoparticles have a high surface-to-volume ratio, their surface atoms influence their magnetic properties. There are incomplete coordination atoms on the surface, and A-B coupling is broken by superexchange interactions mediated by oxygen. As a result of the distribution of exchange and crystal fields, surface anisotropy is induced [190]. When nanoparticles are coated with chitosan, their surface stress anisotropy is reduced, reducing their overall effective anisotropy. With increasing x, i.e., Co-content, magnetocrystalline anisotropy gains effective anisotropy [190]. As a result, the magnetic softness of the coated sample decreases with x. For the samples with lower cobalt content ($0 \leq x \leq 0.3$), the M-H hysteresis curves of these materials are similar to those of diamagnetic materials. Cobalt content influences the magnetic properties of the sample. When cobalt content is increased, the material will exhibit stronger ferromagnetic behavior, meaning it will retain some degree of magnetization even after being removed from a magnetic field. The material may possess weaker magnetic properties if it contains less cobalt and behaves more like a diamagnetic material when it has a lower cobalt content. According to FTIR spectroscopy,

Mg2+ ions tend to occupy A sites, and Fe^{3+} ions tend to occupy B sites. A significant reduction in the magnetic moment of Fe^{3+} ions on the B sites can be attributed to their antiparallel orientation among themselves. Small particles with a low cobalt content are found agglomerated in TEM images. Therefore, their magnetic moment is oriented randomly, similar to a paramagnetic material. But when these particles are coated with chitosan, they are found dispersed in the solution and quickly respond to the applied magnetic field though the value of their saturation magnetization is low. The law of approach to saturation was used to determine the saturation magnetization [213]. In only a few coated samples with positive slope, the highest observed value of magnetization is considered saturation magnetization. Some coated particles exhibit a positive slope on the M-H hysteresis curve for a variety of reasons. The positive slope may be caused by the presence of a coating on the particles. As a result of the coating, additional magnetic interactions can be introduced or the magnetic properties of the particles may be altered, resulting in deviations from the typical hysteresis behavior. Coatings can affect magnetic anisotropy, exchange interactions, or domain wall dynamics, resulting in a modified hysteresis curve. The presence of magnetic interactions between the coated particles can also contribute to a positive slope. As a result of dipolar interactions, exchange interactions, or other magnetic coupling mechanisms, these interactions can occur. It is possible for the magnetic behavior of particles to be affected by their interactions if they are close to one another or in contact, resulting in deviations from the expected hysteresis behavior. A positive slope can also be explained by the size and shape of the coated particles. A particle's magnetic behavior can be significantly influenced by size effects and shape anisotropy at the nanoscale. Hysteresis behavior may be altered by the presence of a coating, resulting in deviations from what is expected. Figures 4.11 and 4.12 show the saturation magnetization of bare and chitosan-coated

MCFO nanoparticles plotted against cobalt content. Increasing cobalt content x increases saturation magnetization because cobalt has a higher magnetic moment (3.88B) than magnesium (0B) [214,215]. According to their saturation magnetization, MCFO nanoparticles as-dried have a saturation magnetization of 6.9, 11.4, 14.67, 22.26, 25.21, 32.29, 43.44, 49.12, 55.54, 56.54, and 59.29 emu/gm, respectively.

Figure 4.13(a-b) exhibits the coercive field, remanent magnetization, and anisotropy constant increase with cobalt content supported by Mund et al. [215]. Increasing Mg^{2+} content, i.e., lower x, dilutes magnetic moment. When x increases, magnetic moment increases, and magnetocrystalline anisotropy of Co^{2+} enhances effective anisotropy. As shown in Figure 4.13, the bare state has a higher coercivity ratio and remanent ratio. Pervaiz et al. [216] synthesized the $CoFe_2O_4$ by sol-gel auto-combustion technique. Their saturation magnetic moment and anisotropy constant are 63 emu/g and 0.35 x 106 erg/cm3, which are close to this study. Coated particles exhibit a lower magnetization than uncoated particles, as shown in Figures 4.11 and 4.12. A dead layer on the surface of the nanoparticles causes this. Although coated particles respond faster to the applied field, the coating reduces the effective anisotropy and surface of the particles. As a result, the layer clusters. Therefore, coated particles have lower coercivity and remanent magnetization values than uncoated particles[174,186,217]. The cubic anisotropy constant, $K_{1,}$ was determined considering M_s by the law of approach to saturation, which characterizes the dependence of magnetization M on the applied magnetic field for $H>>H_{c,}$ and this relation is expressed as,

$$M = M_S\left[1 - \frac{8}{105}\left(\frac{K_1}{M_S H}\right)^2\right] + \chi H \quad (4.2)$$

where, K_1 is the cubic anisotropy constant, M_s is the saturation magnetization, and χ is the high-field susceptibility [218]. An increase in x increases the cubic anisotropy constant K_1, but the coating layer. The surface anisotropy effect at lower x causes a cubic anisotropy. A cubic anisotropy results from surface anisotropy and magnetocrystalline anisotropy at higher x. The coating cannot reduce magnetocrystalline anisotropy, but surface and stress anisotropy can be reduced. As a result, cubic anisotropy increases with x as chitosan-coated MCFO is layered.

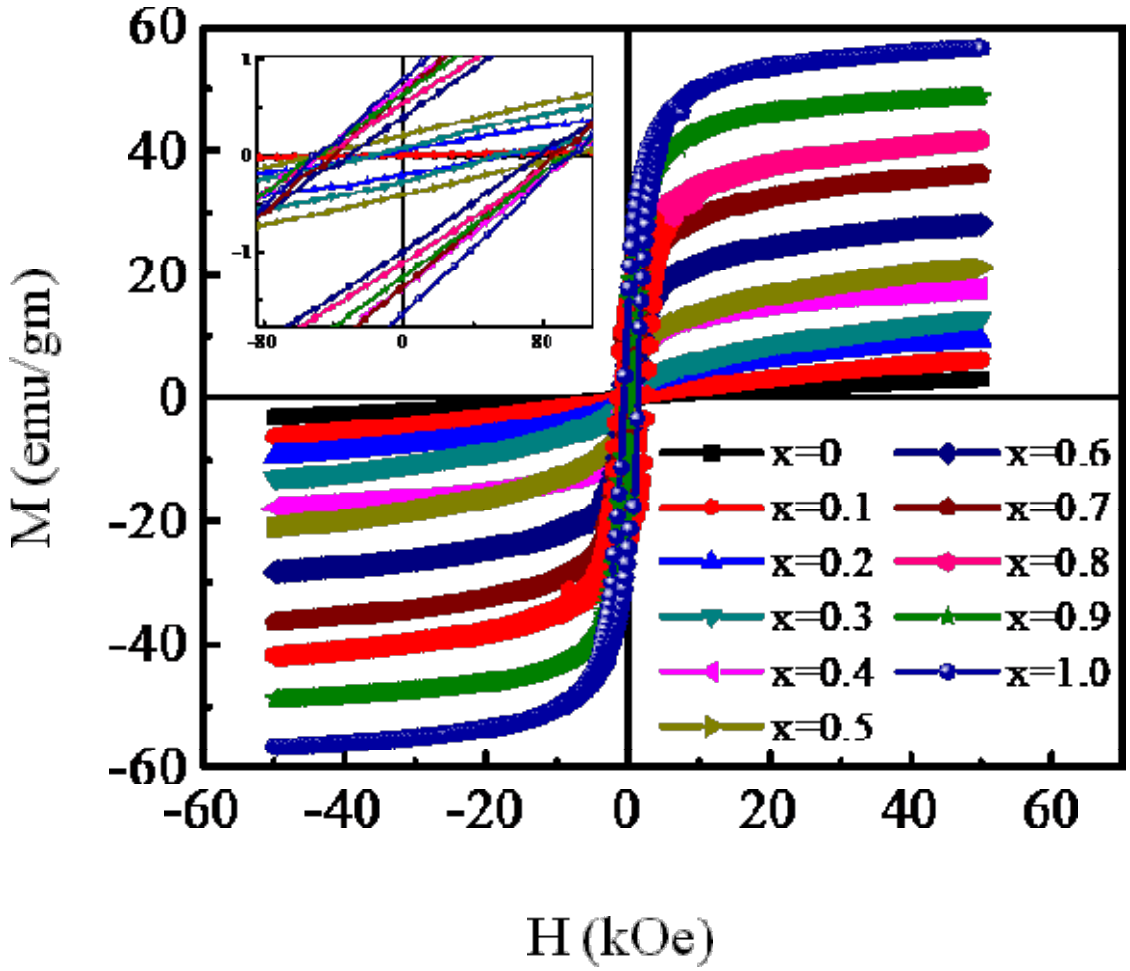

Figure 4.11: Representative M–H curves of bare $Mg_{1-x}Co_xFe_2O_4$ ($0 \leq x \leq 1$ with $\Delta x = 0.1$) nanoparticles were measured on the powder samples in the bare with a maximum magnetic field of 5 T. Magnetic moment increases with an increase in cobalt content x.

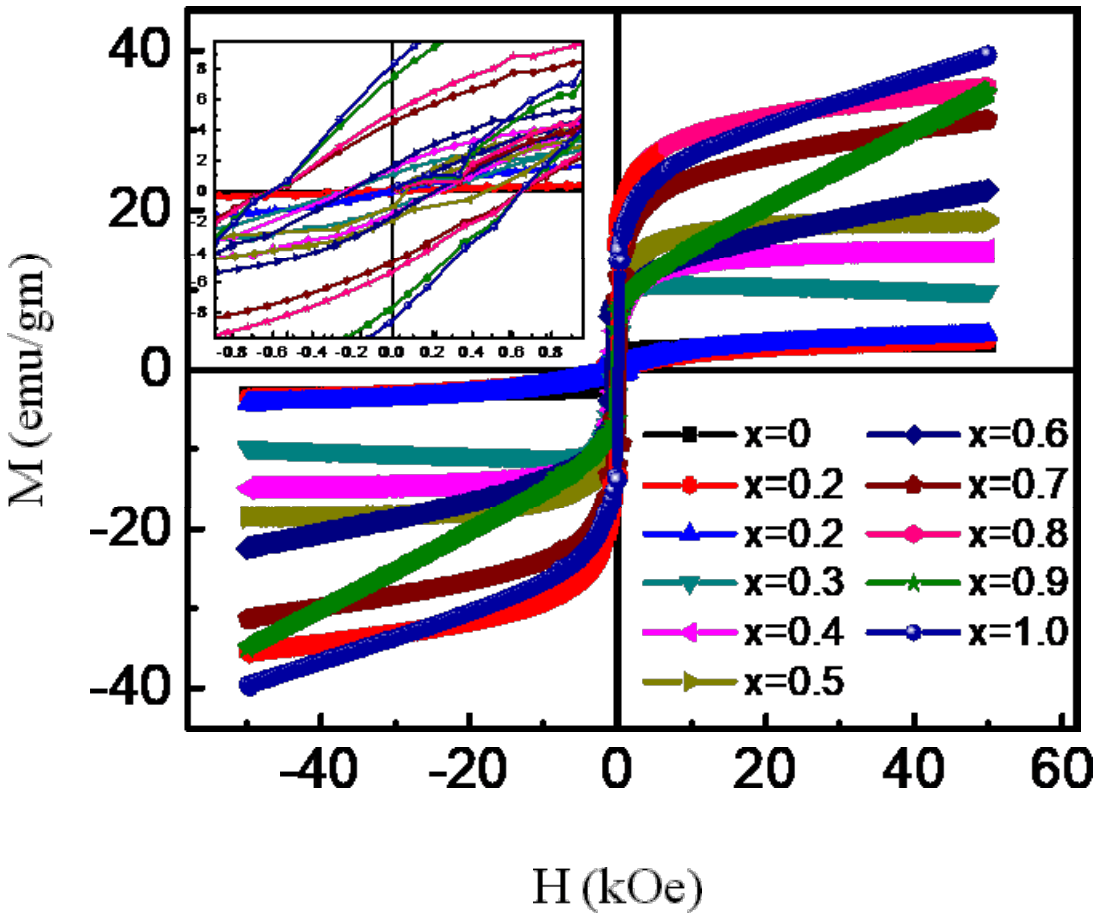

Figure 4.12: The variation of magnetization with an applied field for chitosan-coated $Mg_{1-x}Co_xFe_2O_4$ ($0 \leq x \leq 1$ with $\Delta x = 0.1$) nanoparticles with a maximum magnetic field of 5. It is interesting to note the M-H curves' shape, composition, and coating variations. Extensive variations in the M-H curves of coated samples demonstrate that the nanoparticles of all compositions have undergone surface functionalizations.

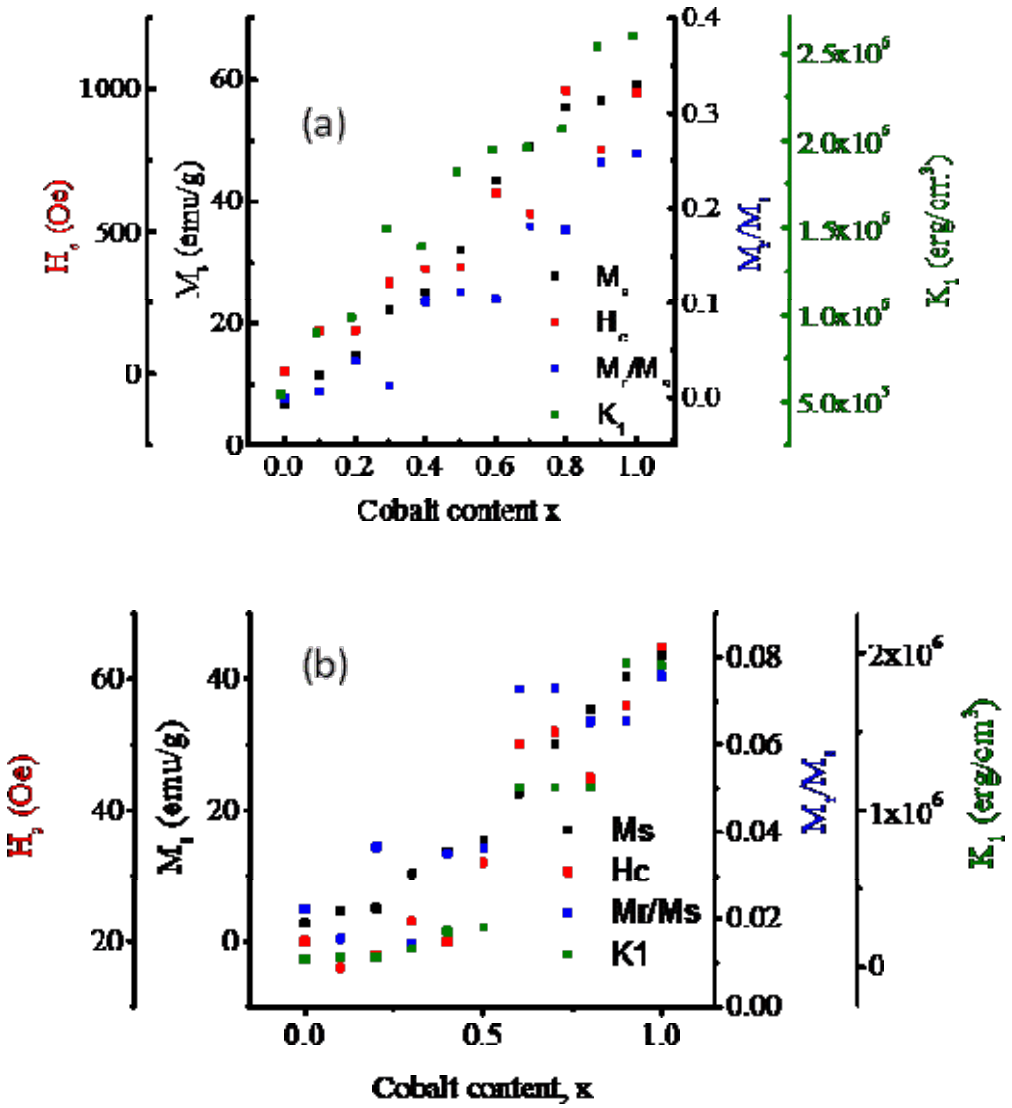

Figure 4.13: Variation of saturation magnetization (M_s), coercivity (H_c), remnant ratio (M_r/M_s), magnetic anisotropy constants (K_1) with cobalt content, x of (a) uncoated, and (b) chitosan-coated $Mg_{1-x}Co_xFe_2O_4$.

4.3. Cytotoxicity

MCFO nanoparticles coated with chitosan and bare MCFO nanoparticles were studied using the HeLa cell line. HeLa cell lines were used to inoculate tumours for future in-vivo MRI and hyperthermia studies. The nanoparticles must be excluded from cytotoxic effects on HeLa cells before in-vivo tumour studies. According to Figure 4.14, uncoated MCFO nanoparticles are not viable under bare conditions. Meanwhile, chitosan-coated MCFO nanoparticles show a remarkable difference. Since chitosan and chitosan-coated MCFO nanoparticles had more than 80% cell viability, both were nontoxic. Across the entire composition range of as-synthesized MCFO, toxicity increases with increasing cobalt content x. Increasing cobalt content x decreases cell viability slightly[219–223].

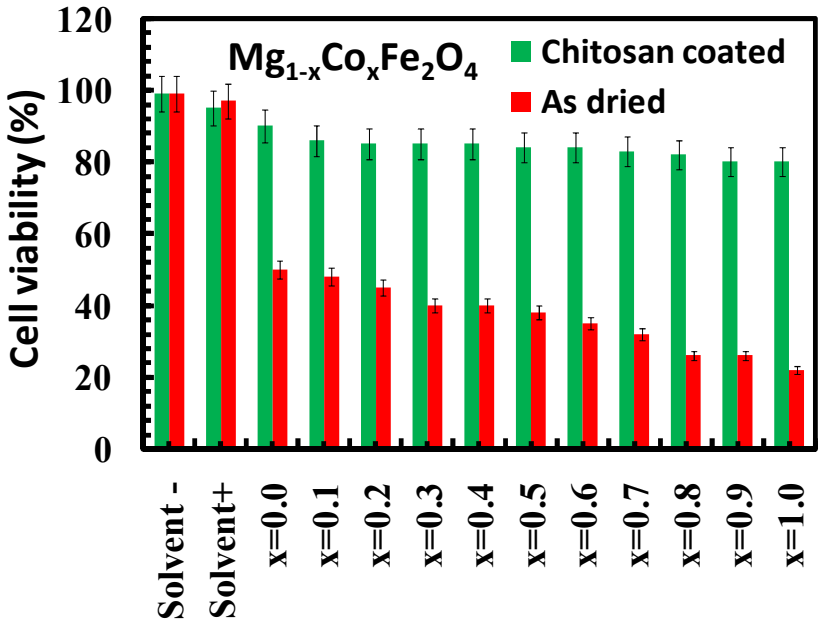

Figure 4.14: Survival of HeLa cells of different as-dried and Chitosan-coated $Mg_{1-x}Co_xFe_xO_4$ samples.

4.4. Hyperthermia

As shown in Figure 4.15 (a), chitosan-coated MCFO reaches a plateau temperature after a rise in temperature with time. According to equations (2.10) and (2.11) the temperature rises with time due to a loss of Néel and Brownian relaxations. According to Figure 4.15 (a), the plateau temperature has a higher value over time as anisotropy constants and particle sizes increase, generating more heat due to Neel's relaxation. The Brownian relaxation of nanoparticle solutions is influenced by particle size and viscosity. The temperature rise shown in Figure 4.15 (a) is also a result of Brownian relaxation. Viscosity increases with an increase in colloidal suspension concentration. The size of the nanoparticles increases with the addition of Co content. Therefore, Brownian relaxation also influences the concentration of magnetic nanoparticles and the increase in plateau temperature with x[10,221,222]. The effective relaxation time is given in equation (2.12). Figure 4.15 (b) illustrates how the solution concentration for MCFO causes the maximum temperature (at the plateau zone), T_{max}, to rise. For a field of 26 mT and a concentration of 4 mg/ml, the maximum temperature ranges between 41 and 72°C. Figure 13(b) further shows that chitosan-coated $MgFe_2O_4$ requires 8 mg/ml to reach hyperthermia temperature (42–46°C) for an AC magnetic field of 26 mT. x=0.1, 0.2, and 0.3, a concentration of 4 mg/ml is needed, 1 mg/ml for x=0.4, 0.5, 0.5 mg/ml for x=0.6, 0.7, and 0.25 mg/ml for x=0.8, 0.9, and 1. Different compositions and concentrations produce various specific loss powers (SLPs), as seen in Figure 13(c). The SLP rises with increasing cobalt content x; it falls with increasing nanoparticle concentration[10,221,222]. Up to a 4 mg/ml concentration, $MgFe_2O_4$ does not exhibit hyperthermia properties. Nevertheless, magnesium is minimally substituted with cobalt in the studied samples, making them suitable for hyperthermia at a concentration of 4 mg/ml.

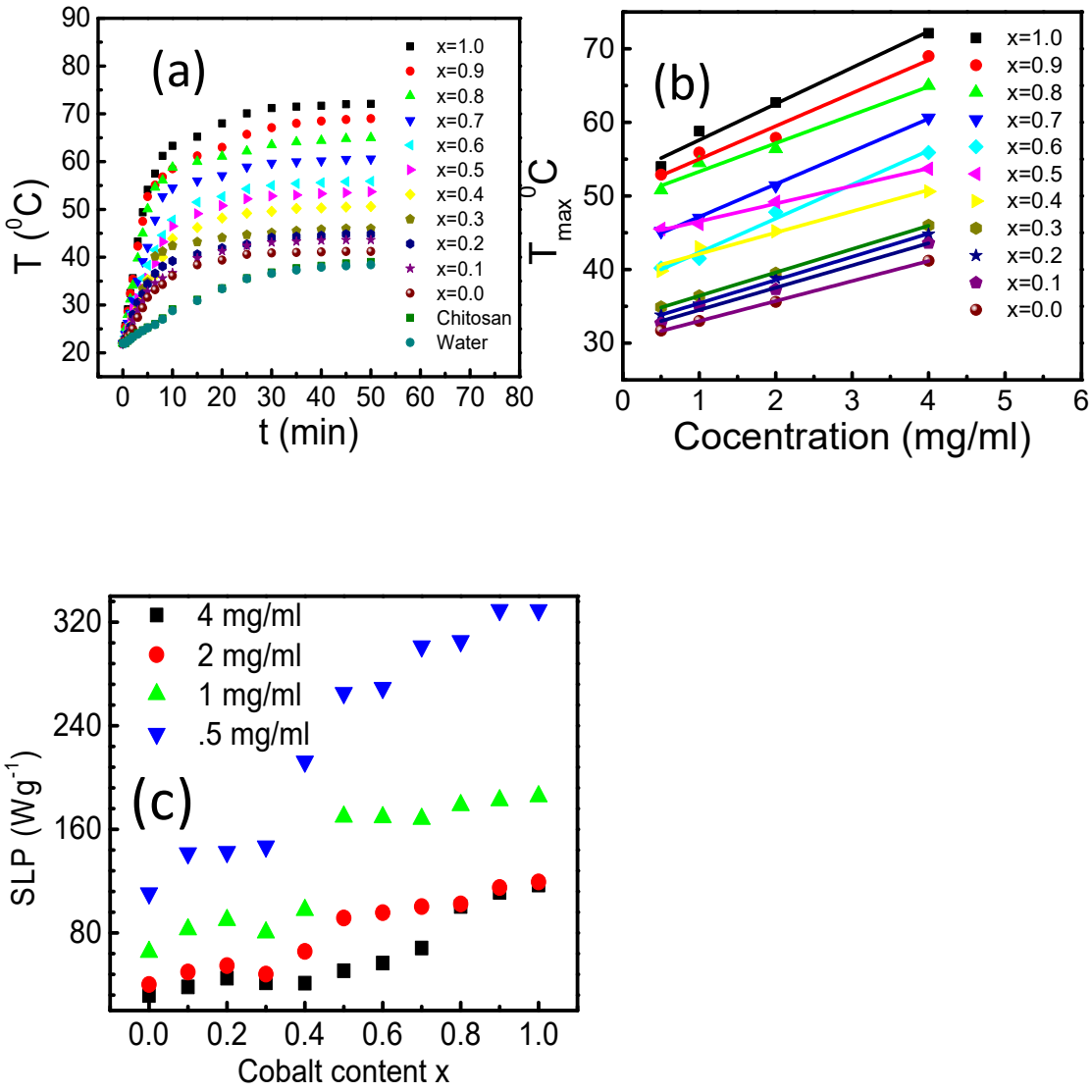

Figure 4.15: (a) The increase in temperature of dried $Mg_{1-x}Co_xFe_2O_4$ nanoparticles coated with chitosan at a concentration of 4 mg/ml; (b) The variation in maximum temperature with a concentration of magnetic nanoparticles; and (c) The variation in specific loss power (SLP) with cobalt content x.

4.5. Magnetic Resonance Imaging (MRI)

The T_2 maps of phantoms containing chitosan-coated MCFO nanoparticles were acquired with different concentrations. An imaging sequence used a 7-tesla static magnetic field with a flip angle of 90°, repeated time of 4000 ms, and echo times of 7 ms, 14 ms, 21 ms, 28 ms, 35ms, 42ms, 49ms, 56ms, 63ms, 70ms, 77ms, 84ms, 91ms, 98ms, 105ms, and 112ms. An image matrix of 128x128 pixels and a field of view (FOV) of 40x40 mm^2 were used. Pulses induce a change in net magnetization, measured by transverse relaxation time (T_2). T_2 maps of phantoms coated with chitosan-coated MCFO nanoparticles at different concentrations are presented in Figure 4.16 (a). Since T_2 relaxation time decreases with increasing concentration, each voxel becomes darker [21]. The magnetic characterization by Mössbauer and PPMS showed a change from superparamagnetic to ferromagnetic with increasing x. When pulses are produced by ultrafine magnetic nanoparticles and their magnetic field gradients, ferrite nanoparticles speed up transverse or spin-spin relaxation, which causes magnetic moments to dephase quickly. Keonig and Keller provide a mathematical interpretation, which is given in equation 2.12.2[21]. Transverse relaxivities were measured using equations 2.12.3, 2.12.4, and 2.12.5. The differences in relaxation rate with concentration are depicted in Figure 14(b). The relationship between $1/T_2$ and nanoparticle concentrations was linear, and the slope provides values for the relaxivities for each x. The change in r_2 relaxivities with x as magnetic moments rise is depicted in Figure 4.16 (a-d). Chitosan-coated MCFO ferrite nanoparticles have recorded r_2 relaxivities ranging from 15.2 to 185.5 $mM^{-1}s^{-1}$, which results in virtually linear relaxivities with the saturation magnetic moment that follows a linear fluctuation. The variations of relaxivity with anisotropy in Figure 4.16 (c) are scattered, but there is a tendency to increase.

A similar trend is present in Figure 4.16 (d), where relaxivity increases with initial

susceptibility but in a scattered manner. Kim[16] reported identical results for $MnFe_2O_4$, $CoFe_2O_4$, and Fe_3O_4 synthesized by a diol reduction of organic metals. Wang[15] observed the r_2 relaxivities of commercially approved MRI phase-contrast agent Ferumoxtran-10 (AMI-227; Combidex, AMAG Pharma; Sinerem, Guerbet), Ferucarbotran (Resovist, Bayer Healthcare), and Ferumoxides (FeridexIV, Berlex Laboratories; and Endorem, Guerbet) as 60,151, and 98.3, respectively. The r_2 relaxivities of chitosan-coated MCFO ferrite nanoparticles are comparable to the above-mentioned commercial contrast agents. Accordingly, MCFO ferrite nanoparticles are potential contrast agents for MRI. A fast Spin Echo (FSE) pulse sequence was used to acquire T_2-weighted in-vivo MRI images of the rat brain. MCFO nanoparticles coated with chitosan were studied to determine their efficacy. For all the investigated samples, T_2 FSE MR images of rat brains were taken before and after using chitosan-coated MCFO nanoparticles as contrast agents, shown in Figure 4.17. The regions of interest ROI 1 and 2 were marked prior to and during the administration of the contrast agents with x. Before the animals were vaccinated, there were 17818 counts of signal intensity at x = 0 and ROI 1. After the injection of the contrast agent, the signal decreased to 17820, 16578, 10398, 11605, and 13247 counts at 15, 30, 60, 90, and 120 minutes. Following the injection of chitosan-coated MCFO contrast agent, Figure 4.18 shows an average intensity fall of (%) in both the brain and the muscle after 60 minutes. Intensity loss of the T_2 image of the rat brain after injecting chitosan-coated MCFO ferrite nanoparticles ranged from 29.2 - 41.6% in Figure 4.18. Hong et al.[17] registered a 31.7% intensity loss in the T_2 image of a rabbit liver after injecting the aqueous solution of chitosan-coated Fe_3O_4, which supported our result.

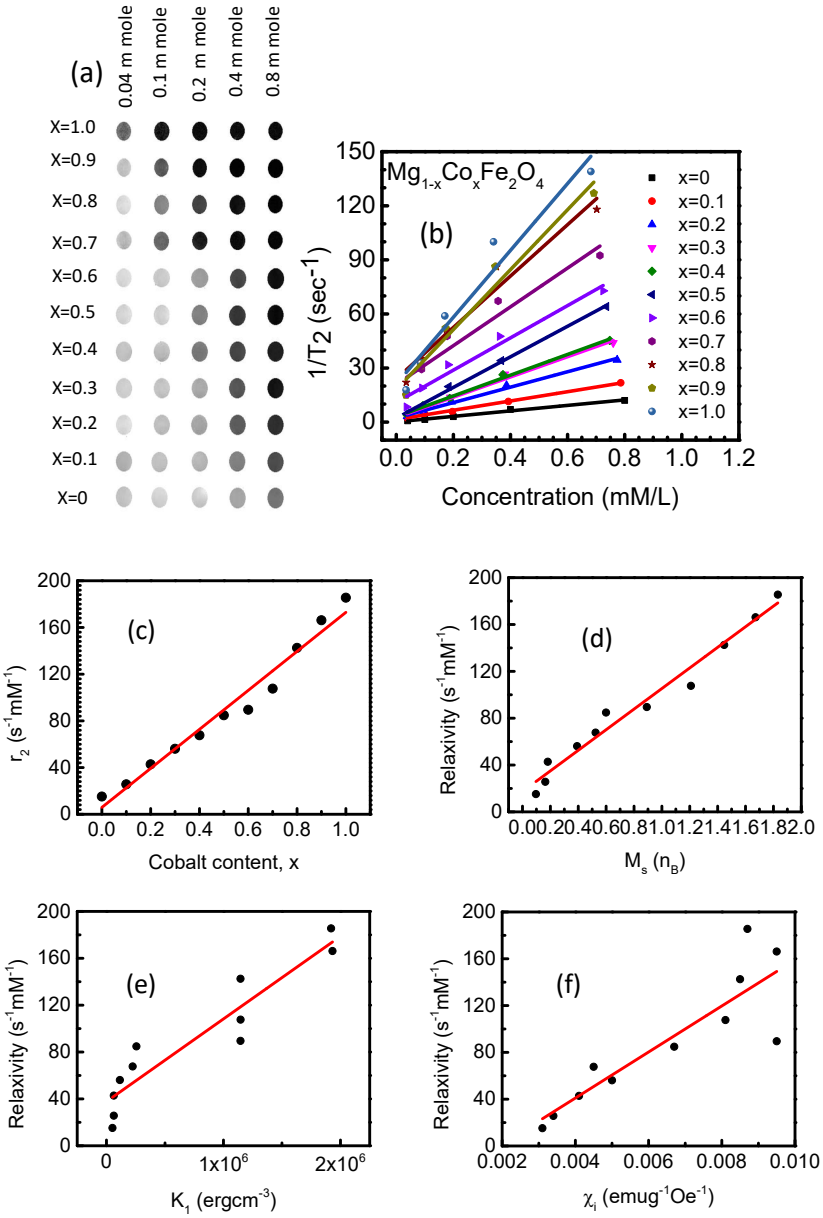

Figure 4.16: We acquired phantom images for chitosan-coated $Mg_{1-x}Co_xFe_2O_4$ ($0 \leq x \leq 1$ with $\Delta x = 0.1$) nanoparticles. TheT2 weighted fast spin-echo (FSE) magnetic resonance images were acquired using the machine of model: Bo = 7T, the repetition time(TR) was 4000ms, slice thickness(THK) was 1.0 mm, and FOV was 40 x 40. We acquired T2 mapping; several echo times(TE) were 7ms,14ms,21ms,28ms,35ms,42 ms, 49 ms, 56 ms, 63 ms, 70 ms, 77 ms, 84 ms, 91 ms, 98 ms, 105ms, and 112ms. (a) Slices for different cobalt content x with concentrations of 0.04, 0.10, 0.20, 0.40, and 0.80 mM in each phantom. (b) concentration dependence of relaxation with the linear fitting, the slope of which provides the values of relaxivity for different values of x, (c) variation of relaxivity with the cobalt content x, (d) with saturation magnetization, (e) with susceptibility, and (f) with the magnetocrystalline anisotropy.

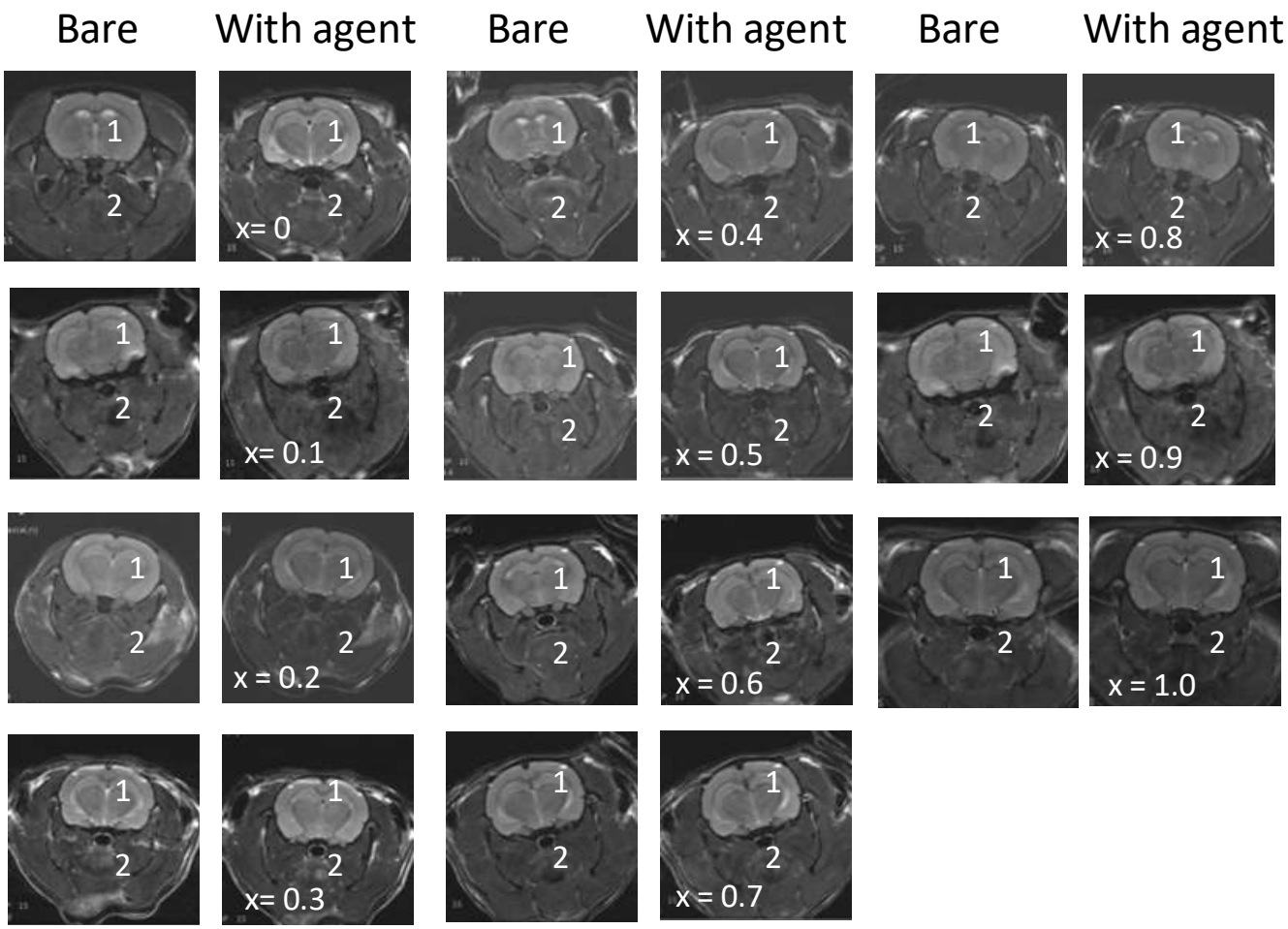

Figure 4.17: The T_2 weighted MRI imaging of the rat brain using the Fast Spin Echo (FSE) pulse sequence. Some representative T_2 FSE MR images of rat brains before and after administering the chitosan-coated $Mg_{1-x}Co_xFe_2O_4$ nanoparticles as contrast agents. We marked the region of interest (ROI) 1 and 2 to observe the (%) intensity fall before and after administering the contrast agents of all the values of x.

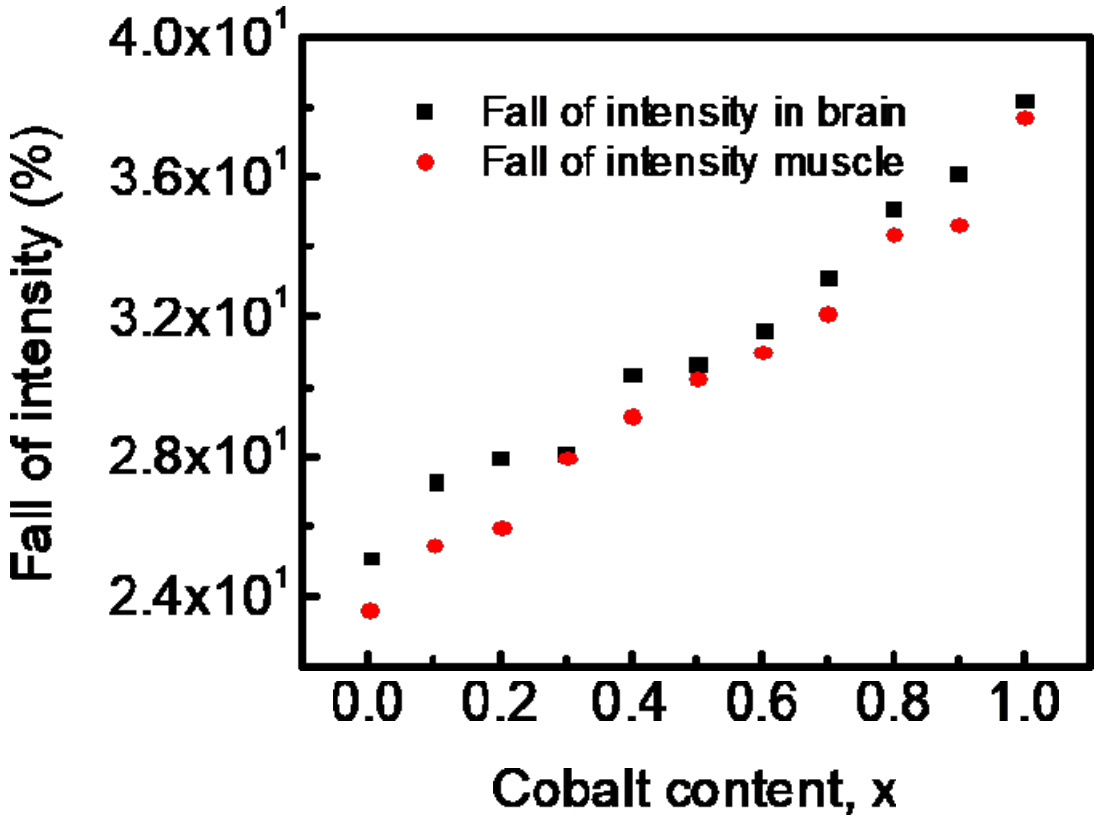

Figure 4.18: Variation of fall of intensity with cobalt content at brain and muscle of a rat without and with chitosan-coated $Mg_{1-x}Co_xFe_2O_4$ nanoparticles agent.

CHAPTER 5: SIZE AND COMPOSITION DEPENDENCE OF LOCAL MAGNETIC HYPERTHERMIA OF CHITOSAN-MCFO NANOHYBRID

In this chapter, the MCFO materials' particle sizes varied by annealing them at different temperatures. Then, the structural and magnetic properties of uncoated and chitosan-coated MCFO particles with varying particle sizes were investigated. Finally, this study examined how particle size affects the hyperthermia and MRI properties of chitosan-coated MCFO materials.

5.1. Structural Characterizations

5.1.1. The X-ray Diffraction (XRD)

The XRD spectrum of our investigated MCFO annealed at 200^{o}C, 400^{o}C, 600^{o}C, and 800^{o}C are presented in Figure 5.1. The observed peaks are the characteristic peaks of the single-phase spinel structure with space group Fd-3m[44,46]. A broad diffused (311) peak was observed for the MCFO ferrite nanoparticles with Co^{2+} content $0 \leq x \leq 0.4$ annealed at 200^{o}C and 400^{o}C. The peaks become narrower with the increase in both Co^{2+} content and annealing temperature. The intensity of the (311) peaks becomes sharper, and their positions are shifted towards the lower value with an increase in $Co2^{+}$ content and annealing temperature, ensuring their high degree of crystallinity[14]. The particle sizes were calculated using Debye-Scherrer's formula in equation (3.34)[224]. Figure 5.2 (a) represents the variation of particle size with Co^{2+} content of MCFO ferrite nanoparticles annealed at 200^{o}C, 400^{o}C, 600^{o}C, and 800^{o}C. Particle size increases with increases in cobalt content and annealing temperature. The observed lattice parameter for each plane was calculated using Bragg's law presented in equation (2.32)[224]. The precise values of the lattice parameters were determined using the Nelson-Riley function shown in equation (2.33)

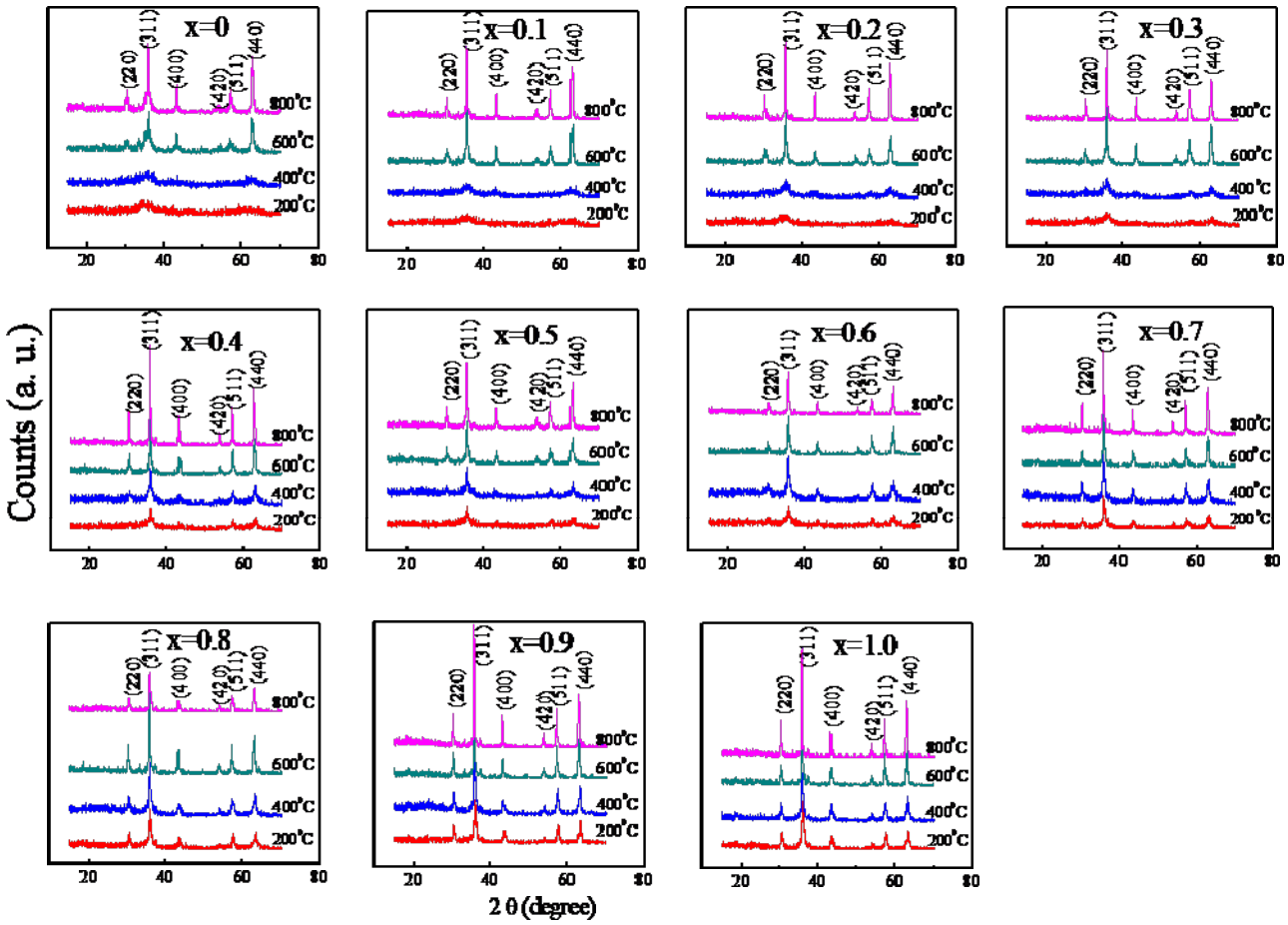

Figure 5.1: X-ray diffraction pattern of $Mg_{1-x}Co_xFe_2O_4$ nanoparticles annealed at 200°C, 400°C, 600°C, and 800°C.

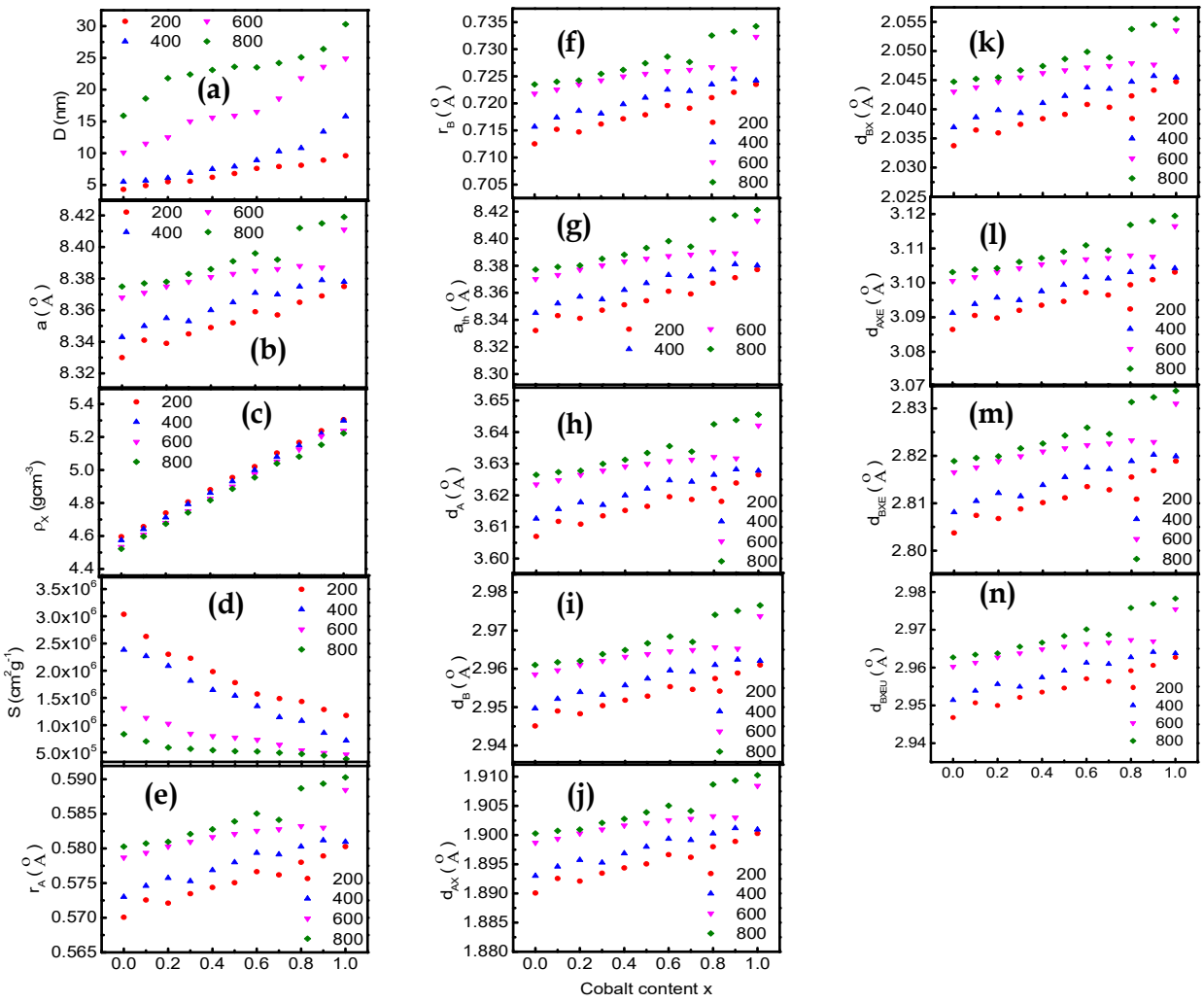

Figure 5.2: Variation of (a) the particle size D, (b) the observed lattice parameter a, (c) the X-ray density, (d) the specific surface area of the particles S, (e) the ionic radius of the tetrahedral site r_A, (f) the ionic radius of octahedral site r_B, (g) the theoretical lattice parameter a_{th}, (h) the hopping length for tetrahedral site d_A, (i) the hopping length for octahedral site d_B, (j) the bond length of tetrahedral site d_{AX}, (k) the bond length of octahedral site d_{BX}, (l) the tetrahedral edge d_{AXE}, (m) the shared octahedral edge d_{BXE}, and (n) the unshared octahedral edge d_{BXEU} of $Mg_{1-x}Co_xFe_2O_4$ nanoparticles annealed at 200°C, 400°C, 600°C, and 800°C.

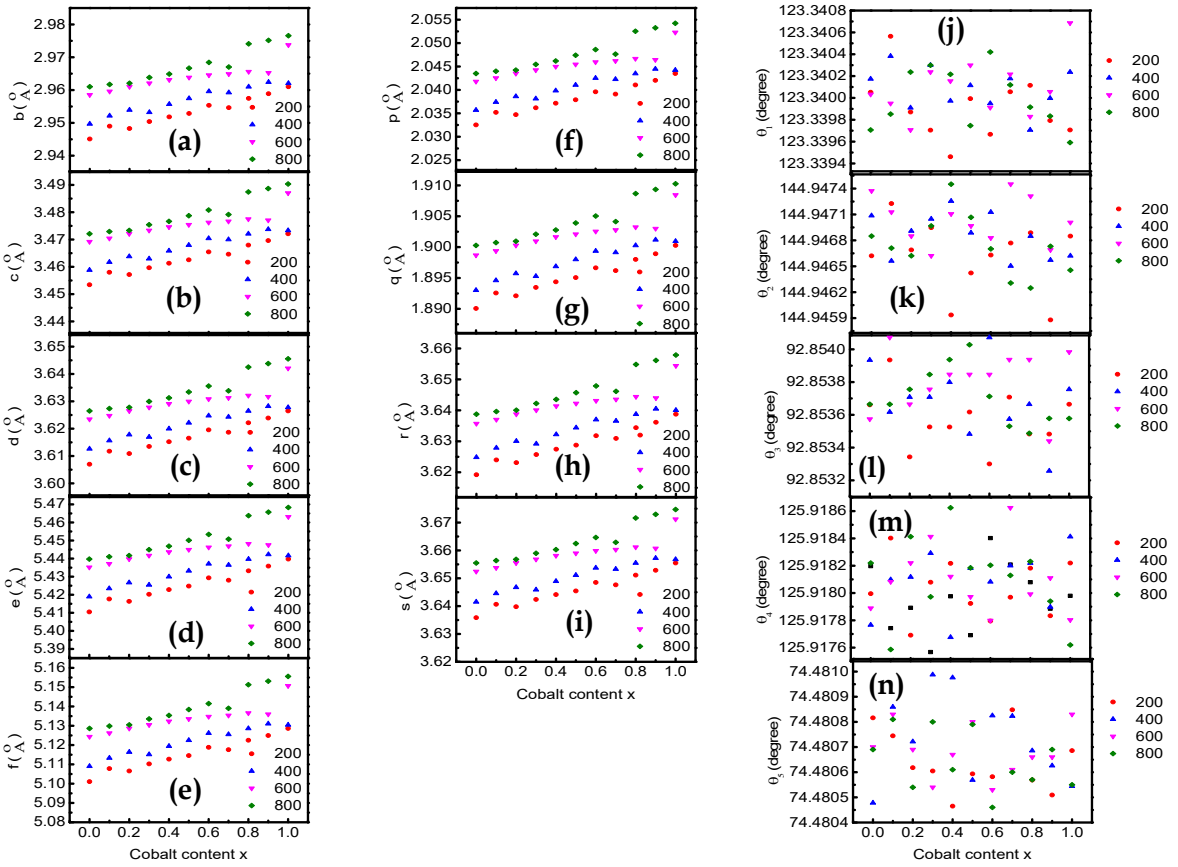

Figure 5.3: Variation of (a-e) the interionic distances between the cations, (f-i) the cation-anion distance, and (j-n) the bond angle of $Mg_{1-x}Co_xFe_2O_4$ nanoparticles annealed at 200°C, 400°C, 600°C, and 800°C.

The values of the lattice constant, a for each plane are plotted as a function of $F(\theta)$, and the actual value of the lattice parameter was found from the intercept of the linear extrapolation of a_0 vs. $F(\theta)$ lines[225,226]. Figure 5.2 (b) represents the variation of the observed lattice parameter with Co^{2+} content of MCFO nanoparticles annealed at 200°C, 400°C, 600°C, and 800°C. The lattice parameter increases linearly with the increase in Co^{2+} content and annealing temperature, indicating that the lattice parameter's dependence on Co^{2+} content and annealing temperature follows Vegard's Law[227,228]. The lattice parameter increases with an increase in Co^{2+} content because the ionic radius of Mg^{2+} (0.065 nm) ion is smaller than that of Co^{2+} (0.072 nm) ion[182]. The lattice parameter also increases with an increase in annealing temperature because grain size increases with an increase in annealing temperature. The spinel ferrite nanoparticles' X-ray density (d_x) is calculated using equation (3.5)[144]. Figure 5.2 (c) represents the variation of X-ray density with Co^{2+} content of MCFO nanoparticles annealed at 200°C, 400°C, 600°C, and 800°C. The X-ray density increases with an increase in Co^{2+} content and annealing temperature. The specific surface area of the particles (S), the radius of the tetrahedral site (r_A), the radius of the octahedral site (r_B), the theoretical lattice parameter (a_{th}), the hopping length for the tetrahedral site (d_A), hopping length for the octahedral site (d_B), the tetrahedral bond length (d_{AX}) and the octahedral bond length (d_{BX}), the tetrahedral edge (d_{AXE}), the shared and unshared octahedral edge (d_{BXE} and d_{BXEU}) for cubic spinel ferrite nanoparticles are calculated using equation 3.6 to 3.16[144,229,230]. Figure 5.2 (d)-(n) shows the variation of S, r_A, r_B, d_A, d_B, d_{AX}, d_{BX},d_{AXE}, d_{BXE}, and d_{BXEU} with Co^{2+} content of MCFO nanoparticles annealed at 200°C, 400°C, 600°C, and 800°C. The value of S decreases with an increase in Co^{2+} content and annealing temperature because particle size increases with an increase in Co^{2+} content and annealing temperature. The

value of r_A, r_B, d_A, d_B, d_{AX}, d_{BX}, d_{AXE}, d_{BXE}, and d_{BXEU} increases with an increase in Co^{2+} content and annealing temperature because particle size increases with an increase in Co^{2+} content and annealing temperature, which is associated with cation redistribution on grain size growth.

The interionic distances between cations $b, c, d, e,$ and f were obtained using the equation (3.17) to (3.21). The spaces between cations and anions $p,\ q,\ r,$ and s were found using the equations (3.22) to (3.25). The cation-cation distances $b, c, d, e,$and$f$ with particle size are plotted in Fig 5.3 (a)-(e) and the cation-anion distances $p, q, r,$ and s are plotted with particle size in Fig 5.3 (f)-(i), and the bond angles θ_1, θ_2, θ_3, θ_4, and θ_5 with the particle size plotted in Fig. 5.3 (j)-(n)[144,229,230]. The cation-cation distances and cation-anion distances increase with an increase in Co^{2+} content and annealing temperature because the ionic radius of Co^{2+}(0.072 nm) is higher than that of Mg^{2+}(0.065 nm)[182]. The bond angles θ_1, θ_2, θ_3, θ_4, and θ_5 decreases with increasing Co^{2+} content.

5.1.2. Transmission electron microscopy (TEM)

Fig. 5.4 (a-b) shows TEM images of MCFO nanoparticles annealing at 200°C, 400°C, 600°C, and 800°C temperatures. Semi-spherical particles were observed in the TEM images. The figure indicates that particle size and degree of crystallinity increase with increasing cobalt content x. The figure also shows that particle size rises with increasing annealing temperature. The particle size is obtained from the histogram of the size distribution, which follows a log-normal distribution.

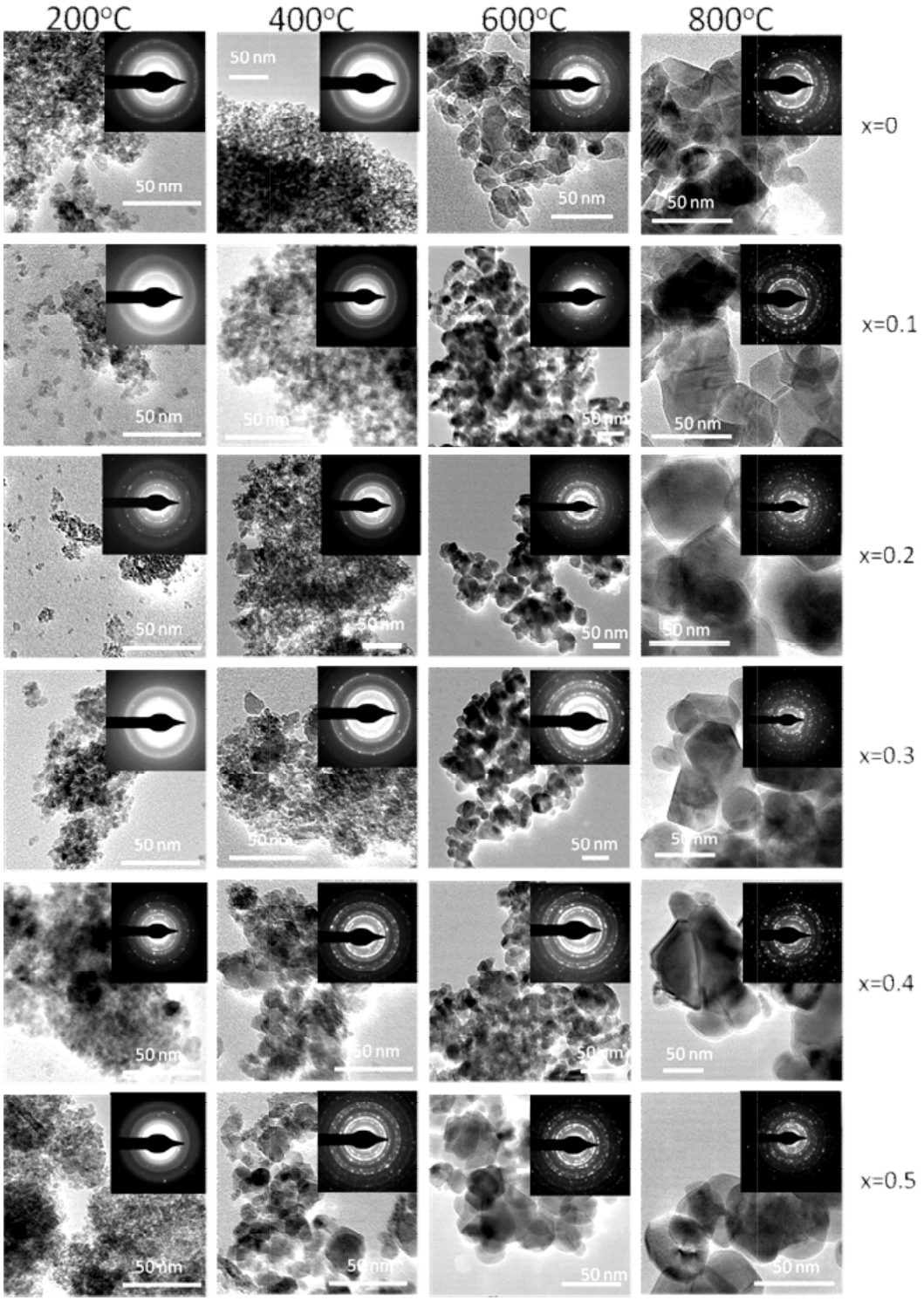

Figure 5.4 (a): TEM image of $Mg_{1-x}Co_xFe_2O_4$ nanoparticle ($0 \leq \Delta x \leq 0.5$) annealed at 200°C, 400°C, 600°C, and 800°C. Particle size increases with increasing cobalt content x and annealing temperature.

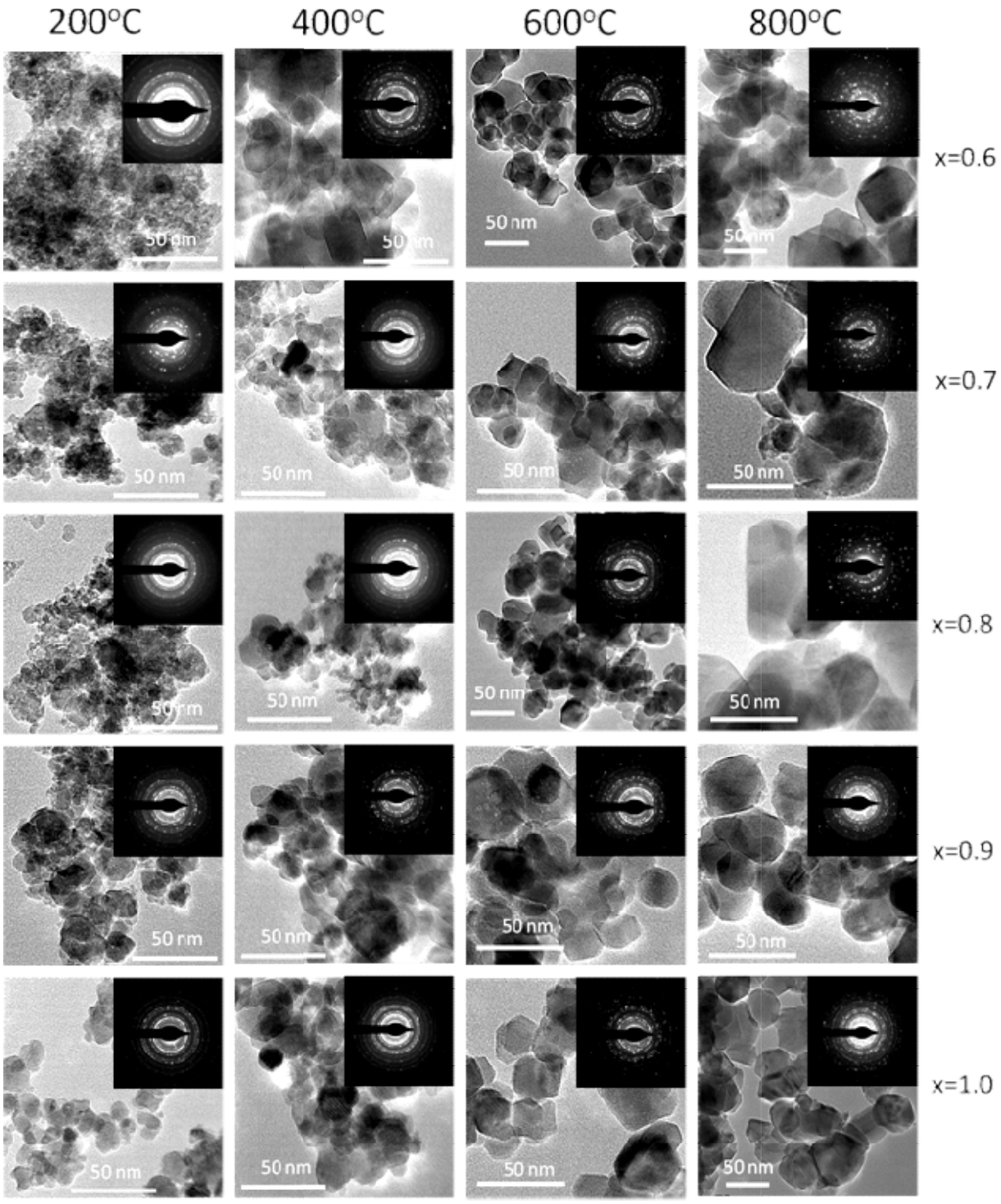

Figure 5.4 (b): TEM image of $Mg_{1-x}Co_xFe_2O_4$ nanoparticle ($0.6 \leq \Delta x \leq 1.0$) annealed at 200°C, 400°C, 600°C, and 800°C. Particle size increases with increasing cobalt content x and annealing temperature.

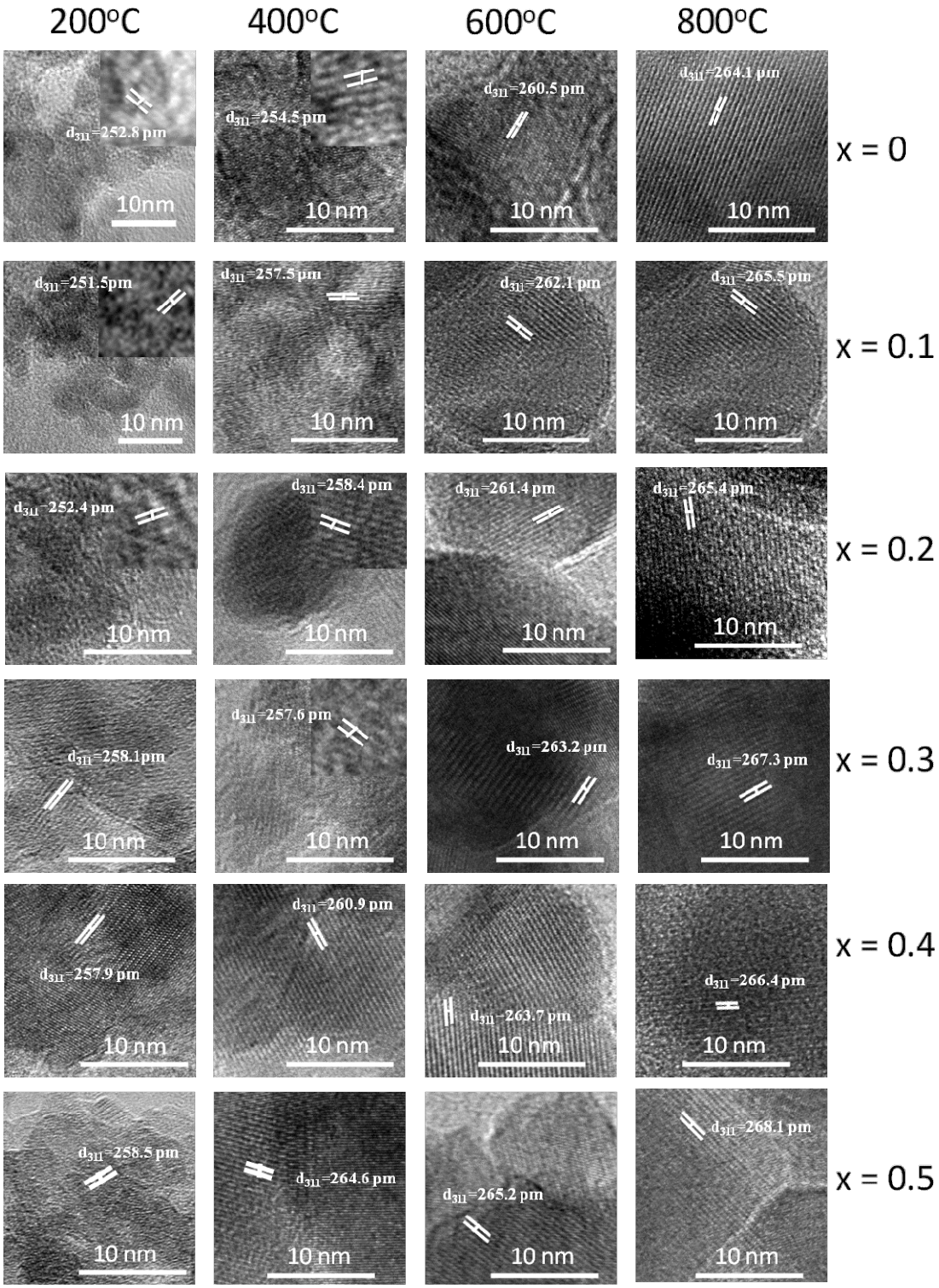

Figure 5.4 (c): HTEM image of $Mg_{1-x}Co_xFe_2O_4$ nanoparticle annealed at 200°C, 400°C, 600°C, and 800°C.

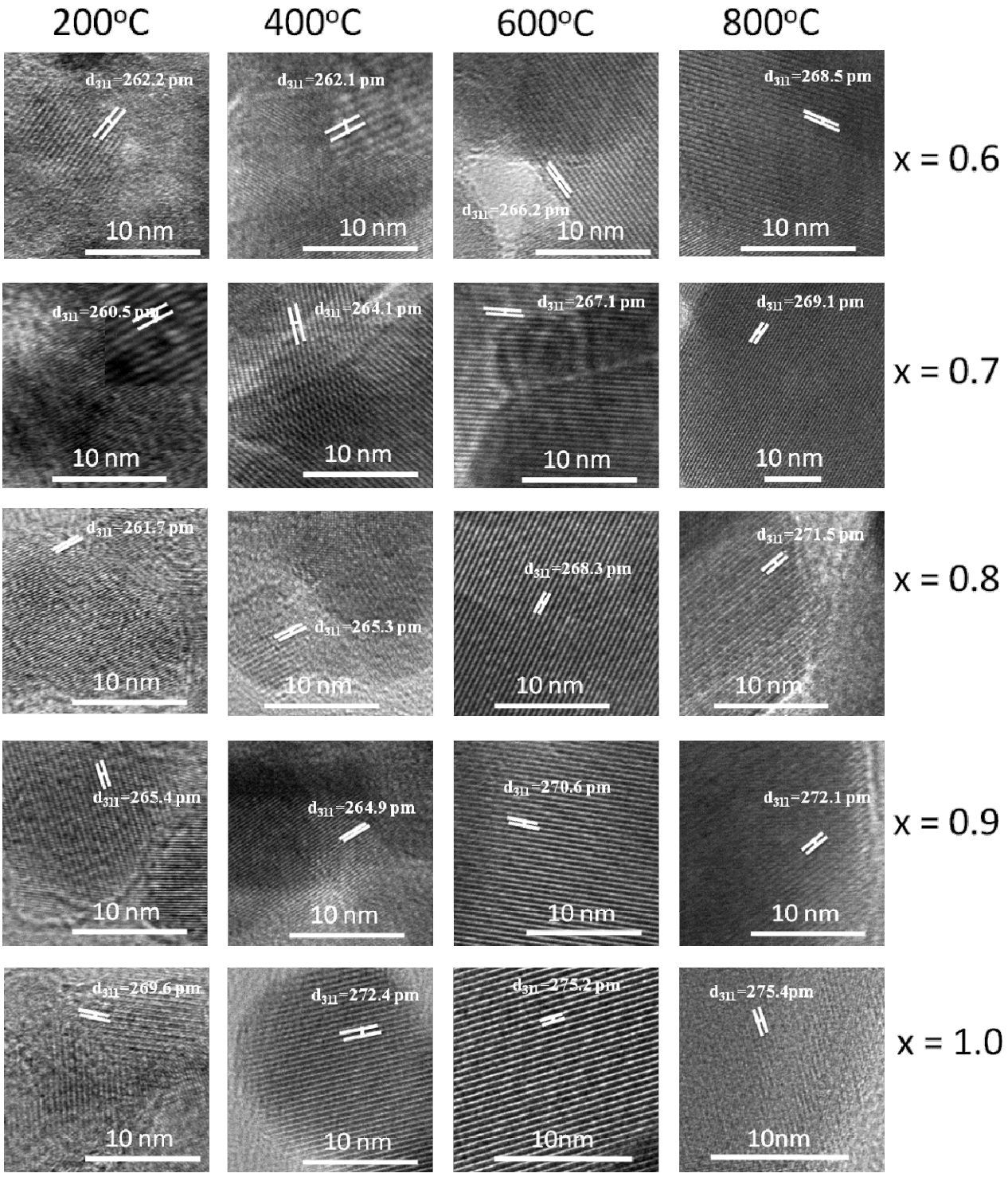

Figure 5.4 (d): HTEM image of $Mg_{1-x}Co_xFe_2O_4$ nanoparticle (x=0.1, 0.3, 0.5, 0.7, and 0.9) annealed at different temperature. Particle size increases with increasing cobalt content x and annealing temperature.

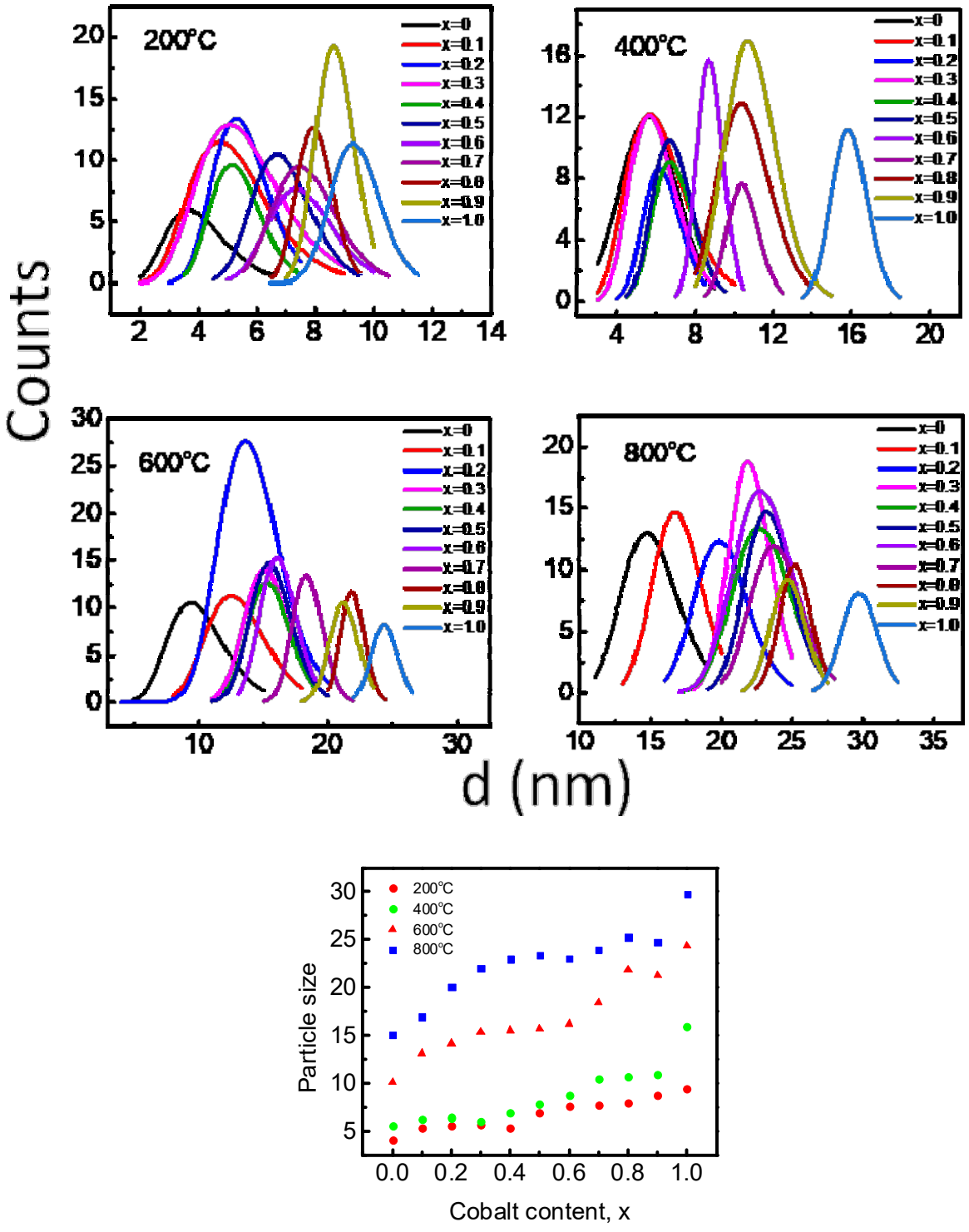

Figure 5.4 (e): A graph of the lognormal distribution of $Mg_{1-x}Co_xFe_2O_4$nanoparticle annealed at 200°C, 400°C, 600°C, and 800°C and variations of particle size with cobalt content. Particle size increases with increasing cobalt content and annealing temperature.

Particles are generally agglomerated for samples at 200°C annealing temperature due to magnetic dipole interactions between ferrite nanoparticles to reduce surface energy. Increasing the annealing temperature decreases dipole interactions, resulting in less aggregation[183,188,231]. The SAED patterns of MCFO nanoparticles are shown in the right corner of figure-5.4 (a-b). An intense Debye circle in the SAED pattern indicates a nanocrystalline structure with higher crystallinity. In the SAED pattern, the highest intensity plane (311), along with the other planes (220), (400), (420), (511), and (440), are found. The SAED pattern d_{hkl} values were determined using Velox software, and the diffractograms were indexed accordingly[43,186,187,232–234]. Figure-5.4 (c-d) shows HRTEM images of MCFO nanoparticles heated at 200°C, 400°C, 600°C, and 800°C. HRTEM images show all investigated samples are nanocrystalline, with crystallinity increasing as cobalt concentration and heating temperature increase. More prominent lattice fringes in the HRTEM image were observed in materials with higher cobalt content and heat treatment temperature. It is because of the higher degree of crystallinity with increased cobalt content and processing temperature. Figure-5.4(e) shows the lognormal distribution of MCFO nanoparticles. This study shows particle size increases when cobalt content and annealing temperature increase. Figure-5.4(f) depicts the variation in particle size with the cobalt content of the sample heated at 200°C, 400°C, 600°C, and 800°C. The figure also suggests particle size increases with increasing cobalt content and annealing temperature. The particle size observed in this study is similar to that in the previous study based on XRD analysis.

5.1.3. Raman spectroscopy

For further structural investigation, we employed Raman spectroscopy of MCFO nanoparticles annealed at 200°C, 400°C, 600°C, and 800°C to identify several vibrational modes. Fig. 5.5 (a)

shows the Fig. 5.5 (a) shows the Raman spectra of MCFO nanoparticles annealed at 200°C, 400°C, 600°C, and 800°C in the range of 190–1000 cm^{-1} at ambient temperature. It was well established by the literature that MCFO ferrites have a partially inverse spinel structure of the $Fd\bar{3}m$ space group. The vibrational modes associated with this space group are A_{1g}(R), E_g(R), F_{1g}, $3F_{2g}$(R), $2A_{2u}$, $2E_u$, $4F_{1u}$(IR), and 2 F_{2u}. The notation R denotes vibrational modes active in the Raman regime, IR denotes vibrational modes active in the infrared regime, and the other modes are silent. The Raman spectrum should therefore contain the Raman active modes A1g, E_g, F_{2g}(3), F_{2g}(2), and F_{2g}(1)[53,206,235]. Figure 5.5 (b-e) illustrates the visible Raman modes of the studied samples after deconvolution and Gaussian fitting of the whole spectra at different compositions and annealing temperatures. After background subtractions and deconvolution, the Gaussian function produced the most accurate fit between experimental and theoretical data. The A_{1g} modes are associated with symmetric stretching of MeO_4 (Me stands for Co and/or Mg) and FeO_4 at the A-site. The E_g modes represent oxygen bending concerning Fe at the B-site. The F_{2g}(3) modes represent oxygen's antisymmetric bending for Fe, the F_{2g}(2) modes describe Fe's asymmetric stretching with O. The F_{2g}(1) modes demonstrate the complete translational motion of Fe and O. The Raman peaks in the region of 660–720 cm^{-1} indicate the vibrational modes of the A-site, and the Raman peaks in the region of 460–660 cm^{-1} represent the vibrational modes of the B-site of the ferrites[53,184,206,207,235]. Figure 5.5 (f-i) depicts the variations in the area integrals with the cobalt concentration x of MCFO nanoparticles annealed at 200°C, 400°C, 600°C, and 800°C. These integrals were acquired by Gaussian fitting A_{1g}, E_g, F_{2g}(3), F_{2g}(2), and F_{2g}(1) peaks allocated to the Raman spectra, as shown in Figure 5.5 (b-e). Figure 5.5 (f) exhibits that for the annealing temperature of 200°C, i.e. for the particle size of 4.3-9.6 nm, the area integral for A_{1g} (i.e., A-site occupancy for both Fe and Me) is the largest

for $MgFe_2O_4$. With the increase of Co, A-site occupancy of both Me and Fe decrease and B-site occupancy represented by $F_{2g}(2)$ increase, where Me represents Mg and Co and Fe for iron. This shows that Mg-rich compositions prefer normal spinel structure for the particle size range of 4.3-9.6 nm. In contrast, cobalt-rich compositions show a preference for inverse spinel structure. The variation of the area integral of other peaks, E_g, $F_{2g}(1)$ and $F_{2g}(3)$ are almost nonvariant, which shows that the site occupancies of the ions representing these peaks with the composition variation do not change considerably.

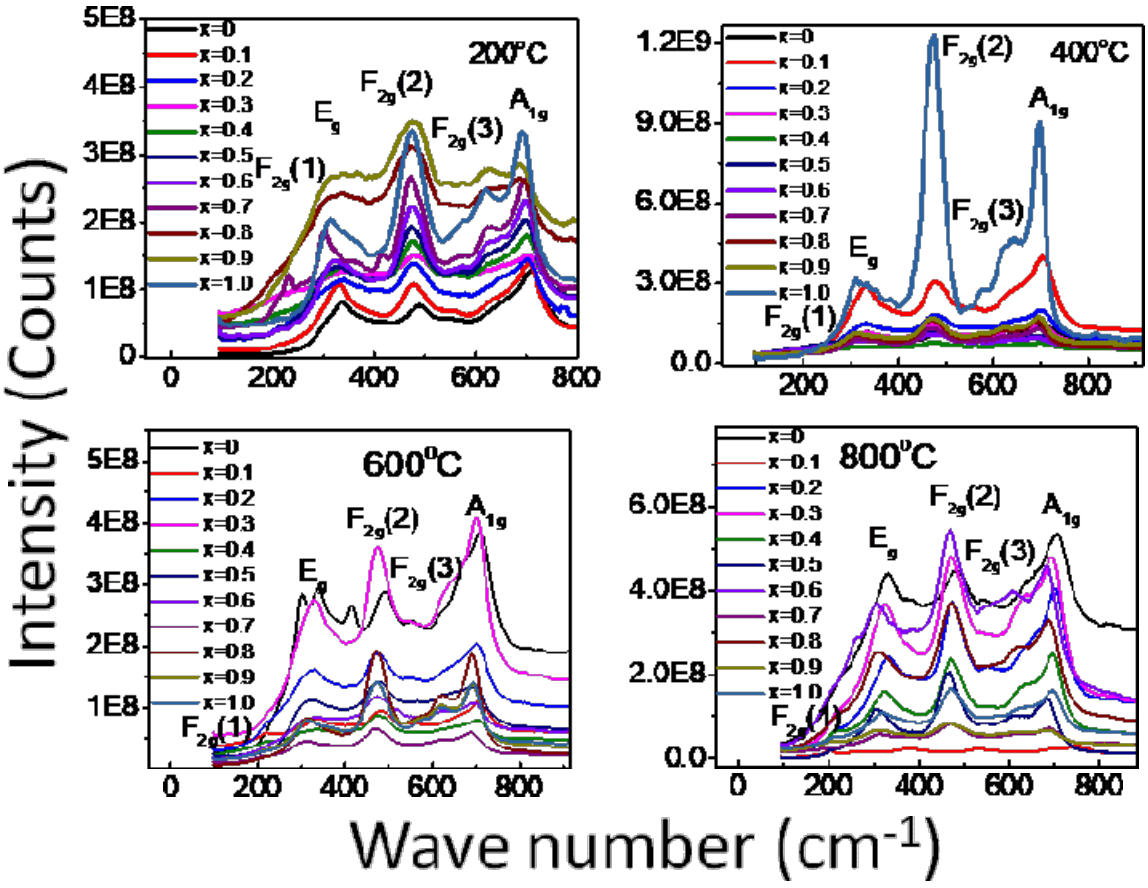

Figure 5.5 (a): Room temperature Raman spectra of $Mg_{1-x}Co_xFe_2O_4$nanoparticles annealed at 200°C, 400°C, 600°C, and 800°C in the range of 190–1000 cm^{-1} usingthe pelletized solid samples. Five Raman active modes A_{1g}, E_g, $F_{2g}(1)$,$F_{2g}(2)$, and $F_{2g}(3)$ are assigned in the Raman spectra.

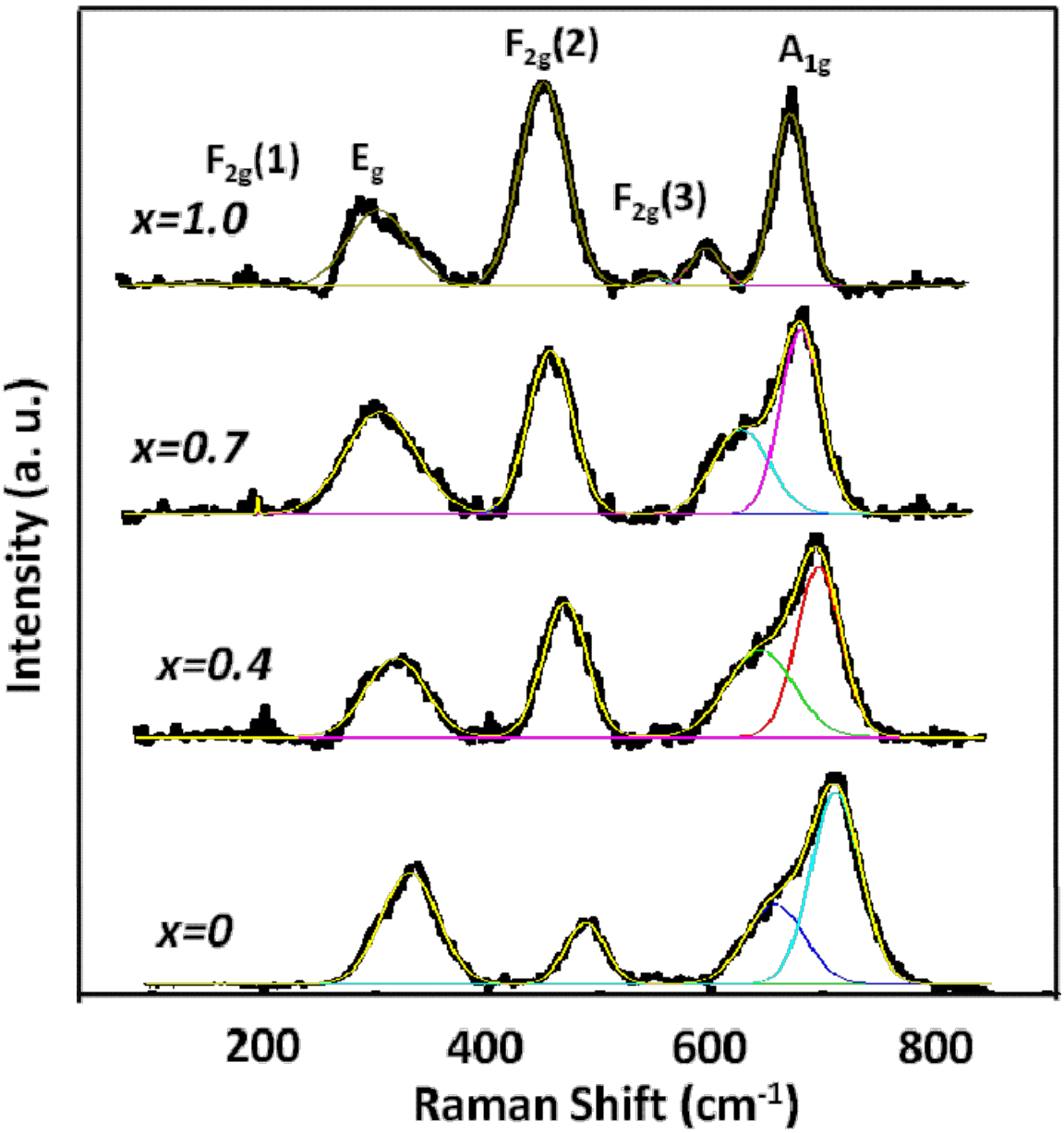

Figure 5.5 (b): Representative best fitting of the Raman spectra of $Mg_{1-x}Co_xFe_2O_4$ nanoparticles annealed at 200°C using the Gaussian function after background subtraction and deconvolution.

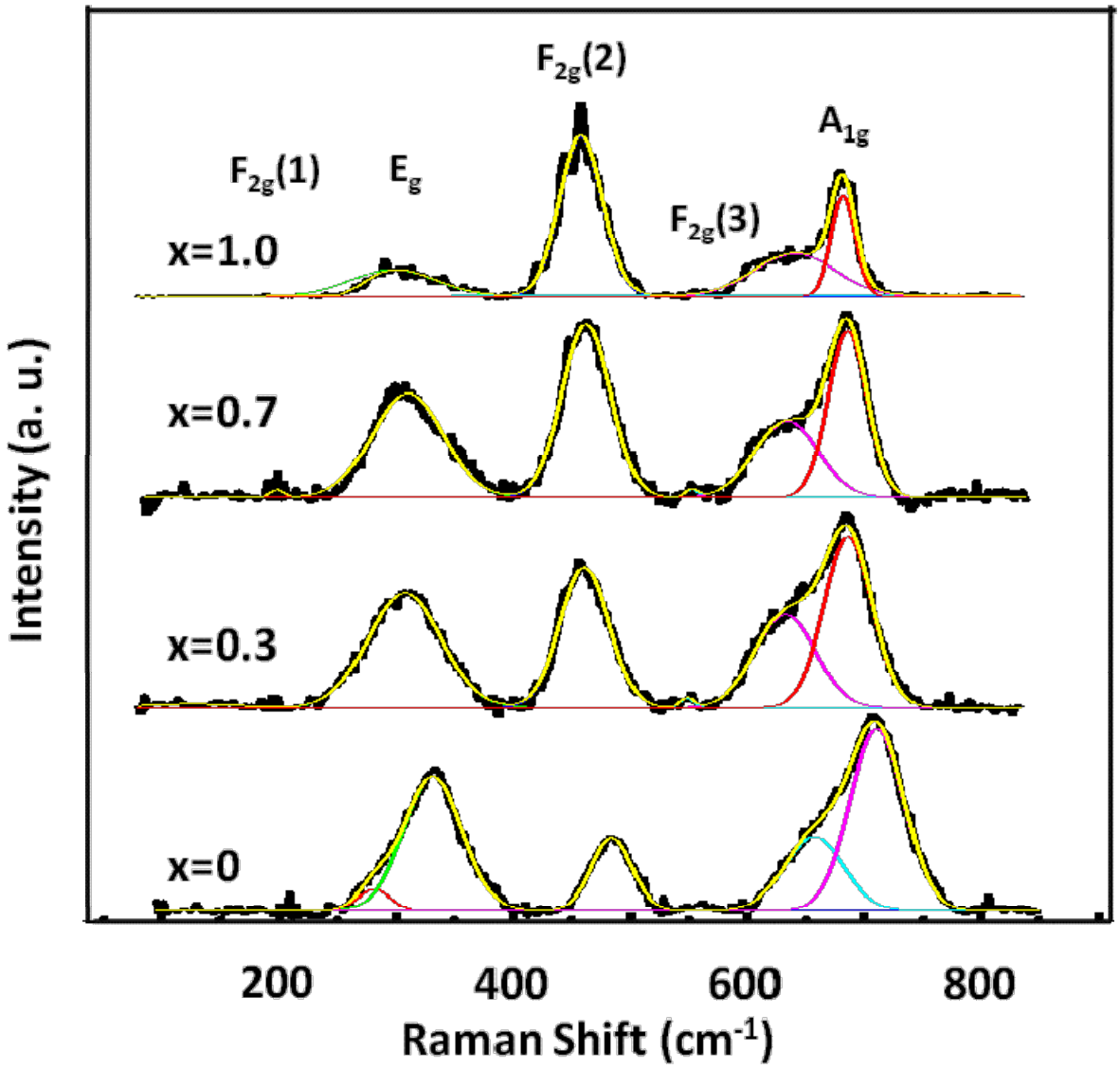

Figure 5.5(c): Representative best fitting of the Raman spectra of $Mg_{1-x}Co_xFe_2O_4$ nanoparticles annealed at 400°C using the Gaussian function after background subtraction and deconvolution.

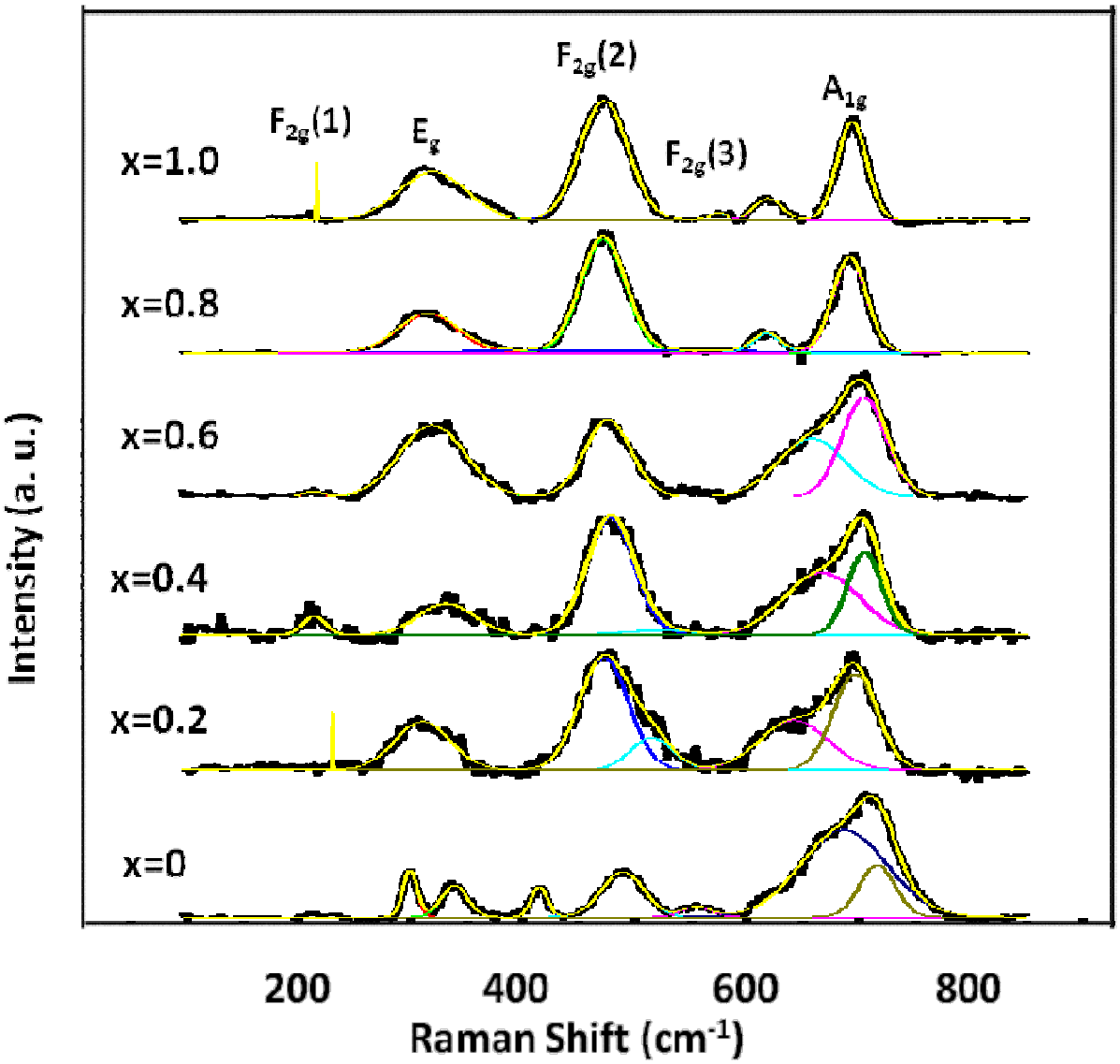

Figure 5.5 (d): Representative best fitting of the Raman spectra of $Mg_{1-x}Co_xFe_2O_4$ nanoparticles annealed at 600°C using the Gaussian function after background subtraction and deconvolution.

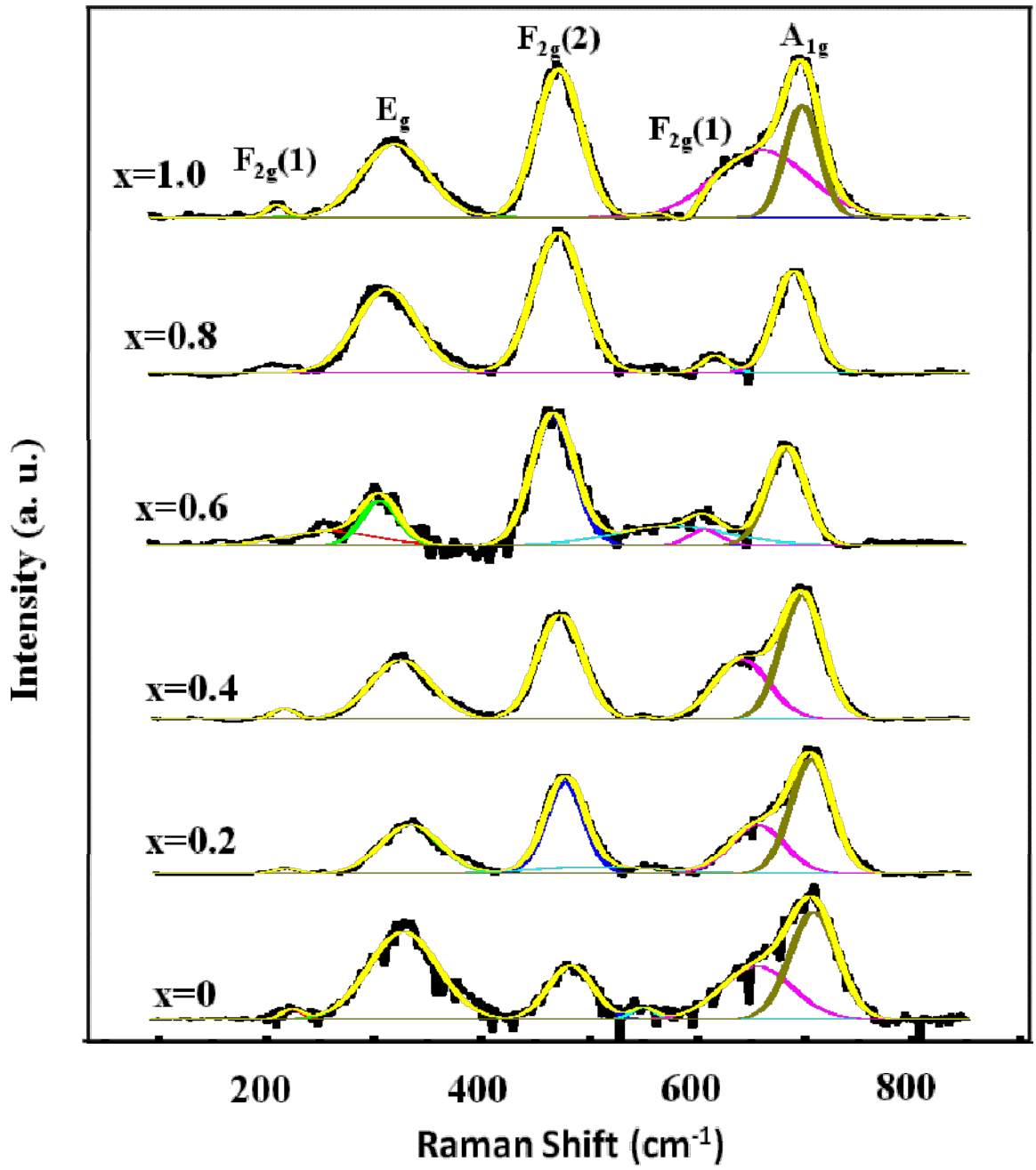

Figure 5.5 (e): Representative best fitting of the Raman spectra of $Mg_{1-x}Co_xFe_2O_4$ nanoparticles annealed at 800°C using the Gaussian function after background subtraction and deconvolution.

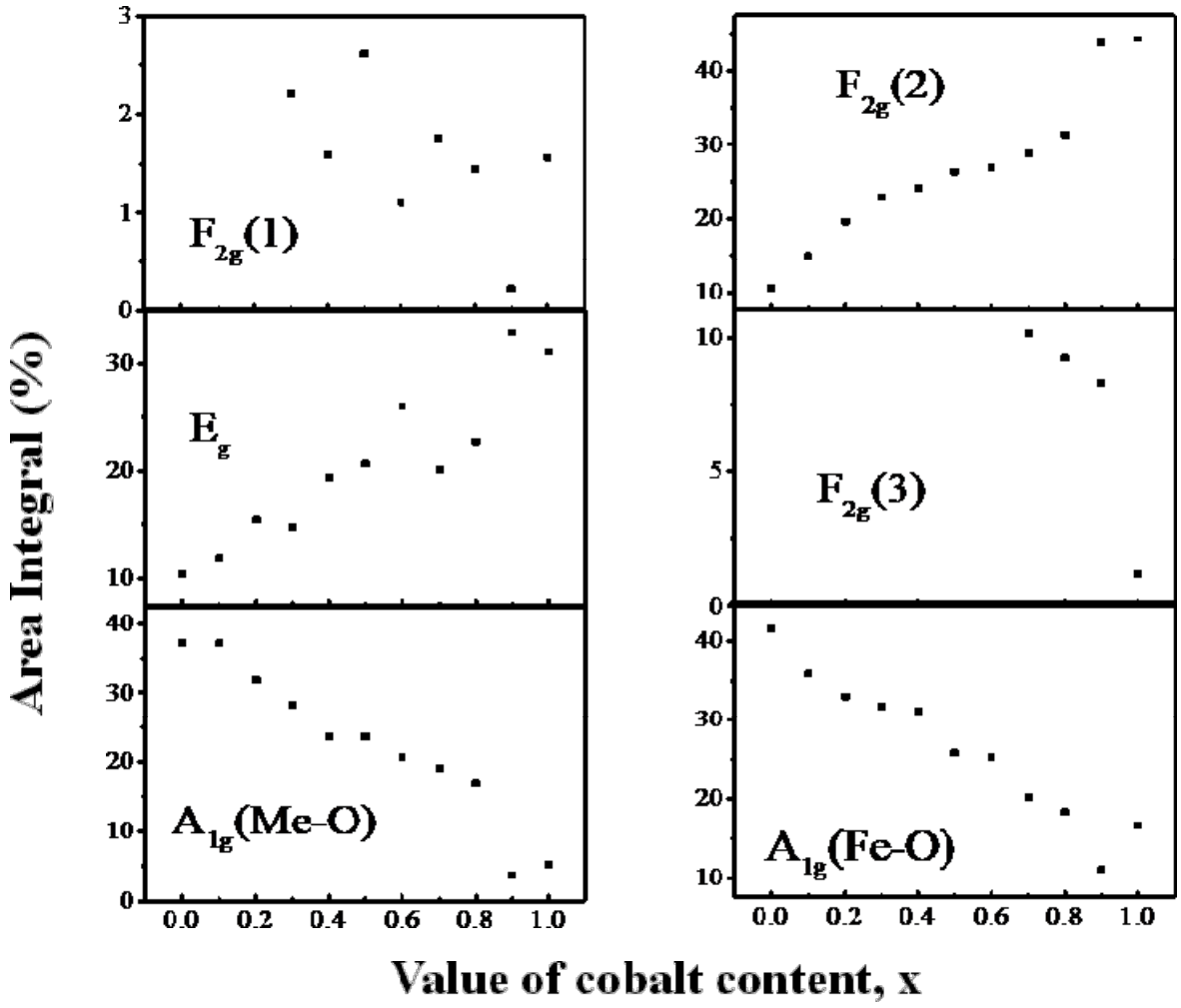

Figure 5.5 (f): Variation of area integral with Co concentration x of the A_{1g}, E_g, $F_{2g}(1)$, $F_{2g}(2)$, and $F_{2g}(3)$ peaks assigned to the Raman spectra of $Mg_{1-x}Co_xFe_2O_4$nanoparticles annealed at 200°C obtained by Gaussian fitting and deconvolution.

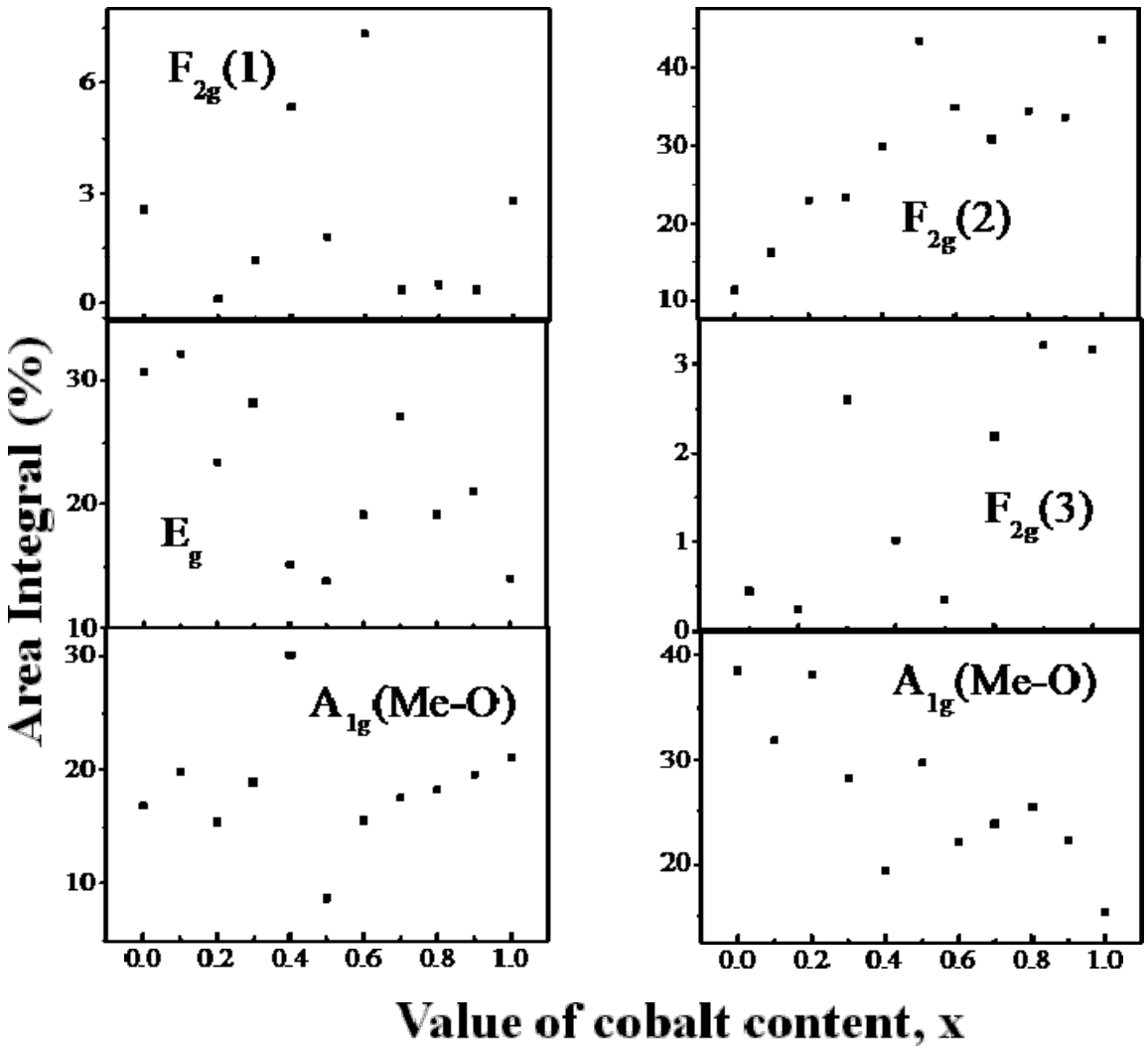

Figure 5.5 (g): Variation of area integral with Co concentration x of the A_{1g}, E_g,$F_{2g}(1)$, $F_{2g}(2)$, and $F_{2g}(3)$ peaks assigned to the Raman spectra of $Mg_{1-x}Co_xFe_2O_4$nanoparticles annealed at 400^{o}C obtained by Gaussian fitting and deconvolution.

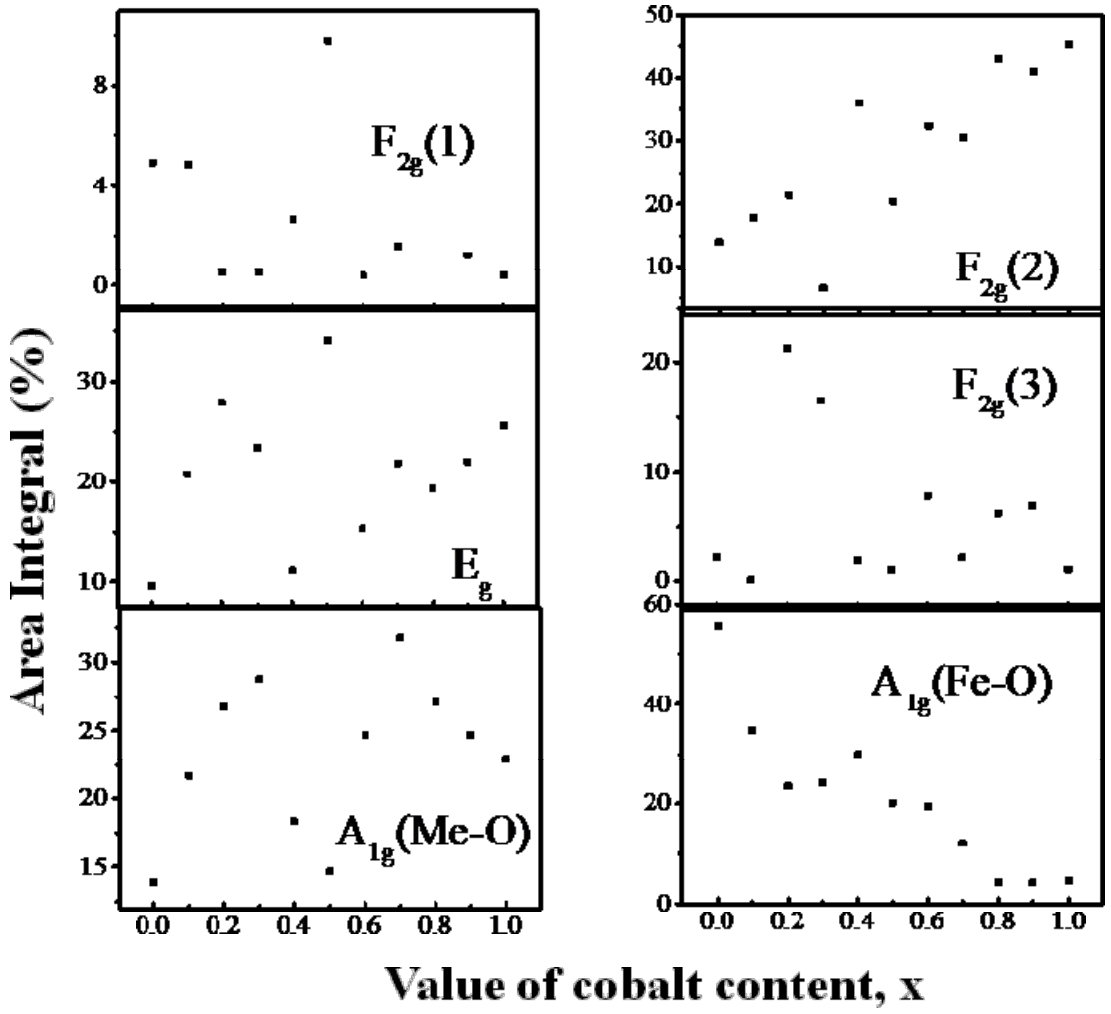

Figure 5.5 (h): Variation of area integral with Co concentration x of the A_{1g}, E_g, $F_{2g}(1)$, $F_{2g}(2)$, and $F_{2g}(3)$ peaks assigned to the Raman spectra of $Mg_{1-x}Co_xFe_2O_4$nanoparticles annealed at 600^{o}C obtained by Gaussian fitting and deconvolution.

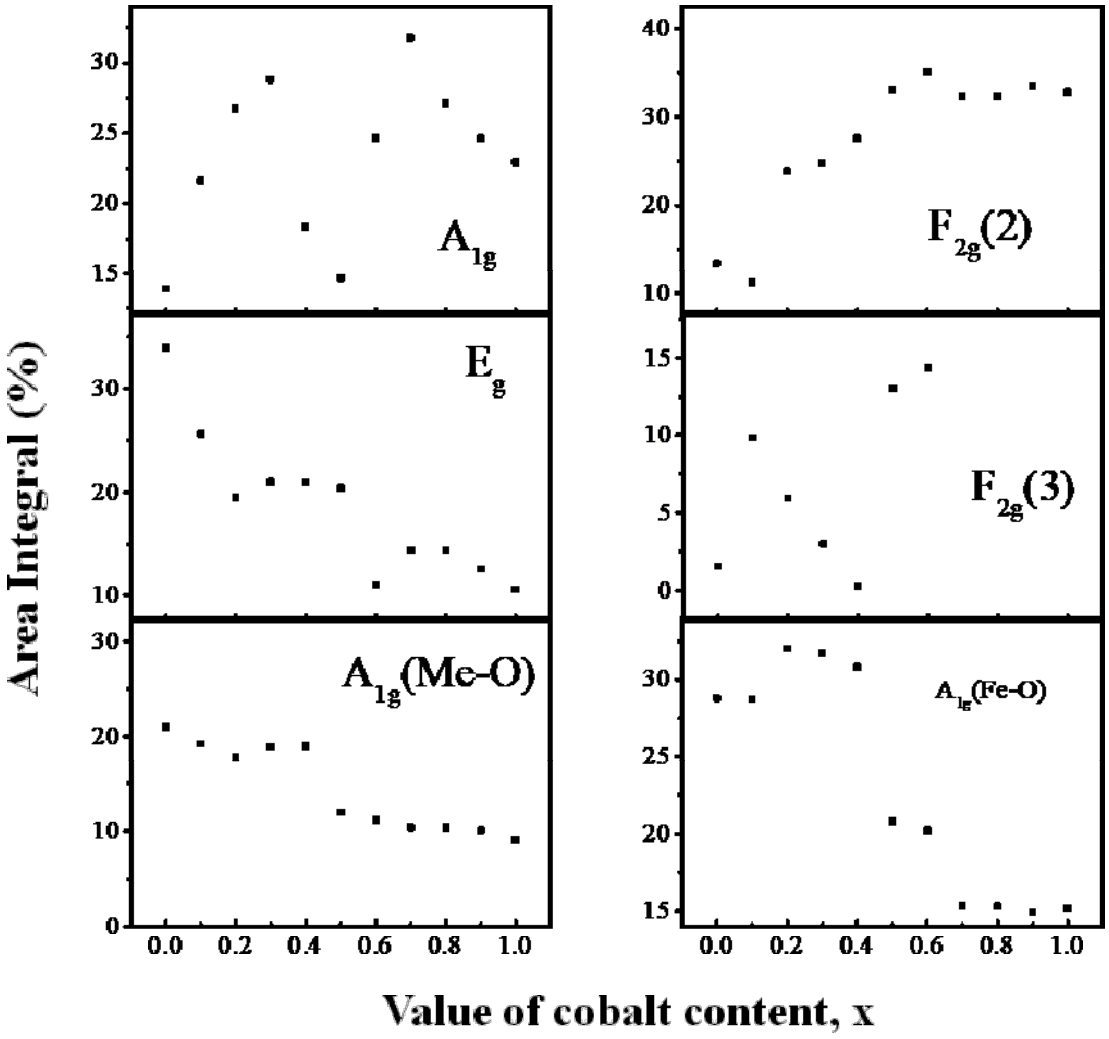

Figure 5.5 (i): Variation of area integral with Co concentration x of the A_{1g}, E_g, $F_{2g}(1)$, $F_{2g}(2)$, and $F_{2g}(3)$ peaks assigned to the Raman spectra of $Mg_{1-x}Co_xFe_2O_4$nanoparticles annealed at 800^{o}C obtained by Gaussian fitting and deconvolution.

Table 5.1: Wavenumbers of the five Raman active modes A_{1g}, E_g, $F_{2g}(1)$,$F_{2g}(2)$, and $F_{2g}(3)$ of $Mg_{1-x}Co_xFe_2O_4$ nanoparticles annealed at 200°C assigned to the Raman spectra.

x	Main Raman mode peak energy (cm-1)					
	$F_{2g}(1)$	E_g	$F_{2g}(2)$	$F_{2g}(3)$	A_{1g} (Me-O)	A_{1g}(Fe-O)
0	-	330	487	-	656	711
0.1	-	327	478	-	673	707
0.2	-	327	477	-	675	706
0.3	210	341	480	-	674	706
0.4	208	326	476	-	651	703
0.5	207	325	475	-	653	700
0.6	214	323	475	-	645	698
0.7	181	323	474	553	642	697
0.8	174	323	472	-	638	692
0.9	146	322	474	545	621	691
1	164	325	473	570	618	690

Table 5.2: Wavenumbers of the five Raman active modes A_{1g}, E_g, $F_{2g}(1)$,$F_{2g}(2)$, and $F_{2g}(3)$ of $Mg_{1-x}Co_xFe_2O_4$ nanoparticles annealed at 400°C assigned to the Raman spectra.

x	Main Raman mode peak energy (cm-1)					
	$F_{2g}(1)$	E_g	$F_{2g}(2)$	$F_{2g}(3)$	A_{1g} (Me-O)	A_{1g}(Fe-O)
0	281	331	484	-	657	711
0.1	-	330	479	-	652	706
0.2	162	333	479	-	645	702
0.3	142	323	476	564	648	702
0.4	214	334	480	581	664	705
0.5	127	336	479	591	653	697
0.6	182	333	476	566	642	695
0.7	208	320	472	563	644	696
0.8	210	320	471	524	640	694
0.9	243	317	473	490	646	697
1	215	319	471	574	618	693

Table 5.3: Wavenumbers of the five Raman active modes A_{1g}, E_g, $F_{2g}(1)$,$F_{2g}(2)$, and $F_{2g}(3)$ of $Mg_{1-x}Co_xFe_2O_4$ nanoparticles annealed at 600°C assigned to the Raman spectra.

x	Main Raman mode peak energy (cm-1)					
	$F_{2g}(1)$	E_g	$F_{2g}(2)$	$F_{2g}(3)$	A_{1g} (Me-O)	A_{1g}(Fe-O)
0	298	338	488	554	686	715
0.1	219	331	481	589	677	712
0.2	213	318	475		657	704
0.3	200	325	466	480	651	702
0.4	213	331	478	519	666	704
0.5	205	317	474	553	650	698
0.6	229	310	472	514	641	696
0.7	212	313	470	507	629	687
0.8		314	471	476	617	691
0.9	198	316	471	535	616	691
1	215	319	471	574	618	693

Table 5.4: Wavenumbers of the five Raman active modes A_{1g}, E_g, $F_{2g}(1)$,$F_{2g}(2)$, and $F_{2g}(3)$ of $Mg_{1-x}Co_xFe_2O_4$ nanoparticles annealed at 800°C assigned to the Raman spectra**.**

x	Main Raman mode peak energy (cm-1)					
	$F_{2g}(1)$	E_g	$F_{2g}(2)$	$F_{2g}(3)$	A_{1g} (Me-O)	A_{1g}(Fe-O)
0	224	337	482	550	655	708
0.1	202	331	479	549	654	707
0.2	216	331	474	505	653	703
0.3	216	329	474	532	653	703
0.4	216	324	472	548	640	697
0.5	204	311	465	486	626	685
0.6	263	309	469	580	609	685
0.7	208	317	471		607	690
0.8	208	317	471		607	690
0.9	206	311	468		626	686
1	206	310	467	579	626	685

For the annealing temperature of 400°C, i.e., particle size in the 5.5-15.8 nm range, the variation of area integral A_{1g} and $F_{2g}(2)$ even becomes more scattered. However, they change perceivably as in Figure 5.5 (g), i.e., with the increase of Co, the spinel structure change from inverse to mixed spinel structure. For the annealing temperature of 600°C, in Figure 5.5(h), i.e., the structure is primarily disordered for the particle size range of 10.1-24.9 nm. However, a decrease of the area integral of A_{1g} for Me ions decreases, and $F_{2g}(2)$ increases, demonstrating that A-site occupancy decreases while B-site occupancies increase. For the annealing temperature of 800°C, however, i.e., for the particle size in the range of 15.9-30.3 nm, site occupancy is almost nonvariant up to x=0.2. Above x=0.2, A-site occupancy decreases, and B-site occupancy increases with the increase of Co, showing that the spinel structure changes from inverse to mixed spinel structure.

Table 5.1-5.4 provides the wavenumbers of the Raman active modes A_{1g}, E_g, $F_{2g}(1)$, $F_{2g}(2)$, and $F_{2g}(3)$ of $Mg_{1-x}Co_xFe_2O_4$nanoparticles annealed at 200°C, 400°C, 600°C, and 800°C obtained from the Raman spectra. For all the samples, the frequencies of A_{1g} vibrational modes decline with an increase in the cobalt content, x, because the heavier cobalt (58.9332 amu) ions replace iron (55.8470 amu) ions or magnesium (24.3050 emu) ions. The frequencies of $F_{2g}(2)$ decrease with increased cobalt content. This is because cobalt (58.9332 amu) ions with higher atomic mass replace magnesium (24.3050 emu). In conclusion, for comparatively smaller particles (particles annealed at 200°C and 400°C have smaller particle sizes than particles annealed at 600°C and 800°C), particles with higher magnesium have a greater degree of normal spinel structure. On the other hand, particles with more cobalt exhibit a more inverse spinel structure. From Figure 5.5 (h-i), the total area of B-sites increases with increasing cobalt content. From

the results, we can conclude that when particle size increases, i.e., when the particles shift from nanoparticles to bulk particles, particles with higher magnesium tend to form an inverse spinel structure. Particles with more cobalt tend to exhibit a mixed spinel structure.

5.1.4. Fourier-transform infrared spectroscopy (FTIR)

Fourier-transform infrared spectroscopy (FTIR) of MCFO ferrite nanoparticles annealed at 200^{o}C, 400^{o}C, 600^{o}C, and 800^{o}C are presented in Figure 5.6 (a). Two characteristic peaks of spinel ferrite of the cubic structure at the lower frequency region were observed. The higher frequency band is related to the stretching vibration of a metal-oxide bond at the tetrahedral (A) site, and the lower frequency band is related to the stretching vibration of a metal-oxide bond at the octahedral (B) site because the bond length of the A site is shorter than the bond length of the B site[204,236–241]. As the Co^{2+} content increased, the higher frequency band shifted to a lower frequency region, and the lower frequency band shifted to a higher frequency region because Co^{2+} (0.072 nm) took the place of Mg^{2+} (0.065 nm) at the A site, resulting in a reduction of the covalent bond. Additionally, at the B site, Fe^{2+} (0.0645 nm) replaces Co^{2+} (0.072 nm), which increases the covalent bond. The Raman spectroscopy of magnesium-rich compositions displays a preference for normal spinel structures, while that of cobalt-rich compositions reveals a preference for mixed spinel structures. Both Raman spectroscopy and FTIR spectroscopy yield comparable results. This is because the vibrational modes of the inverse spinel structure are much better defined than those of the normal spinel structure and, thus, are detected more easily by Raman spectroscopy. FTIR spectroscopy, however, detects a broader range of vibrational modes, enabling it to identify inverse and normal spinel structures. These two techniques can

therefore be used together to identify and differentiate between different spinel structures. They are also helpful in characterizing the vibrational modes of various materials. The MCFO that was annealed at different temperatures had varying absorption bands. At 200°C, a lower frequency absorption band (ν_1) was observed between 403 to 418 cm^{-1}, and a higher frequency absorption band (ν_2) was observed between 603 to 622 cm^{-1}. At 400°C, the lower frequency absorption band (ν_1) was observed between 398 to 415 cm^{-1}, and the higher frequency absorption band (ν_2) was observed between 597 to 618 cm^{-1}. At 600°C, the lower frequency absorption band (ν_1) was observed between 395 to 412 cm^{-1}, and the higher frequency absorption band (ν_2) was observed between 593 to 610 cm^{-1}. Lastly, at 800°C, the lower frequency absorption band (ν_1) was observed between 391 and 408 cm^{-1}, and the higher frequency absorption band (ν_2) was observed between 580 and 600 cm^{-1}. Both the frequency band shifted toward the lower frequency region with increasing particle size (annealing temperature) because the covalent bond shrinks with an increase in particle size (annealing temperature). Both the frequency bands shifted toward the lower frequency because bond length increased with particle size. The force constants (F_C) for the A site (F_{CT}) and B site (F_{CO}) are obtained using equation (4.1). Variations of the obtained values of F_{CT} and F_{CO} of $Mg_{1-x}Co_xFe_2O_4$ ferrites annealed at 200°C, 400°C, 600°C, and 800°C with Co^{2+} content, x are presented in figure -5.6 (b). The value of F_{CT} decreases, and F_{CO} increases with increasing Co^{2+} content x because the A site's bond length increases, and the B site's bond length decreases with an increase in Co^{2+} content x[201]. The absorption peaks at 3430-3493 cm^{-1} were observed for the stretching vibration of the O-H group[242].

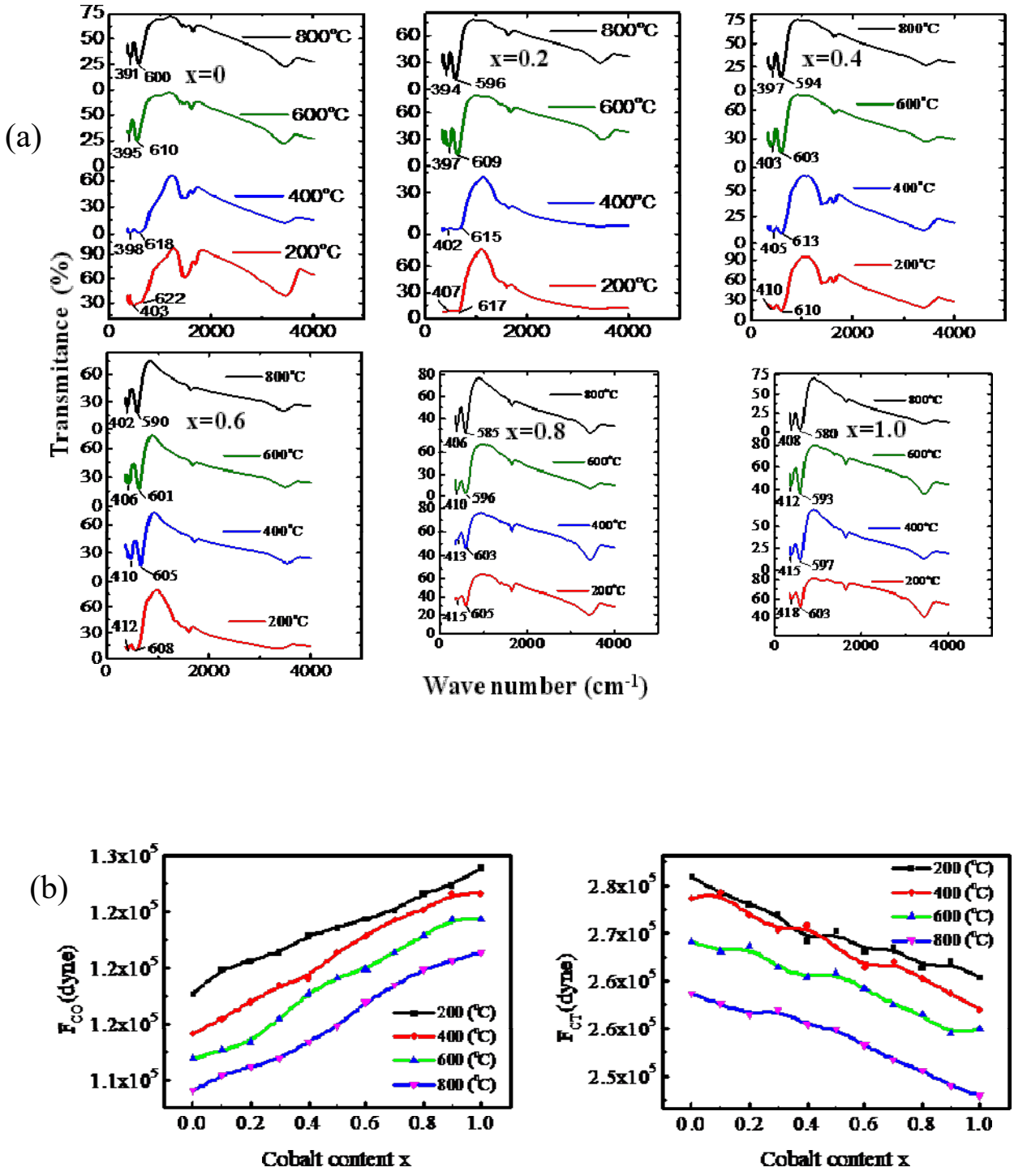

Fig. 38 (a): (a) The FTIR spectrum of $Mg_{1-x}Co_xFe_2O_4$ nanoparticles annealed at 200°C, 400°C, 600°C, and 800°C, (b) variation of the octahedral, and the tetrahedral force constant with cobalt content x of $Mg_{1-x}Co_xFe_2O_4$ nanoparticles annealed at 200°C, 400°C, 600°C, and 800°C.

5.2. Thermo-gravimetric analysis (TG) and differential scanning calorimetry (DSC)

Thermal traits of studied MCFO ferrite nanoparticles were investigated using thermo-gravimetric analysis (TG) and differential scanning calorimetry (DSC) measurement. As-synthesized ferrites-powder was heated in a nitrogen atmosphere from 25 to 1300^{o}C. Endothermic and exothermic peak positions are determined from the first derivative of the DSC (DDSC) and TG (DTG) curves. The phenomenological data of DSC and TG measurements are presented in Table -5.5. The first exothermic peak of studied MCFO was found at 90 to 130^{o}C, associated with removing physically absorbed water molecules because no other volatile components are present in the sample. The second exothermic peak of the studied sample was found at 219 to 339^{o}C, which is associated with eliminating the lattice water and the water from the pores. Other weight losses are related to the reformation of metal oxide bond[243–250]. In the TG curve of Chitosan-coated $Mg_{0.9}Co_{0.1}Fe_2O_4$ ferrite, a significant portion of weight loss was found at 230 to 300^{o}C due to the chitosan release.

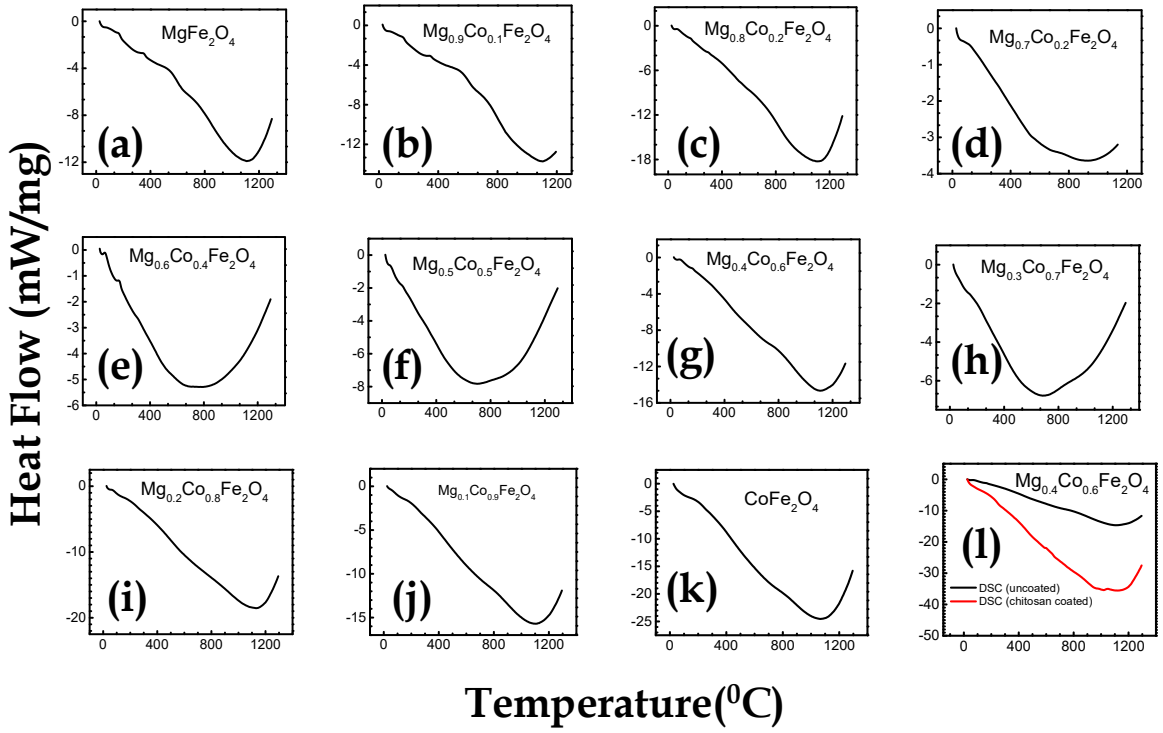

Figure 5.7: The thermo-gravimetric analysis (TG) and differential scanning calorimetry (DSC) spectrum of $Mg_{1-x}Co_xFe_2O_4$ nanoparticles annealed at 200°C, 400°C, 600°C, and 800°C.

Table 5.5: Data of peak position, mass loss, and enthalpy of TG measurement of MCFO ferrite nanoparticles.

Value of x	Data of TG measurement				Data of TG measurement			
	Data range	Peak position	Mass loss	Nature	Data range	Peak position	Enthalpy ($erg g^{-1}$)	Nature
0	35-220^{0}C	130^{0}C	12.8%	Exo	85-310^{0}C	200^{0}C	186×10^7	Exo
	220-500^{0}C	330^{0}C	12.3%	Exo	310-485^{0}C	390^{0}C	340×10^7	Exo
	500-1300^{0}C	-	4%	Exo	486-685^{0}C	845^{0}C	112×10^7	Exo
0.1	37-224^{0}C	128^{0}C	11.8%	Exo	26-84^{0}C	30^{0}C	70×10^7	Exo
	224-480^{0}C	324^{0}C	11%	Exo	85-314^{0}C	199^{0}C	301×10^7	Exo
	550-1020^{0}C	890^{0}C	4%	Exo	314-489^{0}C	384^{0}C	114×10^7	Exo
					489-679^{0}C	600^{0}C	116×10^7	Exo
					679-940^{0}C	804^{0}C	154×10^7	Exo
0.2	34-224^{0}C	115^{0}C	15.7%	Exo	294-609^{0}C	469^{0}C	285×10^7	Exo
	224-414^{0}C	314^{0}C	9.68%	Exo	609-1019^{0}C	814^{0}C	215×10^7	Exo
	414-1300	-	6.6%	Exo				
0.3	30-206^{0}C	106^{0}C	8%	Exo	27-94^{0}C	46^{0}C	113×10^7	Exo
	206-386^{0}C	291^{0}C	7%	Exo	94-441^{0}C	269^{0}C	236×10^7	Exo
	386-1300^{0}C	-	3%	Exo	542-911^{0}C	811^{0}C	119×10^7	Exo
0.4	35-220^{0}C	96^{0}C	15.5%	Exo	28-145^{0}C	105^{0}C	116×10^7	Exo
	220-436^{0}C	296^{0}C	8.6%	Exo	145-280^{0}C	210^{0}C	128×10^7	Exo
	436-1300^{0}C	-	5.4%	Exo	280-560^{0}C	445^{0}C	237×10^7	Exo
0.5	34-210^{0}C	95^{0}C	14.3%	Exo	30-160^{0}C	140^{0}C	93×10^7	Exo
	210-550^{0}C	294^{0}C	9.6%	Exo	160-304^{0}C	234^{0}C	231×10^7	Exo
	550-1300^{0}C	-	3.7%	Exo	304-810^{0}C	695^{0}C	243×10^7	Exo
0.6	34-219^{0}C	99^{0}C	13%	Exo	40-174^{0}C	109^{0}C	95×10^7	Exo
	219-420^{0}C	279^{0}C	6.3%	Exo	174-304^{0}C	204^{0}C	101×10^7	Exo
	420-1300^{0}C	-	5%	Exo	304-589^{0}C	424^{0}C	225×10^7	Exo
				Exo	589-729^{0}C	629^{0}C	103×10^7	Exo
				Exo	729-1109^{0}C	929^{0}C	93×10^7	Exo
0.7	27-200^{0}C	93^{0}C	7.2%	Exo	32-155^{0}C	103^{0}C	90×10^7	Exo
	200-400^{0}C	315^{0}C	4.8%	Exo	155-340^{0}C	275^{0}C	276×10^7	Exo
	400-1300^{0}C	-	5%	Exo	340-685^{0}C	410^{0}C	91×10^7	Exo
0.8	32-164^{0}C	94^{0}C	8%	Exo	32-169^{0}C	104^{0}C	91×10^7	Exo
	164-260^{0}C	219^{0}C	2.6%	Exo	169-319^{0}C	244^{0}C	123×10^7	Exo
	260-434^{0}C	339^{0}C	3.6%	Exo	319-660^{0}C	499^{0}C	115×10^7	Exo
	434-1300^{0}C	-	5.4%	Exo	660-1134^{0}C	954^{0}C	95×10^7	Exo
0.9	32-194^{0}C	95^{0}C	5.5%	Exo	30-160^{0}C	99^{0}C	200×10^7	Exo
	194-500^{0}C	310^{0}C	4.5%	Exo	160-380^{0}C	250^{0}C	342×10^7	Exo
	500-1300^{0}C	-	4.5%	Exo	380-764^{0}C	425^{0}C	115×10^7	Exo
				Exo	764-1104^{0}C	909^{0}C	95×10^7	Exo
1.0	31-180^{0}C	92^{0}C	7%	Exo	32-140^{0}C	96^{0}C	212×10^7	Exo
	180-420^{0}C	330^{0}C	4.2%	Exo	140-710^{0}C	455^{0}C	313×10^7	Exo
	420-1300^{0}C	-	3.8%	Exo	710-1075^{0}C	900^{0}C	99×10^7	Exo

5.3. Magnetization measurements

The variation of magnetization (M) with an applied magnetic field (H) of MCFO ferrite nanoparticles annealed at 200°C, 400°C, 600°C, and 800°C are presented in Figure 7. The value of M increases with an increase in Co^{2+} content because Co^{2+} replaces $Mg^{2+,}$ and the magnetic moment of $Co^{2+}(3.88\mu_B)$is higher than that of $Mg^{2+}(0\mu_B)$[214,215]. The value of M also increases with an increase in annealing temperature because grain size increases with an increase in annealing temperature. The saturation magnetizations (M_s) were obtained by extrapolating M - $\frac{1}{H}$ curve at $\frac{1}{H} \rightarrow 0$ for a higher value of H[213]. The anisotropy constants (K) were obtained by using the relation,

$$K = \frac{H_c \times M_S}{0.96} \tag{5.3}$$

where H_c is the coercive field[144]. The variation of H_c, M_s, remanence ratio (M_r/M_s), and K with the particle size of MCFO ferrite nanoparticles annealed at 200°C, 400°C, 600°C, and 800°C are presented in Figure 5.9. The values of M_s, K, $H_{c,}$ and M_r/M_s increase with increased particle size and Co^{2+} content. In general, the values of Ms, K, Hc, and Mr/Ms tend to increase with increasing particle size up to a certain point. This is because larger particles tend to have more magnetic moments or spins, which can align with an external magnetic field, leading to a more robust overall magnetization. Additionally, larger particles can have a more ordered array of magnetic moments, leading to a giant magnetic anisotropy (the preference of the magnetic moments to align in a particular direction).

However, further increases in particle size may lead to a decrease in magnetic properties beyond a certain point. It is because as particles become too large, they may become more susceptible to

thermal fluctuations, which can lead to a loss of magnetic order and a decrease in magnetization. Additionally, larger particles may have a less uniform distribution of magnetic moments, which can decrease magnetic anisotropy and coercivity[251–254]. The values of M_s increase with an increase in Co^{2+} content because the magnetic moment of $Co^{2+}(3.88\mu_B)$ is higher than that of $Mg^{2+}(0\mu_B)$. The values of H_c increase with an increase in Co^{2+} content because K increases with an increase in Co^{2+} content[215].

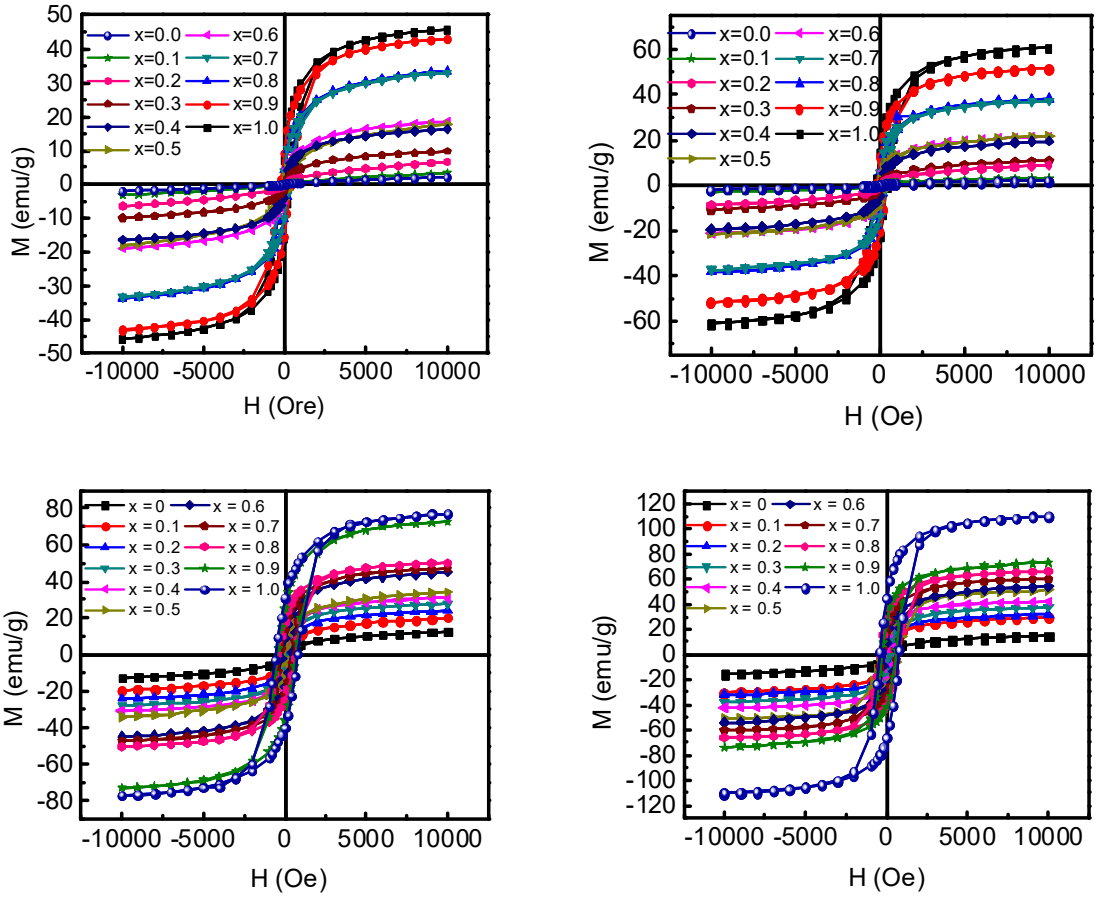

Figure 5.8 (a): Variation of magnetization with an applied magnetic field of $Mg_{1-x}Co_xFe_2O_4$ nanoparticles annealed at 200°C, 400°C, 600°C, and 800°C.

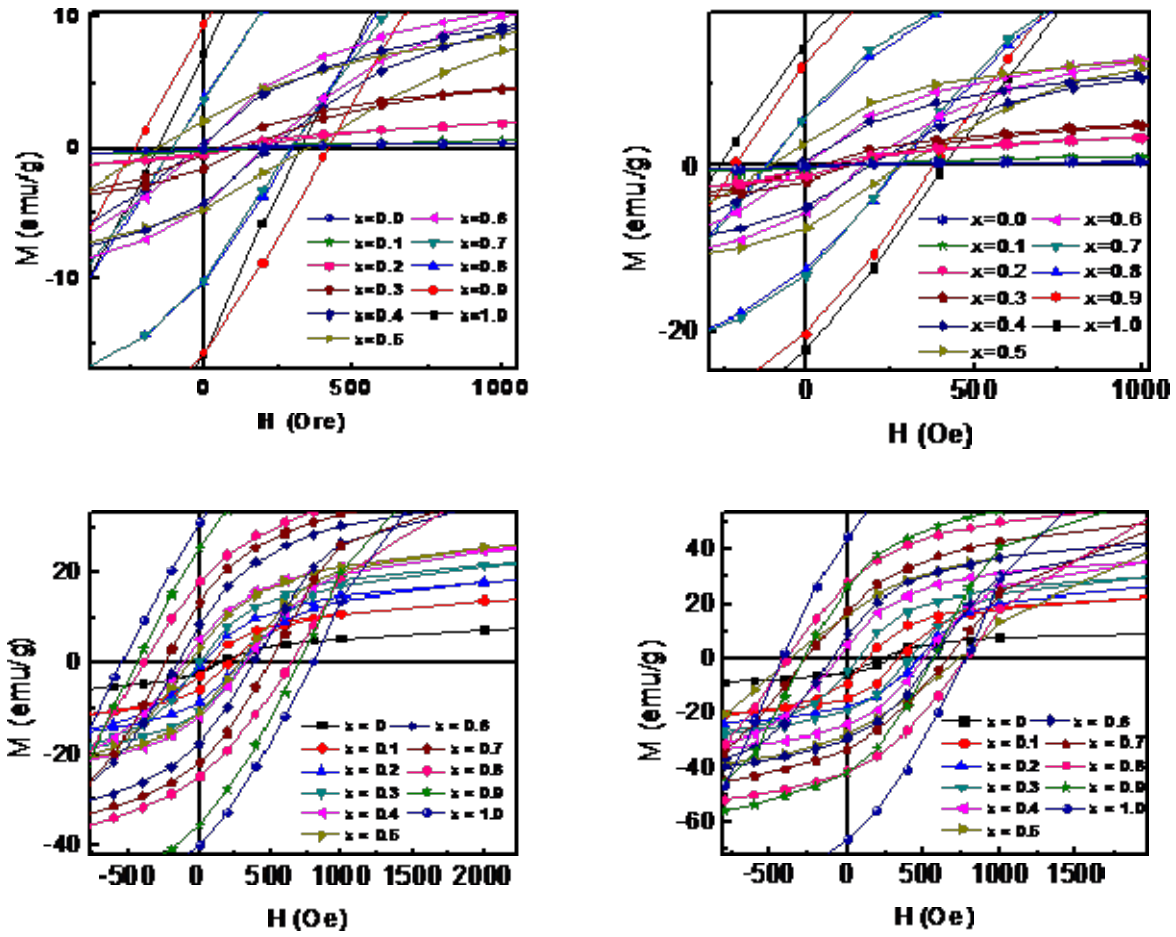

Figure 5.8 (b): Variation of magnetization with an applied magnetic field of $Mg_{1-x}Co_xFe_2O_4$ nanoparticles annealed at 200°C, 400°C, 600°C, and 800°C.

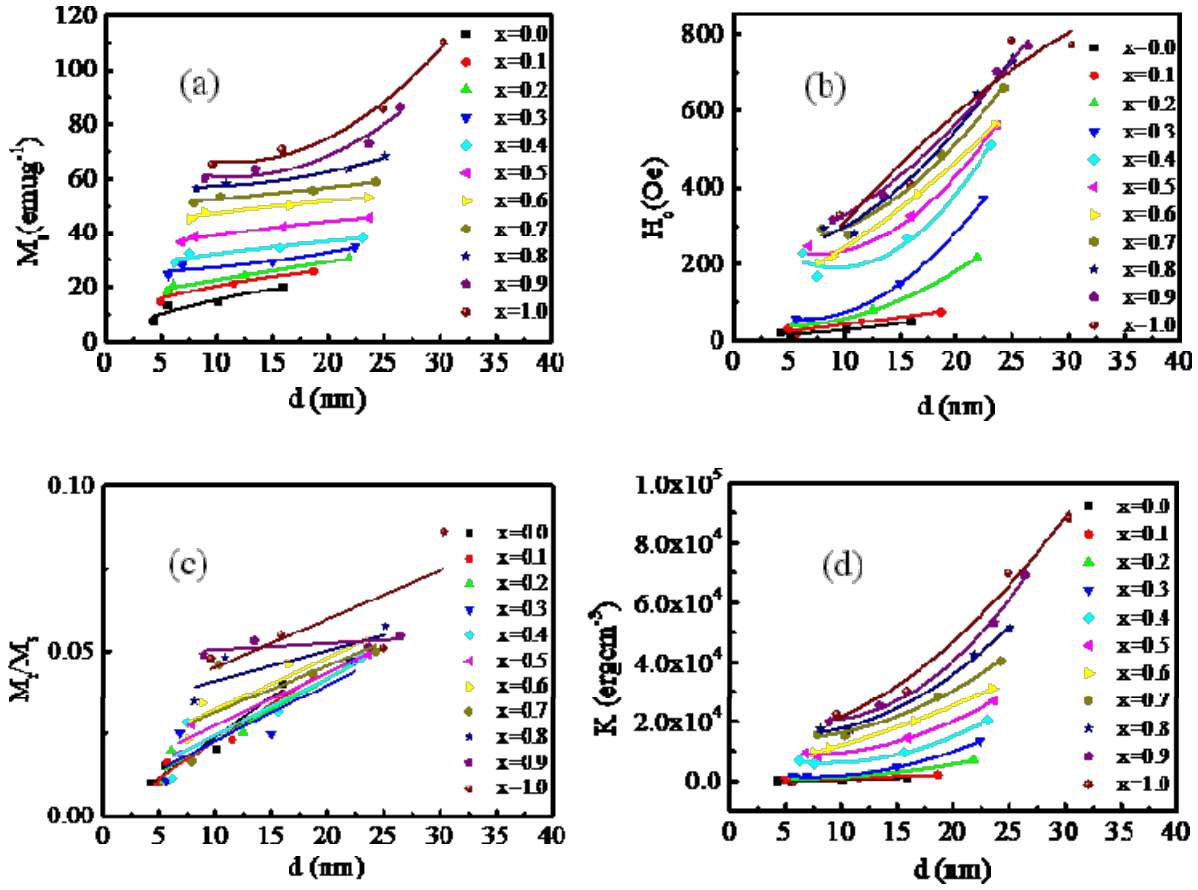

Figure 5.9: Variation of the (a) saturation magnetization M_s, (b) coercive field H_c, (c) remnant ratio M_r/M_s, and (d) anisotropy constant K with the particle size of $Mg_{1-x}Co_xFe_2O_4$ nanoparticles annealed at 200°C, 400°C, 600°C, and 800°C.

5.4. Hyperthermia

Heating profiles of chitosan-coated MCFO nanoparticles annealed at 200°C, 400°C, 600°C, and 800°C are presented in Figure 5.10. For chitosan-coated MCFO nanoparticles annealed at 200°C, the heating rate and maximum achieved temperature increase with an increase in Co^{2+} content because the magnetic moment increases with an increase in Co^{2+} content.

For chitosan-coated MCFO nanoparticles annealed at 400°C, the heating rate and maximum achieved temperature increase with an increase in Co^{2+} content x up to $x \leq 0.8$; after then, the heating rate and maximum achieved temperature decrease with an increase in Co^{2+} content x. For chitosan-coated MCFO nanoparticles annealed at 600°C, the heating rate and maximum achieved temperature increase with an increase in Co^{2+} content x up to $x \leq 0.3$; after then, the heating rate and maximum achieved temperature decrease with an increase in Co^{2+} content x.

For chitosan-coated MCFO nanoparticles annealed at 800°C, the heating rate and maximum achieved temperature increase with an increase in Co^{2+} content x up to $x \leq 0.1$; after then, the heating rate and maximum achieved temperature decrease with an increase in Co^{2+} content x. The heating rate and maximum achieved temperature fall because the Brown contribution to losses attains a maximum at a particular particle size for all materials. After then, it drops sharply, and the Néel contribution to the losses varies exponentially with the product of the magnetic anisotropy constant and the particle volume[11,12,47,98,99,255–257].

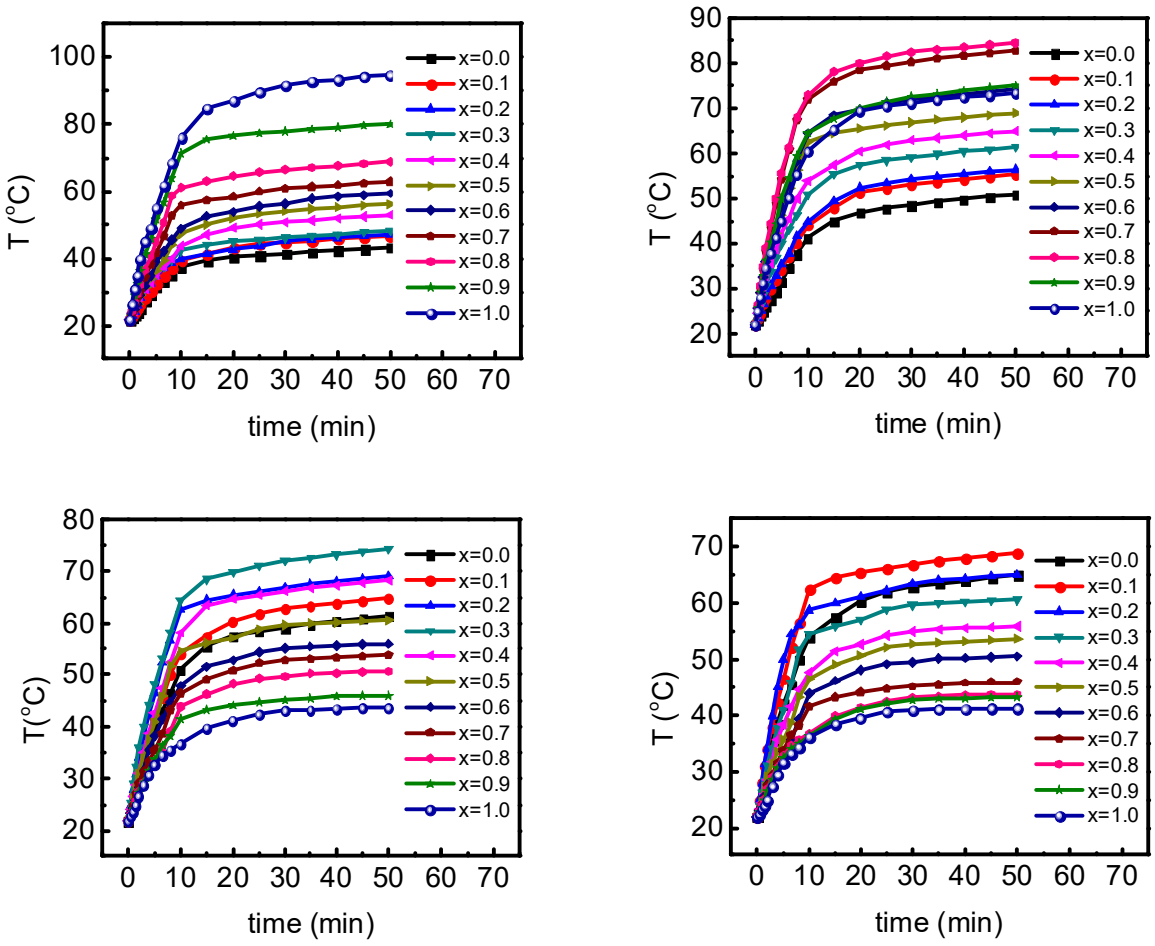

Figure 5.10: Heating profile of Chitosan-coated $Mg_{1-x}Co_xFe_2O_4$ nanoparticles annealed at 200°C, 400°C, 600°C, and 800°C.

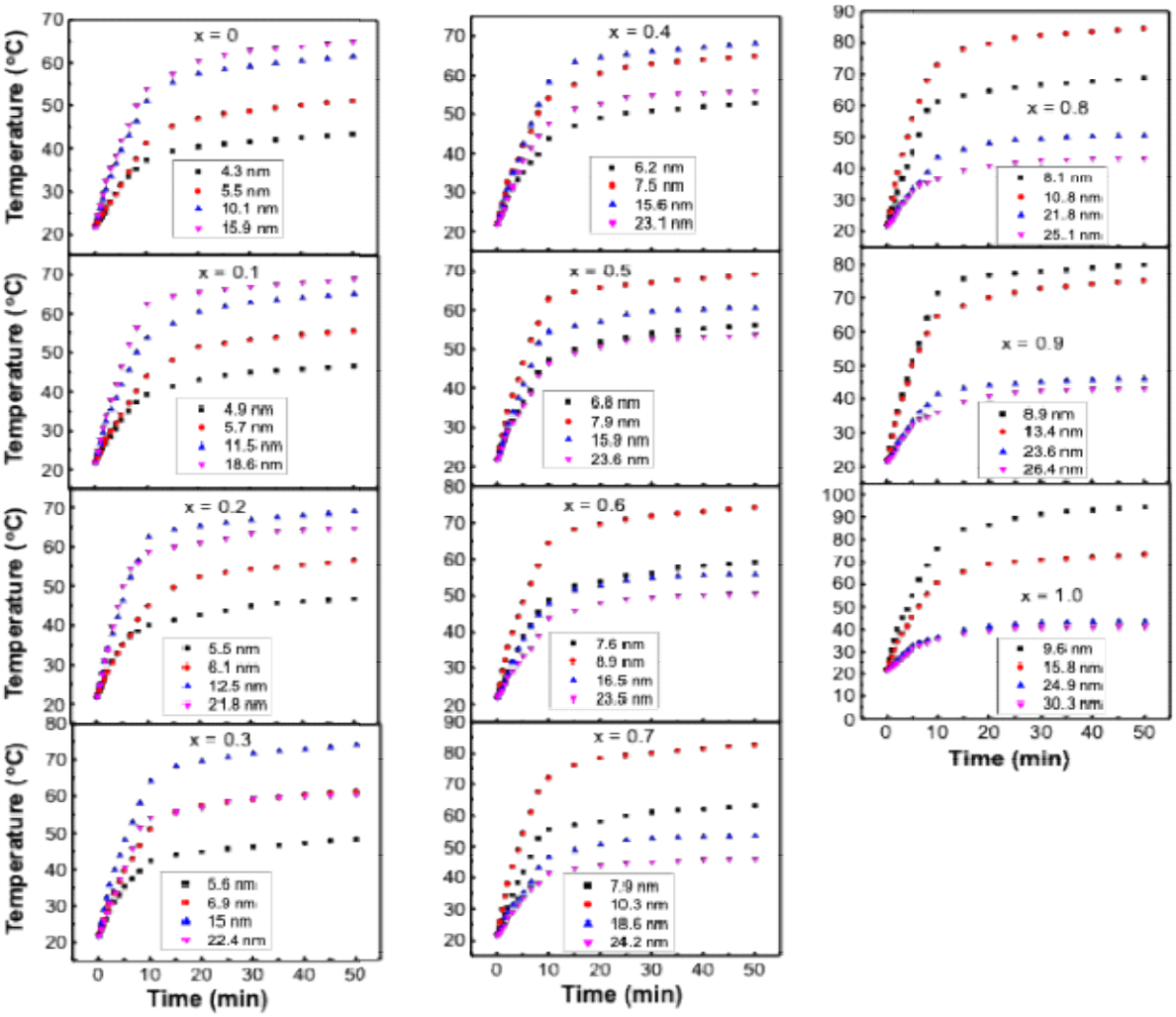

Figure 5.11: Heating profile of Chitosan-coated $Mg_{1-x}Co_xFe_2O_4$ nanoparticles showing the variation of temperature with particle size.

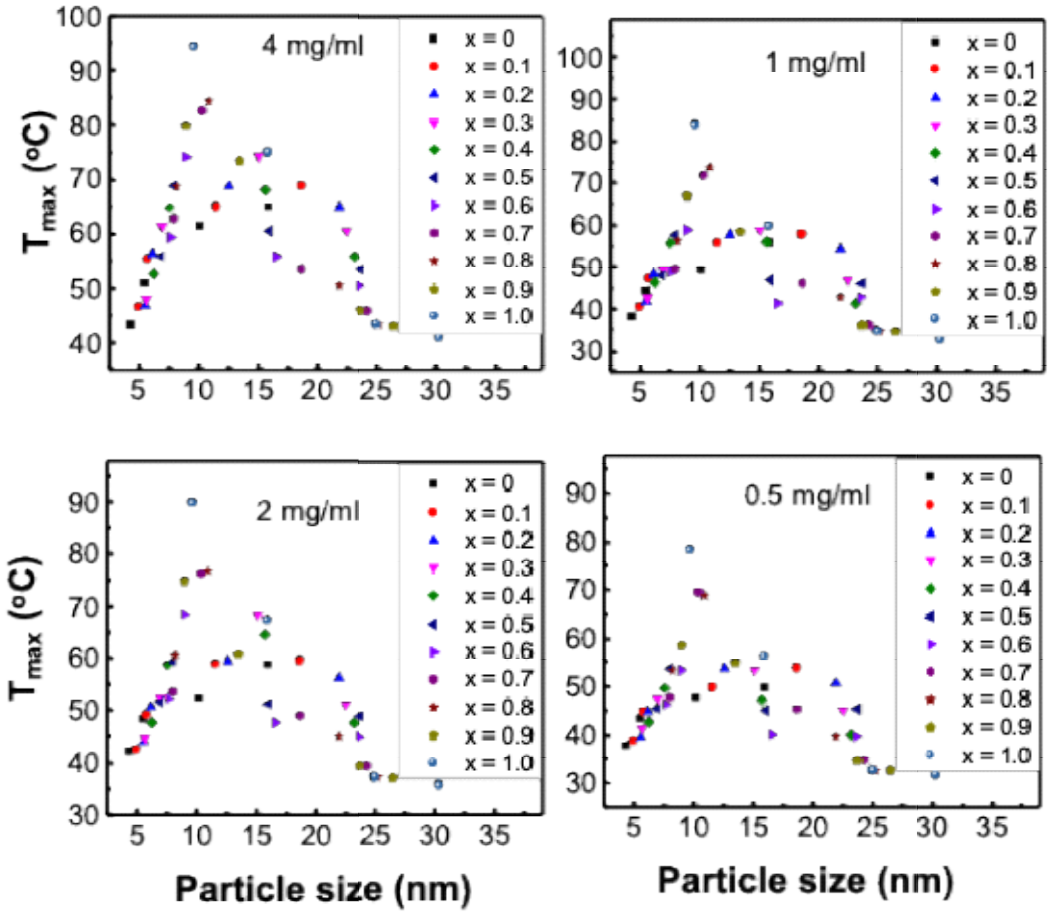

Figure 5.12: Variation of maximum temperature with the particle size of Chitosan-coated $Mg_{1-x}Co_xFe_2O_4$ nanoparticles for different solution concentrations.

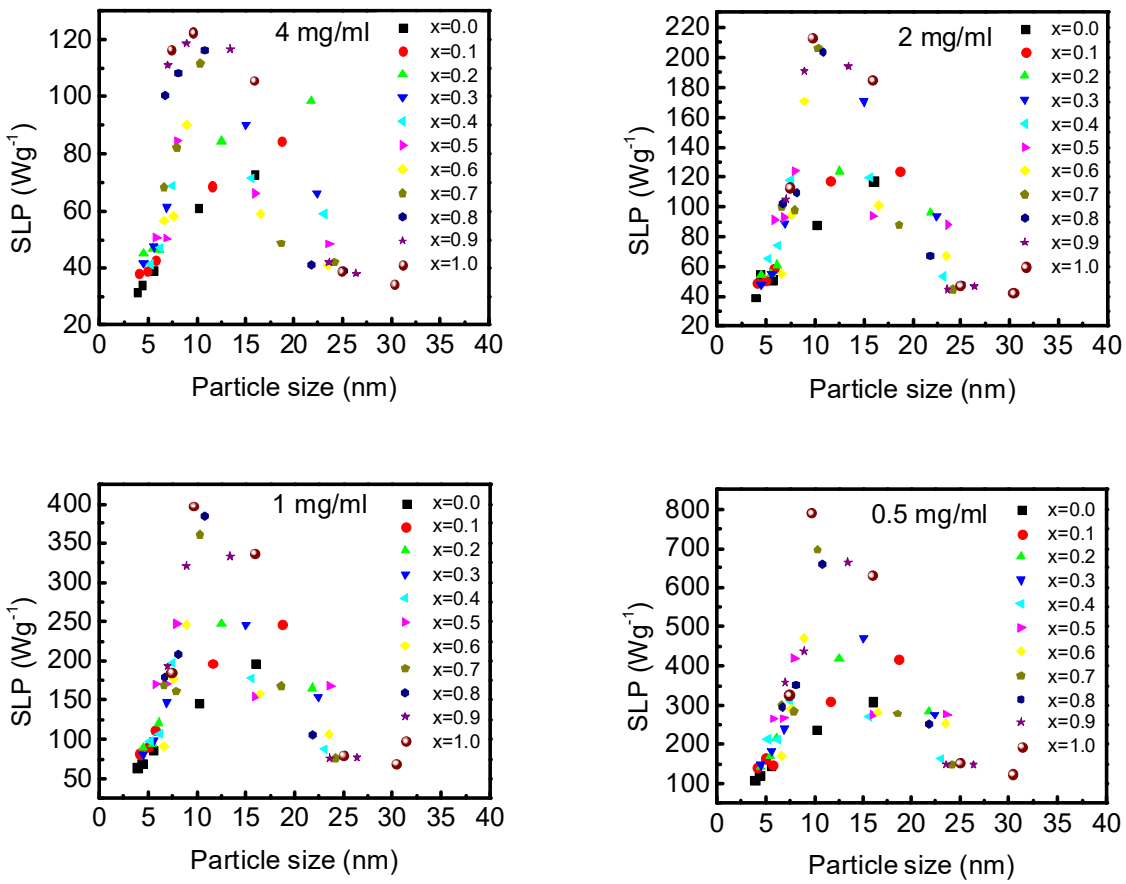

Figure 5.13: Variation of SLP with the particle size of Chitosan-coated $Mg_{1-x}Co_xFe_2O_4$ nanoparticles for different solution concentrations.

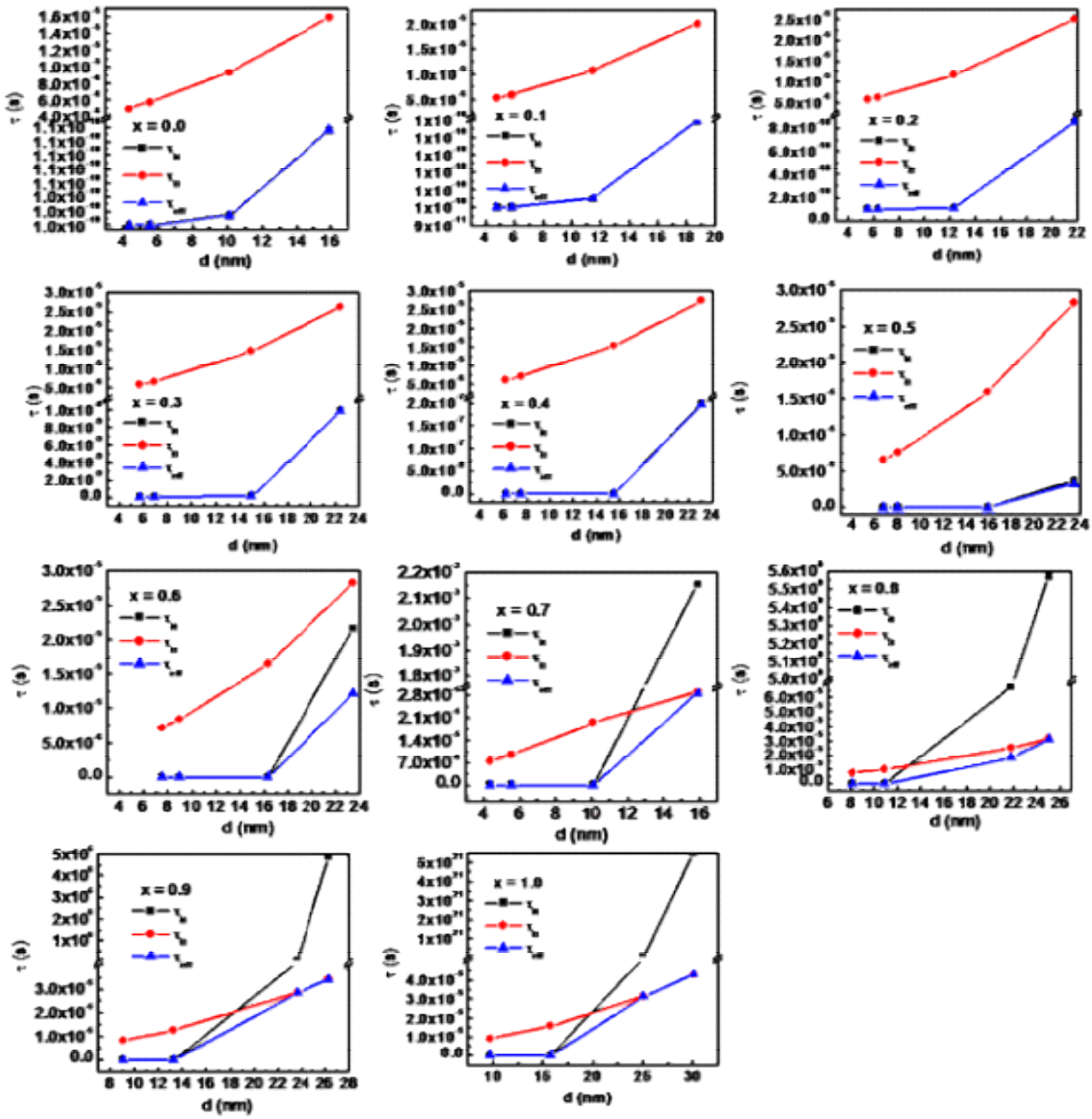

Figure 5.14: The particle size dependence of Néel relaxation time, τ_N, Brownian relaxation time, τ_B and effective relaxation time, τ_{eff} *of* $Mg_{1-x}Co_xFe_2O_4$ nanoparticles.

Figure 5.13 represents the variation of specific loss power (SLP) with the particle size of chitosan-coated MCFO nanoparticles having different concentrations. Initially, the value of SLP increases with an increase in particle size for each sample and concentration because, in that region, the Brown contribution to losses increases with an increase in particle size. After then, the value of SLP decreases with an increase in particle size. The Néel relaxation time varies exponentially with the product of the magnetic anisotropy constant and the particle volume, which is also another region of shifting the zenith of the SLP curve. The zenith of the SLP curve moved towards the lower particle size value with an increase in Co2+ content due to the rise in the anisotropy constant. Habib[255] et al. reported similar behavior for Fe-Co alloy, magnetite, and maghemite nanoparticles. Figure 5.14 depicts the variation of Néel relaxation time, Brownian relaxation time, and the effective relaxation time with the particle size of MCFO nanoparticles. Upto x=0.5 effective relaxation time mostly coincides with the Néel relaxation. From x =0.6, Brownian relaxation starts to dominate, and above a critical diameter, the relaxation time coincides with Brownian relaxation. When the particle size is less than 10-16 nm, the Néel relaxation dominated the effective relaxation time. After then, Brownian relaxation is the relaxation time. The critical diameter above which hysteresis loss is dominant was determined by the formula,

$$D_{CT} = \left[\frac{6\ln\left(t_m f_0\right) k_B T}{\pi K}\right]^{\frac{1}{2}}$$

Considering the anisotropy constant K of MCFOs, f_0 as10^9 Hz, k_B the Boltzmann's constant, T the temperature, and t_m the measurement time[258]. The critical diameter decreases with increasing Co^{2+} content due to increasing anisotropy constant. Above the critical diameter and higher Co^{2+}

content, anisotropy increases, for which Néel relaxation cannot occur because of the higher anisotropy. Therefore relaxation mechanism is dominated by Brownian relaxation mainly.

CHAPTER 6: INVESTIGATING CONTRAST ENHANCEMENT IN MAGNETIC RESONANCE ANGIOGRAPHY WITH PEG/CHITOSAN/DEXTRAN AND MCFO NANOHYBRID AS CONTRAST DYE IN THE RAT MODEL

In this chapter, MCFO particles were coated with chitosan, PEG, and dextran, and the hyperthermia and MRI properties were investigated to obtain suitable MRI contrast dye.

6.1. Structural characterization

6.1.1. X-ray diffraction (XRD) analysis

Figure 6.1 demonstrates the variation of lattice parameters and particle size of MCFO with cobalt content. The average crystallite size was determined using Debye-Scherrer's formula[187], which was 3.8 to 7.3 nm. Both the lattice parameter and particle size increase with increasing x, which is expected because the ionic radius of the Mg^{2+} (0.065 nm) ion is smaller than that of the Co^{2+} (0.072 nm) ion[44,46,183]. Smaller crystallite size is one of the requirements of in-vivo MRA applications.

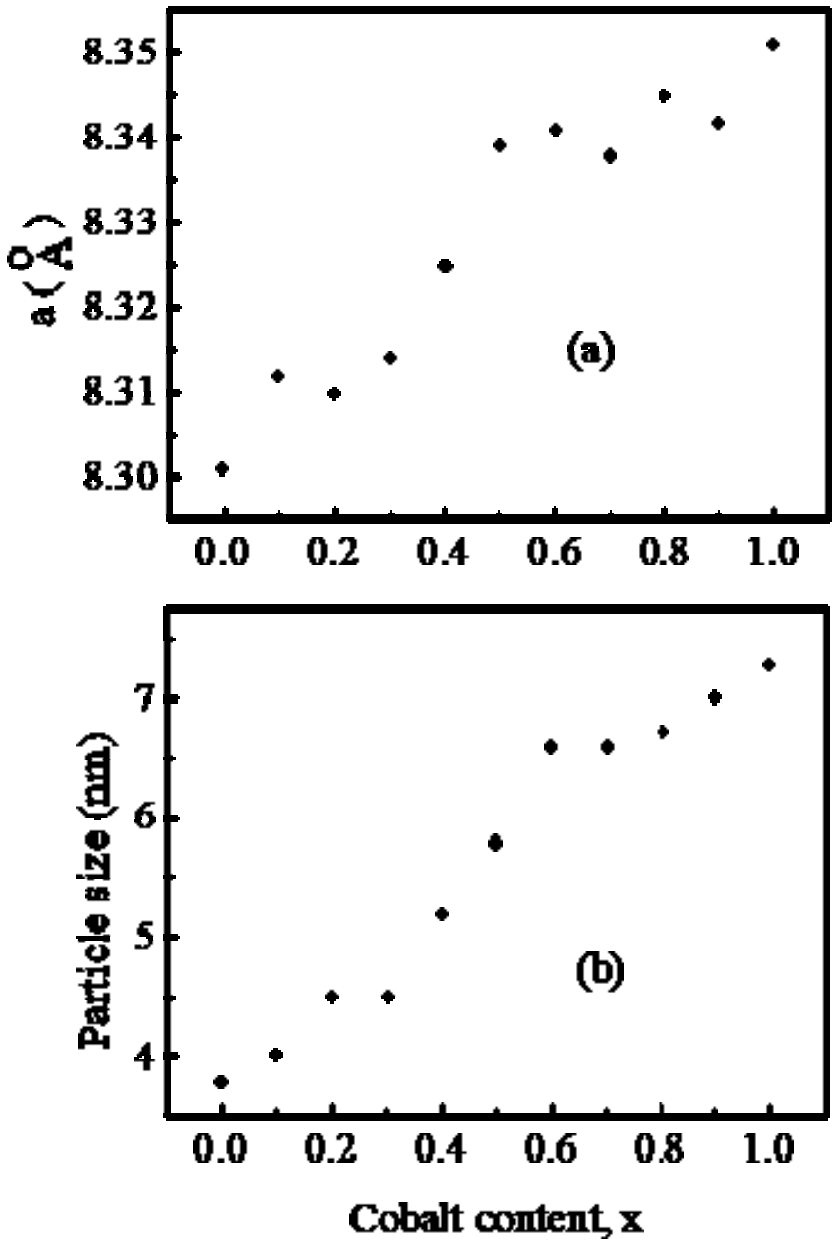

Figure 6.1: Variation of (a) lattice parameter and (b) particle size with cobalt content, x of MCFO ferrite nanoparticle in the as-dried condition.

6.1.2. Transmission Electron Microscopy (TEM)

Figure 6.2-(A) depicts TEM images of bare, Chitosan-coated, Dextran-coated, and PEG-coated MCFO ferrite nanoparticles. Clusters are present in uncoated particles. Particles with a lower cobalt content are smaller and more agglomerated. Uncoated samples cluster by magnetic dipole interactions between ferrite nanoparticles, minimizing surface-free energy. Dipole interactions are decreased, and particles are dispersed after coating with Chitosan, Dextran, and PEG. Chitosan-coated samples with lower cobalt content are more widely scattered. On the other hand, Dextran-covered MCFO ferrite nanoparticles are more scattered in samples with higher cobalt content. The PEG-coated particles agglomerate more than the other two coatings. The nature of particle dispersion in the solution is independent of the cobalt content in PEG-containing solutions. The bare and coated MCFO nanoparticle SAED patterns are shown in the right corner of figure-6.2 (A). The SAED patterns indicate that (311) is the highest intensity plane along with the other (220), (400), (420), (511), and (440) planes. The d values of the SAED pattern were obtained using Velox software, which indexes the diffractograms. The SAED patterns are consistent with the noncrystalline structure documented in the literature[43,232–234]. The Debye circles are more intense for uncoated than coated nanoparticles because of the higher degree of dispersion in Dextran-coated particles in a region. Figure 6.2 (B) presents HRTEM images of bare, Chitosan-coated, Dextran-coated, and PEG-coated particles. The lattice fringes of the HRTEM image of both uncoated and coated particles are shown in the figure. 6.2 (B) suggests high crystallinity. In the HRTEM pictures in Figure 6.2 (B), Chitosan-treated particles are found more dispersed with lower cobalt content, and Dextran-coated particles are found more dispersed with higher cobalt content. PEG-coated particles are more agglomerated, and the solution nature does not significantly depend on cobalt content[42,43,186,198,217,232–234,259].

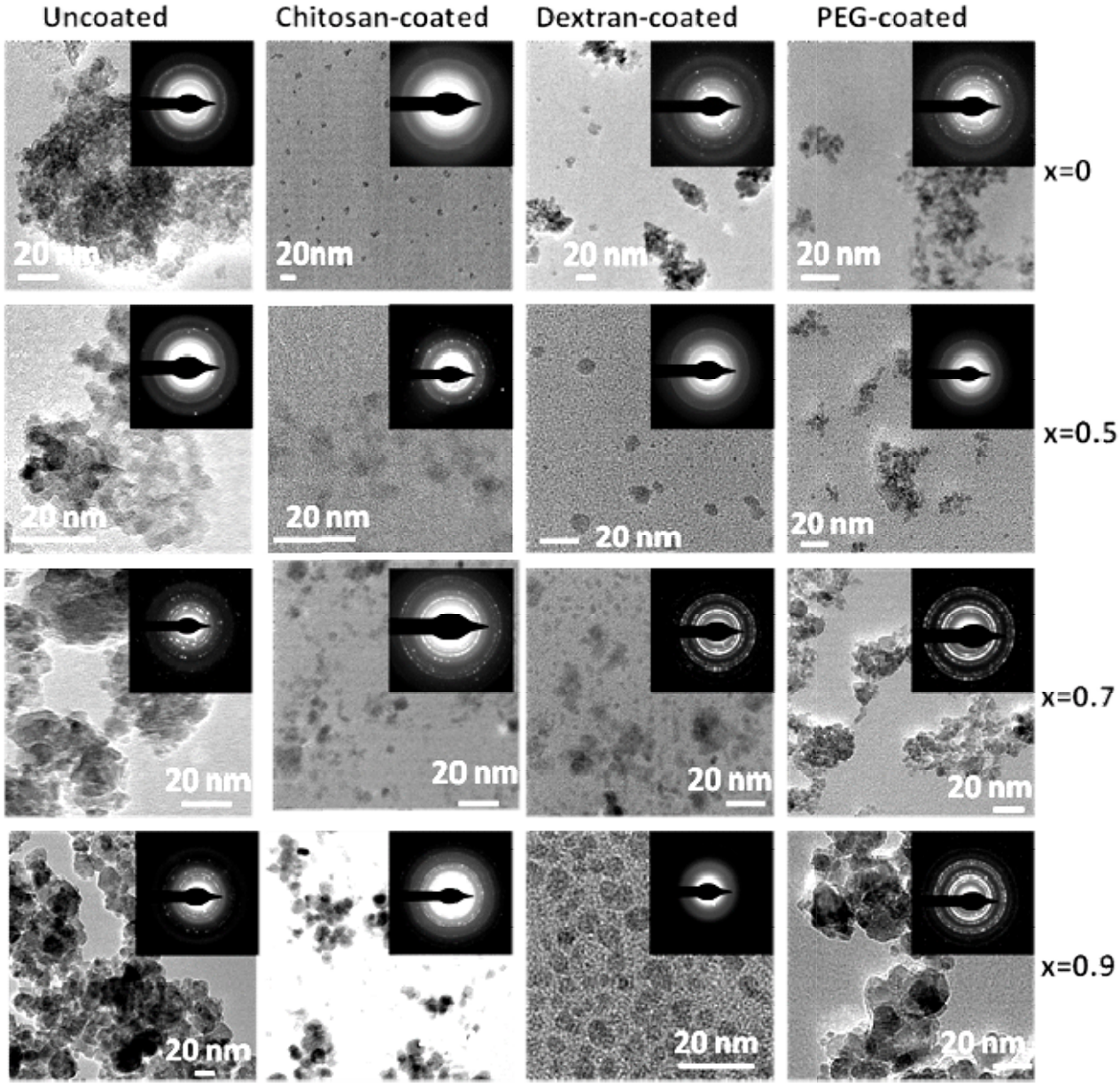

Figure 6.2 (A): TEM images of uncoated, Chitosan-coated, Dextran-coated, PEG-coated $Mg_{1-x}Co_xFe_2O_4$ ferrites nanoparticles.

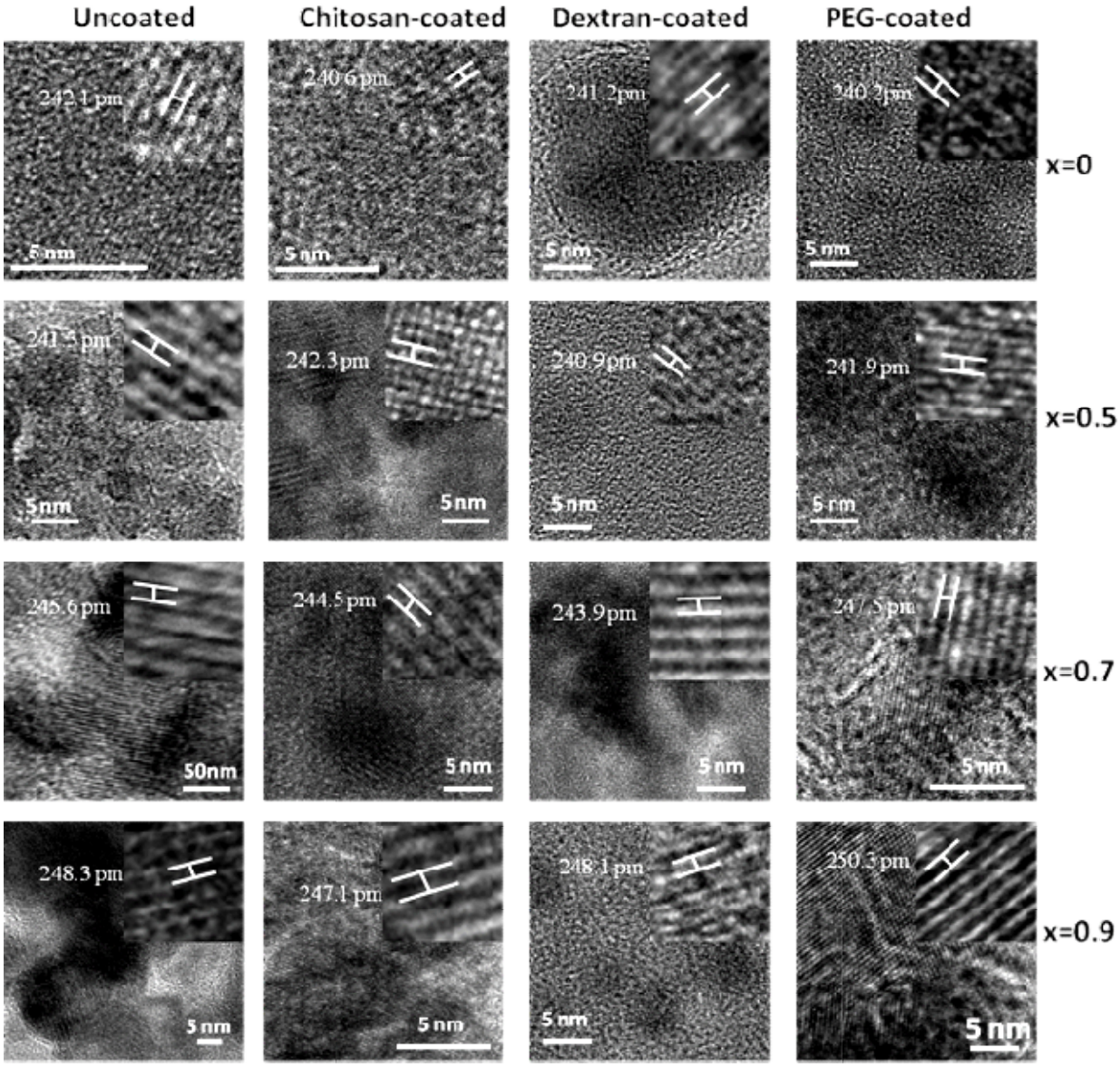

Figure 6.2 (B): HTEM images of uncoated, Chitosan-coated, Dextran-coated, PEG-coated $Mg_{1-x}Co_xFe_2O_4$ ferrites nanoparticles.

6.1.3. Fourier-transform infrared spectroscopy (FTIR)

The FTIR spectroscopy of the studied samples was taken to investigate the covalent bond length of PEG-coated, dextran-coated, and chitosan-coated MCFO ferrite nanoparticles, which are associated with the nature of the coating[38,39]. Figure-6.3 depicts the FTIR spectrum of as-dried, PEG-coated, dextran-coated, and chitosan-coated MCFO ferrite nanoparticles. The higher frequency bands of all coated samples are shifted towards the lower frequency region, indicating stable coating. Coating extended the bond length of the tetrahedral site. So, the higher frequency band is shifted towards the lower frequency region[38,39,260,261]. Turning off the higher frequency band is higher for chitosan-coated samples and lower for PEG-coated models. The result concludes that chitosan coating is thicker among these three coatings, and PEG coating is thinner than dextran coating. Covalent bond length extends more when the layer gets thicker. The absorption bands located at 1633-1639 cm^{-1} and 994-1054 cm^{-1} confirmed the bending mode of O-H bonds. The peak at 1394-1454 cm^{-1}, 1153-1157 cm^{-1}, 2902-2921 cm^{-1}, 2980-2983 cm^{-1}, and 3281-3305 cm^{-1} is due to the vibration of the CH3 functional group, C-O-C stretching bond, C-H stretching bond, the vibration of C-N active group, and O-H stretching vibration.

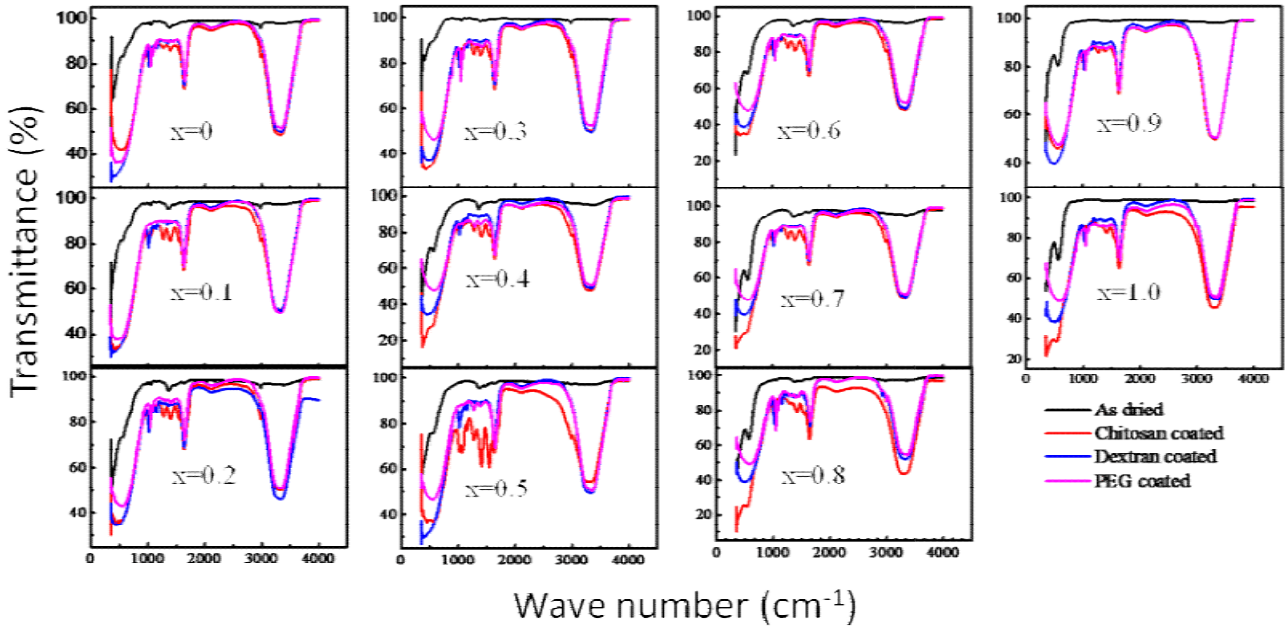

Figure 6.3: FTIR spectrum of as-dried, chitosan-coated, dextran-coated, and PEG-coated of $Mg_{1-x}Co_xFe_2O_4$ ferrite nanoparticle.

6.1.4. Hydrodynamic diameter and Zeta potential

A small hydrodynamic diameter is assigned for achieving a suitable MRI contrast agent. Hydrodynamic diameters and zeta potential of analyzed coated MCFO ferrite nanoparticles solutions with a concentration of 4 mg/ml are illustrated in figure-6.4. The average hydrodynamic diameter for chitosan-coated MCFO ferrite nanoparticle solutions is 144 nm to 170 nm. The poly dispersive index (PDI) exists at 0.101 to 0.239, and the Zeta potential remains 35 to 59 mV. The small PDI value and the higher zeta potential value are evidence of good coating[169,261–263]. Therefore there is no sedimentation at the bottom of the coated solution even after one year of preparation. The average hydrodynamic diameter reduces with temperature rise and the concentration reduction of the solution. When the average hydrodynamic size decreases, the PDI and zeta potential of the solution decreases very slightly. So it is expected that chitosan-coated MCFO ferrite nanoparticle solutions not be agglomerated inside a human body. The average hydrodynamic diameter for PEG-coated MCFO ferrite nanoparticle solutions is 122 nm to 135 nm. The solution's poly dispersive index (PDI) is 0.235 to 0.371, and the Zeta potential stands at 0 to 3 mV. Although PDI indicates that the solution is well dispersed and coated, some sedimentation was found at the bottom after six months. Hydrodynamic size decreases with an increase in temperature and a decrease in the solution's concentration. The average hydrodynamic diameter for dextran-coated MCFO nanoparticle solutions is 140 nm to 160 nm. The solution's poly dispersive index (PDI)is 0.221 to 0.369, and the Zeta potential stands at 08 to 15 mV. This solution has been well dispersed and stable for six months. Both PEG-coating and dextran-coating are independent of the pH of the solution.

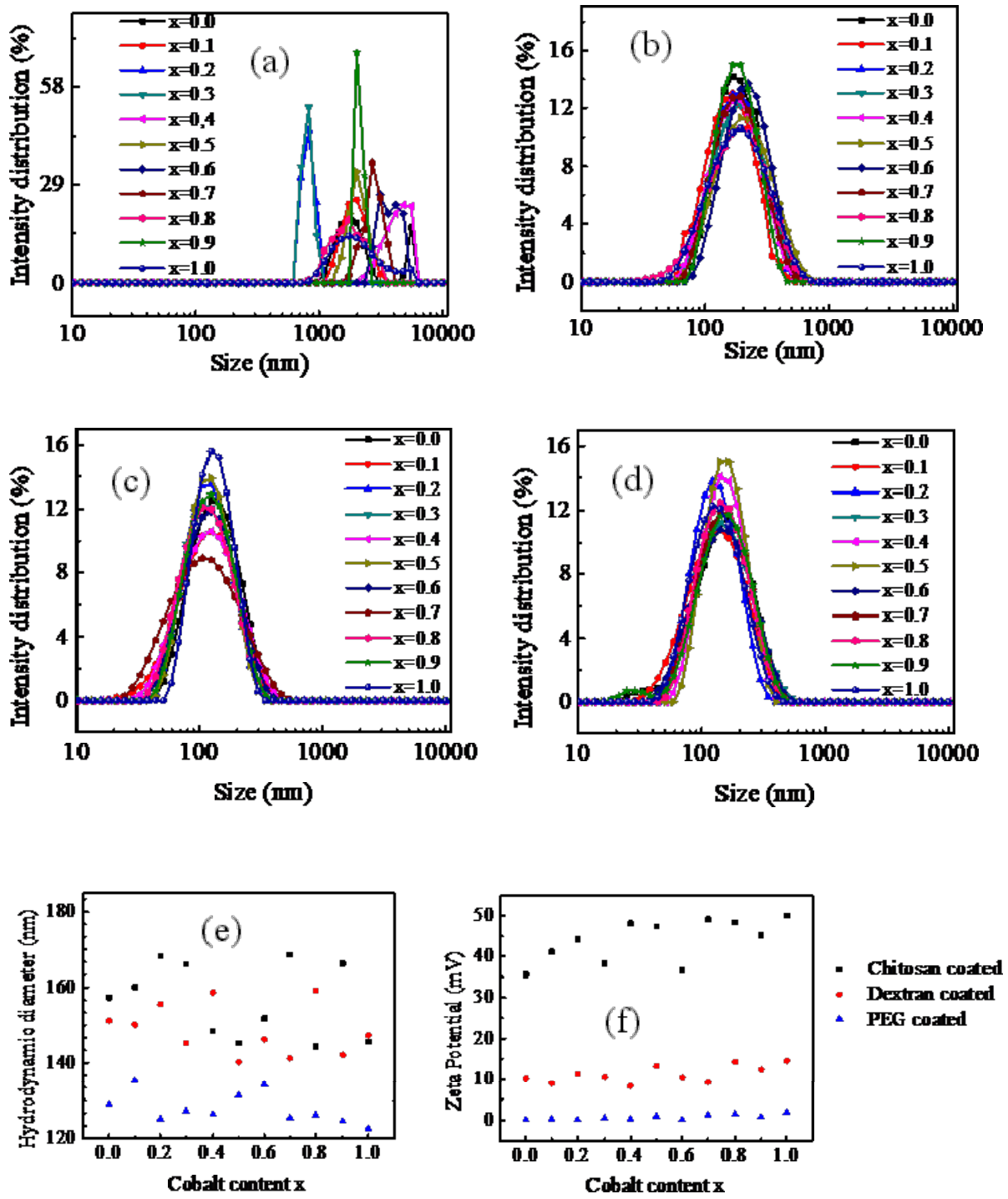

Figure 6.4: Hydrodynamic size distribution of (a) uncoated, (b) chitosan-coated, (c) dextran-coated, and (d) PEG-coated $Mg_{1-x}Co_xFe_2O_4$ ferrite nanoparticle. Variation of (e) average hydrodynamic size and (f) zeta potential with cobalt content x of chitosan-coated, dextran-coated, and PEG-coated of $Mg_{1-x}Co_xFe_2O_4$ ferrite nanoparticle.

6.2. Magnetic measurement

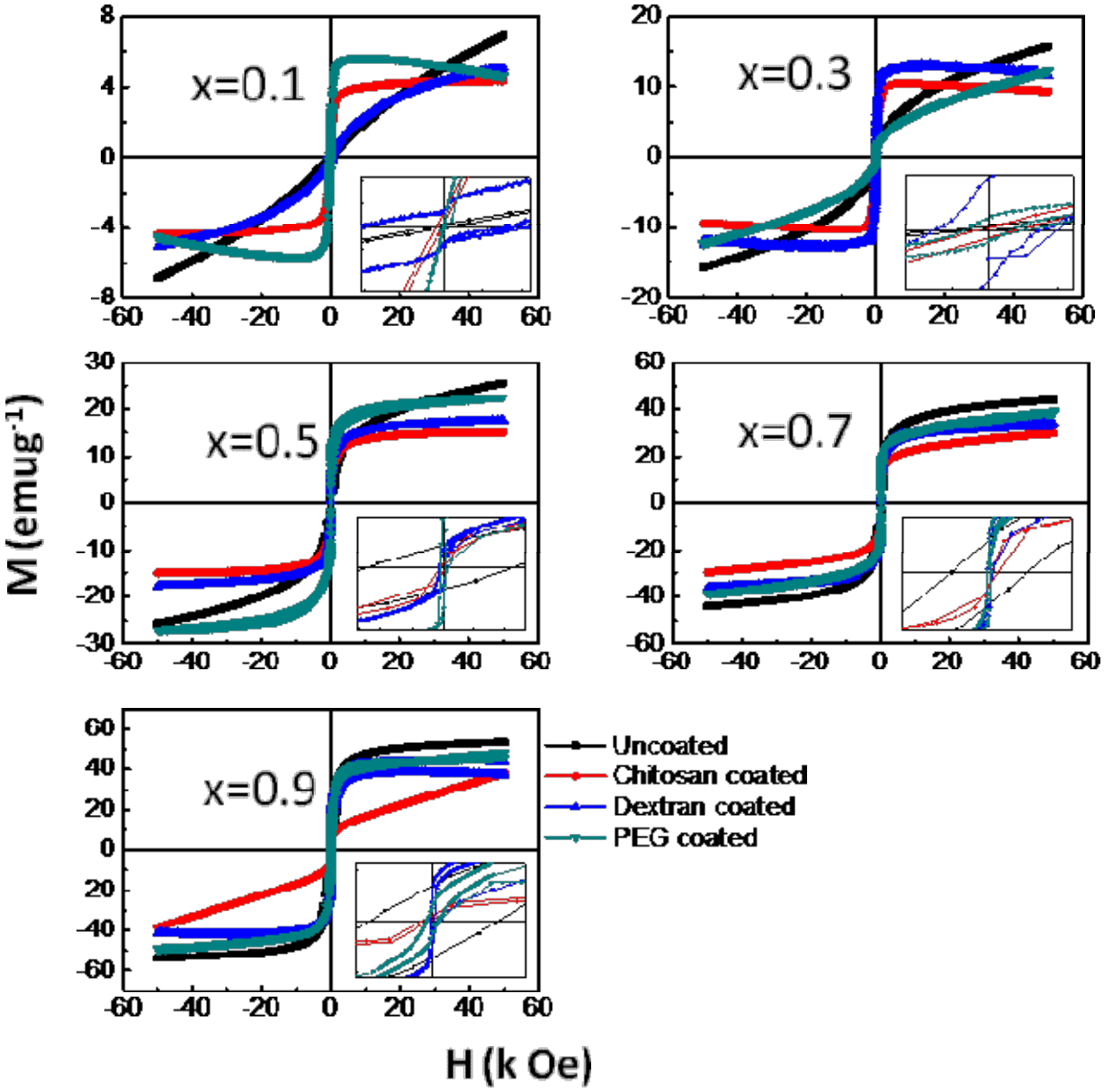

Figure 6.5 (A): M-H curve of uncoated, Chitosan-coated, Dextran-coated, PEG-coated $Mg_{1-x}Co_xFe_2O_4$ ferrites nanoparticles.

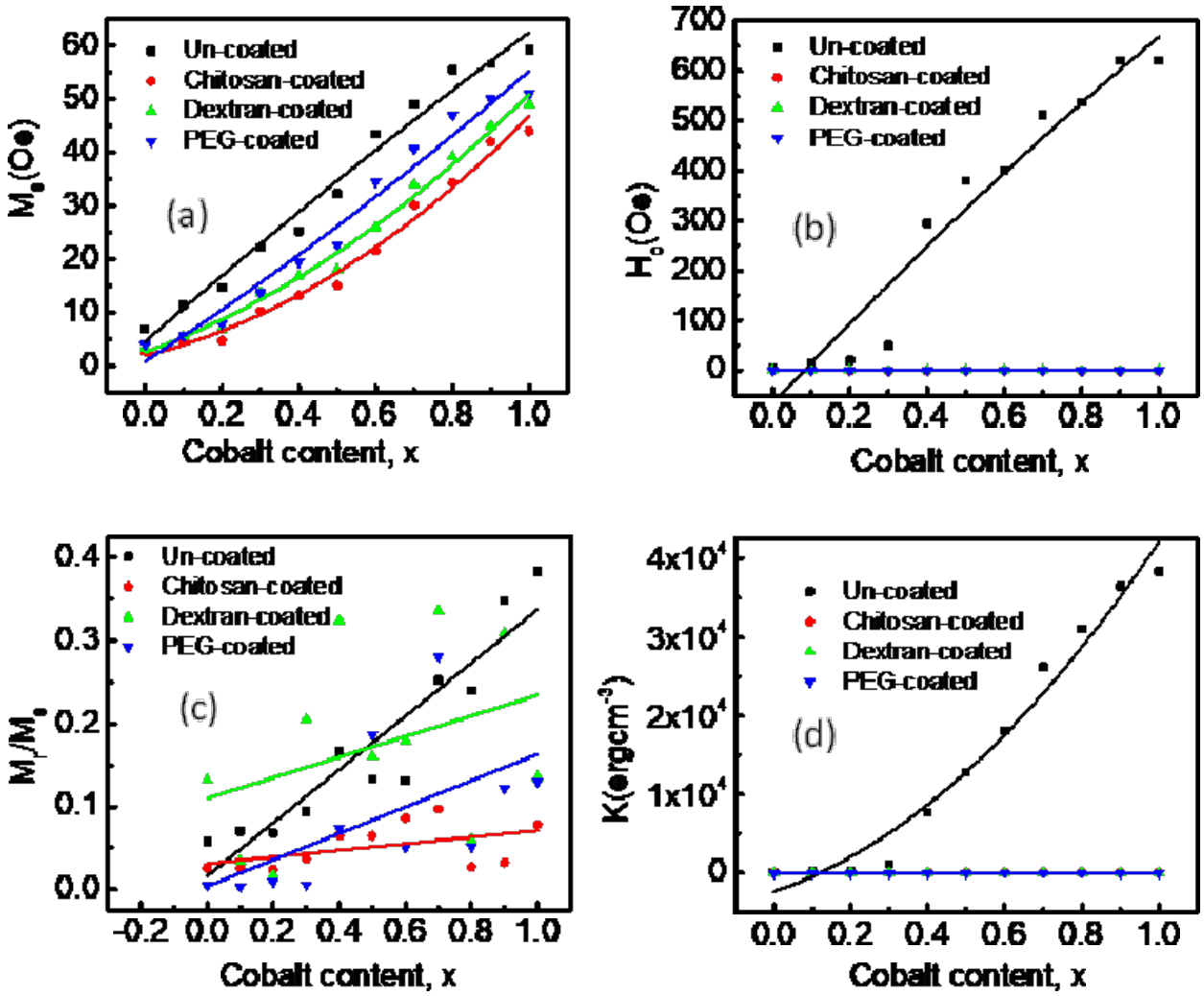

Figure 6.5 (B): Variation of (a) the saturation magnetization M_s, (b) Coercive field H_c, (c)remnant ratio M_r/M_s, and (d) anisotropy constant K with cobalt content x of uncoated, chitosan-coated, dextran-coated, and PEG-coated $Mg_{1-x}Co_xFe_2O_4$ nanoparticles.

Figure 6.5 (A) illustrates a variation in magnetization with an applied magnetic field of bare, Chitosan-coated, Dextran-coated, and PEG-coated MCFO ferrite nanoparticles. The saturation magnetic moment of uncoated particles is greater than that of coated particles because ferromagnetic cores are inside the nonmagnetic shell. Among the three coated materials, the thinner PEG-coating (PEG molecular weight 400) exhibits a higher magnetic moment, whereas relatively thicker chitosan-coated samples display a lower magnetic moment. As chitosan-coated MCFO ferrite nanoparticles with lower cobalt content are more dispersed in the solution, as observed in the previous TEM images, they exhibit less anisotropic energy, which gets a saturation magnetic moment in a comparatively lower magnetic field. On the other hand, the solution with a higher cobalt content, which displays more clusters in TEM pictures, exhibits an anisotropic nature and needs a much higher field to saturate. Dextran-coated samples, which produce more agglomeration in the TEM images with lower cobalt content, show a more anisotropic nature and gradually reach saturation with the applied magnetic field. A solution with a higher cobalt content shows less anisotropy and gets the saturation magnetic moment more quickly.

PEG-coated MCFO ferrite nanoparticles solution has less anisotropic energy and a sharp magnetic moment[129,144,215,264,265]. Figure 6.5 (B) represents a variation in saturation magnetization, coercive force, remnant magnetization, remnant ratio, and anisotropic energy with cobalt content, x of bare, chitosan, dextran, and PEG-coated MCFO ferrite nanoparticles. Since coated particles are dispersed in a solution, they have a significantly smaller coercive force, remnant magnetization, remnant ratio, and an anisotropic constant. The coercive field, remnant magnetization, remnant ratio, and anisotropic constant of chitosan-coated MCFO ferrite nanoparticles solution increases with increasing cobalt content due to increasing cluster size of

the nanoparticles in the solution with increasing cobalt content. The coercive force and magnetic anisotropy of the dextran-coated MCFO ferrite nanoparticles solution diminish with increasing cobalt because the degree of dispersity increases with increasing cobalt content. In the case of the PEG-coated sample, a slight increase in coercive force, remnant magnetization, remnant ratio, and an anisotropic constant was observed with increasing cobalt content. The variations in magnetic parameters of bare and coated particles greatly depend on the coating type. Although all coatings reduced the anisotropy significantly, the reduction of anisotropy with chitosan and dextran is much higher than PEG. Since PEG in this experiment is of molecular weight 400, the barrier to inhibit dipolar interaction was lower than chitosan and dextran. Again the coercive field and anisotropy of dextran-coated particles are lower than the chitosan-coated particles, showing that dextran provided a more efficient coating to the Co-rich compositions than chitosan.

6.3. Cytotoxicity Study

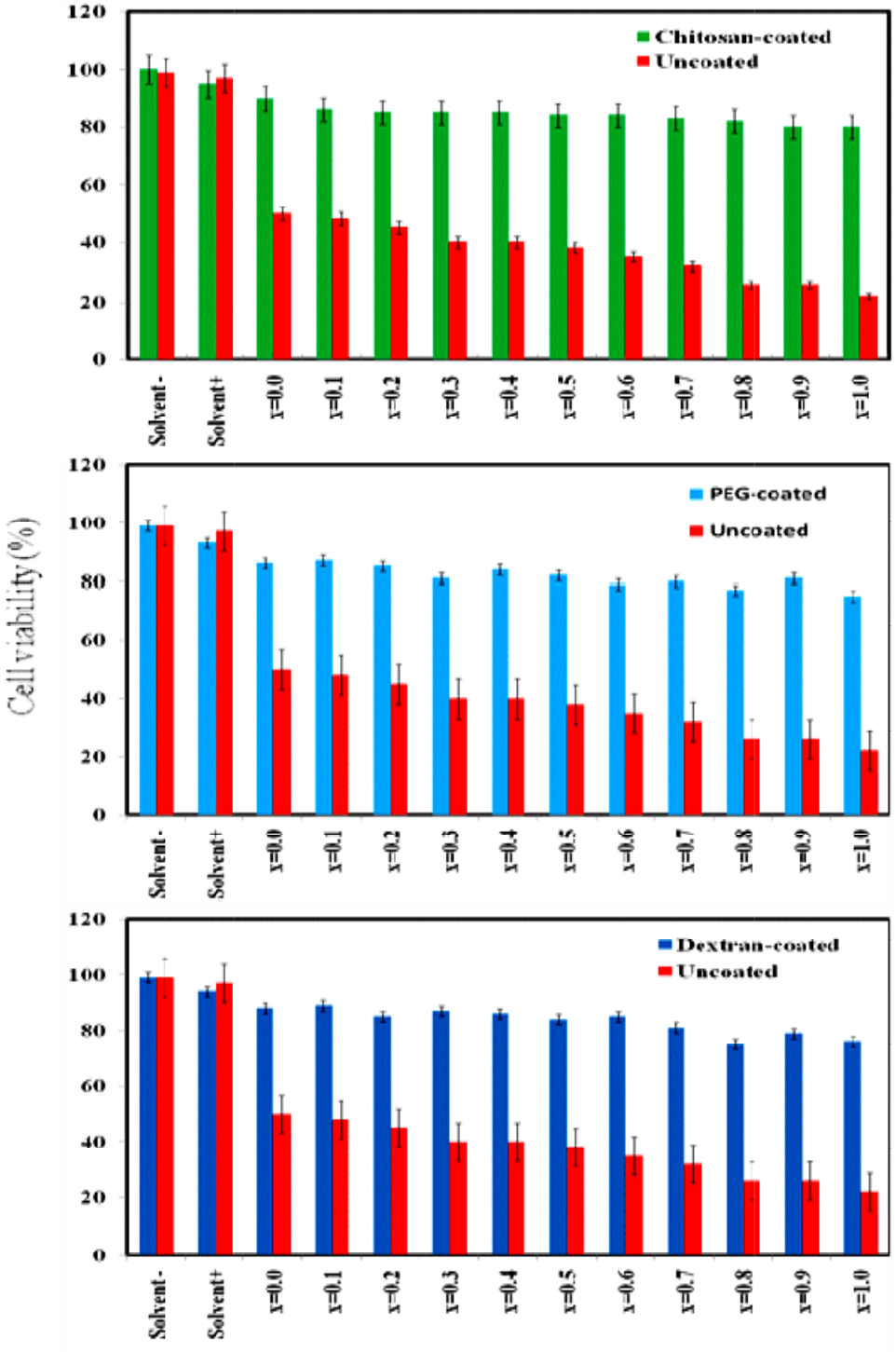

Figure 6.6: Cytotoxicity assay of Chitosan-coated, Dextran-coated, and PEG-coated of $Mg_{1-x}Co_xFe_2O_4$ ferrite nanoparticle.

Cytotoxicity measurement is essential because it allows researchers to assess and characterize the potentially harmful effects of chemicals or substances on living cells. Cytotoxicity assays are frequently used in fundamental research, drug development, and other areas to assess the ability of cytotoxic compounds to cause cell damage or death. It is essential to measure the cytotoxicity of substances before their in-vivo application, as this can help to ensure that they are not harmful to living organisms. Overall, cytotoxicity measurement is critical for assessing the safety and toxicity of new compounds and substances to prevent any adverse side effects. The measurement of cytotoxicity also plays a vital role in cancer research, as it helps to determine the effectiveness of new cancer treatments[266,267]. Figure 6.6 represents the cytotoxic assay of PEG-coated, chitosan-coated, and dextran-coated MCFO nanoparticles. They are found nontoxic though uncoated MCFOs are found toxic in the Hela cell line. After 48 hours of incubation, the viability of Hela cells with 4 mg/ml PEG-coated, chitosan-coated, and dextran-coated MCFOs was 75 to 90%.

6.4. Magnetic resonance angiography

Magnetic resonance angiography (MRA) is a considerably advanced clinical tool for noninvasive vascular imaging[22–24]. Therefore, it is extensively utilized to diagnose injuries like stenosis, intracranial aneurysms, aortic coarctation, aortic dissection, the cause of a stroke, heart disease, and blockage of vessels[25–29]. Also, MRA is one of the best additions for investigating suspected venous thrombosis inside the chest, abdomen, and pelvis, which will most probably replace formal X-ray angiography by resuming technical progress[27,30].

Contrast agents provide information on blood flow dynamics for tumour detection and enhancing the venous structures. In MRA, signal phase or intensity on the macroscopic motion of water

protons, yielding an intrinsic contrast between the stationary tissue and flowing blood[10]. MRA used two types of motion properties of blood: phase-contrast (PC) angiography and time-of-flight (TOF) angiography[26,31]. PC MRA visualizes and quantifies the blood flow by encoding the flow velocity in the MR signal phase. The movement of blood along a magnetic field gradient generates a change in the phase of the MR signal. In PC, pairs of pictures with distinct sensitivities to flow are received. For instance, a gradient of positive polarity is used to produce positive phase shifts during one image of each couple. For the other image, a negative polarity gradient induces negative phase shifts. Image subtraction eliminates motionless tissues so that entirely blood vessels are shown[32–34]. TOF in MRA is based on the concept that T_1 of moving water is effectively shorter than T_1 of standing water. The variation is attributed to the fact that, when stationary, the spins would be saturated by radiofrequency excitation.

Furthermore, fresh spins with total magnetization would replace the static spins increasing the signal when flowing. The idea of spin saturation is a key to the perception of TOF MRA systems. A contrast agent (CA) in the TOF MRA study increases the contrast between blood and tissue, shortening the T_1 relaxation time. The vasculature tree was shown more precisely with CA in the TOF MRA study[35–37].

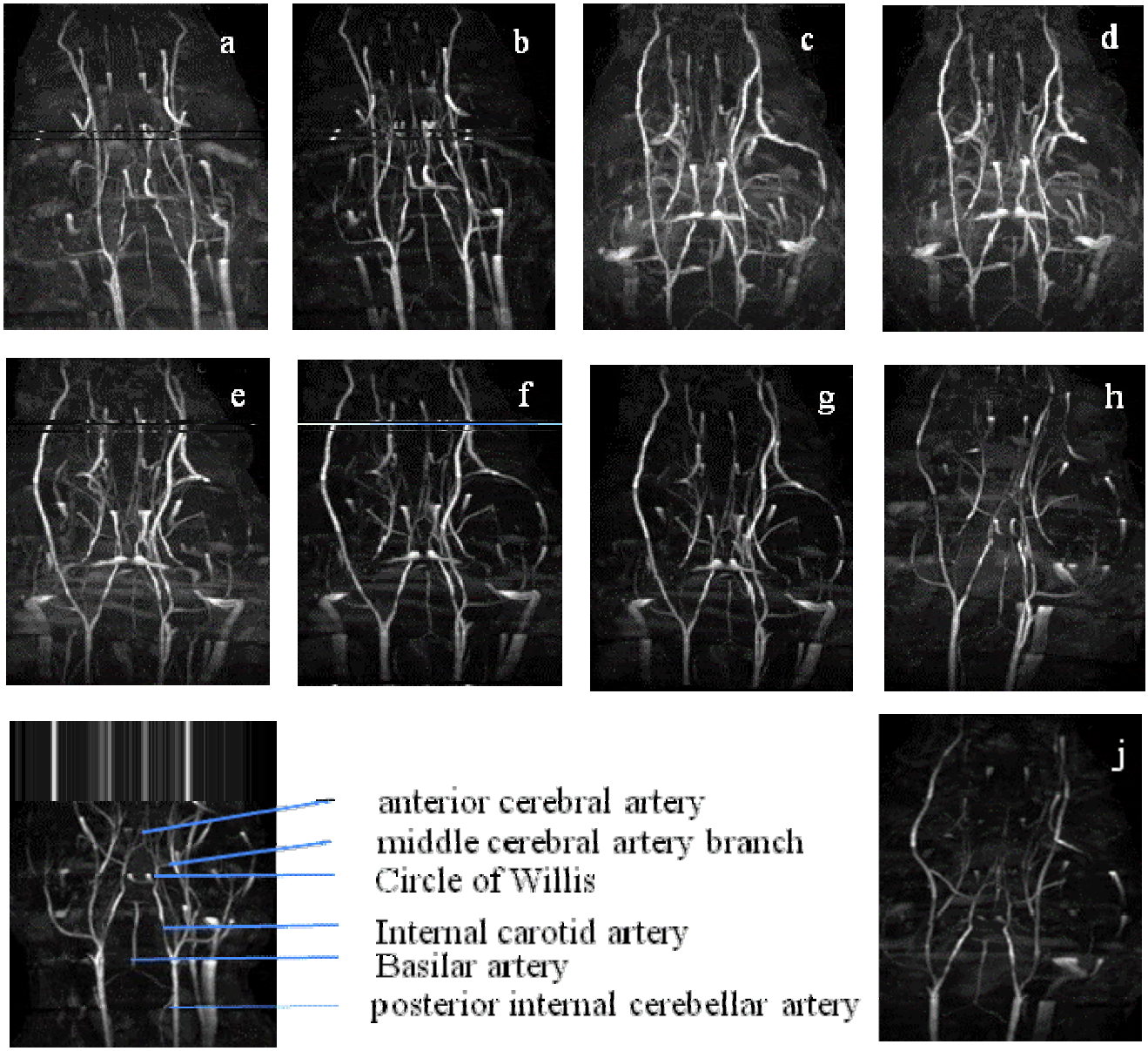

Figure 6.7: The MRA images of rat brain taken a) without an agent, b) half an hour, c) 1 hour, d) 2 hours, e) 3 hours, f) 4 hours, g) 12 hours, h) 24 hours, i) 48 hours, and j) 72 hours after injecting chitosan-coated $Mg_{0.2}Co_{0.8}Fe_2O_4$ ferrite nanoparticles contrast agent.

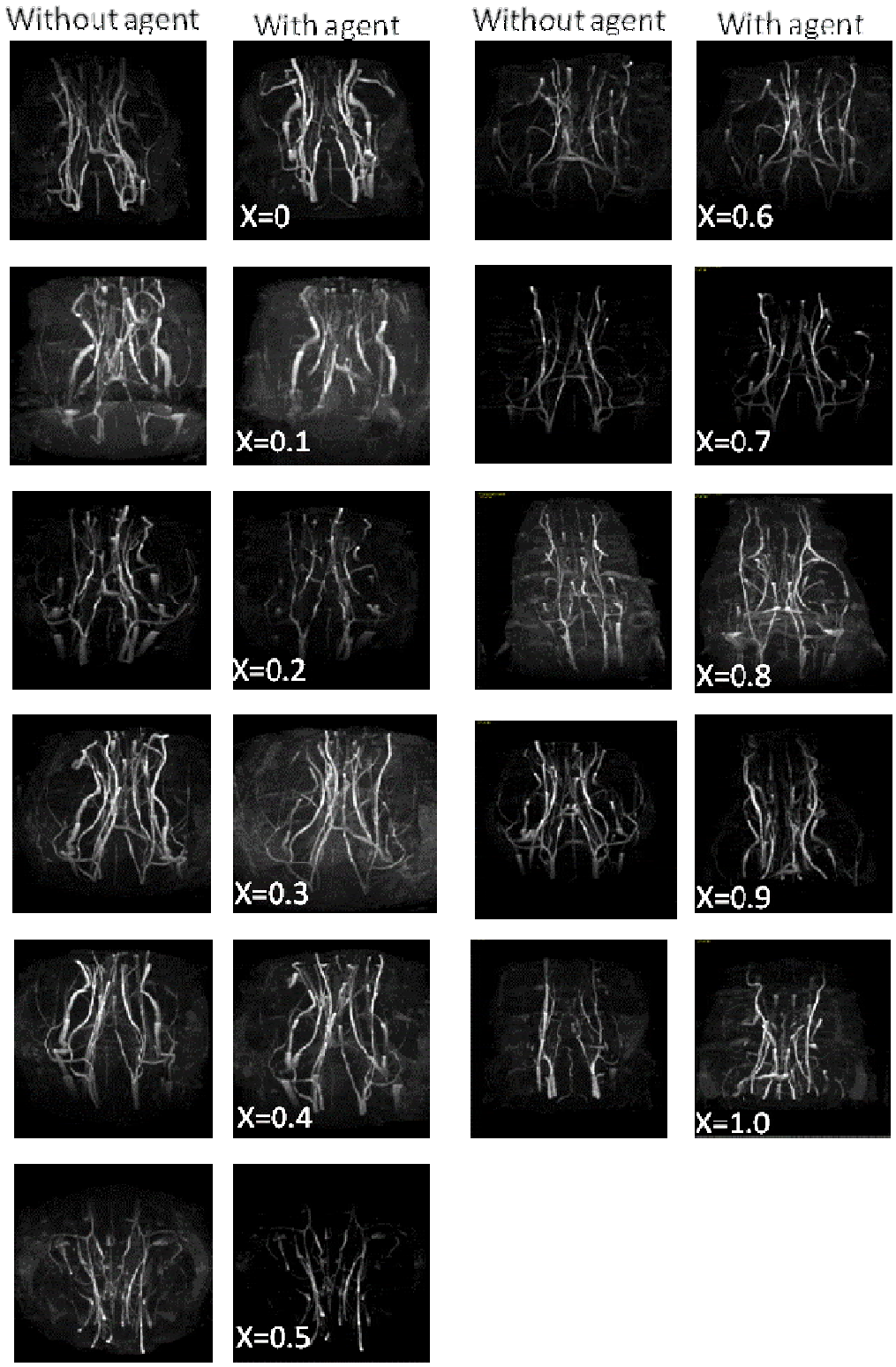

Figure 6.8: MRA images of rat brain without and with chitosan-coated $Mg_{1-x}Co_xFe_2O_4$ ferrite nanoparticles contrast agent.

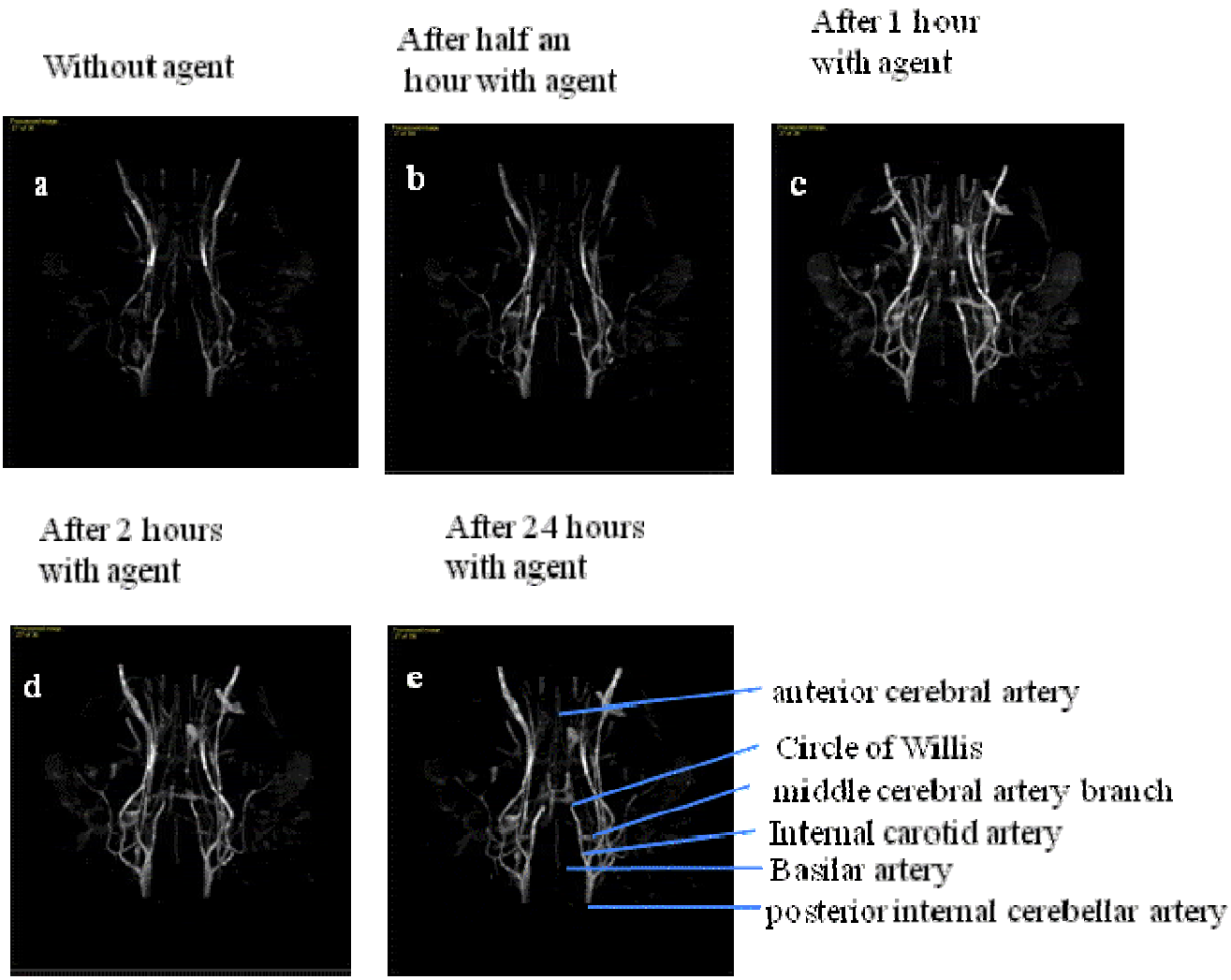

Figure 6.9: The MRA images of rat brains taken at different time intervals with PEG-coated $CoFe_2O_4$ ferrite nanoparticles contrast agent.

In the TOF experiment, arteries appeared hyperintense, which produced a significant signal difference between arteries and stationary tissues. This signal difference conceived a strong contrast for which the rat head's angiogram was visualized using the maximum intensity projection (MIP) algorithm. Magnetic nanoparticle intensifies this signal difference which produces better contrast of the image. In this view, PEG-coated, chitosan-coated, and dextran-coated$Mg_{1-x}Co_xFe_2O_4$ ferrite nanoparticles were injected through the tail vein without altering the rat's position. After injecting 1 ml PEG-coated or chitosan-coated or dextran-coated $Mg_{1-x}Co_xFe_2O_4$ ferrite nanoparticles with 2 mg/ml concentration, TOF images were taken after different time intervals. MRA of other rats with and without PEG-coated, chitosan-coated, and dextran-coated $Mg_{1-x}Co_xFe_2O_4$ ferrite was produced using the MIP algorithm. A significant number of tiny blood vessels were visible in the MRA after injecting the Chitosan-coated, Dextran-coated, and PEG-coated agents. More precise images were obtained after 0.5 hours of injecting Dextran-coated agents. Similar results were found after 1 hour of applying Chitosan-coated and Dextran-coated agents. The intensity of MRA with Dextran-coated images decreases slowly after 1 hour of administering agents. After 72 hours of injecting Chitosan-coated agents, the intensity gradually decreases with time. Figure 6.9 shows the MRA of the PEG-coated $CoFe_2O_4$ ferrite agent taken at different time intervals. Clear images were found 1 hour subsequent injecting the agent. Numerous arteries are visible in the MRA with PEG-coated MCFO ferrite agent, most obscure without contrast agent. The middle cerebral arteries (MCAs), a bundle of vessels of the posterior cerebral arteries (PCA), and the anterior cerebral artery complex (ACA) are noticeable in the MIP images along the x-axis[49,130–133,268,269]. A significant number of tiny blood vessels were seen in the MRA, taken after 1 hour following injecting the PEG-coated $Mg_{1-x}Co_xFe_2O_4$ ferrite agent. Images of MRA after 2 and 24 hours with PEG-coated

$CoFe_2O_4$ ferrite agent were also clear. It indicated that the PEG-coated sample had been circulating in the blood for quite a long time. Figure 6.10 represents the MRA of the rat head along with the x-axis one hour after injecting PEG-coated $Mg_{1-x}Co_xFe_2O_4$ ferrite.

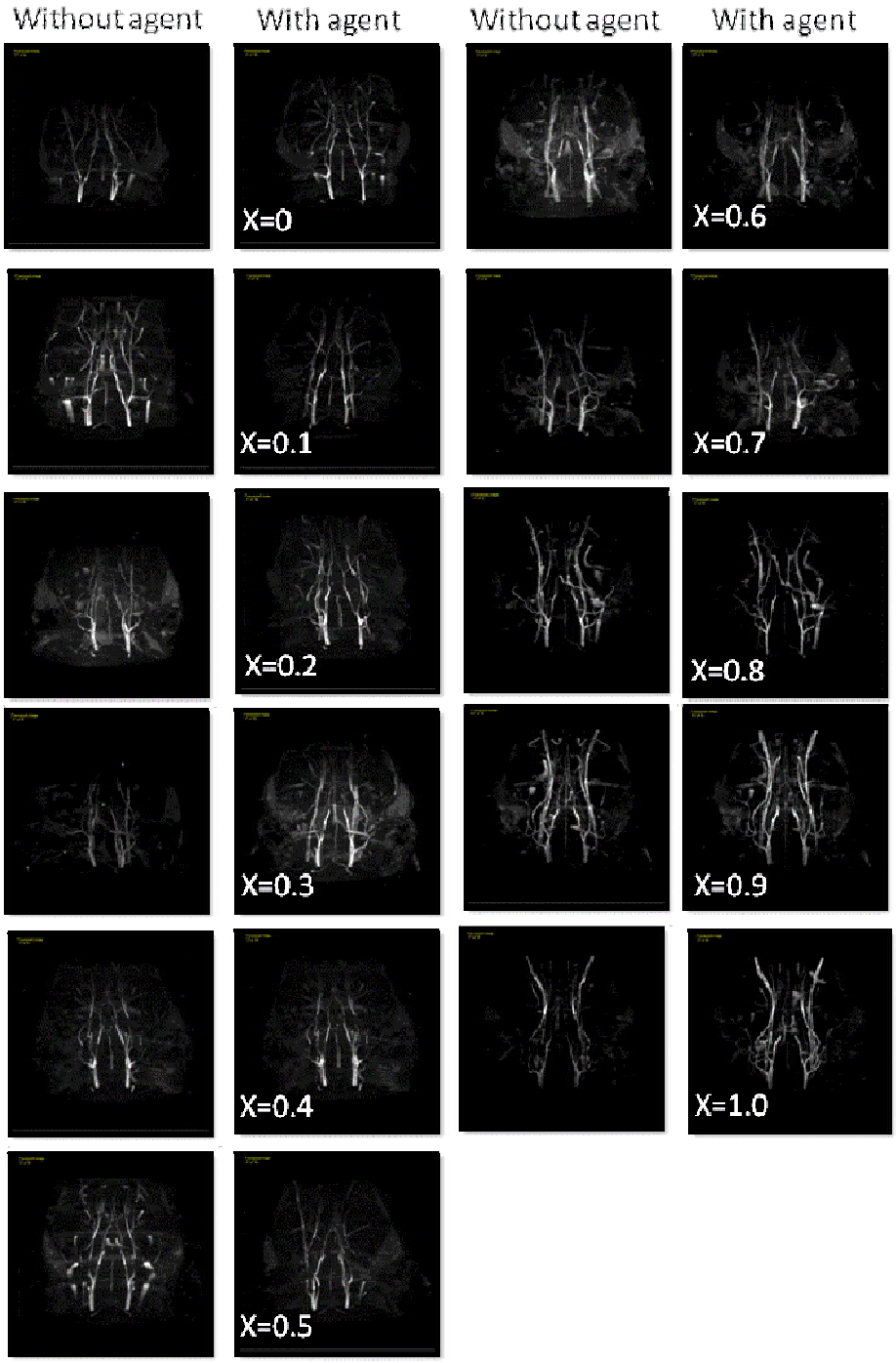

Figure 6.10: MRA images of rat brain without and with PEG-coated $Mg_{1-x}Co_xFe_2O_4$ ferrite nanoparticles contrast agent.

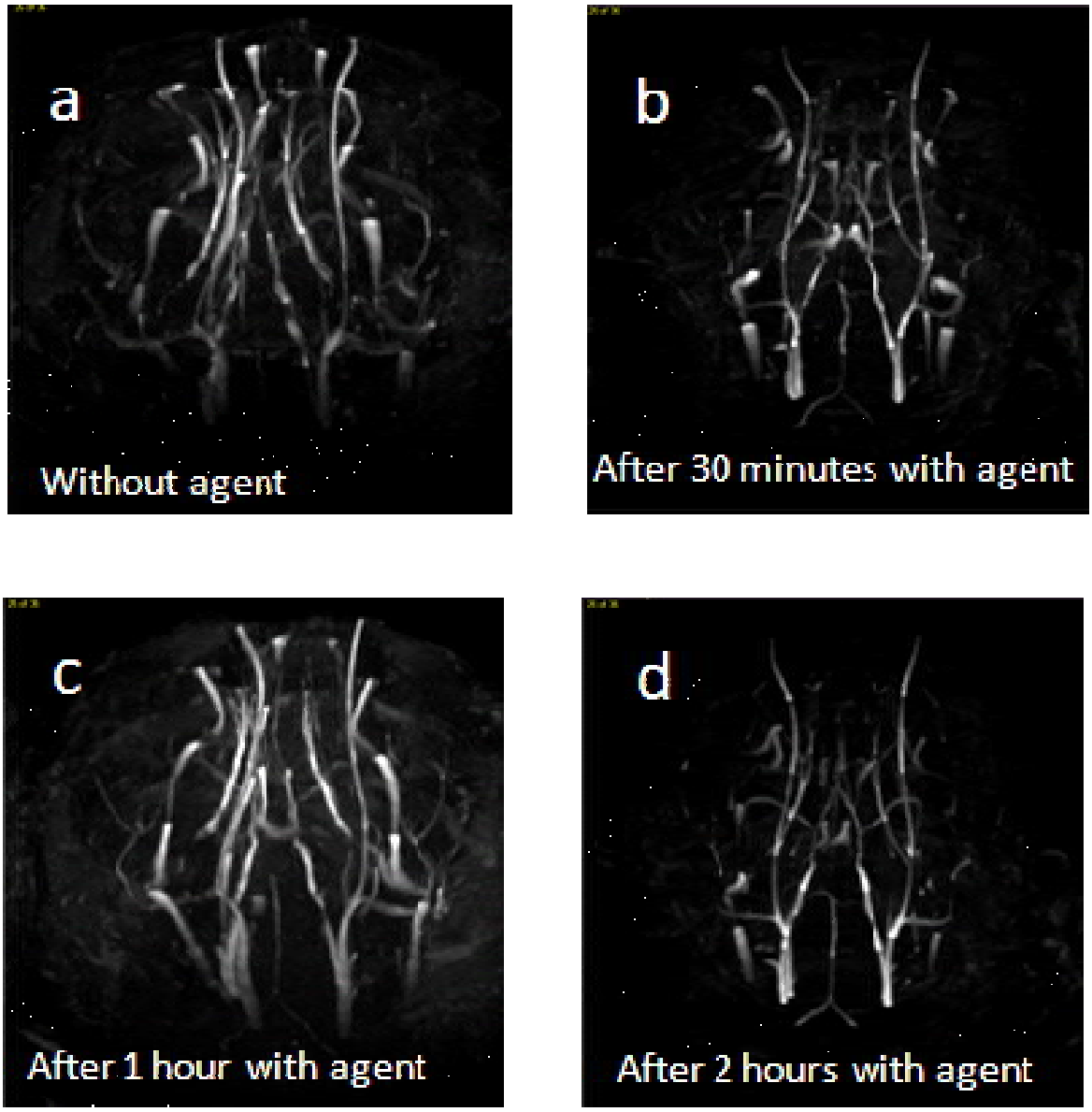

Figure 6.11: The MRA images of rat brains taken at different intervals of time with dextran-coated $Mg_{0.2}Co_{0.8}Fe_2O_4$ ferrite nanoparticles contrast agent.

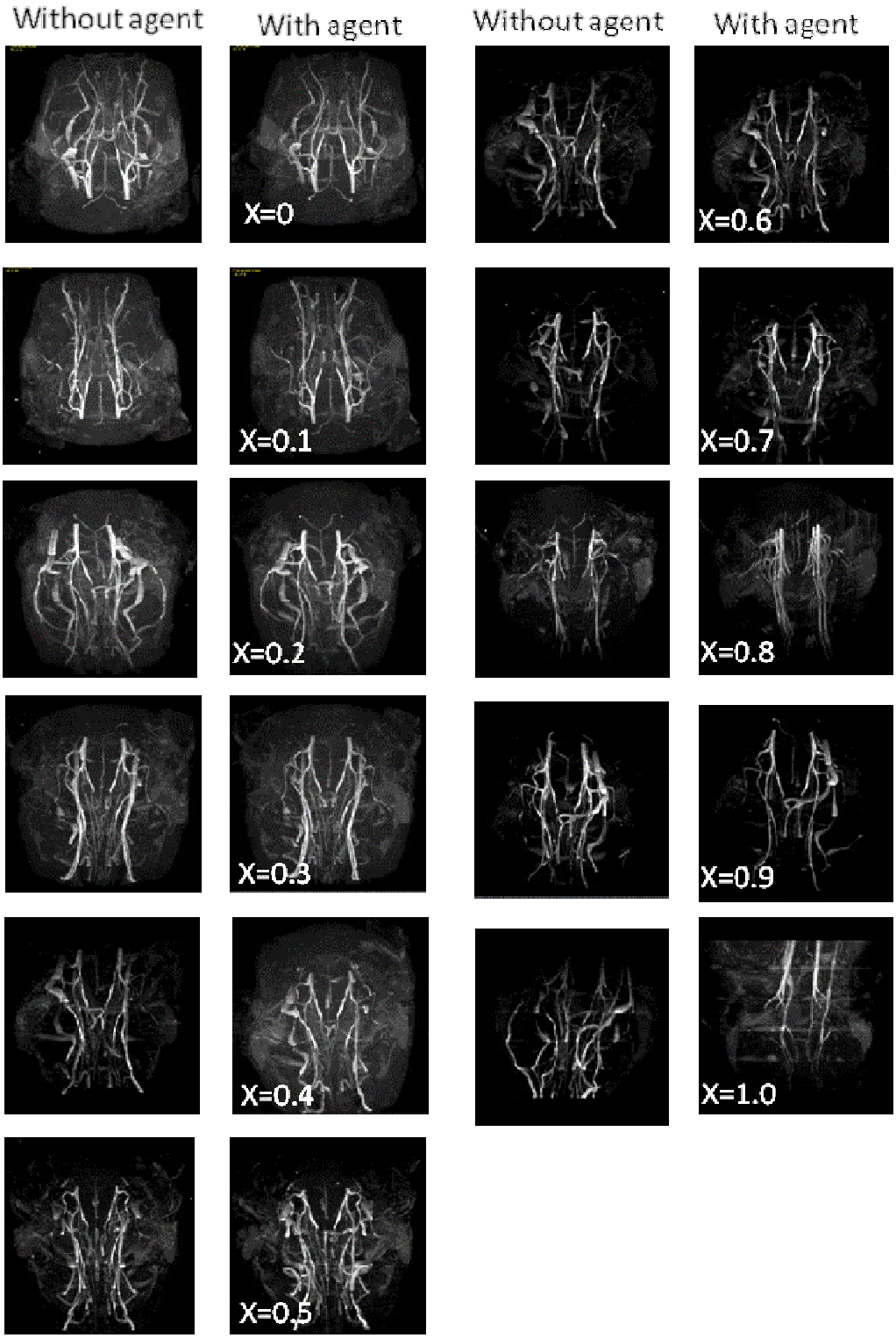

Figure 6.12: MRA images of rat brain without and with dextran-coated $Mg_{1-x}Co_xFe_2O_4$ ferrite nanoparticles contrast agent.

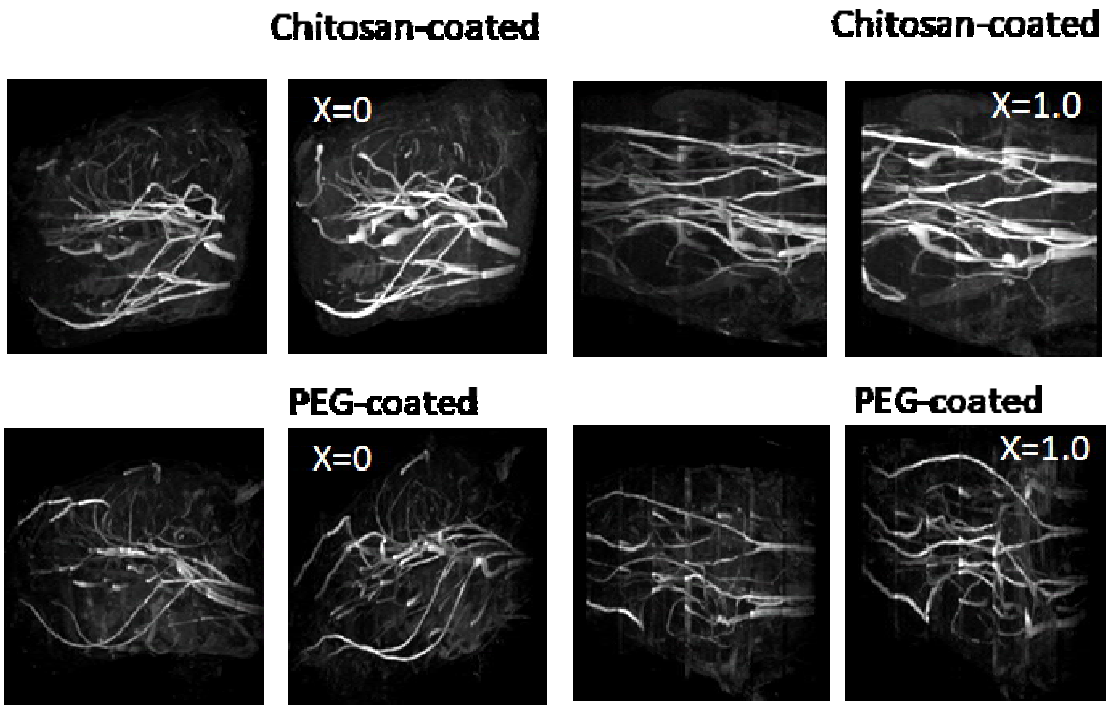

Figure 6.13: Sagittal view of MRA with chitosan-coated and PEG-coated $Mg_{1-x}Co_xFe_2O_4$ ferrite nanoparticles contrast agent.

Conclusion

In this study, cobalt-substituted magnesium ferrite MCFO [$Mg_{1-x}Co_xFe_2O_4$ ($0 \leq x \leq 1$ with $\Delta x = 0.1$)] and polymer nanohybrid were synthesized by chemical co-precipitation to tune structure-properties relationship to examine their potentials for biomedical applications. Initially, the applications of as-synthesized nanoparticle-chitosan nanohybrid without further heat treatment were examined. From FTIR, Raman, and Mössbauer spectrum, we observe an increase of cobalt on octahedral sites with the rise of x. Therefore, adding cobalt condenses covalent bonds at the octahedral site and expands covalent bonds at the tetrahedral site. The peak shifts of the absorption bands representing A and B FTIR sites indicate an excellent coating with chitosan with an optimum hydrodynamic diameter and zeta potential. Room temperature Mössbauer spectra of MCFO show that the Mössbauer absorption area of A site decreases, and the Mössbauer absorption area of B site increases with x. Mössbauer spectra and M-H hysteresis loops at room temperature confirmed that a transition from fast relaxation (superparamagnetic) to a mixed slow/fast (superparamagnetic/ ferrimagnetic) relaxation occurs with cobalt content. The magnetization increases with x in the bare condition because of the rise in A-B interactions and higher magnetic moment of Co. The cobalt ions tend to occupy the octahedral B site, which enhances the A-B interaction. The T_{max} and SLP of hyperthermia increase with x due to a higher magnetic moment and anisotropy.

The values of T_2 relaxivity, r_2, increase with x because of the rise of magnetic moment, susceptibility, and anisotropy. The intensity of T_2 fast spin echo MRI images and T_2 mapping MRI shows that the contrast enhancement increases with increasing cobalt content and concentration of the solution. The r_2 relaxivities of chitosan-coated MCFO ferrite nanoparticles

vary between 15.2 to 185.5 $mM^{-1}s^{-1}$, which shows an almost linear increase with the saturation magnetic moment and Co content. Variations of the relaxivity with the anisotropy are scattered, but there is an increasing trend of relaxivity with anisotropy and susceptibility. In-vivo studies of rat-brain show 29.2 to 41.6% fall of intensity. Intensity drop after 60 minutes of injection of contrast agent. The present study validates that the chitosan-coated MCFO ferrite nanoparticles are potential candidates for hyperthermia therapy and MRI contrast. However, adding cobalt reduces the dose concentration required for hyperthermia therapy and MR imaging. The as-synthesized particles were annealed at 200, 400, 600, and 800°C for the detailed study in thermotherpeutic cancer applications, namely magnetic nanoparticle-mediated hyperthermia and laser ablation. The lattice parameter, the particle size, the X-ray density, the ionic radius of the A and B site, the hopping length of the A and B site, the bond length of the A and B site, the cation-cation distance, and cation-anion distance of the nanoparticles increase with an increase in cobalt content and annealing temperature. As the Co^{2+} content increased, FTIR spectroscopy shows that the higher frequency band shifted to a lower frequency region, and the lower frequency band shifted to a higher frequency region because Co^{2+} (0.072 nm) took the place of Mg^{2+} (0.065 nm) at the A site, resulting in a reduction of the covalent bond. Additionally, at the B site, Fe^{2+} (0.0645 nm) replaces Co^{2+} (0.072 nm), which increases the covalent bond. The Raman spectroscopy of magnesium-rich compositions displays a preference for normal spinel structures, while that of cobalt-rich compositions reveals a preference for mixed spinel structures. Both Raman spectroscopy and FTIR spectroscopy yield comparable results. The value of force constant F_{CT} decreases, and F_{CO} increases with increasing Co^{2+} content x because the A site's bond length decreases, and the B site's bond length increases with an increase in Co^{2+} content. TEM studies revealed that the lognormal distribution of the particle size was in the

range of 4.3-9.6 nm for the annealing temperature of 200^{o}C, 5.5-15.8 nm for the annealing temperature of 400^{o}C, 10.1-24.9 nm for 600^{o}C and 15.9-30.3 nm for 800^{o}C.

Further, it was found from the HRTEM studies that the degrees of crystallinity increase with increasing cobalt content and annealing temperature.TEM images indicate that coated particles are dispersed in the solution. Chitosan-coated particles are more dispersed in the solution with lower cobalt content, and dextran-coated particles are more dispersed in the solution with higher cobalt content. The dispersity of PEG-coated solutions does not depend on the cobalt concentration because of the steric repulsion. The hydrodynamic diameter of the chitosan, dextran, and PEG-coated nanoparticles are 144-170 nm, 122-135 nm, and 140-160 nm, respectively. It decreases with increasing solution concentration and temperature, which is favorable for many biomedical applications. A lower polydispersity index (0.101-0.239) and higher zeta potential value (35-59 mV) of chitosan-coated particles ensure the higher stability of the solution. The saturation magnetization, coercivity, remanent magnetization, remnant ratio, and anisotropy constant of the bare magnesium-cobalt ferrite nanoparticles increase with increasing cobalt content and annealing temperature. Hyperthermia studies revealed that both the specific loss power (SLP) and maximum temperature T_{max} attained by all compositions for the nanohybrid concentrations of 0.5, 1, 2, and 4 mg/ml increase with the increase of particle size, reaches a peak at around 10-15 nm and then sharply decreases. It shows that increased particle size and Co-content increase both the anisotropy and particle volume, which are detrimental to Neel and Brownian relaxation and severely impede hyperthermia performance.

As-synthesized MCFO-polymer nanohybrid potential applications were examined as the contrast agents for magnetic resonance angiography (MRA). The as-synthesized nanoparticles were coated with chitosan, dextran, and PEG to synthesize MCFO-nanohybrid formulations.

Magnetization studies by PPMS revealed that compared to uncoated nanoparticles, all coated nanoparticles have significantly lower coercive forces and anisotropy energies. For chitosan-coated $Mg_{1-x}Co_xFe_2O_4$ ferrite nanoparticle solutions, the average hydrodynamic diameter stands at 144 nm to 170 nm. The poly dispersive index (PDI) exists at 0.101 to 0.239, and the Zeta potential remains 35 to 59 mV. For PEG-coated $Mg_{1-x}Co_xFe_2O_4$ ferrite nanoparticle solutions, the average hydrodynamic diameter stands at 122 nm to 135 nm. The solution's poly dispersive index (PDI)is 0.235 to 0.371, and the Zeta potential stands at 0 to 3 mV. For dextran-coated $Mg_{1-x}Co_xFe_2O_4$ ferrite nanoparticle solutions, the average hydrodynamic diameter is 140 nm to 160 nm. The solution's poly dispersive index (PDI) is 0.221 to 0.369, and the Zeta potential stands at 8 to 15 mV. Cytotoxicity experiments on HeLa cells revealed that chitosan-coated, dextran-coated, and PEG-coated magnesium cobalt ferrite nanoparticles are viable for the HeLa cells. The particles with lower cobalt content are more viable for the HeLa cells. In MRA study, Chitosan-coated agents gradually reduce their effects after 72 hours. PEG-coated agents circulated for more time in the blood. The impacts of dextran-coated reduce gradually after half an hour. In this study, extensive MRA studies were conducted with all three nanohybrids with variations in the composition of MCFO. Chitosan-MCFO nanohybrid produces better MRA images with lower cobalt concentrations. On the other hand, PEG-coated and dextran-coated samples provide better images with higher cobalt concentrations. The diminishing effects of the contrast enhancement were also studied after the initial inoculation with time. It shows that contrast enhancements diminish faster for dextran-MCFO nanohybrid and slower for PEG-MCFO nanohybrid, while chitosan-MCFO nanohybrid diminishes between the abovementioned nanohybrid.

Hence, cobalt ferrite is the better option for hyperthermia treatment, and magnesium ferrite is the better choice for MRI agents. Based on the results of this study, the chitosan-coated magnesium-cobalt ferrite having a lower x value ($0.2 \leq x \leq 0.4$) is a better choice to perform both the hyperthermia and MRI studies simultaneously. Also, PEG-coated samples should be the better choice for magnetic resonance angiography images for prolonged circulation half-time applications.

Reference

1. Sharma, V. K., Filip, J., Zboril, R. & Varma, R. S. Natural inorganic nanoparticles-formation, fate, and toxicity in the environment. *Chem. Soc. Rev.* **44**, 8410–8423 (2015). doi:10.1039/c5cs00236b.
2. Arruebo, M., Fernández-pacheco, R., Ibarra, M. R. & Santamaría, J. Magnetic nanoparticles for drug delivery. *Nanotoday*. **2(3)**, 22–32 (2007). doi:10.1016/S1748-0132(07)70084-1.
3. Hoque, S. M., Khairul, I. M., Amitra, H., Manjurul, H. M., Maritim, S., Daniel, C., & Hyder, F. Comparative Study of Specific Loss Power and Transverse Relaxivity of Spinel Ferrite Nanoensembles Coated With Chitosan and Polyethylene Glycol. *Front. Nanotechnol*. **3**, 1–13 (2021). doi:10.3389/fnano.2021.644080.
4. Habib, A. H., Ondeck, C. L., Chaudhary, P., Bockstaller, M. R. & Mchenry, M. E. Evaluation of iron-cobalt/ferrite core-shell nanoparticles for cancer thermotherapy. *J. Appl. Phys*. **103**, 7–10 (2008). doi:10.1063/1.2830975.
5. Gupta, A. K. & Gupta, M. Synthesis and surface engineering of iron oxide nanoparticles for biomedical applications. Biomaterials **26**, 3995–4021 (2005). doi:10.1016/j.biomaterials.2004.10.012.
6. Chomoucka, J., Drbohlavovaa, J., Huskab, D., Adamb, V., Kizekb, R. & Hubalek, J. Magnetic nanoparticles and targeted drug delivering. *Pharmacol. Res*. **62**, 144–149 (2010). doi:10.1016/j.phrs.2010.01.014.
7. Hakeem, A., Alshahrani, B., T., Muhammad, G., Alhossainy, M. H., Laref, A., Khan, A.

R., Ali, A., Farid, H. M. T., Ghrib, T., Ejaz, S. R. & Khosa, R. Y. Magnetic, dielectric and structural properties of spinel ferrites synthesized by sol-gel method. *J. Mater. Res. Technol*. **11**, 158–169 (2021). doi:10.1016/j.jmrt.2020.12.064.

8. Stuart, B. Chapter 1: Intruduction. Infrared Spectroscopy: Fundamentals and Applications. *John Wiley & Sons, Ltd*. 1-13 (2004). ISBNs: 0-470-85427-8 (HB); 0-470-85428-6 (PB).

9. Shakil, M. S. Hasan, M. A., Uddin, M. F., Islam, A., Nahar, A., Das, H., Khan, M. N. I., Dey, B. P., Rokeya, B. & Hoque, S. M. In Vivo Toxicity Studies of Chitosan-Coated Cobalt Ferrite Nanocomplex for Its Application as MRI Contrast Dye. *ACS Appl. Bio Mater*. **30**, 1-13 (2020). doi:10.1021/acsabm.0c01069.

10. Hoque, S. M., Huanga, Y., Coccod, E., Maritimc, S., Alessandro, D. S., Erik., M. S., Comana, D. & Hyder, F. Improved specific loss power on cancer cells by hyperthermia and MRI contrast of hydrophilic $Fe_xCo_{1-x}Fe_2O_4$ nanoensembles. Contrast Media Mol. Imaging **11**, 514–526 (2016). doi:10.1002/cmmi.1713.

11. Tang, J. T., Zeng, X. W., Xia, Q. S., Wang, X. X. & Zhao, D. L. Preparation and inductive heating property of Fe_3O_4–chitosan composite nanoparticles in an AC magnetic field for localized hyperthermia. *J. Alloys Compd*. **477**, 739–743 (2009). doi:10.1016/j.jallcom.2008.10.104.

12. Sonvico, F., Mornet, S., Vasseur, S., Dubernet, C., Jaillard, D., Degrouard, J., Hoebeke, J., Duguet, E., Colombo, P. & Couvreur, P. Folate-Conjugated Iron Oxide Nanoparticles for Solid Tumor Targeting as Potential Specific Magnetic Hyperthermia Mediators : Synthesis, Physicochemical Characterization, and in Vitro Experiments. *Bioconjugate Chem*. **16**, 1181–1188 (2005). doi:10.1021/bc050050z.

13. Amiri, S. & Shokrollahi, H. The role of cobalt ferrite magnetic nanoparticles in medical

science. *Mater. Sci. Eng*. C **33**, 1–8 (2013). doi:10.1016/j.msec.2012.09.003.

14. Khanna, L. & Tripathi, S. K. Effect of temperature on the structural, morphological and magnetic properties of magnesium ferrite nanoparticles. *Res. J. Recent Sci*. 6, 1–9 (2017). issn: 2277-2502.

15. Wang, Y. J. Superparamagnetic iron oxide based MRI contrast agents : Current status of clinical application. *Quant. Imaging Med Surg*. **1**, 35-40 (2011). doi:10.3978/j.issn.2223-4292.2011.08.03.

16. Mfe, T., Kim, D., Zeng, H., Ng, T. C. & Brazel, C. S. $MFe_2^{3+}O_4$ (M = Mn^{2+}, Fe^{2+}, and Co^{2+}) inverse spinel ferrites for potential use as phase-contrast agents in medical MRI. *J. Magn. Magn. Mater*. **321**, 3899–3904 (2009). doi:10.1016/j.jmmm.2009.07.057.

17. Hong, S. Chitosan-coated Ferrite (Fe_3O_4) Nanoparticles as a T_2 Contrast Agent for Magnetic Resonance Imaging. Journal of the Korean Physical Society. **56**, 868–873 (2010). Doi:10.3938/jkps.56.868.

18. Muldoon, L. L., Gahramanov, S., Li, X., Deborah, J. M., Dale, F. K. & Edward, A. N. Dynamic magnetic resonance imaging assessment of vascular targeting agent effects in rat intracerebral tumor models. *Neuro-Oncology*. **13**, 51–60 (2011). doi:10.1093/neuonc/noq150.

19. Norman, B., Thomas, S. R., Pratt, R. G., Samaratunga, R. C. & Vt, A. R. S. T. T_1 and T_2 Weighted Magnetic Resonance Imaging of Excitotoxin Lesions and Neural Transplants in Rat Brain in Viva. *Experimental Neurology*. **109(2)**, 164–170 (1990). doi:10.1016/0014-4886(90)90070-9.

20. Valdés-hernández, P. A., Sumiyoshi, A., Nonaka, H., Haga, R., Aubert-Vásque, E., Ogawa, T., Iturria-Medina1, Y., Riera, J. J., & Kawashima, R. An in vivo MRI template

set for morphometry, tissue segmentation, and fMRI localization in rats. *Frontiers in Neuroinformatics*. **5**, 1–19 (2011). doi: 10.3389/fninf.2011.00026.

21. Bin, N. H., Song, I. C. & Hyeon, T. Inorganic nanoparticles for MRI contrast agents. *Adv. Mater*. **21**, 2133–2148 (2009). doi:10.1002/adma.200802366.

22. Kuo, A. H., Nagpal, P., Ghoshhajra, B. B. & Hedgire, S. S. Vascular magnetic resonance angiography techniques. *Cardiovasc. Diagn. Ther*. **9**, S28–S36 (2019). doi: 10.21037/cdt.2019.06.07.

23. Young, P. & Brinjikji, W. Update on state of the art magnetic resonance angiography techniques. *J. Vasc. Diagnostics.* **3**, 9-16 (2015). doi:10.2147/jvd.s73647.

24. Kato, Y., Ambale-Venkatesh, B., Kassai, Y,. Kasuboski, L., Schuijf, J., Kapoor, K., Caruthers, S. & Lima, J. A. C. Non-contrast coronary magnetic resonance angiography: current frontiers and future horizons. Magn. *Reson. Mater. Physics, Biol. Med*. **33**, 591–612 (2020). doi:10.1007/s10334-020-00834-8.

25. Alkashkari, W., Albugami, S. & Hijazi, Z. M. Management of coarctation of the aorta in adult patients: State of the art. *Korean Circ. J*. **49**, 298–313 (2019). doi: 10.4070/kcj.2018.0433.

26. Polachini, J. I. & Magalhães, A. C. Principles of magnetic resonance angiography. *Rev. Hosp. Clin. Fac. Med. Sao. Paulo*. **50**, 205–211 (1995). pmid: 8560151.

27. Kiruluta, A. J. M. & González, R. G. Magnetic resonance angiography: physical principles and applications. Handb. Clin. Neurol. **135**, 137–149 (2016). doi:10.1016/B978-0-444-53485-9.00007-6.

28. Nederkoorn, P. J., Van Der Graaf, Y. & Hunink, M. G. M. Duplex ultrasound and magnetic resonance angiography compared with digital subtraction angiography in carotid

artery stenosis: A systematic review. *Stroke*. **34**, 1324–1331 (2003). doi:10.1161/01.STR.0000068367.08991.A2.

29. Young, R. J. & Knopp, E. A. Brain MRI: Tumor evaluation. *J. Magn. Reson. Imaging*. **24**, 709–724 (2006). doi: 10.1002/jmri.20704.

30. Laissy, J. P., Trillaud, H. & Douek, P. MR angiography: Noninvasive vascular imaging of the abdomen. *Abdom. Imaging*. **27**, 488–506 (2002). doi: 10.1007/s00261-001-0063-2.

31. Edelman, R. R. MR angiography: Present and future. *Am. J. Roentgenol*. **161**, 1–11 (1993). doi: 10.2214/ajr.161.1.8517285.

32. Wymer, D. T., William, F., Iii, B. & Bhatia, V. K. Phase-Contrast MRI : Physics, Techniques, and Clinical Applications. *Radiographics*. **40**, 122–140 (2020). doi:10.1148/rg.2020190039.

33. Goldberg, A. & Jha, S. Phase-contrast MRI and applications in congenital heart disease. *Clin. Radiol*. **67**, 399–410 (2012). doi: 10.1016/j.crad.2011.08.016.

34. Van Goethem, J. W. M., Van den Hauwe, L., Ozsarlak, O. & Parizel, P. M. Phase-contrast magnetic resonance angiography. *Journal Belge de Radiologie*. **86,** 340–344 (2003). doi: 10.1109/iembs.1989.95850.

35. Peng, S. H., Shen, C. Y., Wu, M. C., Lin, Y. D., Huang, C. H., Kang, R. J., Tyan, Y. S. & Tsao, T. F. Image quality improvement in three-dimensional time-of-flight magnetic resonance angiography using the subtraction method for brain and temporal bone diseases. *J. Chinese Med. Assoc*. **76**, 458–465 (2013). doi: 10.1016/j.jcma.2013.04.006.

36. Wang, J., Guan, M., Yamada, K., Hippe, D. S., Kerwin, W. S., Y., Börnert, C. & Xihai, P. Z. In vivo validation of simultaneous non-contrast angiography and intraPlaque

hemorrhage (SNAP) magnetic resonance angiography: An intracranial artery study. *PLoS One*. **11**, 1–10 (2016). doi: 10.1371/journal.pone.0149130.

37. Ross, J. S. Newer sequences for spinal MR imaging: Smorgasbord or succotash of acronyms. *Am. J. Neuroradiol*. **20**, 361–373 (1999). pmid:10219397.

38. Ramnandan, D., Mokhosi, S., Daniels, A. & Singh, M. Chitosan, polyethylene glycol and polyvinyl alcohol modified $MgFe_2O_4$ ferrite magnetic nanoparticles in doxorubicin delivery: *A comparative study in vitro. Molecules*. **26**, (2021). doi: 10.3390/molecules26133893.

39. Khot, V. M., Salunkhe, A. B., Thorat, N. D., Ningthoujam, R. S. & Pawar, S. H. Induction heating studies of dextran coated $MgFe_2O_4$ nanoparticles for magnetic hyperthermia. *Dalt. Trans.* **42**, 1249–1258 (2013). doi: 10.1039/c2dt31114c.

40. Mazarío, E., Cañete, M., Herranz, F., Sánchez-Marcos, J., De la Fuente, J. M., Herrasti, P. & Menéndez, N. Highly efficient T_2 cobalt ferrite nanoparticles vectorized for internalization in cancer cells. *Pharmaceuticals* **14**, 1–13 (2021). doi:10.3390/ph14020124.

41. Zahraei, M., Monshi, A., Shahbazi-gahrouei, D., Amirnasr, M., Behdadfar, B. & Rostami, M. Synthesis and Characterization of Chitosan Coated Manganese Zinc Ferrite Nanoparticles as MRI Contrast Agents. *Journal of nanostructures*. **5**, 77–86 (2015). doi: 10.7508/jns.2015.02.001.

42. Chandekar, K. V & Kant, K. M. Synthesis and characterization of low temperature superparamagnetic cobalt ferrite nanoparticles. *Advanced Materials Letter*s. **8(4)**, 435-443 (2017) doi:10.5185/amlett.2017.6900.

43. Balavijayalakshmi, J. & Sudha, T. Effect of Cobalt Substitution on Structural and Magnetic Properties of Magnesium Ferrite Nanoparticles. *Springer Proceedings in Physics*. **189**, 289-297 (2017). doi:10.1007/978-3-319-44890-9.

44. Diaconu, A., Borhan, A. I., Diaconu, A., Iordan, A. R., Nedelcu, G. G., Leontie, L. & Palamaru, M. N. How cobalt ions substitution changes the structure and dielectric properties of magnesium ferrite. *Ceram. Int*. **40**, 13573–13578 (2014). doi:10.1016/j.ceramint.2014.05.071.

45. Liu C., Zou B., Rondinone A. J. & Zhang Z. J. Chemical Control of Superparamagnetic Properties of Magnesium and Cobalt Spinel Ferrite Nanoparticles through Atomic Level Magnetic Couplings. *J. Am. Chem. Soc*. **122**, 6263–6267 (2000). doi:10.1021/ja000784g.

46. Varshney, D., Verma, K. & Kumar, A. Substitutional effect on structural and magnetic properties of $A_xCo_{1-x}Fe_2O_4$ (A = Zn, Mg and x = 0.0, 0.5) ferrites. *J. Mol. Struct*. **1006**, 447–452 (2011). doi: 10.1016/j.molstruc.2011.09.047.

47. Joshi, H. M., Lin, Y. P., Aslam, M., Prasad, P. V., Schultz-Sikma, E. A., Edelman, R., Meade, T. & Dravid, V. P. Effects of shape and size of cobalt ferrite nanostructures on their MRI contrast and thermal activation. *J. Phys. Chem. C*. **113**, 17761–17767 (2009). doi:10.1021/jp905776g.

48. Hoque, S, M., Tariq, M., Liba, S. I., Salehin, F., Mahmood, Z. H., Khan, M. N. I., Chattopadhayay, K., Islam, R. & Akhter, S. Thermo-therapeutic applications of chitosan- and PEG-coated $NiFe_2O_4$ nanoparticles . *Nanotechnology*. **27**, 285702 (2016). doi:10.1088/0957-4484/27/28/285702.

49. Miraux, S., Serres, S., Thiaudi, E. & Merle, M. Gadolinium-enhanced small-animal TOF magnetic resonance angiography. *Magnetic Resonance Materials in Physics, Biology and*

Medicine, **17(3–6)**, 348–352 (2004). doi:10.1007/s10334-004-0064-6.

50. Alawi, A. M. A., Majoni, S. W. & Falhammar, H. Review Article Magnesium and Human Health : Perspectives and Research Directions. *International Journal of Endocrinology*. **2018**, 1-17 (2018). doi: 10.1155/2018/9041694.

51. Lison, D. Chapter 25–Cobalt. *Hand b. Toxicol. Met*. 511–528 (2007). doi:10.1016/B978-0-12-369413-3.50080-X.

52. Mourdikoudis, S., Pallares, R. M. & Thanh N. T. K. Characterization techniques for nanoparticles: Comparison and complementarity upon studying nanoparticle properties. *Nanoscale*. **10(27)**,12871-12934 (2018). doi:10.1039/c8nr02278j.

53. Baig, N., Kammakakam, I., Falath, W. & Kammakakam, I. Nanomaterials: A review of synthesis methods, properties, recent progress, and challenges. *Mater Adv.* **2(6)**, 1821-1871 (2021). doi:10.1039/d0ma00807a.

54. Saravanan, R. S. S., Pukazhselvan, D., Mahadevan, C. K. Investigation on the synthesis and quantum confinement effects of pure and Mn^{2+} added $Zn_{(1-x)}Cd_xS$ nanocrystals. *J Alloys Compd*. **509(10)**, 4065-4072 (2011). doi:10.1016/j.jallcom.2010.12.198.

55. Schoenhalz, A. L., Arantes, J. T., Fazzio, A. & Dalpian, G. M. Surface and Quantum Confinement Effects in ZnO Nanocrystals. *J. Phys. Chem. C*. **114**, 18293–18297 (2010). doi: 10.1021/jp103768v.

56. Schneider, M. G. M., Martín, M. J., Jessica, O., Vakarelska, E., Simeonov, V., Lassalle, V. & Nedyalkova, M. Biomedical Applications of Iron Oxide Nanoparticles: Current Insights Progress and Perspectives. *Pharmaceutics* **14 (204)**, 1-25 (2022). doi:10.3390/pharmaceutics14010204.

57. Medeiros, S. F., Santos, A.M., Fessi, H. & Elaissari, A. Stimuli-responsive magnetic

particles for biomedical applications. Int J Pharm. **403(1-2)**, 139-161 (2011). doi:10.1016/j.ijpharm.2010.10.011

58. Anik, M. I., Hossain, M. K., Hossain, I., Mahfuz, A. M. U. B., Rahman, M. T. & Ahmed, I. Recent progress of magnetic nanoparticles in biomedical applications: A review. *Nano Sel.* **2**, 1146–1186 (2021). doi: 10.1002/nano.202000162.

59. Kanoda, K., Takahashi, T., Kawagoe, T., Mizoguchi, T., Kagoshima, S., & Hasumi, M. Antiferromagnetic transition in Y_2BaCuO_5. *Japanese journal of applied physics*, **26(12A)**, 1–31 (1987). URL: https://www.unf.edu/~michael.lufaso/chem4627/ch8_solid_state.pdf.

60. Greensite, *J. PHYSICS 430 Lecture Notes on Quantum Mechanics Fall 2003. Astronomy* (2003). URL: http://stanford.edu/~oas/SI/QM/papers/QMGreensite.pdf

61. Cresser, J. D. *Quantum Physics Notes 54–69 (Macquarie University*, 2009). URL: http://physics.mq.edu.au/~jcresser/Phys301/Chapters/Chapter6.pdf.

62. Kong, L. B., Liu, L., Yang, Z., Li, S., Zhang, T., & Wang, C. Theory of ferrimagnetism and ferrimagnetic metal oxides. *Magnetic, Ferroelectric, and Multiferroic Metal Oxides (Elsevier Inc.,* 2018). doi:10.1016/B978-0-12-811180-2.00015-3.

63. Diamagnetic, D. Chapter 7 Types of magnetic materials. *Curr. Methods Inorg. Chem.* **1**, 345–370 (1999). doi: 10.1016/S1873-0418(99)80008-6.

64. Shahri, M. M. Magnetic materials and magnetic nanocomposites for biomedical application. Harnessing Nanoscale Surface Interactions: Contemporary Synthesis, Applications and Theory (*Elsevier Inc.*, 2019). doi:10.1016/B978-0-12-813892-2.00003-3.

65. Wilcox, W. M. & Thron C. P. Chapter 6: Magnetostatics. *Macroscopic Electrodynamics: An Introductory Graduate Treatment* 247–259 (2016). URL: https://books.google.com.bd/books?id=xZhIDQAAQBAJ&pg=PA247&dq=Section+6+m

agnetostatics+notes&hl=en&newbks=1&newbks_redir=1&sa=X&ved=2ahUKEwiq1drzk-uDAxXo-DgGHcy3CBUQ6AF6BAgJEAI.

66. Gore, S. K. & Jadhav, S. S. Basics of ferrites. Spinel Ferrite Nanostructures for Energy *Storage Devices (Elsevier Inc.*, 2020). 1-11(2020). doi:10.1016/b978-0-12-819237-5.00001-8.

67. Kua, S. 1.1 A brief history of magnetism. *Magnetism and Magnetic Materials*. 1–23 (2009). isbn: 9780511845000.

68. Slimani, Y., Hannachi, E., Tombuloglu, H., Güner, S., Almessiere, M., Baykal, A., Aljafary, M., Al-Suhaimi, E., Nawaz, M. & Ercan, I.. Magnetic nanoparticles based nanocontainers for biomedical application. *Smart Nanocontainers Micro Nano Technol*. 229–250 (2019) doi:10.1016/B978-0-12-816770-0.00014-9.

69. Butler, R. L. Ferromagnetic minerals. Paleomagn. *Magn. Domains to Geol. Terranes* 1, 16–30 (1992). URl: http://www.geo.arizona.edu/Paleomag/book/.

70. Hrabec, A. *Domain wall dynamics in magnetic nanostructures : Effect of magnetic field and electric current Etude de la dynamique de l ' aimantation dans des nanostructures à aimantation perpendiculaire : effet du champ magnétique et du courant électrique.* 7-131 (2012). URL: https://theses.hal.science/tel-00767418.

71. Szczyglowski, J. Influence of eddy currents on magnetic hysteresis loops in soft magnetic materials. *J. Magn. Magn. Mater*. 223, 97–102 (2001). doi: 10.1016/S0304-8853(00)00584-9.

72. Miyao, M. Miscellaneous methods and materials for silicon-germanium (SiGe) based heterostructures. *Silicon-Germanium (SiGe) Nanostructures (Woodhead Publishing Limited,* 2011). doi:10.1533/9780857091420.2.190.

73. Buttle, D., Scruby, C. Residual Stresses: Measurement using Magnetoelastic Effect. Encyclopedia of Materials: Science and Technology. *Elsevier Science Ltd.* 8172-8180 (2001). isbn: 0-08-0431526.

74. Kafrouni, L. & Savadogo, O. Recent progress on magnetic nanoparticles for magnetic hyperthermia. *Prog. Biomater*. (2016) doi:10.1007/s40204-016-0054-6.

75. Müller, M., Harada, H. & Warlimont, H. Magnetic materials. *Springer Handbooks* 753–807 (2018) doi:10.1007/978-3-319-69743-7_22.

76. Bozorth, R. M. Ferromagnetism. *Van Nostrand, New York.* 957 (1951).

77. Jadhav, V. V, Mane, R. S. & Shinde, P. V. *Bismuth- Ferrite-Based Electrochemical Supercapacitors*. (2020). doi: 10.1007/978-3-030-16718-9.

78. Hoque, S. M., Choudhury, M. A. & Islam, M. F. Characterization of Ni-Cu mixed spinel ferrite. *J. Magn. Magn. Mater*. **251**, 292–303 (2002). doi:10.1016/S0304-8853(02)00700-X.

79. Silva, F. G. D., Depeyrot, J., Campos, A. F. C., Aquino, R., Fiorani1, D., & Peddis, D. Structural and Magnetic Properties of Spinel Ferrite Nanoparticles. *J. Nanosci. Nanotechnol.* **19**, 4888–4902 (2019). doi:10.1166/jnn.2019.16877.

80. Mathew, D. S. & Juang, R. S. An overview of the structure and magnetism of spinel ferrite nanoparticles and their synthesis in microemulsions. *Chem. Eng. J.* **129**, 51–65 (2007). doi: 10.1016/j.cej.2006.11.001.

81. Berggren, J., Foss, O., Roti, I., Okinaka, H., Kosuge, K. & Kachi, S. Refinement of the Crystal Structure of Dicalcium Ferrite, $Ca_2Fe_2O_5$. *Acta Chemica Scandinavica*. **25**, 3616–3624 (1971). doi: 10.3891/acta.chem.scand.25-3616.

82. Tatarchuk, T., Bououdina, M., Vijaya, J. J. & Kennedy, L. J. Spinel Ferrite Nanoparticles :

Synthesis , Crystal Structure , Properties , and Perspective Applications. *Springer Proceedings in Physics*. **195**, 305–325 (2017) doi:10.1007/978-3-319-56422-7.

83. Sarkar, N., Rewatkar, K. & Nanoti, V. Chapter 9: Soft Ferrite: A Brief Review on Structural, Magnetic Behavior of Nanosize Spinel Ferrites. *Magnetic Oxide and Composites.* **5**, 237-263 (2018). isbn: 9781945291685.

84. Pourmadadi, M., Rahmani, E., Shamsabadipour, A., Mahtabian, S., Ahmadi, M., Rahdar, A. & Díez-Pascual, A. M. Role of Iron Oxide (Fe_2O_3) Nanocomposites in Advanced Biomedical Applications: A State-of-the-Art Review. *Nanomaterials*. **12(21)**, 3873 (2022). doi:10.3390/nano12213873.

85. Lee, S.-W., Lee, J.-G., Chae, K.-P., Kwon, W.-H. & Kim, C.-S. Superparamagnetic Properties of $MnFe_2O_4$ Nanoparticles . *J. Korean Magn. Soc*. **19**, 57–61 (2009). doi:10.4283/jkms.2009.19.2.057.

86. Zipare, K., Dhumal, J., Bandgar, S., Mathe, V. & Shahane, G. Superparamagnetic Manganese Ferrite Nanoparticles: Synthesis and Magnetic Properties. *J. Nanosci. Nanoeng*. **1(3)**, 178–182 (2015). URL: http://www.aiscience.org/journal/jnn.

87. Farheen, A. & Singh, R. Structure and magnetic properties of superparamagnetic ferrite nanoparticles. *IOP Conf. Ser. Mater. Sci. Eng*. **577**, 6–12 (2019). doi:10.1088/1757-899X/577/1/012057.

88. Obaidat, I. M., Narayanaswamy, V., Alaabed, S., Sambasivam, S. & Muralee Gopi, C. V. V. Principles of magnetic hyperthermia: A focus on using multifunctional hybrid magnetic nanoparticles. *Magnetochemistry* **5**, (2019). doi: 10.3390/magnetochemistry5040067.

89. Cheng, Y., Weng, S., Yu, L., Zhu, N., Yang, M., & Yuan, Y.. The Role of Hyperthermia in the Multidisciplinary Treatment of Malignant Tumors. *Integr. Cancer Ther.* **18**, (2019).

doi: 10.1177/1534735419876345.

90. Hegyi, G., Szigeti, G. P. & Szász, A. Hyperthermia versus oncothermia: Cellular effects in complementary cancer therapy. *Evidence-based Complement. Altern. Med*. 2013, (2013). doi:10.1155/2013/672873.

91. Seynhaeve, A. L. B., Amin, M., Haemmerich, D., van Rhoon, G. C. & ten Hagen, T. L. M. Hyperthermia and smart drug delivery systems for solid tumor therapy. *Adv. Drug Deliv. Rev*. **163–164**, 125–144 (2020). doi:10.1016/j.addr.2020.02.004.

92. Gao, S., Zheng, M., Ren, X., Tang, Y. & Liang, X. Local hyperthermia in head and neck cancer: Mechanism, application and advance. *Oncotarget.* **7**, 57367–57378 (2016). doi: 10.18632/oncotarget.10350.

93. Ashoor, H. E. Hyperthermia: Clinical Applications and Theoretical Models. *J. Biosci. Med*. **10**, 56–71 (2022). doi: 10.4236/jbm.2022.103007.

94. Davie-Smith, F., Coulter, E., Kennon, B., Wyke, S., & Paul, L.. Hyperthermia Using Nanoparticles–Promises and Pitfalls. *Physiol. Behav.* **176**, 498–503 (2017). doi:10.3109/02656736.2015.1120889.Hyperthermia.

95. Chatterjee, D. K., Diagaradjane, P. & Krishnan, S. Nanoparticle-mediated hyperthermia in cancer therapy. *Ther. Deliv*. **2**, 1001–1014 (2011). doi: 10.4155/tde.11.72.

96. Miura, Y., Okabayashi, J. Understanding magnetocrystalline anisotropy based on orbital and quadrupole moments. *J. Phys.: Condens. Matter*. **34**, 473001 (2022). doi:10.1088/1361648X/ac943f.

97. Sechovský, V. Magnetism in Solids: General Introduction. *Encycl. Mater. Sci. Technol*. 5018–5032 (2001). doi:10.1016/b0-08-043152-6/00872-x.

98. Lee, J. H., Jang, J. T., Choi, J. S., Moon, S. H., Noh, S. H., Kim, J. W., Kim, J. G., Kim, I. S., Park, K. I. & Cheon, J. Exchange-coupled magnetic nanoparticles for efficient heat induction. *Nat. Nanotechnol*. **6**, 418–422 (2011). doi: 10.1038/nnano.2011.95.

99. Hoque, S. M., Huang, Y., Emiliano, C., Maritim, S., Santin, A. D., Shapiro, E. M., Coman, D. & Hyder, F. Improved specific loss power on cancer cells by hyperthermia and MRI contrast of hydrophilic $Fe_xCo_{1-x}Fe_2O_4$ nanoensembles. *Contrast Media Mol. Imaging.* **11**, 514–526 (2016). doi: 10.1002/cmmi.1713.

100. Egea-Benavente, D., Ovejero, J. G., Morales, M. D. P. & Barber, D. F. Understanding mnps behaviour in response to amf in biological milieus and the effects at the cellular level: Implications for a rational design that drives magnetic hyperthermia therapy toward clinical implementation. *Cancers (Basel)*. **13**, (2021). doi: 10.3390/cancers13184583.

101. Wildeboer, R. R., Southern, P. & Pankhurst, Q. A. On the reliable measurement of specific absorption rates and intrinsic loss parameters in magnetic hyperthermia materials. *J. Phys. D. Appl. Phys*. **47**, (2014). doi: 10.1088/0022-3727/47/49/495003.

102. Yankeelov, T. & Gore, J. Dynamic Contrast Enhanced Magnetic Resonance Imaging in Oncology: Theory, Data Acquisition, Analysis, and Examples. *Curr. Med. Imaging Rev*. **3,** 91–107 (2007). doi: 10.2174/157340507780619179.

103. Ladd, M. E., Bachert, P., Meyerspeer, M., Moser, E., Nagel, A. M., Norris, D. G. & Zaiss, M. Pros and cons of ultra-high-field MRI/MRS for human application. *Prog. Nucl. Magn. Reson. Spectrosc*. **109**, 1–50 (2018). doi:10.1016/j.pnmrs.2018.06.001.

104. Iriguchi, N., Sekino, M. & Ueno, S. Principles of Magnetic Resonance Imaging. *Biomagn. Princ. Appl. Biomagn. Stimul. Imaging*. **50**, 121–144 (2018). doi: 10.1201/b18831-11.

105. McGowan, J. C. Basic Principles of Magnetic Resonance Imaging. *Neuroimaging Clin. N.*

Am. **18**, 623–636 (2008). doi: 10.1016/j.nic.2008.06.004.

106. Mastrogiacomo, S., Dou, W., Jansen, J. A. & Walboomers, X. F. Magnetic Resonance Imaging of Hard Tissues and Hard Tissue Engineered Bio-substitutes. *Mol. Imaging Biol*. **21**, 1003–1019 (2019). doi: 10.1007/s11307-019-01345-2.

107. Giovannetti, G., Frijia, F. & Flori, A. Resonance Scanners : Experience from a Research Lab – Manufacturing Companies Cooperation. *Electronics*. **11**, 4233 (2022). doi:10.3390/electronics11244233.

108. Bushberg, J. T., Seibert, J. A. & Leidholdt, E. M. Magnetic Resonance Basics: Magnetic Fields, Nuclear Magnetic Characteristics, Tissue Contrast, Image Acquisition. Essent. *Phys. Med. Imaging.* 402–448 (2011). ISBN: 9781469821559.

109. Paramasivam, G., Palem, V. V., Sundaram, T., Sundaram, V., Kishore, S. C. & Bellucci, S. Nanomaterials: Synthesis and applications in theranostics. *Nanomaterials* 11, (2021). doi: 10.3390/nano11123228.

110. Bokov, D., Jalil, A., Chupradit, S., Suksatan, W. J., Ansari, M., Shewael, I. H., Valiev, G. H. & Kianfar, E. Nanomaterial by Sol-Gel Method: Synthesis and Application. *Adv. Mater. Sci. Eng*. **2021**, (2021). doi: 10.1155/2021/5102014.

111. Ali, A. H. Review on the Synthesis Method of Nanocomposites and Approach to Making Semiconductors Visible Light Active. *J. Chem. Educ. Res. Pract.* **6**, 1–20 (2022). doi:10.33140/jcerp.06.02.09.

112. Baig, N., Kammakakam, I., Falath, W. & Kammakakam, I. Nanomaterials: A review of synthesis methods, properties, recent progress, and challenges. *Mater. Adv*. **2**, 1821–1871 (2021). doi: 10.1039/d0ma00807a.

113. Dudchenko, N., Pawar, S., Perelshtein, I. & Fixler, D. Magnetite Nanoparticles: Synthesis

and Applications in Optics and Nanophotonics. *Materials (Basel)*. **15**, (2022). doi:10.3390/ma15072601.

114. Sun, L., Huang, C., Gong, T. & Zhou, S. A biocompatible approach to surface modification: Biodegradable polymer functionalized super-paramagnetic iron oxide nanoparticles. *Mater. Sci. Eng. C* **30**, 583–589 (2010). doi:10.1016/j.msec.2010.02.009.

115. Zia, M., Phull, A. R. & Ali, J. S. Challenges of Iron Oxide Nanoparticles. Powder Technol. **7**, 49–67 (2016). doi: 10.2147/NSA.S99986.

116. Torres, T. E., Ibarra, M. R. & Goya, G. F. Fe 3 O 4 Nanoparticles for Biomedical Applications. *Biochemistry Research International*. **6**, 2008–2009 (2009). doi:10.1155/2016/7840161.

117. Dutz, S., Andrä, W., Hergt, R., Müller, R., Oestreich, C., Schmidt, C., Töpfer, J., Zeisberger, M. & Bellemann, M. E. Influence of dextran coating on the magnetic behaviour of iron oxide nanoparticles. *J. Magn. Magn. Mater*. **311**, 51–54 (2007). doi:10.1016/j.jmmm.2006.11.168.

118. Herdiana, Y., Wathoni, N., Shamsuddin, S. & Muchtaridi, M. Drug release study of the chitosan-based nanoparticles. *Heliyon* **8**, (2022). doi:10.1016/j.heliyon.2021.e08674.

119. Tassa, C., Shaw, S. Y. & Weissleder, R. Dextran-coated iron oxide nanoparticles: A versatile platform for targeted molecular imaging, molecular diagnostics, and therapy. *Acc. Chem. Res.* **44**, 842–852 (2011). doi: 10.1021/ar200084x.

120. Tong, S., Hou, S., Ren, B., Zheng, Z. & Bao, G. Self-assembly of phospholipid-PEG coating on nanoparticles through dual solvent exchange. *Nano Lett.* **11**, 3720–3726 (2011). doi:10.1021/nl201978c.

121. Ngo, A. N., Ezoulin, M. J. M., Murowchick, J. B., Gounev, A. D. & Youan, B. B. C.

Sodium Acetate Coated Tenofovir-Loaded Chitosan Nanoparticles for Improved Physico-Chemical Properties. *Pharm. Res.* **33**, 367–383 (2016). doi:10.1007/s11095-015-1795-y.

122. Juang, J. H., Wang, J. J., Shen, C. R., Kuo, C. H., Chien, Y. W., Kuo, H. Y., Tsai, Z. & Yen, T. Magnetic resonance imaging of transplanted mouse islets labeled with chitosan-coated superparamagnetic iron oxide nanoparticles. *Transplant. Proc.* **42**, 2104–2108 (2010). doi: 10.1016/j.transproceed.2010.05.103.

123. Frank, L. A., Onzi, G. R., Morawski, A. S., Pohlmann, A. R., Guterres, S. S. & Contri, R. V. Chitosan as a coating material for nanoparticles intended for biomedical applications. *React. Funct. Polym*. **147**, 104459 (2020). doi:10.1016/j.reactfunctpolym.2019.104459.

124. Smolensky, E. D., Park, H. Y. E., Berquó, T. S. & Pierre, V. C. Surface functionalization of magnetic iron oxide nanoparticles for MRI applications - effect of anchoring group and ligand exchange protocol. *Contrast Media Mol. Imaging*. **6**, 189–199 (2011). doi:10.1002/cmmi.417.

125. Hoskins, C., Wang, L., Cheng, W. P. & Cuschieri, A. Dilemmas in the reliable estimation of the in-vitro cell viability in magnetic nanoparticle engineering: Which tests and what protocols. *Nanoscale Res. Lett*. **7**, 1–12 (2012). doi: 10.1186/1556-276X-7-77.

126. Zhang, Y. & Zhang, J. Surface modification of monodisperse magnetite nanoparticles for improved intracellular uptake to breast cancer cells. *J. Colloid Interface Sci*. **283**, 352–357 (2005). doi:10.1016/j.jcis.2004.09.042.

127. Nath, S., Kaittanis, C., Ramachandran, V., Dalal, N. S. & Perez, J. M. Synthesis, magnetic characterization, and sensing applications of novel dextran-coated iron oxide nanorods. *Chem. Mater.* **21**, 1761–1767 (2009). doi: 10.1021/cm8031863.

128. Borny, R., Lechleitner, T., Schmiedinger, T., Hermann, M., Tessadri, R., Redhammer, G., Kerjaschki, D., Berzaczy, G., Erman, G., Popovic, M., Lammer, J. & Funovics, M.. Nucleophilic cross-linked, dextran coated iron oxide nanoparticles as basis for molecular imaging: Synthesis, characterization, visualization and comparison with previous product. *Contrast Media Mol. Imaging*. **10**, 18–27 (2015). doi:10.1002/cmmi.1595.

129. Shokrollahi, H. Structure, synthetic methods, magnetic properties and biomedical applications of ferrofluids. *Mater. Sci. Eng. C.* **33**, 2476–2487 (2013). doi:10.1016/j.msec.2013.03.028.

130. Beraza, M., Padro, D. & Reese, T. A general protocol of ultra-high resolution MR angiography to image the cerebro-vasculature in 6 different rats strains at high field. *J. Neurosci*. Methods (2017) doi:10.1016/j.jneumeth.2017.07.003.

131. Edelman, R. R. Review Article MR Angiography : Present and Future. *American Journal of Roentgenology.* **161,** 1–11 (1993). doi: 10.2214/ajr.161.1.8517285.

132. Reese, T., Bochelen, D., Sauter, Â., Beckmann, N. & Rudin, M. Magnetic resonance angiography of the rat cerebrovascular system without the use of contrast agents. *NMR Biomed.*189–196 (1999). doi: 10.1002/(SICI)1099-1492(199906)12:4<189::AID-NBM557>3.0.CO;2-O.

133. Edelman, R., Ahn, S. S., Chien, D., Li, W., Goldmann, A., Mantello, M., Kramer, J. & Kleefield, J. Improved Time-of-Flight MR Angiography of the Brain with Magnetization Transfer Contrast. *Radiology*. **184**, 395–399 (1992). doi:10.1148/radiology.184.2.1620835.

134. Veni, A. K. In-vitro Cytotoxic Activity of Enicostemma axillare Extract against Hela cell line. *International Journal of Pharmacognosy and Phytochemical Research*. **6(2)** 320-323

(2014). ISSN: 09754873.

135. Okon, E. U., Hammed, G., Abu, P., Wafa, E., Abraham, O., Case, N., & Henry, E.. In-vitro cytotoxicity of Polyethyleneimine on HeLa and Vero Cells. *International Journal of Innovation and Applied Studies.* **5(3)**, 192–199 (2014). ISSN:2028-9324.

136. Vero, A., Lines, M. C. F. C., Prasetyaningrum, P. W. & Bahtiar, A. Synthesis and Cytotoxicity Evaluation of Novel Asymmetrical Mono-Carbonyl Analogs of Curcumin. *Sci. Pharm*. **86 (25)** 1-13 (2018) doi:10.3390/scipharm86020025.

137. Rickwood, D. Centrifugation Techniques. *Encyclopedia of Life Sciences.* (2001) doi:10.1038/npg.els.0002704.

138. Ranjha, M. M. A. N., Irfan, S., Lorenzo, J. M., Shafique, B., Kanwal, R., Pateiro, M. & Aadil, R. M.. Sonication, a potential technique for extraction of phytoconstituents: A systematic review. *Processes.* **9(8)**, (2021). doi: 10.3390/pr9081406.

139. Tadano, S. & Giri, B. X-ray diffraction as a promising tool to characterize bone nanocomposites. *Sci. Technol. Adv. Mater*. **12**, 064708 (2011). doi:10.1088/1468-6996/12/6/064708.

140. Adams, C. S., Sigel, M. & Mlynek, *J. Atom optics. Phys. Rep*. **240**, 143–210 (1994). doi:10.1016/0370-1573(94)90066-3.

141. Kumar, A. A. & Venkatathri, N. Development of Porous Titanosilicate-Based hybrid Nanocomposites for Photocatalytic Applications under UV and Solar light irradiation. *Doctoral Thesis*. (2018). URL: https://www.researchgate.net/publication/338547781.

142. Li, Y., Ma, B., Chen, N., Lu, J., Wang, A., Liu, L. & Cao, G. Structural and magnetic properties of $LiMn_{1.5}Fe_{0.5}O_4$ spinel oxide. *Phys. B Condens. Matter*. **405**, 4733–4739 (2010). doi: 10.1016/j.physb.2010.08.050.

143. Bokuniaeva, A. O. & Vorokh, A. S. Estimation of particle size using the Debye equation and the Scherrer formula for polyphasic TiO2 powder. *J. Phys. Conf. Ser*. **1410**, (2019). doi: 10.1088/1742-6596/1410/1/012057.

144. Yadav, R. S., Kuřitka, I., Vilcakova, J., Havlica, J., Masilko, J., Kalina, L. & Hajdúchová, M.. Impact of grain size and structural changes on magnetic, dielectric, electrical, impedance and modulus spectroscopic characteristics of $CoFe_2O_4$ nanoparticles synthesized by honey mediated sol-gel combustion method. *Adv. Nat. Sci. Nanosci. Nanotechnol*. **8**, (2017). doi:10.1088/2043-6254/aa853a.

145. Peng, Y., Xia, C., Cui, M., Yao, Z. & Yi, X. Effect of reaction condition on microstructure and properties of (NiCuZn)Fe2O4 nanoparticles synthesized via co-precipitation with ultrasonic irradiation. Ultrason. Sonochem. **71**, 105369 (2021). doi:10.1016/j.ultsonch.2020.105369.

146. Satalkar, M. & Kane, S. N. On the study of Structural properties and Cation distribution of $Zn_{0.75-x}Ni_xMg_{0.15}Cu_{0.1}Fe_2O_4$ nano ferrite: Effect of Ni addition. *J. Phys. Conf. Ser*. **755**, (2016). doi:10.1088/1742-6596/755/1/012050.

147. Plana Ruiz, S. Development & Implementation of an Electron Diffraction Approach for Crystal Structure Analysis. *Doctoral Thesis* (2021). URL:https://widgets.ebscohost.com/prod/customerspecific/ns000545/customproxy.php?url=https://search.ebscohost.com/login.aspx?direct=true&db=edstdx&AN=edstdx.10803.670887&amp%0Alang=pt-pt&site=eds-live&scope=site.

148. Bonnamy, S. & Oberlin, A. Transmission Electron Microscopy. *Materials Science and Engineering of Carbon: Characterization (Elsevier Ltd,* 2016). doi:10.1016/B978-0-12-805256-3.00004-0.

149. Bonnamy, S. & Oberlin, A. Transmission Electron Microscopy. *Mater. Sci. Eng. Carbon Charact*. 45–70 (2016) doi:10.1016/B978-0-12-805256-3.00004-0.

150. Alamdar, S. H. S. Vibrating Sample Magnetometery : Analysis and Construction. *Thesis.* (2013).

151. Lashley, J. C., Hundley, M. F., Migliori, A., Sarrao, J. L., Pagliuso, P. G., Darling, T. W. & Phillips, N. E.. Critical examination of heat capacity measurements made on a quantum design physical property measurement system. *Cryogenics (Guildf)*. **43**, 369–378 (2003). doi: 10.1016/S0011-2275(03)00092-4.

152. Liu, X. W., Zhao, S., Meng, Y., Peng, Q., Dearden, A. K., Huo, C. F. & Wen, X. D. . Mossbauer Spectroscopy of Iron Carbides: From Prediction to Experimental Confirmation. *Sci. Rep*. **6**, 1–10 (2016). doi: 10.1038/srep26184.

153. Campbell, S. J. & Aubertin, F. Evaluation of Distributed Hyperfine Parameters. Mössbauer Spectrosc. *Appl. to Inorg. Chem*. 183–242 (1989) doi:10.1007/978-1-4899-2289-2_4.

154. Harami, T., Kitao, S., Kobayashi, Y. & Mitsui, T. Mössbauer spectroscopic evidence on the heme binding to the proximal histidine in unfolded carbonmonoxy myoglobin by guanidine hydrochloride. *Hyperfine Interact*. **181**, 179–187 (2008). doi:10.1007/s10751-008-9711-z.

155. Dasireddy, V. D. B. C., Bharuth-Ram, K., Harilal, A., Singh, S. & Friedrich, H. B. Fe phase complexes and their thermal stability in iron phosphate catalysts supported on silica. *Hyperfine Interact*. **231**, 137–142 (2015). doi: 10.1007/s10751-014-1119-3.

156. Celis, J. A., Olea, M. O. F., Cabral-Prieto, A., García-Sosa, I., Derat-Escudero, R., Baggio, S. E. M. & Alzamora, C. M.. Synthesis and characterization of nanometric

magnetite coated by oleic acid and the surfactant CTAB: Surfactant coated nanometric magnetite/maghemite. *Hyperfine Interact*. **238**, (2017). doi: 10.1007/s10751-017-1414-x.

157 Taylor, P. & Pyykkö, P. Spectroscopic nuclear quadrupole moments. *Molecular Physics*. **99** 1617–1629 (2001). doi: /10.1080/00268970110069010.

158. Dillon, K. B. Nuclear quadrupole resonance spectroscopy. Spectrosc. *Prop. Inorg. Organomet. Compd*. **45**, 248–259 (2014). doi: 10.1039/9781782621485-00248.

159. Junk, M. J. N. Electron Paramagnetic Resonance Theory. *Assess. Funct. Struct. Mol. Transp. by EPR Spectrosc*. 7–52 (2012) doi:10.1007/978-3-642-25135-1_2.

160. Khan, S. A., Khan, S. B., Khan, L. U., Farooq, A., Akhtar, K. & Asiri, A. M. Fourier transform infrared spectroscopy: Fundamentals and application in functional groups and nanomaterials characterization. *Hand b. Mater. Charact*. 317–344 (2018) doi:10.1007/978-3-319-92955-2_9.

161. Kamnev, A. A., Tugarova, A. V., Dyatlova, Y. A., Tarantilis, P. A., Grigoryeva, O. P., Fainleib, A. M. & De Luca, S. Methodological effects in Fourier transform infrared (FTIR) spectroscopy: Implications for structural analyses of biomacromolecular samples. Spectrochim. *Acta - Part A Mol. Biomol. Spectrosc*. **193**, 558–564 (2018). doi: 10.1016/j.saa.2017.12.051.

162. Alvarez-Ordóñez, A. & Prieto, M. Fourier Transform Infrared Spectroscopy in Food Microbiology. *Springer Briefs in Food, Health, and Nutrition*. (2012) doi:10.1007/978-1-4614-3813-7.

163. Buckner, C. A., Lafrenie, R. M., Dénommée, J. A., Caswell, J. M. & Want, D. A. Complementary and alternative medicine use in patients before and after a cancer diagnosis. *Current Oncology*. **25(4)**, e275-e281 (2018). doi: 10.3747/co.25.3884.

164. Peak, D. Fourier Transform Infrared Spectroscopy. *Encycl. Soils Environ*. **4**, 80–85 (2004). doi: 10.1016/B0-12-348530-4/00174-0.

165. Gore, R. C. Infrared Spectroscopy. *Anal. Chem*. **24**, 8–13 (1952). doi:10.1021/ac60061a002.

166. Hassan, P. A., Rana, S. & Verma, G. Making sense of Brownian motion: Colloid characterization by dynamic light scattering. *Langmuir* **31**, 3–12 (2015). doi:10.1021/la501789z.

167. Thomas, S. & Kalarikkal, N. Chapter 2 - Dynamic Light Scattering(DLS). *Thermal and Rheological Measurement Techniques for Nanomaterials Characterization (Elsevier Inc*., 2017). doi:10.1016/B978-0-323-46139-9.00002-5.

168. Derjaguin, V. The Derjaguin-Landau-Verwey- Overbeek (DLVO) Theory Stability of Lyophobic Colloids. Surface Forces. *Springer Science+Business Media New York*. (1987).

169. Bhattacharjee, S. Review article DLS and zeta potential – What they are and what they are not . *J. Control. Release.* **235**, 337–351 (2016). doi: 10.1016/j.jconrel.2016.06.017.

170. Jones, R. R., Hooper, D. C., Zhang, L., Wolverson, D. & Valev, V. K. Raman Techniques: Fundamentals and Frontiers. *Nanoscale Res. Lett*. **14**, (2019). doi:10.1186/s11671-019-3039-2.

171. Bashir, S. & Liu, J. Nanocharacterization. *Advanced Nanomaterials and Their Applications in Renewable Energy (Elsevier Inc*., 2015). doi:10.1016/B978-0-12-801528-5.00003-8.

172. Nasrin, S., Chowdhury, F. U. Z., Hasan, M. M., Hossen, M. M., Ullah, S. M. & Hoque, S. M. Effect of zinc substitution on structural, morphological and magnetic properties of

cobalt nanocrystalline ferrites prepared by co-precipitation method. *J. Mater. Sci. Mater. Electron*. **29**, 18878–18889 (2018). doi: 10.1007/s10854-018-0013-1.

173. Hoque, S. M., Hossain, M. S., Choudhury, S., Akhter, S. & Hyder, F. Synthesis and characterization of ZnFe2O4 nanoparticles and its biomedical applications. *Mater. Lett*. **162**, 60–63 (2016). doi: 10.1016/j.matlet.2015.09.066.

174. Hoque, S. M., Srivastava, C., Venkatesha, N. & Chattopadhyay, K. Synthesis, Characterization, and Nuclear Magnetic Resonance Study of Chitosan-Coated Nanocrystals. *Ieee transactions on nanobioscience*. **12**, 298–303 (2014). doi:10.1109/TNB.2013.2279845.

175. Islam, M. K., Haque, M. M., Rashid, R., Hasan, R., Islam, M. A., Khan, M. N. I. & Hoque, S. M. Manganese ferrite nanoparticles ($MnFe_2O_4$): Size dependence for hyperthermia and negative/positive contrast enhancement in MRI. *Nanomaterials* **10**, 1–23 (2020). doi: 10.3390/nano10112297.

176. Kai, W., Xiaojun, X., Ximing, P., Zhenqing, H. & Qiqing, Z. Cytotoxic effects and the mechanism of three types of magnetic nanoparticles on human hepatoma BEL-7402 cells. *Nanoscale Res. Lett*. **6**, 1–10 (2011). doi: 10.1186/1556-276X-6-480.

177. Grudzinski, I. P., Bystrzejewski, M., Cywinska, M. A., Kosmider, A., Poplawska, M., Cieszanowski, A., & Ostrowska, A. Cytotoxicity evaluation of carbon-encapsulated iron nanoparticles in melanoma cells and dermal fibroblasts. *J. Nanoparticle Res*. **15**, (2013). doi:10.1007/s11051-013-1835-7.

178. Hoskins, C., Cuschieri, A. & Wang, L. The cytotoxicity of polycationic iron oxide nanoparticles: Common endpoint assays and alternative approaches for improved understanding of cellular response mechanism. *J. Nanobiotechnology*. **10**, 1–11 (2012).

doi: 10.1186/1477-3155-10-15.

179. Lodhi, M. Y., Mahmood, K., Mahmood, A., Malik, H., Warsi, M. F., Shakir, I. & Khan, M. A. New $Mg_{0.5}Co_xZn_{0.5-x}Fe_2O_4$ nano-ferrites: Structural elucidation and electromagnetic behavior evaluation. *Curr. Appl. Phys*. **14**, 716–720 (2014). doi:10.1016/j.cap.2014.02.021.

180. Carter, C. B., Norton, M. G. Chapter 4: Bonds and Energy Bands. Science and Engineering. Springer. 51-66 (2007), ISBN:0387462708.

181. Maguire, M. E. & Cowan, J. A. Magnesium chemistry and biochemistry. *BioMetals*. **15**, 203–210 (2002). doi: 10.1023/A:1016058229972.

182. Abraham, A. G., Manikandan, A., Manikandan, E., Vadivel, S., Jaganathan, S. K., Baykal, A. & Renganathan, P. S. Enhanced magneto-optical and photo-catalytic properties of transition metal cobalt (Co^{2+}ions) doped spinel $MgFe_2O_4$ ferrite nanocomposites. *J. Magn. Magn. Mater*. **452**, 380–388 (2018). doi: 10.1016/j.jmmm.2018.01.001.

183. Stein, C. R., Bezerra, M. T. S., Holanda, G. H. A. & Morais, P. C. Structural and magnetic properties of cobalt ferrite nanoparticles synthesized by co-precipitation at increasing temperatures. *AIP Adv*. **8(5)**, (2018). doi: 10.1063/1.5006321.

184. Chandekar, V. K. & Mohan, K. K. Synthesis and characterization of low temperature superparamagnetic cobalt ferrite nanoparticles. *Adv. Mater. Lett*. **8**, 435–443 (2017). doi: 10.5185/amlett.2017.6900.

185. Vemuri, R., Raju, G., Gnana, K. M., Prasad, M. S. N. A., Rajesh, E., Pavan, K. G. & Murali, N.. Effect on structural and magnetic properties of Mg^{2+} substituted cobalt nano ferrite. *Results Phys*. **12**, 947–952 (2019). doi: 10.1016/j.rinp.2018.12.032.

186. Issa, B., Obaidat, I. M., Albiss, B. A. & Haik, Y. Magnetic Nanoparticles : Surface Effects

and Properties Related to Biomedicine Applications. *International Journal of Molecular Sciences*. **14**, 21266–21305 (2013). doi:10.3390/ijms141121266.

187. Branka, B. S, Vukoman. J., Dušan, M., Zvonko, J., Makovec, D., Nataša, J. & Marinovic-Cincovic, M. Magnetic and Structural Studies of $CoFe_2O_4$ Nanoparticles Suspended in an Organic Liquid. *Journal of Nanomaterials*. **2013**, 9-18 (2013). doi: 10.1155/2013/741036.

188. Ramos, G. J. A., Bustamante, A., Flores, J., Mejía, S. M., Osorio, A. M., Martínez, A. I., Valladares, L. D. L. S. & Barnes, C. H. W. Mössbauer study of intermediate superparamagnetic relaxation of maghemite (γ-Fe_2O_3) nanoparticles. *Hyperfine Interact*. **224**, 89–97 (2014). doi: 10.1007/s10751-013-0864-z.

189. Lin, Q., He, Y., Xu, J., Lin, J., Guo, Z. & Yang, F. Effects of Al^{3+} substitution on structural and magnetic behavior of $CoFe_2O_4$ ferrite nanomaterials. *Nanomaterials*. **8**, 1–11 (2018). doi:10.3390/nano8100750.

190. Estournès, C., Manova, E., Kurmoo, M., Kunev, B., Rehspringer, J., D'Orléan, C., Petrov, L., Paneva, D. & Mitov, I. Mechano-Synthesis, Characterization, and Magnetic Properties of Nanoparticles of Cobalt Ferrite, $CoFe_2O_4$. *Chem. Mater*. **16**, 5689–5696 (2004). doi: 10.1021/cm049189u.

191. Lin, Q., Dong, J., He, Y., Yang, X. & Lin, J. Mössbauer Spectroscopy, Structural and Magnetic Studies of Zn^{2+} Substituted Magnesium Ferrite Nanomaterials Prepared by Sol-Gel Method . *J. Nanomater*. **2015**, 1–8 (2015). doi: 10.1155/2015/854840.

192. He, Y., Lei, C., Lin, Q., Dong, J., Yu, Y. & Wang, L. Mössbauer and Structural properties of La-substituted $Ni_{0.4}Cu_{0.2}Zn_{0.4}Fe_2O_4$ nanocrystalline ferrite. *Sci. Adv. Mater*. **7**, 1809–1815 (2015). doi: 10.1166/sam.2015.2394.

193. Gupta, M. & Randhawa, B. S. Mössbauer, magnetic and electric studies on mixed Rb-Zn

ferrites prepared by solution combustion method. *Mater. Chem. Phys*. **130**, 513–518 (2011). doi: 10.1016/j.matchemphys.2011.07.017.

194. Guivar, J. A. R., Flores, A. B. J., Santillan, M. M., Martínez, A. M. O. A. I. & Barnes, L. D. L. S. V. C. H. W. Mössbauer study of intermediate superparamagnetic relaxation of maghemite (γ-Fe_2O_3) nanoparticles. *Hyperfine Interact*. (2013) doi:10.1007/s10751-013-0864-z.

195. Ghasemi, A., Paesano, A. Machado, C. F. C., Shirsath, S. E., Liu, X. & Morisako, A. Mössbauer spectroscopy, magnetic characteristics, and reflection loss analysis of nickel-strontium substituted cobalt ferrite nanoparticles. *J. Appl. Phys*. **115**, 2012–2015 (2014). doi: 10.1063/1.4866232.

196. Yousef, A., Lee, C, G., Alimuddin, B. K. M., Kumar, S., Koo, B. H. & Farea, A. M. M. Mössbauer studies of $Co_{0.5}Cd_xFe_{2.5-x}O_4$ ($0.0 \leqslant x \leqslant 0.5$) ferrite. *Phys. B Condens*. Matter **403**, 3604–3607 (2008). doi: 10.1016/j.physb.2008.06.001.

197. Druc, A. C., Borhan, A. I., Diaconu, A., Iordan, A. R., Nedelcu, G. G., Leontie, L. & Palamaru, M. N.. How cobalt ions substitution changes the structure and dielectric properties of magnesium ferrite. *Ceram. Int*. **40**, 13573–13578 (2014). doi:10.1016/j.ceramint.2014.05.071.

198. Kumar, D. R., Ahmad, S. I., Lincoln, C. A., Ravinder, D., Kumar, D. R., Ahmad, S. I. & Ravinder, D. Structural, Optical, Room-temperature and Low-temperature Magnetic Properties of Mg-Zn Nanoferrite Ceramics. *J. Asian Ceram. Soc*.**7(1)**, 53-68 (2018). doi: 10.1080/21870764.2018.1563036.

199. Chandekar, K. V & Kant, K. M. Synthesis and characterization of low temperature superparamagnetic cobalt ferrite nanoparticles. *Advanced Materials Letters*. **8**, 435–443

(2017). doi:10.5185/amlett.2017.6900.

200. Dragu, D. & Bleotu, C. Synthesis and characterization of new magnetite nanoparticles by using the different amino acids such as stabilizing agents Synthesis And Characterization Of New Magnetite Nanoparticles By Using The Different Amino Acids Such As Stabilizing Agents. *U.P.B. Sci. Bull., Series B*. **80**(1) 33-45 (2018). ISSN:1454-2331.

201. Zeeshan, T., Anjum, S., Iqbal, H. & Zia, R. Substitutional effect of copper on the cation distribution in cobalt chromium ferrites and their structural and magnetic properties. *Materials Science-Poland*. **36(2)**, 255–263 (2018). doi:10.1515/msp-2018-0011.

202. Soler, M. A. G., Lima, E. C. D., Da Silva, S. W., Melo, T. F. O., Pimenta, A. C. M., Sinnecker, J. P., Azevedo, R. B., Garg, V. K., Oliveira, A. C., Novak, M. A., Morais, P. C., Quı, I. D. F. & Instituto, D. Aging Investigation of Cobalt Ferrite Nanoparticles in Low pH Magnetic Fluid. *Langmuir*. **23(19)**, 9611–9617 (2007). doi: 10.1021/la701358g.

203. Galinetto, P., Albini, B., Bini, M. & Mozzati, M. C. Raman Spectroscopy in Zinc Ferrites Nanoparticles Raman Spectroscopy in Zinc Ferrites Nanoparticles. *Raman Spectroscopy (InTech*, 2018). doi:10.5772/intechopen.72864.

204. Mund, H. S. & Ahuja, B. L. Structural and magnetic properties of Mg doped cobalt ferrite nano particles prepared by sol-gel method. *Mater. Res. Bull*. (2016) doi:10.1016/j.materresbull.2016.09.027.

205. Kreisel, J., Lucazeau, G. & Vincent, H. Raman Spectra and Vibrational Analysis of $BaFe_{12}O_{19}$ Hexagonal Ferrite. *Journal of Solid State Chemistry*. **137**, 127–137 (1998).

206. Soler, M. A. G., Melo, T. F. O., Da Silva, S. W., Lima, E. C. D., Pimenta, A. C. M., Garg, V. K. & Morais, P. C. . Structural stability study of cobalt ferrite-based nanoparticle using micro Raman spectroscopy. *Journal of Magnetism and Magnetic Materials*. **276**, 2357–

2358 (2004). doi:10.1016/j.jmmm.2003.12.582.

207. Ita, C. O. E. B. I. & Iweala, E. E. J. Low-temperature combustion synthesis of cobalt magnesium ferrite magnetic nanoparticles : effects of fuel-to-oxidizer ratio and sintering temperature. *J. Sol-Gel Sci. Technol*. (2015) doi:10.1007/s10971-015-3777-2.

208. Wu, X., Ding, Z., Song, N., Li, L. & Wang, W. Effect of the rare-earth substitution on the structural , magnetic and adsorption properties in cobalt ferrite nanoparticles. *Ceram. Int*. 1–10 (2015) doi:10.1016/j.ceramint.2015.11.100.

209. Malekfar, R., Parishani, M. & Cheraghi, A. Spectroscopy , Structural , and Optical Investigations of $NiFe_2O_4$ Ferrite. *International Journal of Optics and Photonics*. **9**, 73–78 (2015).

210. Islam, M. A., Hasan, M. R., Haque, M. M., Rashid, R., Syed, I. M., & Hoque, S. M. Efficacy of surface-functionalized $Mg_{1-x}Co_xFe_2O_4$ $(0 \leq x \leq 1; \quad \Delta x = 0.1)$ for hyperthermia and in vivo MR imaging as a contrast agent. *RSC Adv*. **12**, 7835–7849 (2022). doi: 10.1039/d2ra00768a.

211. Arakha, M., Pal, S., Samantarrai, D. & Panigrahi, T. K. Antimicrobial activity of iron oxide nanoparticle upon modulation of nanoparticle-bacteria interface. *Nat. Publ. Gr*. 1–12 doi:10.1038/srep14813.

212. Alborzi, Z., Hassanzadeh, A., & Golzan, M. M. Superparamagnetic Behavior of the Magnetic Hysteresis Loop. *Int. J. Nanosci. Nanotechnol*. **8(2)**, 93–98(2012). URL: http://ijnnonline.net/pdf_3911_8518066af2eba06ebe9780fcbf1a091d.html.

213. Franco, A. & Silva, M. S. High temperature magnetic properties of magnesium ferrite nanoparticles. J. Appl. Phys. **109**, 2011–2014 (2011). doi: 10.1063/1.3536790.

214. Anis-ur-Rehman, M., Ali-Malik, M., Khan, K. & Maqsood, A. Structural, Electrical and

Magnetic Properties of Nanocrystalline Mg-Co Ferrites Prepared by Co-Precipitation. *J. Nano Res.* **14**, 1–9 (2011). doi: 10.4028/www.scientific.net/jnanor.14.1.

215. Mund, H. S. & Ahuja, B. L. Structural and magnetic properties of Mg doped cobalt ferrite nano particles prepared by sol-gel method. *Mater. Res. Bull*. **85**, 228–233 (2017). doi:10.1016/j.materresbull.2016.09.027.

216. Pervaiz, E. & Gul, I. H. Structural , Electrical and Magnetic Studies of Gd Nanoparticles doped Cobalt Ferrite. *Int. J. Curr. Eng. Technol*. 377–387 (2012) doi:10.4414/smw.2015.14210.

217. Girgis, E., Wahsh, M. M. S., Othman, A. G. M., Bandhu, L. & Rao, K. V. Synthesis , magnetic and optical properties of core/shell $Co_{1-x}Zn_xFe_2O_4/SiO_2$ nanoparticles. *Nanoscale Research Letters*. 2–9 (2011). URL:http://www.nanoscalereslett.com/content/6/1/460.

218. Franco, A., Silva, F. C., Franco, A. & Silva, F. C. High temperature magnetic properties of cobalt ferrite nanoparticles. *J. Appl. Phys*. **172505**, 2010–2013 (2012). doi:10.1063/1.3536790.

219. Prasetyaningrum, P. W., Bahtiar, A. & Hayun, H. Synthesis and cytotoxicity evaluation of novel asymmetrical mono-carbonyl analogs of curcumin (AMACs) against vero, HeLa, and MCF7 cell lines. *Sci. Pharm*. **86**, (2018). doi: 10.3390/scipharm86020025.

220. Krishna, V. A. & Mohandass, S. In-vitro cytotoxic activity of Enicostemma axillare extract against HeLa cell line. *Int. J. Pharmacogn. Phytochem. Res*. **6**, 320–323 (2014). ISSN: 09754873.

221. Lee, J. H., Jang, J., Choi, J., Moon, S., Noh, S., Kim, J., Kim, J., Kim, I., Park, K. & Cheon, J. Exchange-coupled magnetic nanoparticles for efficient heat induction. *Nat. Nanotechnol*. **6**, 418–422 (2011). doi:10.1038/nnano.2011.95.

222. Joshi, H. M., Lin, Y., Aslam, M., Prasad, P., Schultz-Sikma, E., Edelman, R., Meade, T. & Dravid, V.. Effects of shape and size of cobalt ferrite nanostructures on their MRI contrast and thermal activation. *J. Phys. Chem. C*. **113**, 17761–17767 (2009). doi:10.1021/jp905776g.

223. Okon, E. U., Hammed, G., Abu, P., Wafa, E., Abraham, O., Case, N., & Henry, E. In-vitro cytotoxicity of Polyethyleneimine on HeLa and Vero Cells. *International Journal of Innovation and Applied Studies*. **5**, 192–199 (2014). ISSN:2028-9324.

224. Kumar, G., Rani, R., Sharma, S., Batoo, K. M. & Singh, M. Electric and dielectric study of cobalt substituted MgMn nanoferrites synthesized by solution combustion technique. *Ceram. Int*. **39**, 4813–4818 (2013). doi: 10.1016/j.ceramint.2012.11.071.

225. Suryanarayana, C., Norton, M. G. Precise Lattice Parameter Measurements. In X-Ray Diffraction. *Springer US*. 153–166 (1998).doi:10.1007/978-1-4899-0148-4_6.

226. Hossein-Zadeh, M. & Mirzaee, O. Synthesis and characterization of V_8C_7 nanocrystalline powder by heating milled mixture of V_2O_5, C and Ca via mechanochemical activation. *Advanced Powder Technology*. **25(3)**, 978-982 (2014). doi: 10.1016/j.apt.2014.01.017.

227. Lee, S. & Randall, C. A. A modified Vegard's law for multisite occupancy of Ca in $BaTiO_3$ -$CaTiO_3$ solid solutions. *Appl. Phys. Lett*. **92**, 1–4 (2008). doi:10.1063/1.2857475.

228. Mukherjee, S., Ranjan, V., Gupta, R. & Garg, A. Composition Dependence of Structural Parameters and Properties of Gallium Ferrite. *ArXiv Preprint ArXiv*: 1107.3623 (2011). URL:http://arxiv.org/abs/1107.3623.

229. Patange, S. M., Shirsath, S. E., Jangam, G. S., Lohar, K. S., Jadhav, S. S., & Jadhav, K. M. Rietveld structure refinement, cation distribution and magnetic properties of Al^{3+} substituted $NiFe_2O_4$ nanoparticles. *J. Appl. Phys.* **109**, (2011). doi:10.1063/1.3559266.

230. Pandit, A. A., More, S. S., Dorik, R. G. & Jadhav, K. M. Structural and magnetic properties of $BiFe_{1-x}Cr_xO_3$ synthesized samples. *Bull. Mater. Sci*. **26**, 517–521 (2003).

231. Ortiz-Quiñonez, J. L., Umapada, P. & Martin, S. VillanuevaStructural, Magnetic, and Catalytic Evaluation of Spinel Co, Ni, and Co–Ni Ferrite Nanoparticles Fabricated by Low-Temperature Solution Combustion Process. *ACS Omega*. **3 (11)**, 14986-15001 (2018). doi: 10.1021/acsomega.8b02229.

232. Datasheet Velox. The imaging and analysis engine for your applications, *Thermoscientific*. URL:https://assets.thermofisher.com/TFS-Assets/MSD/Datasheets/velox-datasheet.pdf.

233. Lu, P., Romero, E., Lee, S., Macmanus-driscoll, J. L. & Jia, Q. Chemical Quantification of Atomic-Scale EDS Maps under Thin Specimen Conditions. *Microsc. Microanal*. **20**, 1782–1790 (2014) doi:10.1017/S1431927614013245.

234. Allen, L. J., Alfonso, A. J. D., Findlay, S. D., LeBeau, J. M., Lugg, N. R. & Stemmer, S. Elemental mapping in scanning transmission electron microscopy. *Journal of Physics: Conference series*. **241**, (2010). doi:10.1088/1742-6596/241/1/012061.

235. Galinetto, P., Albini, B., Bini, M. & Mozzati, M. C. Raman spectroscopy in Zinc Ferrites Nanoparticles. Raman Spectrosc. 223-251 (2018). doi:10.5772/intechopen.72864.

236. Gore, R. C. Infrared Spectroscopy. *Analytical Chemistry*. **30,** 570–579 (1958). doi: 10.1021/ac50163a004.

237. Goodarz, M., Hossein, M., Ara, M., Saion, E. B. & Halim, A. Superparamagnetic

magnesium ferrite nanoparticles fabricated by a simple, thermal-treatment method. *J. Magn. Magn. Mater*. **350**, 141–147 (2014). doi:10.1016/j.jmmm.2013.08.032.

238. Gadkari, A. B., Shinde, T. J. & Vasambekar, P. N. Structural analysis of Y^{3+} -doped Mg – Cd ferrites prepared by oxalate co-precipitation method. *Materials Chemistry and Physics*. **114**, 505–510 (2009). doi:10.1016/j.matchemphys.2008.11.011.

239. Pawlak, A. & Mucha, M. Thermogravimetric and FTIR studies of chitosan blends. *Thermochimica Acta*. **396**, 153–166 (2003). doi:10.1016/S0040-6031(02)00523-3.

240. Sobhanadri, J. The Far-Infrared Spectra of Some Mixed Cobalt Zinc and Magnesium Zinc Ferrites. *Phys. stat. sol*. (a). **65(2)**, 479–483 (1981). issn:0031-8965.

241. Sharma, R., Thakur, P., Kumar, M., Thakur, N., Negi, N. S., Sharma, P., & Sharma, V. Improvement in magnetic behaviour of cobalt doped magnesium zinc nano-ferrites via co-precipitation route. *J. Alloys Compd*. **684**, 569–581 (2016). doi:10.1016/j.jallcom.2016.05.200.

242. Rana, S., Philip, J. & Raj, B. Micelle based synthesis of cobalt ferrite nanoparticles and its characterization using Fourier Transform Infrared Transmission Spectrometry and Thermogravimetry. *Mater. Chem. Phys*. **124**, 264–269 (2010). doi:10.1016/j.matchemphys.2010.06.029

243. Yu, Q. & Su, Y. Synthesis and characterization of low-density porous nickel zinc ferrites. *RSC Advances*. **9**, 13173–13181 (2019) doi:10.1039/c9ra01076a.

244. Singh, G., Kapoor, I. P. S., Dubey, S., Siril, P. F., Yi, J. H., Zhao, F. Q. & Hu, R. Z. Effect of mixed ternary transition metal ferrite nanocrystallites on thermal decomposition of ammonium perchlorate. *Thermochimica Acta*. **477**, 42–47 (2008). doi:10.1016/j.tca.2008.08.005.

245. Taylor, P., Rajput, A. B., Hazra, S. & Ghosh, N. N. Synthesis and characterisation of pure single-phase $CoFe_2O_4$ nanopowder via a simple aqueous solution-based EDTA- precursor route. *Journal of Experimental Nanoscience*. **8(4)**, 629–639 (2013). doi:10.1080/17458080.2011.582170.

246. Bujoreanu, V. M. & Segal, E. Dsc Study Of Water Elimination From The Coprecipitated Ferrite Powders. *Journal of Thermal Analysis and Calorimetry*. **68**, 191–197 (2002).

247. Ehi-eromosele, C. Low-temperature combustion synthesis of cobalt magnesium ferrite magnetic nanoparticles: effects of fuel-to-oxidizer ratio and sintering temperature. *J. Sol-Gel Sci. Technol*. **76**, 298–308 (2015). doi:10.1007/s10971-015-3777-2.

248. Ajroudi, L., Mliki, N., Bessais, L., Madigou, V., Villain, S. & Leroux, C. Magnetic , electric and thermal properties of cobalt ferrite nanoparticles. *Mater. Res. Bull.* **59**, 49–58 (2014). doi:10.1016/j.materresbull.2014.06.029.

249. Streckova, M., Mudra, E., Sebek, M., Sopcak, T., Dusza, J. & Kovac, J. Preparation and Investigations of $Ni_{0.2}Zn_{0.8}Fe_2O_4$ Ferrite Nanofiber Membranes by Needleless Electrospinning Method. *Acta Physica Polonica A*. **131**, 729–731 (2017). doi:10.12693/APhysPolA.131.729.

250. Warsi, M. F., Gilani, Z. A. A., Al-Khalli, N. F., Sarfraz, M., Khan, M. A. A., Anjum, M. N. N. & Shakir, I. New $LiNi_{0.5}Pr_xFe_{2-x}O_4$ nanocrystallites: Synthesis via low cost route for fabrication of smart advanced technological devices. *Ceramics International*. **43(17)**, 14807–14812 (2017). doi: 10.1016/j.ceramint.2017.07.228.

251. Li, Q., Kartikowati, C. W., Horie, S., Ogi, T., Iwaki, T. & Okuyama, K. Correlation between particle size/domain structure and magnetic properties of highly crystalline Fe_3O_4 nanoparticles. *Sci. Rep*. **7**, 1–4 (2017). doi:10.1038/s41598-017-09897-5.

252. Smolenskya, E. D., Parka, H. Y. E., Zhoua, Y., Rollab, G. A., Marjańskac, M., Bottab, M. & Pierre V. C.. Scaling Laws at the Nano Size: The Effect of Particle Size and Shape on the Magnetism and Relaxivity of Iron Oxide Nanoparticle Contrast Agents. *J. Mater Chem B Mater Biol Med*. **1(22)**, 2818–2828 (2013). doi:10.1039/C3TB00369H.

253. Mazumder, R., Ghosh, S., Mondal, P., Bhattacharya, D., Dasgupta, S., Das, N., Sen, A., Tyagi, A., Sivakumar, M., Takami, T. & Ikuta, H. Particle size dependence of magnetization and phase transition near T N in multiferroic $BiFeO_3$. *J. Appl. Phys*. **100**, (2006).doi: 10.1063/1.2229667.

254. Yerin, C. V. Particles size distribution in diluted magnetic fluids. *J. Magn. Magn. Mater*. **431**, 27–29 (2017). doi: 10.1016/j.jmmm.2016.09.122.

255. Habib, A. H., Ondeck, C. L., Chaudhary, P., Bockstaller, M. R. & McHenry, M. E. Evaluation of iron-cobalt/ferrite core-shell nanoparticles for cancer thermotherapy. *J. Appl. Phys*. **103**, 7–10 (2008). doi:10.1063/1.2830975.

256. Mohapatra, J., Xing, M. & Liu, J. P. Inductive Thermal Effect of Ferrite Magnetic Nanoparticles. Materials. 26–29 (2019). doi:10.3390/ma12193208.

257. Gajbhiye, N. S., Vatsa, R. K., Kumar, A., Tewari, R., Meena, S. S., Sharma, S., Ghosh, R., Pradhan, L., Ningthoujam, R. S., Pandey, B. N. & Devi, Y. P.. Induction heating studies of Fe_3O_4 magnetic nanoparticles capped with oleic acid and polyethylene glycol for hyperthermia. *J. Mater. Chem*. **21**, 13388 (2011). doi: 10.1039/c1jm10092k.

258. Islam, M. K., Haque, M. M, Rashid, R., Hasan, M. R., Islam, M. A., Khan, M. N. I. & Hoque, S. M.. Size Effect on MRI/MFH Relaxations by a High Anisotropic $CoFe_2O_4$-Chitosan Conjugate and Imaging/Angiography Efficacy. *J. Inorg. Organomet. Polym. Mater*. **32**, 3459–3475 (2022). doi: 10.1007/s10904-022-02381-2Size.

259. Greene, D., Serrano-garcia, R., Govan, J. & Gun, Y. K. Synthesis Characterization and Photocatalytic Studies of Cobalt Ferrite-Silica-Titania Nanocomposites. *Nanomaterials*. 331–343 (2014) doi:10.3390/nano4020331.

260. Capeletti, L. B. & Zimnoch, J. H. Fourier Transform Infrared and Raman Characterization of Silica-Based Materials. *Appl. Mol. Spectrosc. to Curr. Res. Chem. Biol. Sci*. 3–22 (2016) doi:10.5772/64477.

261. Lesiak, B., Rangam, N., Jiricek, P., Gordeev, I., Tóth, J., Kövér, L., Mohai, M. & Borowicz, P.. Surface Study of Fe_3O_4 Nanoparticles Functionalized With Biocompatible Adsorbed Molecules. *Front. Chem*. **7**, (2019).doi:10.3389/fchem.2019.00642.

262. Danaei, M., Dehghankhold, M., Ataei, S., Hasanzadeh Davarani, F., Javanmard, R., Dokhani, A. & Mozafari, M. R.. Impact of particle size and polydispersity index on the clinical applications of lipidic nanocarrier systems. *Pharmaceutics*. **10**, 1–17 (2018). doi:10.3390/pharmaceutics10020057.

263. Clayton, K. N., Salameh, J. W., Wereley, S. T. & Kinzer-Ursem, T. L. Physical characterization of nanoparticle size and surface modification using particle scattering diffusometry. *Biomicrofluidics*. **10**, (2016). doi: 10.1063/1.4962992.

264. Almessiere, M., Slimani, Y., Güner, S., Nawaz, M., Baykal, A., Aldakheel, F., Akhtar, S., Ercan, I., Belenli & Ozçelik, B. Magnetic and structural characterization of Nb^{3+} - substituted $CoFe_2O_4$ nanoparticles. *Ceram. Int*. **45**, 8222–8232 (2019).

265. Anis-Ur-rehman, M., Malik, M. A., Khan, K. & Maqsood, A. Structural, electrical and magnetic properties of nanocrystalline Mg-Co ferrites prepared by co-precipitation. *J. Nano Res*. **14**, 1–9 (2011). doi:10.4028/www.scientific.net/jnanor.14.1.

266. Adan, A., Kiraz, Y. & Baran, Y. Cell Proliferation and Cytotoxicity Assays. *Curr. Pharm.*

Biotechnol. **17**, 1213–1221 (2016). doi:10.2174/1389201017666160808160513.

267. Mahto, S. K. & Chandra, P. In vitro Models, Endpoints and Assessment Methods for the Measurement of Cytotoxicity. *Toxicol. Environ. Health. Sci*. **2**(2) 87-93 (2010).

268. Zhang, M. Q., Sun, D. N., Xie, Y. Y., Xia, J., Long, H. Y., Xiao, B. Three-dimensional visualization of rat brain microvasculature following permanent focal ischaemia by synchrotron radiation. *Br. J. Radio*. **87**, 1-8 (2014) doi:10.1259/bjr.20130670.

269. Malinova, V., Psychogios, M. N., Tsogkas, I., Koennecke, B., Bleuel, K., Iliev, B., Rohde, V. & Mielke, D.. MR-angiography allows defining severity grades of cerebral vasospasm in an experimental double blood injection subarachnoid hemorrhage model in rats. *PLoS ONE*. **12(2)**, e0171121 (2017) doi:10.1371/journal.pone.0171121.

List of Publications based on this work

1. Islam, M. A., Hasan, M. R., Haque, M. M., Rashid, R., Syed, I. M., & Hoque, S. M. Efficacy of surface-functionalized $Mg_{1-x}Co_xFe_2O_4$ ($0 \leq x \leq 1$; $\Delta x = 0.1$) for hyperthermia and in vivo MR imaging as a contrast agent. *RSC Adv*. **12**, 7835–7849 (2022). doi: 10.1039/d2ra00768a.

2. Islam, M. A., Syed, I. M., Mamun, M. A. & Hoque, S. M. Effect of particle size and composition on local magnetic hyperthermia of chitosan-$Mg_{1-x}Co_xFe_2O_4$ nanohybrid. *Front. Chem.* **12**, 1–23 (2024). doi: 10.3389/fchem.2024.1347423.